Towards Adaptive Impedance Control for Upper-limb Prostheses

Laura Ferrante

University of Birmingham

School of Computer Science

This dissertation is submitted for the degree of

Doctor of Philosophy

Birmingham **December, 2022**

To my family,
to my teachers

Declaration

I hereby declare that except where specific reference is made to the work of others, the contents of this dissertation are original and have not been submitted in whole or in part for consideration for any other degree or qualification in this, or any other university. This dissertation is my own work and contains nothing which is the outcome of work done in collaboration with others, except as specified in the text and Acknowledgements. This dissertation contains fewer than 65,000 words including appendices, bibliography, footnotes, tables and equations and has fewer than 150 figures.

Laura Ferrante
August 2023

Acknowledgements

I am thankful to many people I met during the years of my PhD, for their unique support, friendship and mentorship.
I would like to thank my supervisor and co-supervisors for their guidance and for helping me to get to this point. I am thankful to Dr Mohan Sridharan for his constant mentorship and support and for taking me on board even if my project covered topics far from those previously explored in our research group. I am grateful to Prof Dario Farina for being available to provide help and guidance, and for hosting me different times in his laboratory. The meeting we had, even if more rare, were extremely valuable and motivating. I am grateful to Dr Claudio Zito for pulling strings before my PhD, allowing me to work on my dream research topic. His professional support and friendship throughout the years have been crucial. I also would like to acknowledge the members of the Bioengineering Laboratory of Imperial College London for welcoming me in their lab, for proving technical support with the experimental set up, and for helping with recruiting patients for my experiments.

These years have been challenging, sometimes alienating, but also inspiring and fun thanks to the friendship of many members of the IRLab, the SciPhy group and other students in Computer Science. In particular, I would like to thank Michael, Ermano, Saif, Mo, Nora, Jinyu, John, Michalina, Mark, Hasra, Martin, Jon, Frances, George, and Danny Potter. I am also in debt to everyone who was patient enough to participate in my experiments, this thesis would not have been possible without their help. I would like to single out Frank and Martin for the most beautiful EMG signals I will ever see. A huge thank to Michalina, Pascal, Mark, Martin and Federico for taking the time to read some chapters and provide feedback on my italian English.

Special thanks go to the following potato-people, for making the past years so much fun and for changing my perception of Birmingham: Flo and Frances for being so welcoming and making me feel like at home all the times, and for keeping me properly hydrated. Martin, for passing the climbing virus, for his company in the lab and the most horrible jokes. Giorgi, for always having good stories that gave me SICK abs, for being extra tall and making me look

extra short. Anastasia, for all our more chilled climbing sessions, for witnessing with me the disappearance of the most needed footholds, for all the eggplant salads. Saif, for sharing the master and the PhD years together, for resetting my standards when I was being unrealistic, and for patiently listening to my nonsense about muscle models and impedance control.

Infine, il grazie più grande va alla mia famiglia, per avermi supportato incondizionatamente, in ogni modo e momento. Le casse di vinello hanno anche aiutato. Un grazie immenso a Federico per avermi spinto a volare in Inghilterra, per essere stato il miglior supporto e la migliore compagnia che potessi desiderare. Questo PhD non sarebbe stato possibile senza di voi.

Abstract

This work presents a novel framework that estimates the human motor intent from surface electromyographic (sEMG) signals and executes the motor intent on a simulated robot, allowing the user to adapt the kinematics and dynamics of a Degree of Freedom in static and dynamic environments.

Adaptation of intrinsic mechanical properties of the arm and hand, during the execution of grasping and manipulation tasks, is crucial for humans to physically interact with unpredictable and dynamic environments. These properties are defined as stiffness, damping and inertia, and determine a complex neuromuscular behaviour known as *impedance*. Consider holding an umbrella and grasping the handhold more firmly to counter the action of the wind blowing. To do this we co-contract flexor and extensor muscles spanning the elbow and the wrist to make the arm more rigid. The action of these muscle groups opposes one another to maintain the arm's posture, but it also contributes to increasing limb impedance. As a result, humans can regulate the limb's kinematics and dynamics independently, according to the task requirements.

Inspired by human motor control, researchers have designed biomimetic controllers to enable such impedance behaviour on robotic systems that physically interact with the environment. The most important and challenging requirement of such controllers is to *adapt the robot's impedance* over time, according to task and environment constraints. This requirement is desirable in different physical human-robot interaction applications, and crucial in motor prostheses control where the human motor intent has to be decoded and implemented in real-time on the artificial limb. The latter is the application domain that motivates the work presented in this thesis.

Today, none of the commercially available prostheses allow the user to simultaneously control the kinematics and impedance of a single degree of freedom of the robotic arm. Motor prostheses use low-density surface electromyography as a human-machine interface to allow the user to communicate their motor intent through muscle contraction. However, the estimation of the impedance properties from sEMG signals is not trivial, due to the low bandwidth of sEMG signals and due to the complexity and redundancy of the human musculoskeletal system.

Methods that attempt to fill this gap typically use sEMG-driven muscle-tendon models that potentially allow to predict the torque applied at the joint and the evolution of the muscle-tendon models state, from which the stiffness and damping of the joint can be obtained. However, none of the existing methods coherently estimates the joint impedance from these models and uses it to implement a variable impedance controller on the robot. While the muscle-tendon models are used to obtain the intended joint kinematics, the joint stiffness and damping are estimated from other models, usually polynomial functions of the sEMG signals. Moreover, the obtained joint stiffness and damping are not directly used as gains in the control law, but these are remapped to suitable ranges to ensure control stability and satisfy hardware requirements. As a result, multiple calibration phases are required, which prevent a coherent implementation of the user's motor intent on the robot and may impact the user's control performance.

This thesis presents an sEMG-driven framework that provides the user with 3 Degrees of Control for a single Degree of Freedom of a simulated robot, actuated through wrist flexion-extension. The framework includes a pair of muscle-tendon models to estimate the motor intent from two sEMG signals in terms of reference joint motion, stiffness and damping. Unlike previous work, the parameter values of the muscle-tendon models are estimated such that the obtained joint stiffness and damping can be used directly to implement a variable impedance controller on the robot. This ensures that the user's intended dynamics, represented by the muscle-tendon models, matches that of the robot, enhancing the framework's transparency in implementing the user's motor intent. As a result, the human subject is able to simultaneously adapt the robot's kinematics and dynamics on-the-fly.

We evaluate our framework with eight able-bodied subjects during reaching tasks performed in free space, and in the presence of unexpected external perturbations that require adaptation of the wrist impedance to ensure stable interaction with the environment. A case study is carried out with a transradial amputee. The proposed framework is compared to a baseline consisting of a purely data-driven method that learns a mapping from sEMG signals to desired joint kinematics and a fixed-gains high-stiffness controller that tracks the estimated kinematics. We investigate whether our framework, which enables kinematics as well as stiffness and damping adaptation, provides improved performance with respect to the baseline. We experimentally demonstrate that our approach outperforms the baseline in terms of its ability to adapt to external perturbations, overall controllability provided to the subject, and feedback from participants on their perceived controllability. The amputee performed similarly to the able-bodied participants, indicating that the proposed framework may provide improved performance for the target population of transradial amputees.

Table of contents

List of figures

List of tables

Nomenclature

List of Acronyms and Abbreviations

B	Baseline
CE	Contractile Element
CNS	Central Nervous System
DE	Damping Element
$DoC(s)$	Degree of Control(s)
$DoF(s)$	Degree of Freedom(s)
ECR	*Extensor Carpi Radialis*
ECU	*Extensor Carpi Ulnaris*
EMG	Electromyography
FCR	*Flexor Carpi Radialis*
FCU	*Flexor Carpi Ulnaris*
HMI	Human-Machine interaction
HRI	Human-Robot Interaction
M	Proposed framework
MTU	Muscle-Tendon Unit
NN	Neural Network
PD	Proportional Derivative

PE Parallel Element

pHRI Physical Human-Robot Interaction

SE Serial Element

sEMG Surface ElectroMyoGraphy

List of Symbols

$\ddot{q}$	Generic vector of joint angular acceleration	$[\mathrm{rad/s^2}]$
$\ddot{q}_f$	joint acceleration of the *robot plant* in the prosthesis control block of the framework	$[\mathrm{rad/s^2}]$
$\ddot{q}_r$	joint acceleration of the *simulated robot model* in the detection of motor intent block of the framework	$[\mathrm{rad/s^2}]$
$\dot{q}$	Generic vector of joint angular velocity	$[\mathrm{rad/s}]$
$\dot{q}_f$	joint velocity of the *robot plant* in the detection of motor intent block of the framework	$[\mathrm{rad/s}]$
$\dot{q}_r$	joint velocity of the *simulated robot model* in the detection of motor intent block of the framework	$[\mathrm{rad/s}]$
τ	Vector of joint torques	[Nm]
τ_{ext}	Vector of external joint torques in the framework	[Nm]
τ_f	Joint torques output by the impedance controller in the framework	[Nm]
τ_r	Net joint torque obtained from muscle-tendon models	[Nm]
a	Normalised input activation	–
ch	Processed and normalised sEMG signals input to the framework	–
D	Damping of the MTU mapped to joint space in the proposed framework	$[\mathrm{N/rad^2}]$
D_i	Damping of the muscle-tendon model i	$[\mathrm{N/m^2}]$
D_{MTU}	Damping of MTU	$[\mathrm{N/m^2}]$
D_m	Damping of the muscle component	$[\mathrm{N/m^2}]$

D_t	Damping of the tendon component	$[\mathrm{N/m^2}]$
E	Matrix of 8 raw sEMG signals	[mV]
F_{ce}^i	Force of CE element of muscle-tendon unit i	[N]
F_{de}^i	Force of DE element of muscle-tendon unit i	[N]
F_i	Force of muscle-tendon unit i	[N]
F_{pe}^i	Force of PE element of muscle-tendon unit i	[N]
F_{se}^i	Force of SE element of muscle-tendon unit i	[N]
K	Stiffness of the MTU mapped to joint space in the proposed framework	[N/rad]
K_i	Stiffness of the muscle-tendon model i	[N/m]
K_{MTU}	Stiffness of MTU	[N/m]
K_m	Stiffness of the muscle component	[N/m]
K_t	Stiffness of the tendon component	[N/m]
l_{ce}	Contractile component length	[m]
l_{MTU}	Muscle-tendon unit length	[m]
q	Generic vector of joint angular position	[rad]
q_f	joint position of the *robot plant* in the prosthesis control block of the framework	[rad]
q_r	joint position of the *simulated robot model* in the detection of motor intent block of the framework	
R	Jacobian of moment arms	[m/rad]
r	Moment arm for a muscle-tendon unit	[m/rad]
s_f	Vector of joint state of the *robot plant* in the prosthesis control block of the framework	
s_r	Vector of joint state of the *simulated robot model* in the detection of motor intent block of the framework	[rad]

Chapter 1

Introduction

Consider the simple task of holding an umbrella on a rainy and windy day. Forces arise from the *physical interaction* between the umbrella, the human hand and any perturbation imposed by the wind. To successfully perform this task, humans adapt intrinsic mechanical properties of the limb, known as the stiffness, damping and inertia, to modify the overall limb's *impedance* [94, 144]. Impedance modulation is achieved by modulating the co-activation of agonist and antagonist muscles of the upper limb. This motor control strategy allows humans to make the physical interaction with the umbrella stable by rejecting the perturbations imposed by the wind. As the muscles' co-contraction is increased, the limb becomes less and less compliant to external forces until the force imposed by the wind will not cause any displacement to the human arm. While in this example increasing the limb impedance is necessary to counter the wind's action and maintain the limb's posture, other tasks require our limb to be compliant (i.e., have low impedance). Think about a peg-in-hole type of task. In this case, low limb impedance is needed to reduce the interaction forces that may arise when we insert the object in the hole. Compliance allows us to afford lower manipulation precision and avoid damaging the object or hurting our hand.

Modulation of the *impedance properties* of the robot is thus a crucial aspect in prostheses control given that the user operates in an unpredictable dynamic environment where forces may arise from the mechanical interaction between the prosthetic limb (i.e., robot) and the environment. Despite the efforts of industrial and academic research, enabling the user to voluntarily adapt the impedance of the prosthesis is still an open problem.

This thesis is concerned with enabling a human subject to modulate the impedance of a robotic system. In particular, the main objective is to develop a computational framework that allows a human user to simultaneously control the kinematic (i.e., joint position, velocity, and acceleration) and dynamic properties (i.e., joint stiffness and damping) of a Degree of Freedom (DoF) of a robotic system.

In this Chapter, we describe the driving motivation of this thesis as well as the aims and the contributions of this work. Section 1.1 starts by briefly introducing impedance adaptation of the limb as a crucial motor control strategy for physically interacting with dynamic and unpredictable environments. We then explain why this control strategy is beneficial to any manipulator, human or robotic. In particular, we discuss why allowing the user to modulate the impedance of the robot is essential in upper-limb prostheses control. The latter is the chosen application domain of the work presented in this thesis. We continue by providing an overview of the state-of-the-art methods for the detection and the implementation of the user's motor intent for prostheses control. We conclude the section by discussing the inherent difficulties and open problems in prostheses control and by listing the limitations we address in this thesis. In Section 1.2, we state the research aim and questions. We then describe the contributions and the assumptions – some of which are limitations – of this work (Section 1.2), the research approach and evaluation methods (Section 1.3). Finally, we provide a road map for this thesis (Section 1.4).

1.1 Motivation

Most tasks of everyday life require us to *physically* interact with the environment around us. This physical interaction can involve the grasping or the manipulation of objects. Think about carrying a cup of coffee or the previous example of holding an umbrella when it is windy outside. We execute these tasks effortlessly even if we manipulate highly complex objects with properties that might not be known a priori. Coffee for example contains infinite internal DoFs, and the wind imposes unexpected perturbations on the umbrella we are holding. These are sources of uncertainty that make the physical interaction with the environment potentially unstable. Understanding why humans are exceptionally skilful at these tasks is an ongoing topic of research.

There is evidence suggesting that humans are able to adapt their sensorimotor control to learn and modulate the dynamics of their physical interaction with the environment [98, 69, 170]. In particular, experimental studies have shown that humans leverage adaptation of the limb's impedance to implicitly regulate the forces arising from the mechanical interaction between the human limb and the environment while robustly performing a task. The term *impedance* summarises three properties that quantify the resistance that the limb opposes to a change in position, velocity, and acceleration [97]: stiffness, damping and inertia, respectively. Impedance adaptation of the human limb exploits intrinsic properties of the musculotendinous tissue, and it is mainly achieved through co-activation of agonist and antagonist muscles spanning a joint and through neural feedback. While neural feedback

responses are characterised by a transmission latency, muscle co-activation allows prompt adaptation of the limb's impedance to interaction forces [125]. Considering the example introduced earlier, to keep the umbrella upright and counter the perturbations imposed by the wind, we would increase muscle contractions to grasp the handle more firmly. More specifically, we adapt the co-contraction of the agonist and antagonist muscles spanning the wrist joint to increase the "rigidity" of the arm and hand: the forces generated by these muscle groups oppose one another resulting in a null net torque around the joint and consequently no wrist movement is generated. However, the increase in muscles' co-activation contributes to increasing the rigidity of the limb which allows us to resist external perturbations.

Any manipulator, human or robotic, needs to be capable of adapting the limb's mechanical impedance to robustly operate in dynamic and unpredictable environments. Especially in physical human-robot interaction (pHRI) scenarios, controlling the mechanical impedance of the robotic system is desirable for robustly and safely interacting with humans. This requirement is more pronounced in prostheses control because the user and the robot are two agents of the same system, and the human motor intent has to be replicated on the prosthesis.

While there has been considerable progress in designing upper-limb prostheses that possess hardware compliance, none are yet capable of replicating the functions that neuro-muscular impedance control makes possible. This is due to the difficulties in decoding the human motor intent from the Human-Machine-Interfaces (HMIs) used to connect a human user to the prosthetic device. There are two main reasons for this. Firstly, the most widely used HMI is based on surface Electromyography (sEMG). Surface EMG sensors are used to measure the electrical activity of muscles involved in certain motor functions from which the human motor intent is decoded and executed on the prosthesis. Using sEMG was a breakthrough in technology since it allowed to implement non-invasive and easy-to-use HMIs for active prostheses control. However, sEMG also constitutes the technological bottleneck in the research field of motor prostheses, since it provides noisy low-bandwidth signals that make the problem of decoding the human motor intent highly challenging. Secondly, the human motor control and musculoskeletal system are highly complex and redundant: there is a non-unique association between muscle activation (recorded by the sEMG sensors) and joint kinematics, since the same action can be performed at different levels of muscles' co-contraction (i.e., impedance). In fact, considering the example introduced earlier, we can modulate the muscles' activation to increase the limb's rigidity while maintaining the umbrella in the same configuration. This means that limb's kinematics does not change. The ambiguity in associating changes in muscles' activation to changes in joint kinematics and dynamics is what makes the detection of the motor intent from sEMG signals challenging.

As a result, none of the commercially available prostheses allow the user to simultaneously control the kinematics and the impedance of a DoF.

The state of the art in prostheses control are data-driven methods that learn a direct mapping from sEMG signal to desired kinematics (i.e., motor command) during an offline training phase [152, 109]. These approaches are effective for simple movements in controlled experimental settings, where the task is executed in the absence of external perturbations and the human's muscle activation is kept low. However, these methods do not explicitly represent or use information about the human joint impedance in the controllers. As a result, the control performance deteriorates in practical settings where factors such as the physical interactions with the environment require the user to continuously adapt the muscles' contraction to control the prosthesis. This causes the features of the sEMG signals to change drastically from those observed during the training phase. Moreover, decoding the human motor intent only in terms of kinematics provides a limited representation of the user's intent and makes it difficult for designers and users to understand the prosthesis' operation. In general, this category of purely data-driven methods lacks of evaluation of the methods' robustness to changes in muscles' co-activation, in scenarios where impedance adaptation is required to maintain the system stability.

Methods pursued by researchers to provide simultaneous control of joint kinematics and impedance often employ muscle-tendon models to include domain knowledge about muscle force generation (i.e., muscle contraction dynamics). These muscle-tendon models are sEMG-driven and allow for predicting the muscle contraction dynamics and thus provide an estimation of the muscle-tendon model state, forces and impedance properties; from these muscle-tendon quantities, it is possible to estimate the human motor intent as joint kinematics and impedance. However, works found in literature use partial information from the muscle-tendon models. Typically only the estimated muscle-tendon forces are used to compute the net joint torque and to obtain the intended joint kinematics. Stiffness is not obtained from the muscle-tendon models but estimated from sEMG signals using linear models or other polynomial functions; damping is omitted or computed as a function of stiffness. Moreover, the estimated joint stiffness and damping are not directly used as gains of the controller implemented on the robotic system, but are tuned during a calibration stage, often separated from the optimisation of muscle-tendon models, to satisfy the controller's stability constraints. This approach requires multiple calibration phases, and it creates a mismatch between the dynamics of the muscle-tendon model and the dynamics of the robot. This may affect the user's control performance (i.e., controllability) and limit the transparency of the control methods. In summary, *none of the existing methods estimate the muscle impedance from the*

muscle-tendon models and use it directly to implement a joint space impedance controller on a robotic system.

This thesis investigates the problem of improving the detection of the user motor intent from low bandwidth sEMG signals and implementing this intent on a simulated robotic system. The domain of application chosen for this work is upper-limb prostheses and, in particular, the focus is on the wrist flexion-extension motor function. This is motivated by experimental findings suggesting that wrist control is crucial for successful human-like dexterous grasping and manipulation [148]. Manipulation tasks of daily living are achieved by humans primarily through wrist control while ensuring a stable grasp of the object (e.g., to open a bottle, this is grasped tightly while the wrist rotates the bottle's cap). The wrist must be oriented in a suitable configuration to grasp an object, and the choice of the wrist pose affects the range of feasible grasps and the maximum grip strength that can be applied to the object. Moreover, wrist control is fundamental to maintaining grasp stability during manipulation tasks and adaptation of its impedance directly allows humans to modify impedance at the interaction port with the external environment. A prosthetic device capable of independent finger control for dexterous hand manipulation is thus unlikely to succeed in grasping and manipulation tasks if the user is incapable of actively controlling the wrist.

1.2 Research aim and contributions

The objective of the thesis is to address the limitations discussed in the previous section. In this regard, we propose an sEMG-driven framework that includes the user in the control loop and provides the human subject with three Degrees of Control (DoC), i.e., the control of joint position, stiffness, and damping, per DoF of an upper-limb prosthesis.

The research approach to design the framework ranges from models and algorithms development to experimental design and analysis. One important objective of the framework's design is to gain insight into the representation of the human motor intent and the working principles of the models being used. This is crucial to enhance the transparency of prostheses control. To address this research problem, the following contributions are made [66]:

1. We describe a novel framework to decode the human motor intent about wrist flexion-extension in the form of joint motion, stiffness, and damping, and implement the motor intent on a simulated 1-DoF robot (Chapter 4). The framework can be divided into two components which are nevertheless strictly interconnected. The first block (Section 4.3) of the framework incorporates muscle-tendon models and maps the sEMG signals to an estimate of the user's motor intent in terms of kinematics (i.e., joint position) and impedance (i.e., joint stiffness and joint damping). The inertia is assumed to be the

natural inertia of the robot, as it will be discussed in the framework's design. The second block (Section 4.4) executes this motor intent through a simulated robot system based on a variable position-based impedance controller, allowing online position control and adaptation of the robot's impedance. The variable impedance controller implicitly allows the user to counter external perturbations.

The approach followed for the framework's design is based on the concept that the human user and the robot are two mechanically coupled systems and as a consequence, the muscle-tendon dynamics (which represents the user's intended dynamics) has to match the simulated robot's dynamics. To ensure that the intended dynamics given by the first block matches the robotic system's dynamics (second block), the impedance properties estimated from the muscle-tendon models (i.e., the user's intended dynamics), unlike in prior work, are used directly to implement the dynamic behaviour of the robotic system.

2. We provide a solution to tackle the ill-posed problem of estimating parameters of the muscle-tendon models while ensuring that the estimated parameters' values result in estimates of joint stiffness and damping that enable robust tracking of the intended joint position and adaptation of the joint impedance during online operation. In fact, different parameters' value may provide an estimate of the joint kinematics that matches the reference one, but because a different dynamics may underlie the same kinematics, the estimated stiffness and damping may provide an incorrect representation of the human intended joint impedance. To tackle this problem the muscle-tendon unit models are modified, and we design an optimization framework that uses the output of the position-based impedance controller as optimization signal, since the latter is affected by the muscle-tendon models dynamics.

The two contributions are not independent, but complement one another toward the objective of designing a comprehensive framework.

1.3 Methods and evaluation

We conducted experimental studies with able-bodied participants and a transradial amputee to evaluate the framework performance with respect to that of a state-of-the-art data-driven method during online reaching tasks in a static and dynamic environment. We investigated whether the users could *exploit stiffness and damping adaptation to counter perturbations in the form of force fields that push the simulated wrist away from a target*, making impedance adaptation necessary to maintain stability and complete the task. This constitutes the main

research question of this thesis. We experimentally demonstrate the following properties of the proposed framework:

- The proposed framework supports online adaptation of the simulated robot kinematics and dynamics in response to external disturbances (Section 6.2). A deeper understanding of the impedance adaptation property enabled by our approach is made possible by the framework's transparency. This helped to analyse how changes in the sEMG signals due to modulation of muscles' contraction (i.e., impedance) affected the control performance of the methods being evaluated. This property has not been extensively and explicitly tested in previous work.

- The framework's performance is comparable to a state-of-the-art baseline in the absence of perturbations and substantially better in the presence of perturbations for able-bodied subjects (Section 6.2.1) and the amputee (Section 6.2.2).

- We show that the users' perception of controllability is consistent with the quantitative results regarding the framework performance (Section 5.5.1). In fact, according to the subjects' feedback, the proposed framework provides improved performance compared with the baseline. The term controllability here refers to control stability, robustness, responsiveness to fast-changing features of the sEMG signals, and to the user's capability of making the system stable after an external perturbation. In this work, controllability is quantified using performance measures about the online task performance (Section 5.5.3), and it does not have the classic meaning as in the control system.

1.4 Thesis outline

Chapter 1 provides the context of this thesis, describes the motivation, and specifies the research objectives and contributions of this work. The rest of the thesis is divided into the following chapters:

Chapter 2 covers the necessary background material that allows the reader to understand the content of this thesis. Firstly, we start with an overview of fundamental concepts of robot control, including the description of a generic robotic structure, and classic control methods. We then summarise key aspects of human motor control, focusing on *impedance adaptation* as core human motor control strategy. We provide an overview of the state-of-the-art technology used to interface the user to a robotic system and, in particular, surface electromyography is discussed. Macroscopic properties of the

muscular-tendinous system and approaches to biomechanical modeling of the muscle-tendon complex are explained. Finally, we provide a brief overview of the human wrist kinematics and dynamics.

Chapter 3 describes the state-of-the-art control methods implemented on commercially available prostheses and the control methods developed in academic research. We focus on methods designed for enabling impedance adaptation of a robotic system. Specifically, we highlight the research gap we address in this thesis.

Chapter 4 introduces a novel sEMG-based framework for adaptive impedance control of a DoF of a simulated robot through wrist flexion-extension. We start by providing an overview of the framework and clearly state the framework requirements and main assumptions. The input and output of the framework are described: the choice of HMI is justified, and we investigate the latent space of sEMG signals recorded during wrist movements performed at different levels of muscle co-activations; the choice of relying on the user's visual feedback is explained. We proceed providing an in-depth description and mathematical formulation of each component of the framework. We also include preliminary experimental results used to investigate the framework architecture.

Chapter 5 introduces the experimental setup and methods used to answer the research questions of this thesis. The hypotheses we aim to support with the experimental results are listed. The experimental work consists of an offline tracking experiment during which the data (sEMG signals and wrist kinematics) for training the framework's muscle-tendon models is acquired, and an online reaching task experiment that investigates the online control performance in the presence and absence of external perturbations. We describe the baseline used to contrast the performance of our framework.

Chapter 6 discusses the results of the experiments described in the previous chapter. Moreover, examples of the time evolution of key variables of the proposed framework and the baseline are discussed. These include successful and failed trials for an exemplary able-bodied subject and the amputee.

Chapter 7 draws the conclusions of this thesis by summarising the contributions, discussing the limitations and suggesting future research directions.

Appendix A summarises the main steps of the Simulated Annealing method, used for optimising the muscle-tendon parameters' values.

Appendix B provides an overview of the information theory concepts underlying a performance measure used in the experimental evaluation and describes the measure used to quantify the smoothness of a motion.

Appendix C includes additional experimental results of the offline tracking experiments. Estimated values of the muscle-tendon parameters are summarised in tables for the able-bodied subject and the amputee. An example of force-length-velocity relationship is shown for the elements of a trained muscle-tendon model.

Appendix D summarises the main dynamic parameters and the Denavit-Hartenberg (DH) parameters needed to define the model of the robot used in this work.

Chapter 2

Background

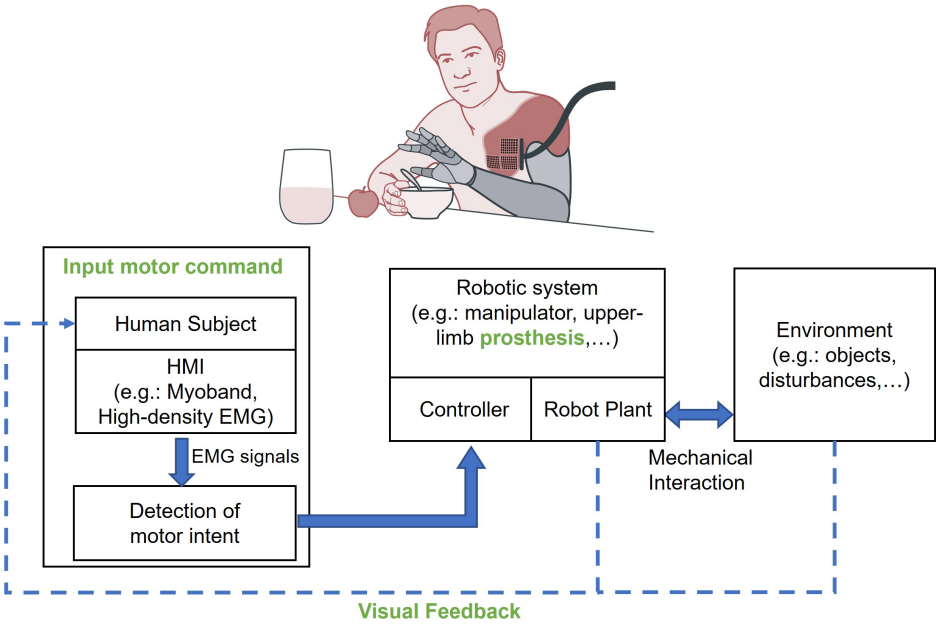

Figure 2.1: Scheme of a generic sEMG-based framework for decoding the human motor intent and controlling a robot (e.g., prosthesis). The system consists of the human user, the robot, and the environment. A Human Machine Interface (HMI), such as low or high-density electromyography sensors, is used to interface the user with the robot. The HMI allows to record biological signals containing information about the user's motor intent. These signals are processed to estimate the user's motor intent and provide it as motor command. Depending on the task, interaction forces may arise from the interaction between the robot and the environment and interfere with the execution of the desired motor command. The user may use visual feedback on the state of the robot to adjust the input motor command and achieve the desired behaviour.

This chapter provides the reader with the necessary background knowledge to understand the chapters that follow which result in the description of an electromyography-based framework for enabling a human subject to independently control the kinematics and the joint impedance of a single DoF of a simulated robot, by contraction of the main wrist flexor and extensor. While this chapter is not meant to be an exhaustive guide on prosthesis control, it aims to highlight key concepts to understand the motivation and scope of this thesis. The reader is referred to additional material to deepen their understanding as desired. The topics reviewed are illustrated in Figure 2.1 and summarised below: Section 2.1 provides an introduction to the control of robotic systems. We define the structure of a generic multi-Degrees of Freedom manipulator and introduce classic control schemes for controlling the robot in the free space and during dynamic interactions with the external environment. Corresponding equations for a single-DoF robot can be obtained as a particular case as described in Chapter 4.4. The concepts of impedance, admittance and mechanical coupling are therefore introduced. In Section 2.2, we present studies on human motor control suggesting that *impedance control* is an essential motor control strategy for stable physical interaction with the external environment. This is important in order to understand the motivation for this thesis and introduce our contribution to the literature. Building on the concepts introduced in the previous sections, we provide in Section 2.3 an introduction to motor prostheses focusing on upper-limb prostheses and explain how a human subject can be interfaced with these robotic systems. Hence, we discuss the Human-Machine interfaces used for active prostheses control focusing on electromyography. The material around muscle-tendon modelling, which lays the ground for our framework formulation, is reviewed in Section 2.4. Finally, in Section 2.5 we discuss the role of wrist control in dexterous grasping and manipulation; we review the kinematics and dynamics properties of the human wrist (i.e., impedance properties). While in this thesis we focus only on the flexion-extension motion of the wrist, a global understanding of wrist kinematics and dynamics is necessary to understand the framework design choices, limitations and future work directions.

2.1 Fundamentals of robot control

The goal of this section is to provide the reader with theoretical background about the control of robotic systems. To do so, basic concepts regarding the definition of the structure of a robot manipulator, robot kinematics and dynamics are introduced. We then discuss two control strategies that may be used to control a manipulator in the presence and absence of dynamic interactions between the robot and the environment. In the first case, the robot is considered an isolated physical system otherwise the robot is considered mechanically coupled with the

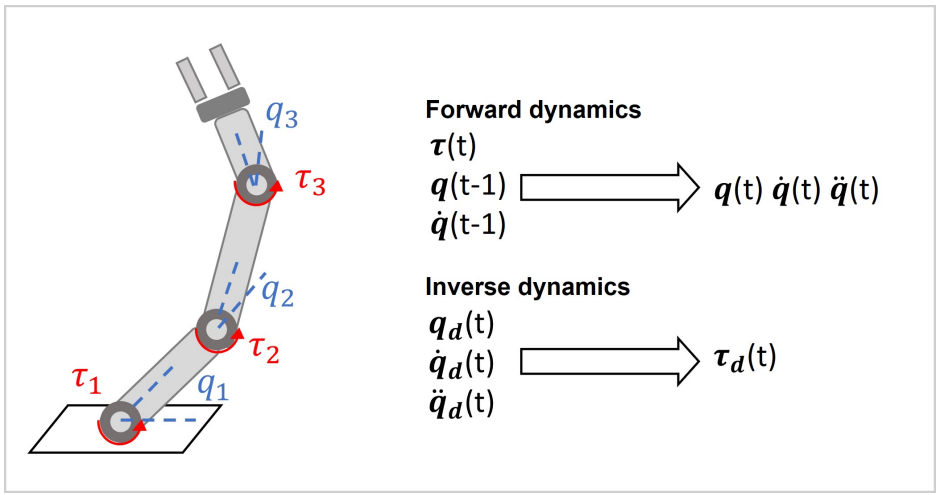

Figure 2.2: Example of 3-DoFs robot manipulator with revolute joints. The variables q_i and τ_i indicate the angular position of DoF_i and applied torque, respectively. A reference scheme for input and output variables of direct and inverse dynamics is provided on the right. The vectors $\boldsymbol{q}, \dot{\boldsymbol{q}}, \ddot{\boldsymbol{q}}, \boldsymbol{\tau}$ contain the joints' position, velocity, acceleration and torque. The subscript "d" indicates the corresponding desired variables.

environment. The time dependency is dropped in the equations of the following sections to ease the reading.

2.1.1 Robot structure

A *manipulator* is an open chain of rigid bodies (*links*) connected by *joints*. One end of the chain may be constrained to a fixed base, while the last link of the robotic chain may be equipped with an end-effector (e.g., a gripper, a robotic hand, or a tool) needed for a specific manipulation task. A simple robot with three links and three joints is illustrated in Figure 2.2. Each *joint* can be regarded as a kinematic constraint that provides the robotic structure with a *Degree of Freedom (DoF)* allowing the next link to move with respect to the previous one. Common types of 1-DoF joints are the *revolute* and *prismatic* joints. A *revolute* joint provides a 1-DoF rotational motion about a single axis, while the prismatic joint provides a 1-DoF linear motion along a single axis. A joint can be actuated if equipped with a motor, whereas it is underactuated if it only responds passively to externally imposed motion. More complex mechanical properties of a joint, such as hysteresis, friction and backlash [196], are out of our scope. In this thesis, *we assume a joint is an ideal kinematic constraint between two rigid bodies*. A joint might contain sensors that acquire information about the robot joints' position (angular or linear for a revolute or prismatic joint, respectively) or force-torque sensors that measure external forces and torques acting on the joints. The number of DoFs of a joint is the

number of independent variables required to define the motion enabled by the joint. Since the joints introduced earlier allow a single DoF motion, *the terms DoF and joint are used interchangeably*. Let us formally define a manipulator of n joints (DoF) and n links. The robot configuration at a point in time can be described by the joints' state $\boldsymbol{s} = \{\boldsymbol{q}, \dot{\boldsymbol{q}}, \ddot{\boldsymbol{q}}\}$. The vectors $\boldsymbol{q}, \dot{\boldsymbol{q}}, \ddot{\boldsymbol{q}} \in \mathbb{R}^n$ contain the position, velocity and acceleration of each joint, respectively. Therefore, the vector $\boldsymbol{q}$ contains n independent variables that uniquely define the robot's configuration in the space.

2.1.2 Robot kinematics and dynamics

In Section 2.1.1, we have defined a generic n-DoF robot, described by the state matrix $\boldsymbol{s} = \{\boldsymbol{q}, \dot{\boldsymbol{q}}, \ddot{\boldsymbol{q}}\}$ of the joints' position, velocity and accelerations recorded by sensors at the joints. The robot state, defined by joint variables, is therefore described in the *joint space*. Below, the state of the robot is defined as the position of the end-effector with respect to a base frame (i.e., Cartesian space), by introducing the concepts of *direct and inverse kinematics*. Given the geometric relationship between variables in the joint space and those in the Cartesian space, the *equation of motion of the robot* is introduced considering the forces and torques acting on the robot structure. These concepts are needed to introduce in the next sections the concept of mechanical coupling between the robot and the environment and two classic control paradigms.

Robot kinematics describes the robot's links motion with respect to a reference frame and with respect to each other without considering the forces generating the motion. On the contrary, *robot dynamics* studies the motion of the robot system as a function of internal (torques at each joint) and external forces (interaction forces with the environment) acting on the robot. Kinematics is useful to define the mapping between the joint space (i.e., the space of the joint variables) of the robot and the so-called operational or Cartesian space (i.e. the space of the end-effector). The Cartesian state of the robot defines the end-effector position with respect to the robot's base frame. *The framework implemented in this thesis operates in the joint space of the robot*, therefore a detailed discussion of the robot's kinematics is out of our scope.

We focus instead on the *robot dynamics* which is concerned with defining the mapping between the forces exerted on the robot structure and the joints' position, velocity and acceleration. Two instances of the dynamic relationship between motion and forces can be identified: forward dynamics and inverse dynamics (see Figure 2.2). The dynamic model of a robot describes the relationship between the robot state $\boldsymbol{s}$ and the torques acting on the robot's joint. These torques may include the actuation torques $\boldsymbol{\tau}$ and the torques due to physical

interaction with the external environment $\boldsymbol{b}$. Given the current joint position and velocity, and the torques $\boldsymbol{\tau}$ and $\boldsymbol{b}$, the *forward dynamics* model predicts the state evolution of the robot. The *inverse dynamic* problem instead describes the torques acting on the robot, given the robot's state.

To mathematically formulate the direct and inverse dynamic problems let us first derive the *dynamic equation* of a *n*-DoF robot. For the moment, external torques u are neglected. The dynamic equation of motion defines the relationship between the joint torques $\boldsymbol{\tau} \in \mathbb{R}^n$ and the joints' motion $\mathbf{s}$ as follows:

$$\boldsymbol{M}(\boldsymbol{q})\ddot{\boldsymbol{q}} + \boldsymbol{C}(\boldsymbol{q},\dot{\boldsymbol{q}}) + \boldsymbol{g}(\boldsymbol{q}) = \boldsymbol{\tau} + \boldsymbol{u} \tag{2.1}$$

where $\boldsymbol{q} \in \mathbb{R}^n$ is the vector joint coordinates, $\boldsymbol{\tau} \in \mathbb{R}^n$ is the vector of joint torques, $\boldsymbol{M}(q) \in \mathbb{R}^{n \times n}$ is the state-dependent positive definite and symmetric joint space inertia matrix, $\boldsymbol{C}(\boldsymbol{q},\dot{\boldsymbol{q}}) \in \mathbb{R}^{n \times n}$ includes the Coriolis and centrifugal forces, and $\boldsymbol{g}(\boldsymbol{q}) \in \mathbb{R}^n$ is the torque exerted by gravity. Equation 2.1 defines the *inverse dynamics equation* of a manipulator. Two main approaches exist to obtain Equation 2.1, the Lagrange and the Newton-Euler formulations. The description of these methods is not in our scope, see [196] for details.

Given Equation 2.1 and knowing the joint position and velocity at time t, the *forward dynamic* problem can be solved. The joint acceleration $\ddot{\boldsymbol{q}}$ at time t when the torque $\boldsymbol{\tau}_t$ is applied to the manipulator can be computed as follows:

$$\ddot{\boldsymbol{q}}_t = \boldsymbol{M}(\boldsymbol{q}_{t-1})^{-1}\big(\tau_t - \boldsymbol{C}(\boldsymbol{q}_{t-1},\dot{\boldsymbol{q}}_{t-1})\dot{\boldsymbol{q}}_{t-1} + \boldsymbol{g}(\boldsymbol{q}_{t-1})\big) \tag{2.2}$$

From the joint acceleration $\ddot{\boldsymbol{q}}_t$, the joint position $\boldsymbol{q}_t$ and velocity $\dot{\boldsymbol{q}}_t$ can be obtained using numerical integration methods (e.g., Runge-Kutta, Euler's method [21]).

2.1.3 Physical interaction between the robot and the environment

In Section 2.1.2, we have introduced the concepts of direct and inverse dynamics. These describe the robot's motion given the forces and torques acting on the robot. In this section, we describe in more detail the mechanical interaction between two physical systems and introduce the concept of impedance and admittance. These concepts will lay the basis to understand the need for controllers that take into account interaction forces, discussed in Section 2.1.4.

Most of the manipulation tasks require the robot to physically interact with the external environment. Classic manipulation tasks might involve the grasping and manipulation of

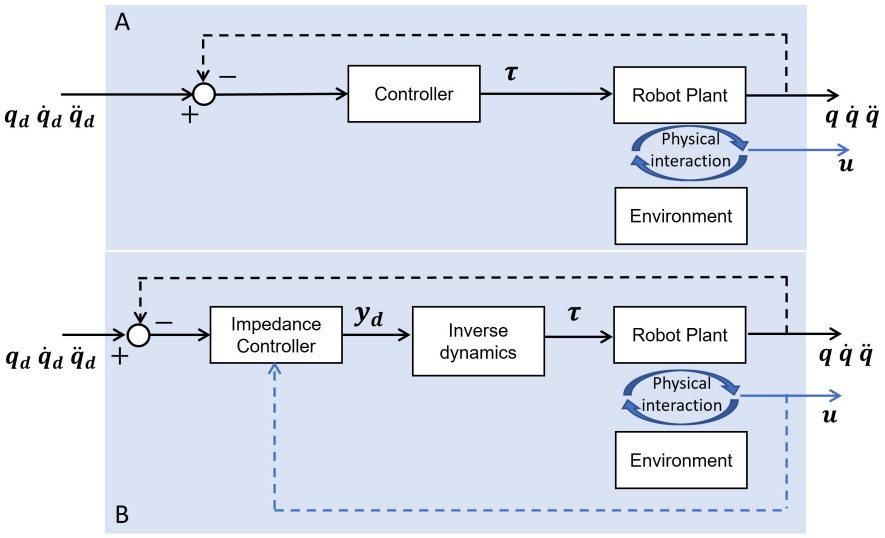

Figure 2.3: A) Scheme of a generic joint space controller; B) Scheme of an impedance controller. Both controllers aim to track a desired joint trajectory $\boldsymbol{q}_d, \dot{\boldsymbol{q}}_d, \ddot{\boldsymbol{q}}_d$. However, A) does not consider the external torques $\boldsymbol{u}$ in the control law.

objects. In these cases, the robot and the object (i.e., the environment) are two physical systems mechanically coupled; the mechanical work exchanged between the robot and the object can be defined in terms of interaction forces. In general, if the interaction forces are negligible the robot is considered an isolated system, otherwise, the robot and environment are treated as mechanically coupled physical systems. To ensure compatibility of the physical interaction, the dynamic behaviour of the two physical systems must complement one another [95]. This means that if the environment applies a force on the robot, the robot's motion is affected and vice versa. A physical system is defined as an *admittance* or as an *impedance* if it can accept force (i.e., accept force, yield motion) or motion (i.e., accept motion, yield force), respectively. Therefore, since the robot and the environment are mechanically coupled if one behaves as an impedance, the other is an admittance, and vice versa (this is the case for linear systems only). Classic motion control techniques based on position control, discussed below, have been extensively applied in tasks where the robot may be considered an isolated system. However, these methods are not sufficient to ensure the safe and successful execution of the task if the robot physically interacts with the environment, especially if the environment is rigid and the contact forces might reach unsafe values. To handle this problem, different control strategies have been proposed in the literature to control the motion of the robot while simultaneously modulating the dynamics of the physical interaction. In Section 2.1, we describe two control schemes belonging to these two categories of control strategies: the *computed torque controller* and the *impedance controller*.

2.1.4 Robot control

In the previous sections, we have introduced fundamental concepts about the terminology and mathematical description of a manipulator, and we have introduced robot kinematics and dynamics. This section describes two control strategies, the *computed torque control* (or *inverse dynamics control*) and the *impedance control*. The first controller allows to achieve the desired robot kinematics, whereas the second controller also allows indirect control of the dynamic interaction between the robot and the environment. In the first case, the robot is regarded as an isolated system, while in the second case the robot is mechanically coupled with the external environment. These two control schemes are illustrated in Figure 2.3 and discussed below.

Computed torque control

The robot motion dynamics (Equation 2.1) is defined as a non-linear equation of a dynamic system describing the actuation torques $\boldsymbol{\tau}$ in relation to the robot joint position, velocity and acceleration. Given the generic n-DoF robot introduced earlier, we consider the problem of designing a suitable torque command to control the robot's joints with the aim of achieving the desired motion trajectory $\boldsymbol{q}_d, \dot{\boldsymbol{q}}_d, \ddot{\boldsymbol{q}}_d$. Ideally, if a perfect model of the robot dynamics was available the equation of the inverse dynamics could be used to obtain the torque trajectory needed to reach the target motion. However, this open-loop approach does not provide a robust solution since a perfect model of the robot is usually unavailable due to different factors contributing to modeling inaccuracy. Moreover, inverse dynamics does not take into account the external torques acting on the robot. The *computed torque scheme* has been proposed to provide a more robust control by including a feedback term to compensate for potential sources of error [196]. A generic scheme of this controller implemented in the joint space of the robot is represented in Figure 2.3-A. The control law is given by the following equation where the new variable $\boldsymbol{y}_d \in \mathbb{R}^n$ is introduced:

$$\boldsymbol{y}_d = \ddot{\boldsymbol{q}}_d + \boldsymbol{K}^p(\boldsymbol{q}_d - \boldsymbol{q}) + \boldsymbol{K}^d(\dot{\boldsymbol{q}}_d - \dot{\boldsymbol{q}}) \tag{2.3}$$

The second and third terms of the equation are the so-called proportional and derivative terms. The error $\boldsymbol{e} = \boldsymbol{q}_d - \boldsymbol{q}$ and its derivative $\dot{\boldsymbol{e}} = \dot{\boldsymbol{q}}_d - \dot{\boldsymbol{q}}$ are weighted by the positive-definite diagonal matrices $\boldsymbol{K}^p \in \mathbb{R}^{n\times n}$ and $\boldsymbol{K}^d \in \mathbb{R}^{n\times n}$, respectively. The torque command needed to achieve the desired motion is obtained by plugging Equation 2.3 in the robot motion dynamics equation (Equation 2.2). This is done by imposing $\ddot{\boldsymbol{q}} = \boldsymbol{y}_d$ as follows:

$$\boldsymbol{\tau} = \boldsymbol{M}(\boldsymbol{q})(\boldsymbol{K}^p\boldsymbol{e} + \boldsymbol{K}^d\dot{\boldsymbol{e}}) + \boldsymbol{M}(\boldsymbol{q})\ddot{\boldsymbol{q}}_d + \boldsymbol{C}(\boldsymbol{q},\dot{\boldsymbol{q}}) + \boldsymbol{g}(\boldsymbol{q}) \tag{2.4}$$

The first term represents the feedback torque that compensates for errors in dynamics modeling; the remaining terms, called feedforward terms, are used to cancel out non-linearities in the system. This can be demonstrated by plugging Equation 2.4 into Equation 2.2, which results in the following equation:

$$\ddot{\boldsymbol{q}} = \ddot{\boldsymbol{q}}_d + \boldsymbol{K}^p \boldsymbol{e} + \boldsymbol{K}^d \dot{\boldsymbol{e}} \tag{2.5}$$

The non-linear dynamic system (Equation 2.2) has been simplified to a second-order linear equation, where the robot is considered as a mass-spring-damper system. In summary, it is possible to define a control law that disregards the robot dynamics, and uses optimal values of the matrices $\boldsymbol{K}^p$ and $\boldsymbol{K}^d$ to bring the motion error to zero:

$$\boldsymbol{\tau} = \boldsymbol{K}^p(\boldsymbol{q}_d - \boldsymbol{q}) + \boldsymbol{K}^d(\dot{\boldsymbol{q}}_d - \dot{\boldsymbol{q}}) = \boldsymbol{K}^p \boldsymbol{e} + \boldsymbol{K}^d \dot{\boldsymbol{e}} \tag{2.6}$$

The role of the proportional and derivative matrices can be visualised by considering a torsional spring and a damper at each joint that pull the adjacent links to achieve the desired joint motion. The matrices $\boldsymbol{K}^p$ and $\boldsymbol{K}^d$ contain n independent springs, and dampers, respectively. The proportional and derivative gain determines the convergence of the proportional and derivative error to zero. Equation 2.6 defines the control law of a *proportional-derivative (PD)* control scheme.

Impedance control

Impedance control is one of the main control schemes used to handle physical interactions (i.e., contact forces) between the robot and the environment. This scheme was first introduced by Neville Hogan [95] and implemented in the Cartesian space of the robot [96], given that for manipulation tasks the end-effector primarily interacts with the environment. Consider the simple task of following a trajectory with the robot's end-effector. Classic motion control schemes lead to successful trajectory tracking if the robot operates in the free space. However, in the presence of interactions with the environment (e.g., sudden forces acting on the end-effector due to contact with objects, or other forms of unpredictable perturbations) successful execution of the task can not be guaranteed unless an accurate model of both the manipulator and the environment (geometry and mechanical features) is provided and the task is planned. In practice, while the dynamic model of the manipulator can be obtained with sufficient precision, it is difficult to derive an accurate model of the environment. As a result inaccuracies during task execution will give rise to interaction forces between the end-effector and the environment until the end-effector deviates from the desired trajectory. Depending on the amplitude of the contact forces, saturation of the robot's actuators and breakage of

the robot could occur. Impedance control provides a solution to this problem, allowing position tracking and modulation of interaction forces without explicitly controlling the latter, but by imposing a desired model of the dynamics between the robot and the environment. This model, called impedance model, *maps external forces to robot displacements, allowing to modulate the interaction force indirectly, via motion control*. The impedance model usually consists of a set of second-order differential equations, defined as mass-spring-damper equations (linear or non-linear), per each DoF. Consider the generalised contact force vector $\boldsymbol{F}_{ext} = \left[\boldsymbol{F}, \boldsymbol{\mu}\right] \in \mathbb{R}^6$ containing the Cartesian forces $\boldsymbol{F} \in \mathbb{R}^3$ and moments $\boldsymbol{\mu} \in \mathbb{R}^3$, defined with respect to the Cartesian reference frame attached to the robot's end-effector. An impedance controller in the Cartesian space modulates the relationship between the position of the end-effector and $\boldsymbol{F}_{ext}$ by defining a reference impedance model consisting of six mass-spring-damper equations, one for each of the six DoFs. The choice of the parameters of these equations (inertia, stiffness and damping matrices) determines the trade-off between accurate position tracking and rejection of interaction forces $\boldsymbol{F}_{ext}$. While key concepts of this control paradigm might be more intuitive to understand when formulated in the Cartesian space, *we now derive the impedance control law in the joint space since this controller is the base for the one utilised in the proposed framework.* Recall the analogy between the gains of the PD controller and the action of a mechanical spring and damper at the joints, introduced with Equation 2.6. Similarly, we consider an impedance model consisting of a set of independent mass-spring-damper equations for each DoF (i.e., joint). Let us rewrite Equation 2.1 considering the vector of external joint torques $\boldsymbol{u}$ acting on the robot's joints:

$$\boldsymbol{M}(\boldsymbol{q})\ddot{\boldsymbol{q}} + \boldsymbol{C}(\boldsymbol{q}, \dot{\boldsymbol{q}}) + \boldsymbol{g}(\boldsymbol{q}) = \boldsymbol{\tau} - \boldsymbol{u} \tag{2.7}$$

To design the control law, we first linearise the system in Equation 2.7 and subsequently impose the desired interaction dynamics using an impedance model. We assume that the robot is equipped with force-torque sensors. The dynamic model of the robot is linearized by plugging Equation 2.8 into Equation 2.7, as described below, to obtain Equation 2.9:

$$\boldsymbol{\tau} = \boldsymbol{M}(\boldsymbol{q})\boldsymbol{y}_d + \boldsymbol{C}(\boldsymbol{q}, \dot{\boldsymbol{q}}) + \boldsymbol{g}(\boldsymbol{q}) \tag{2.8}$$

$$\boldsymbol{M}(\boldsymbol{q})\ddot{\boldsymbol{q}} + \boldsymbol{C}(\boldsymbol{q}, \dot{\boldsymbol{q}}) + \boldsymbol{g}(\boldsymbol{q}) = \boldsymbol{M}(\boldsymbol{q})\boldsymbol{y}_d + \boldsymbol{C}(\boldsymbol{q}, \dot{\boldsymbol{q}}) + \boldsymbol{g}(\boldsymbol{q}) - \boldsymbol{u} \tag{2.9}$$

Notice that the acceleration in Equation 2.8 is indicated as $\boldsymbol{y}_d$. The new variable $\boldsymbol{y}_d$ is defined according to the impedance model, as described below. Let us define the impedance model describing how the external torques $\boldsymbol{u}$ affect the robot's trajectory in the joint space:

$$\boldsymbol{M}_d(\ddot{\boldsymbol{q}} - \ddot{\boldsymbol{q}}_d) + \boldsymbol{D}_d(\dot{\boldsymbol{q}} - \dot{\boldsymbol{q}}_d) + \boldsymbol{K}_d(\boldsymbol{q} - \boldsymbol{q}_d) = \boldsymbol{u} \tag{2.10}$$

where $\ddot{\boldsymbol{q}}_d, \dot{\boldsymbol{q}}_d, \boldsymbol{q}_d$ are the desired joint acceleration, velocity and position. The parameters $\boldsymbol{M}_d > 0$, $\boldsymbol{K}_d > 0$, $\boldsymbol{D}_d \geq 0 \in \mathbb{R}^{n \times n}$ are the desired inertia, damping, and stiffness matrices. Large $\boldsymbol{M}_d$ can lead to slow response, $\boldsymbol{K}_d$ allows attenuating the interaction forces, while $\boldsymbol{D}_d$ shapes the transient behaviour [38]. To obtain the control law, we first isolate $\ddot{\boldsymbol{q}}$ in Equation 2.10 as follows:

$$\ddot{\boldsymbol{q}} = \boldsymbol{M}_d^{-1}\big(\boldsymbol{u} - \boldsymbol{D}_d(\dot{\boldsymbol{q}} - \dot{\boldsymbol{q}}_d) - \boldsymbol{K}_d(\boldsymbol{q} - \boldsymbol{q}_d) + \boldsymbol{M}_d\ddot{\boldsymbol{q}}_d\big) \tag{2.11}$$

We then define the desired dynamic behaviour described by the impedance model onto the robot, by imposing that the acceleration obtained in Equation 2.11 is equal to the desired acceleration $\boldsymbol{y}_d$. To do this, Equation 2.11 is plugged into Equation 2.9 by imposing $\boldsymbol{y}_d = \ddot{\boldsymbol{q}}$:

$$\boldsymbol{M}(\boldsymbol{q})\ddot{\boldsymbol{q}} = \boldsymbol{M}(\boldsymbol{q})(\boldsymbol{M}_d^{-1}\big(\boldsymbol{u} - \boldsymbol{D}_d(\dot{\boldsymbol{q}} - \dot{\boldsymbol{q}}_d) - \boldsymbol{K}_d(\boldsymbol{q} - \boldsymbol{q}_d) + \boldsymbol{M}_d\ddot{\boldsymbol{q}}_d\big)) - \boldsymbol{u} \tag{2.12}$$

The obtained control law may be simplified by assuming that the desired inertia matches the natural inertia of the robot, imposing $\boldsymbol{M}_d = \boldsymbol{M}$. This avoids challenges in choosing the desired inertia and does not require the measurement of external torques. The simplified control law of the joint-space impedance control is the following:

$$\boldsymbol{\tau} = \boldsymbol{M}\ddot{\boldsymbol{q}}_d - \boldsymbol{D}_d(\dot{\boldsymbol{q}} - \dot{\boldsymbol{q}}_d) - \boldsymbol{K}_d(\boldsymbol{q} - \boldsymbol{q}_d) \tag{2.13}$$

Notice that the vector of external torques $\boldsymbol{u}$ is eliminated due to the aforementioned simplification. The obtained control law is a pure motion control law, but the gains are chosen to limit the contact forces and satisfy the desired dynamic behaviour [121].

Variable impedance control

Research in robotics has widely used the impedance control paradigm, introduced in the previous section, to shape the interaction between a robot and the environment. However, the choice of suitable impedance gains is a non-trivial problem since the mechanical interaction between the robot and environment might change during the task due to system constraints and environmental properties [7, 117]. For this reason, a single set of impedance parameters might not be suitable for the successful execution of the entire task, instead, the robot should be capable of adapting its dynamic behaviour [95]. Variable impedance control allows to vary the impedance parameters as a function of some desired system variable (e.g., time, robot state, etc). Based on the fixed-gains impedance model introduced in Equation 2.10, a

variable impedance model can be mathematically formulated as follows:

$$\boldsymbol{M}_d(t)(\ddot{\boldsymbol{q}}-\ddot{\boldsymbol{q}}_d)+\boldsymbol{D}_d(t)(\dot{\boldsymbol{q}}-\dot{\boldsymbol{q}}_d)+\boldsymbol{K}_d(t)(\boldsymbol{q}-\boldsymbol{q}_d)=\boldsymbol{u} \tag{2.14}$$

with the desired inertia, stiffness and damping matrices varying as a function of time. This control method belongs to the class of adaptive controllers. Typically, machine learning algorithms are used to compute an impedance trajectory, learn task-specific policies from which adaptive impedance values are obtained, or variable impedance parameters are learned from human demonstration [27, 22, 119, 99]. An in-depth review of the methods found in the robot manipulation literature to estimate suitable impedance gains is out of the scope of this thesis. However, the need for an impedance model with adaptive impedance gains had to be clarified since *the framework proposed in this thesis implements a variable impedance control scheme to enable a human subject to update the impedance parameters used in the controller*.

2.2 Human neuromuscular impedance control

In Section 2.1.4 we have introduced the impedance control scheme, designed to handle mechanical interactions between the robot and the environment. The impedance control paradigm takes inspiration from human neuromuscular impedance control which constitute the core of the human motor control strategy. In this thesis, we propose a framework to decode the human motor intent in terms of joint kinematics and joint impedance, and to implement the impedance controls strategy on a robotic system. It is therefore important to review the mechanism used by the central nervous system (CNS) to modulate the impedance of the limb.

Object manipulation is a common human activity that involves physical interaction between the limb and the environment. This physical interaction can be stable or unstable. Consider the example of holding an umbrella, introduced in Chapter 1. In an ideal scenario where the umbrella and the human limb are the only physical systems interacting (i.e., absence of unpredictable perturbations), the task of holding the umbrella can be considered dynamically stable. Even if some properties of the object being manipulated are unknown, such as the umbrella's weight, humans learn how to adapt their sensorimotor control (i.e., mapping of neural inputs to motor outcomes) to successfully hold the umbrella. However, in real-life scenarios, it might not be possible to predict when the wind will blow and suddenly displace the umbrella from its upright position. In this case, and in most of the manipulation

tasks, unpredictability is a critical feature of dynamic interactions humans need to counteract. Understanding how the CNS controls the musculoskeletal system to achieve dexterous motion in the presence of instabilities and unpredictable interactions with the external environment has been – and still is – a longstanding goal of different disciplines.

Sources of instabilities arise either from the environment or from the body itself. A stable and repeatable bias (stable dynamics) is easily managed by humans since the repeatability property ensures that similar motor commands generate the same output. In this case, humans incrementally and iteratively learn how to adapt their sensorimotor input to obtain the desired motor outcome [147]. This is achieved through a neural feedback mechanism. However, in an unpredictable environment, this type of control strategy would lead to failure. In fact, neural feedback pathways are characterized by neural delay. Considering the upper limb, the fastest feedback loops (i.e., spinal reflex) are reported to be approximately 25 ms [125], and longer reaction times associated with voluntary contraction (i.e., transcortical feedbacks) can range between 100–200 ms [96]. The effectiveness of neural feedback control is therefore quite limited, especially for tasks involving dynamic interaction with the environment where a prompt reaction is required. In these cases, humans leverage the adaptation of intrinsic mechanical properties of the musculoskeletal system to complement the action of neural feedback [94, 145, 144].

The viscous-elastic properties of the musculoskeletal system were first investigated by Hogan in 1985, when he postulated how the CNS regulates the arm endpoint impedance to counter external perturbations [72]. Mussa-Ivaldi, Hogan and Bizzi [153] investigated the behaviour of the limb when operating in an unstable environment and observed that "when the hand is displaced from an equilibrium posture by an external disturbance, a force is generated to restore the original position". This statement describes the impedance properties of the limb in the Cartesian space, considering the hand as the interaction port between the human limb and the environment. The human arm was modeled as a mass-spring-damping system, and its mechanical interaction with the environment was formalized in terms of mechanical impedance (i.e., inertia, damping, stiffness). The reader should recall that inertia, damping and stiffness were introduced in Section 2.1.4 to define the impedance model of the robot. The validity of the arm model has been supported in several studies [78, 169, 171, 78, 120, 68, 18, 58, 203, 73, 47, 144] showing that regulation of the impedance properties of the arm plays a fundamental role in adaptation to instabilities.

Considering the human upper-limb interacting with the environment, two main mechanisms contribute to the modulation of limb impedance. Muscle co-activation is responsible for early responses to disturbances because it is unaffected by neural delay, whereas neural feedback mediates the response with a delay [80]. In fact, it is shown that modulation

of the muscle impedance might be achieved also in the absence of neural feedback [96] by simultaneous activation of two or more muscles opposing each other and spanning the same joint. Consider a single-DoF motion, involving flexors and extensor muscles acting as agonist-antagonist muscle groups. During isometric contractions, when flexors and extensor muscles coactivate, their actions oppose one another, resulting in a null torque around the joint. As a result, no joint motion is generated, whereas the muscle co-contraction contributes to increasing the stiffness of the arm [94] which allows to stabilize the arm-environment system and to achieve the desired motion and dynamic behaviour. During this process, the tuning of the mechanical impedance parameters occurs. Similarly, the same joint motion can be achieved while modulating the muscles' co-contraction and thus the arm impedance. Going back to our previous example, to compensate for the perturbations imposed by the wind we typically co-contract the muscles spanning the limb's joints to maintain the limb posture while increasing the "rigidity" of the limb to reject unexpected perturbations. More recent studies [28] provided experimental evidence that humans selectively modulate the net impedance of the hand to compensate for destabilizing external perturbations. While regulation of the limb impedance properties by muscle co-contraction allows humans to counter unpredictable instabilities, this mechanism requires energy to maintain the co-contraction and may seem inefficient. For this reason, humans optimally adapt the limb impedance and tune it accordingly to the task's requirements and time. The limb inertia is mainly controlled by changing the limb posture, the damping and stiffness are highly dependent on intrinsic properties of the muscular-tendinous tissue [73, 72] which are discussed in more detail in Section 2.4.

The understanding of the macroscopic properties of the muscular tissue provides the basis for the mathematical formulation of biomechanic muscle-tendon models that predict the contraction forces generated by the muscle-tendinous tissue. These models are used in the proposed framework to include domain knowledge about muscle contraction dynamics, as summarised in Section 1. These models are driven by surface electromyographic (sEMG) signals, which contain information about the neural content of the motor intent. Electromyography is discussed in the next section.

2.3 Human machine interfaces for detection of human motor intent

In the previous section, we have described *impedance adaptation* of the human limb as a fundamental motor control strategy to modulate the dynamics of the interaction (i.e., contact

forces) between our limb and the environment. We have explained that modulation of the limb impedance relies on the intrinsic mechanical properties of the muscles. These concepts are reviewed since the proposed framework draws inspiration from their understanding. As discussed in Section 1, this thesis presents a framework for decoding the human motor intent from sEMG signals in terms of joint kinematics and impedance, and for enabling online adaptive control of the impedance of a robotic system.

In this section, we describe electromyography and discuss why it is the most commonly used type of Human Machine Interface (HMI) in clinical practice (e.g., motor prostheses control, exoskeleton, etc) and in research. In particular, motivated by the goal of the work discussed in this thesis, we are interested in HMIs that record biological signals containing information about the human motor intent. We provide a brief overview of the HMIs used to interface the human nervous and muscular systems, and we then focus on electromyography and provide technical details on the Myoband device, which is part of the experimental setup of this thesis.

2.3.1 How is a human subject interfaced with a motor prosthesis?

A HMI comprises the technology and software needed for a human subject to interact with a machine. Considering the scope of this thesis, we constrain our review to *HMIs that provide insight into human neuromuscular control and allow to record biosignals from which the human motor intent can be extracted and used to control a robotic system* (i.e., any robot manipulator, prosthesis, other rehabilitation devices). In this regard, different HMIs exists: electroencephalography (EEG) [129, 104], electrocorticography (ECoG) [118, 39, 124], electromyography (EMG) [63, 60] and direct cortical control through multi-electrode arrays. These HMIs have been widely used in the rehabilitation field for interfacing patients with robotics devices used to substitute, augment or assist motor functions. The advantages and disadvantages of these HMIs range from signal extraction to signal-to-noise ratio (SNR), invasiveness of signal recording, and signal deterioration over time. EEG and EMG are the two HMIs mostly explored in literature and used in clinical applications. Using EEG requires the user to wear a grid of sensors which record the electrical activity of the brain transmitted through the skull. Some of the drawbacks of EEG are the low SNR, the low spatial resolution compared to ECoG [4, 104], and the discomfort in using the sensors. EMG records the electrical potential generated by the muscles when these contract as a result of neural excitation or electrical stimulation [213]. There are different types of EMG technologies depending on the type of sensors, their size and the measuring site. We can distinguish two main categories: implanted myoelectric sensors (IMES) and surface EMG (sEMG). IMES uses sensors directly implanted in the muscular tissue. The high spatial

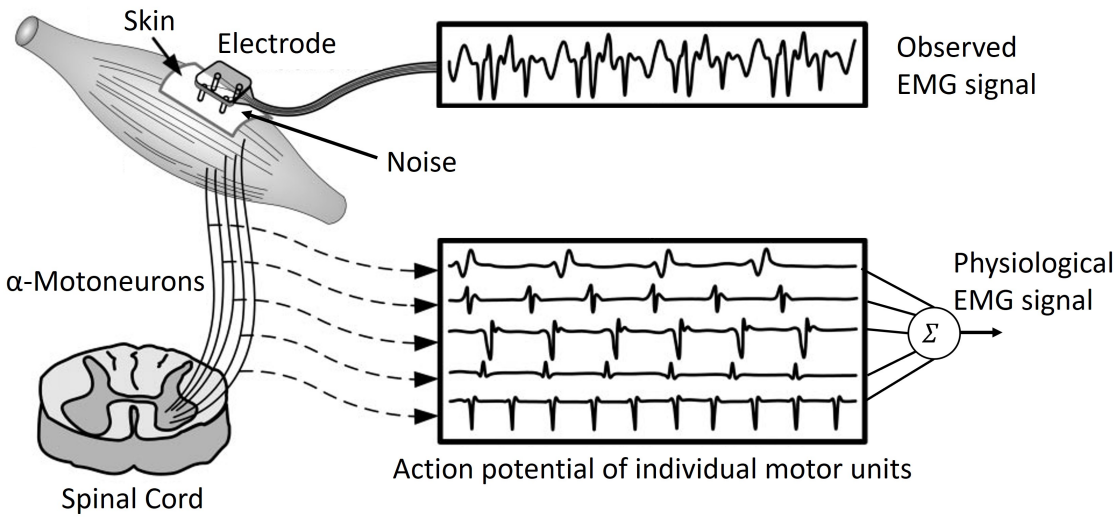

Figure 2.4: Figure adapted from [49]. A simple scheme of the physiological generation of sEMG signals contrasted to the sEMG signal recorded by an sEMG sensor. The summation of the motor unit action potential from the muscle fibers results in a motor unit action potential. The electrode placed on the skin overlaying the muscle belly records the superimposition of the action potentials of the motor units resulting in the observed sEMG signal. This signal is affected by sources of noise.

resolution of this technology allows targeting muscle fibers of superficial and deeper muscles [168, 85]. However, IMES are highly invasive and difficult to deploy in clinical and research settings. On the contrary, surface electromyography, because of its non-invasiveness and ease of use, is the most widely used type of HMI to interface with the human neuromuscular system. *Surface EMG uses electrodes placed on the skin overlying a muscle to record the electrical potential generated by the muscle's contraction*. While sEMG does not interface directly with the nervous system, sEMG signals contain the neural information underlying muscle electrical activity: there is a one-to-one correspondence between the neural events (i.e., axon potential discharges) and the events recorded in the sEMG signals (i.e., action potentials) [59, 60]. *Changes in neuromuscular control and muscular activity result in changes in the sEMG signals. Surface EMG signals can thus be processed to estimate the user's motor intention about the joint spanned by the targeted muscles*. In the field of motor prostheses, which is the domain application of this thesis, surface EMG has been considered the viable way for continuously interfacing with a human subject and it is used in most of the commercially available prostheses due to its non-invasiveness and ease of use. However, surface EMG has different limitations due to the type of technology used (i.e.,

electrodes placed on the skin). An sEMG signal is the result of the superimposition of the electrical activity of the muscle fibers underneath the sensor. This means that surface EMG makes it difficult to target specific muscles, and the sEMG signals might be contaminated by the activity of adjacent muscles. Due to the measuring setup, and depending on the size of the electrodes, sEMG is prone to technical difficulties (e.g., sensor slippage, sensor misalignment, muscle cross-talk [59, 61]) that make the problem of decoding the motor intent highly challenging.

In Section 2.3.2 the physiology underpinning the generation of sEMG signals is discussed more in detail; specific technical issues such as that of crosstalk are discussed.

2.3.2 Surface electromyography (sEMG)

In Section 2.3 we overviewed the main types of HMIs used to detect the motor intent of a human subject. Among the HMIs, we have introduced surface electromyography as a non-invasive way to interface with the neuromuscular system. Below, surface EMG is discussed more in detail since it is the HMI used in this work.

The central nervous system (CNS) conveys commands to the effector muscles through the recruitment and firing of spinal motor neurons (neuronal cells) innervating the target muscles [88]. The motor unit, constituted by the motor neuron plus the muscle fibers it innervates, generates an electrical field called motor unit action potential (Figure 2.4). As a result, when a muscle fiber is excited by a neural drive it starts conducting electricity. Surface electromyography uses electrodes overlying the muscle of interest to measure its electrical activity [50]. The recorded sEMG signal is a superimposition of the measurable potentials generated by the active motor units. The number of active motor units and their firing rate determines the shape and magnitude of the recorded sEMG signal. In particular, the signal appears positive and negative due to the summation of motor units activity and due to the random firing rate of the motor neurons. Figure 2.4 provides an illustration of these concepts. The sEMG signals contain information on the neural drive to the muscles and therefore provide the biosignals from which the central motor control strategy can be inferred using suitable processing methods and detection of intention algorithms.

Different sources of noise might affect the measured signals such as motion artefacts during dynamic experiments, electrical interference from adjacent muscles or equipment, electrode positioning, and skin impedance [48]. Specifically, the layers of tissue between the signal source and the measuring site result in temporal and spatial filtering of the signals [62, 136]. This effect is known as volume conduction. Moreover, classic sEMG sensors do not allow high spatial resolution due to the sensor size. This means that this setup does not allow to record the activity of the single motor unit, but provides the global activity of the

muscle. This leads to another technical issue known as crosstalk: the signal recorded over a muscle might be contaminated by a nearby muscle depending on the muscles' arrangement and sensors' placement. Finally, the random nature of the firing rates introduces low-frequency noise and loss of information. As a result, the recorded sEMG signal differs from the physiological myogram constituted by the superimposition of the action potential of the motor units [48] and requires filtering steps before the signal can be used. Below we describe the device used to record the muscle activity within the experimental work of this thesis and we outline the signal processing procedure.

Myoband

The Myoband developed by Thalmic Lab is the HMI used in this thesis. The device is an array of 8 classic low-density sEMG sensors and a nine-axis Inertial Measurement Unit (IMU). It has a working frequency of 200 Hz and data are transferred via Bluetooth. The raw sEMG signals were bandpass-filtered (20 – 500 Hz) and full-wave rectified before the root-mean-square temporal features were extracted (moving window of length 160 ms and step size 40 ms). Notice that the cut-off frequencies of the filters are specific for this device, in relation to the working frequency and considering the muscles and motions performed according to the experimental protocol discussed in Section 5.3.1. The root-mean-square temporal feature approximates the power of the sEMG signal which provides an estimate of the strength of the neural drive to the muscle [49]. Further processing steps such as sEMG signal normalization according to the maximum voluntary contraction are described in Section 4.3.1.

2.4 Fundamentals of musculoskeletal modeling

Skeletal muscles are the biological actuators of our skeletal system. Muscular tissue is able to contract (i.e., to shorten) while producing a pulling force that, transmitted by the tendon to the bone, may generate movement of the body's segments. Fundamental studies on the biomechanical modeling of the muscular tissue properties date back to 1938 when A. V. Hill [90] proposed the first structure of the well-established phenomenological Hill's model. This model, together with the work led by H. Huxley [101], has laid the foundations of the current understanding of how muscles generate force when activated by a neural input, and how this process can be formalised mathematically. Hill's and Huxley's models have opposite approaches in muscle-tendon modeling [214]: Huxley's model aims at representing the mechanism of the muscle contraction dynamics with great accuracy, at a microscopic

level; the Hill's model is phenomenological in nature, meaning that it aims to explain macroscopic properties of the muscle's contraction dynamics. As a result, Huxley's approach led to complex and computationally expensive models that require in-depth knowledge of neurochemistry, and physiology underlying muscle contraction. On the contrary, Hill based models propose a compromise between the representation accuracy of macroscopic biomechanical behaviour and model simplicity which led to greater transparency and applicability of these models.

In this thesis, we are interested in Hill's approach. This is motivated by the aforementioned characteristics of Hill's approach which are in line with the motivations of this work and the principles followed to design the framework presented in this thesis (Section 1.2).

In Section 2.4 we discuss the basic macroscopic properties of the muscular-tendinous tissue (i.e., force-length and force-velocity relationships) and provide the reader with a "microscopic" explanation of a described behaviour only when it aids the understanding. Based on these macroscopic properties the classic Hill's model is described (Section 2.4.2): the concept of muscle-tendon unit (MTU) is introduced, as well as the modeling of the *activation dynamics* and *contraction dynamics* processes. Mechanical properties of the musculotendinous tissue highly depend on the extrinsic arrangement of fibers and tendons on the skeleton. We, therefore, describe its geometrical arrangement on a generic body segment and introduce the concept of *moment arm* which constitute a basic operator to transform variables from the muscle space to the joint space (e.g., muscle force is related to joint torque, muscle change in length to joint angular displacement). Finally, in Section 2.4.4 we define the muscle impedance, joint impedance and Cartesian impedance of the upper-limb.

At the end of this section, the reader is provided with the background knowledge required to derive the mathematical formulation of Hill's muscle-tendon models and to understand the muscle-tendon model used in the proposed framework.

2.4.1 Macroscopic properties of the muscular-tendinous tissue

Skeletal muscles have a hierarchic structure, as shown in Figure 2.5. A muscle is constituted by fascicles, a fascicle is composed of muscle fibers, each fiber is made of myofibrils and finally, each myofibril contains thousands of sarcomeres connected in series. The sarcomeres are constituted by two main proteins called actin and myosin. Current knowledge on muscle contraction at a microscopic level is based on Hugh Huxley's "Sliding filament theory" [103, 102]. The action potential generated by motor units triggers the formation of actin-myosin cross-bridges, which determine the contraction of the sarcomere and allows the voluntary contraction behaviour of muscles as we know it.

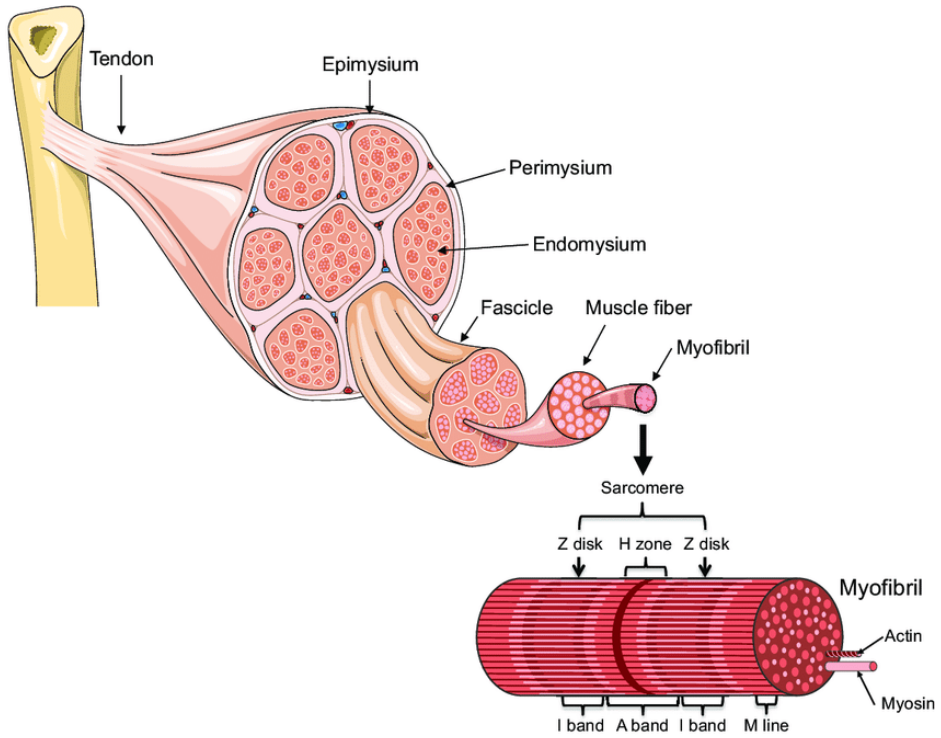

Figure 2.5: Scheme of the structure of a skeletal muscle. Figure from [20].

Collagenous connective tissue links the muscular fibers together and to the bones. Part of the connective tissue surrounding groups of fascicles and the whole muscle constitute the aponeurosis which is contiguous to the tendon and because of its location considered the inner part of the tendon. The tendon attaches to the bone and transmits the contracting force of the muscle to the bone generating motion. The force generated by a muscle can be active or passive. The *active force* is generated by the *contractile elements* within the muscular tissue in response to a neural activation and requires energy expenditure. Contractility is therefore the property of contracting in response to input stimuli. The force generated by the muscle and tendon is dependent on the muscle's and tendon's length. This property is referred to as *elasticity*. However, the connective tissue found in muscles and in tendons is passive (i.e., non-contractile) and it possesses a force-length relationship that differs from the active elasticity of the muscle's fibers. We refer to the force-length property of connective tissue as *passive elasticity*.

Below, we describe the macroscopic properties of the muscle tissue's contraction dynamics, which together with the *activation dynamics* describes the overall dynamics of the musculotendinous system. Recall that in Section 2.3.2 we have explained the basic physiological principles and events characterising the process from neural inputs to the generation of muscle activations. This is the activation dynamic process. The *contraction dynamics*

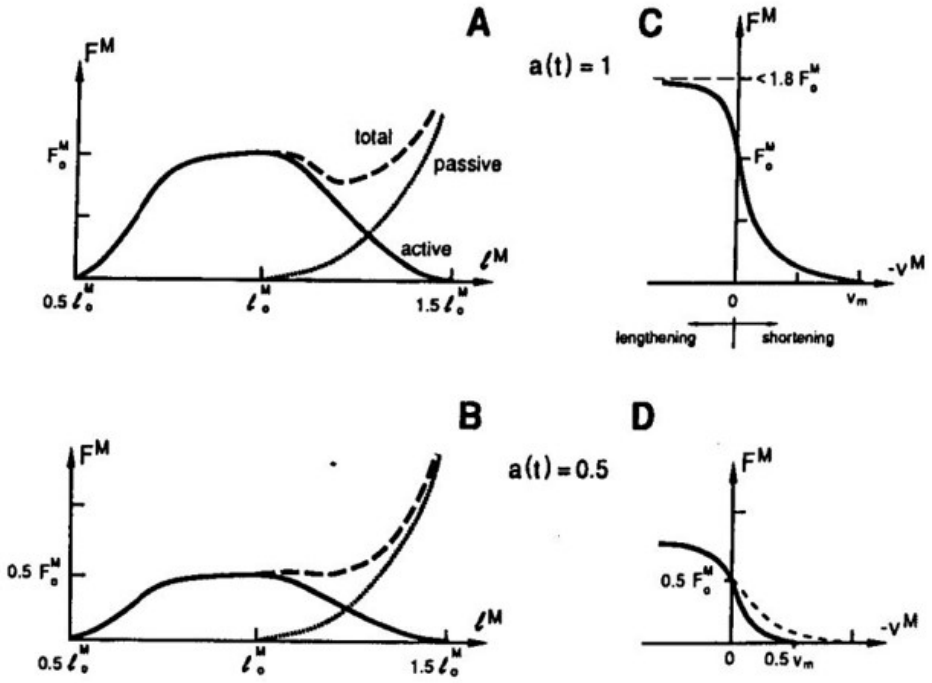

Figure 2.6: Figure from [223]. The muscle force as a function of its length is shown in A and B for two input activations of 1 and 0.5, respectively. In this figure F^M is the isometric force at the muscle length l^M, F_0^M is the maximum isometric force reached at $l^M = l_0^M$. The force-length contribution given by the contractile component and the passive component are shown. The total force is the sum of the active and passive contribution. The experimental curve of the force-velocity relationship for contractile tissue is shown in C and D for maximum activation and 50% of the maximum activation, respectively.

describes the generation of muscular force on the basis of macroscopic properties of the musculotendinous tissue, given the muscle activation. An understanding of the main features of the contraction dynamics will allow us to introduce the mechanical Hill's model described in the following sections.

Muscle contraction dynamics

The *contraction dynamics* describes the process from muscle activation to the generation of muscle force. This process is characterised by two fundamental properties: *the force-length (elasticity) and the force-velocity (viscosity) relationships*. For contractile elements, the force-length and force-velocity properties depend on the input activation. We discuss below the force-length-velocity properties of the muscular tissue and of the tendon.

Muscle: force-length relationship The total tension-length relationship of the skeletal muscles determines the steady-state force generated by active and passive tissue components when the muscle is held isometric (i.e., constant length) against a specific load. Structural changes to the myofibrils at the level of the sarcomere are the basis of the observed active force-length relationship [79]. The active force-length relationship is a function of the input neural activation, the length of the muscle fibers and the maximum isometric force that can be generated by the muscle. Assuming a constant magnitude of the input activation and recording the maximum force reached by the muscle when contracting isometrically at different lengths, the force-length characteristic curve is obtained (an example for constant normalised maximum activation, and 50% of maximum normalised activation in Figure 2.6-A, B). The peak of the curve is the maximum isometric contraction and the corresponding muscle length is called *optimal length* (indicated as l_0^M in Figure 2.6-A, B). The region where the active muscle force is generated is nominally in the range $[0.5l_0^M, 1.5l_0^M]$ [223]. For different magnitudes of input activation, a family of curves with the same properties but different maximum isometric contractions is obtained. The connective tissue surrounding the contractile elements contributes to the force-length relationship. The passive tension-length relationship is obtained when the muscle is stretched in the absence of activation stimuli above the optimal length. For lengths smaller than the optimal length the passive component is in a slack state and does not provide any tension. in Figure 2.6-A,B the passive component of the force-length curve can be observed.

Muscle: force-velocity relationship While the force-length relationship describes the steady-state properties of the musculotendinous tissue, the force-velocity relationship describes the dynamic behaviour of the muscle. The force generated by a muscle is dependent on its contraction velocity: the slower the muscle shortens the greater the force it generates, and vice versa.

Experimentally derived curves of the force-velocity relationship can be obtained by measuring the force generated by the muscle at different shortening and lengthening velocities or during isotonic experiments where the muscle contracts subject to constant tension. The force-velocity curve can then be fitted to the collected force data. Today, there is still disagreement on the shape of this force-velocity curve. The first experimental curve of the force-velocity relationship was reported by Hills [90] for concentric contractions. The relationship was represented as a hyperbolic curve, suggesting that when the fiber shortens the force decreases in a hyperbolic fashion until a null force is reached at the maximum shortening velocity. The length at which shortening terminates corresponds to the length at which the force can be sustained at steady-state. This behaviour has been explained by

different factors [42] related to the kinetics of cross-bridges. Although a hyperbola may provide a good fit to concentric data, it was suggested that a double hyperbola provided better approximation in high-force and low-velocity regions [55]. Subsequent studies showed that the hyperbolic model proposed by Hill was not suitable to describe eccentric contractions [111] and isovelocity acitivities [222]. The model was extended to include the description of the relationship for eccentric contractions [111]: when the muscle undergoes an isotonic contraction (i.e, constant tension) the force increases for low lengthening velocities, then it increases and plateaus as the velocity increases further (1.5 isometric force). The observed force-velocity behaviour may be due to the stretching of cross-bridges [214, 56]: as velocity increases the cross-bridges are stretched to the maximum sustainable values after which they detach limiting the muscle force during lengthening.

An experimental curve of the force-velocity relationship can be observed in Figure 2.6-C,D. Notice that the force-velocity relationship is shown in the figure for a specific muscle length and input activation. At optimal fiber length, the muscular tissue cannot sustain any force when reaching the maximum velocity, independently of the input activation. There is no consensus on the dependence of the velocity axis intercept on muscle length or activation [223]. However, for modeling purposes, it is often assumed to be independent since it does not substantially affect the functionality of the models [216]. Other modeling assumptions are that the relationship scales with length and activation, it does not have any discontinuity on the force axis intercept, and the force-velocity relationship is unaffected by the previous states of the muscles [223]. Experimental studies do not show consensus on these or the opposite assumptions, however, these do not seem to affect the functionality of the models. Isometric contractions lie along the zero-velocity axis of the graph. While we have provided an overview of the current understanding of the force-velocity relationship, the reader is referred to [8] for an exhaustive review of relevant studies investigating the shape of the force-velocity relationship, based on data collected from muscle specimens and during in vivo experiments.

Tendon dynamics

The force generated by the muscle affects the tendon. The tendon generates a force only if extended over the slack length (i.e., relaxed state). Considering the tendon force as a function of its length (Figure 2.7), the curve strain-length is characterised by an initial concave area called “toe region” where the tendon force has low magnitude; to continue elongating the tendon within the toe region a higher force is needed to produce the same change in tendon length meaning that the tendon stiffness increases. Beyond the “toe region” (about 2–4% of strain) the force increases linearly up to tendon breakage if it is stretched beyond the failure

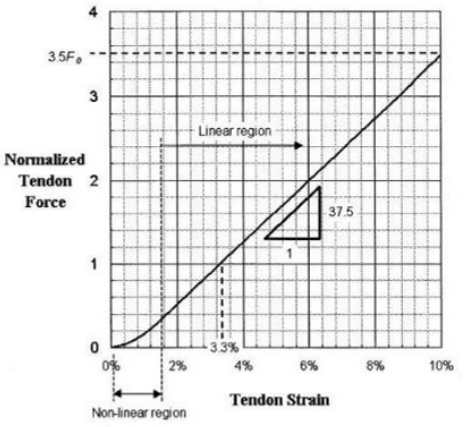

Figure 2.7: Example of the strain-length curve for the tendon. Image taken from [223].

point (usually after 10% strain) [138, 223]. The tendon stiffness is therefore initially low, it then increases non-linearly (within the toe region) and finally increases linearly (linear region). Tendon stiffness increases with tendon thickness and generally decreases with tendon length, long tendons are therefore more compliant. The tendon is characterised by hysteresis, meaning that when the tendon undergoes relaxation it follows a different force-strain path than it does during elongation. In this case, the force generated is slightly lower due to dissipative effects. The energy loss is typically less than 10% indicating that the elastic properties dominate over the dissipative ones.

2.4.2 Hill's mechanical muscle-tendon model

Initial efforts in modeling the mechanical behaviour of the muscle tissue used models composed of passive elements such as springs and damping elements [215]. Maxwell's model uses both elements attached in series; the Voight model uses the elements in parallel, and Kelvin's model modifies Voight's model by adding a spring in series to the damper element. While these models allowed to study of the response of the muscle tissue under compressive and tensile loads, they could not reproduce active muscle contraction. In 1938, Hill proposed a model that combined the passive properties of the Kelvin model by adding in parallel to the damper an active element called *contractile element* [90]. Joint effort in muscle-tendon modeling [133, 25, 211, 224] has led to the definition of a model capable of predicting the contraction dynamics of the musculotendinous tissue. The model structure and parameters identification and estimation were conducted during controlled input-output in vivo experiments where the muscle load, length and stimulation were provided as input and the joint motion was the measured output. It is important to clarify that from here on we

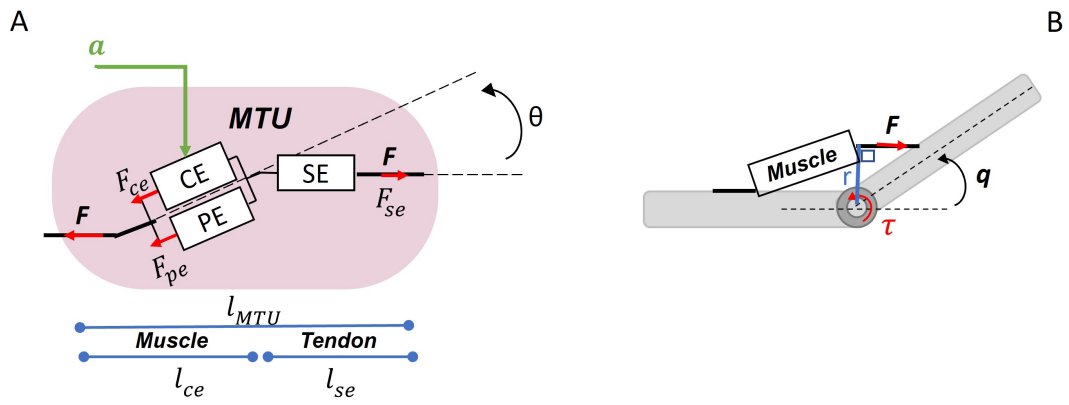

Figure 2.8: A) Generic Hill's type muscle-tendon model [24] made of muscle and tendon elements. The contractile (CE) and a parallel (PE) element compose the muscle; the tendon is modeled as a serial element (SE). The MTU, driven by the input activation a generates the indicated output forces. The muscle line of action with respect to the tendon depends on the pennation angle θ. B) Arrangement of MTU on the links connecting a joint q. The MTU force F generates a torque τ at the joint that depends on the moment arm r.

refer to the muscular or tendinous tissue as a whole, due to homogeneity in structure (i.e., tissue composition), and function. Therefore, we describe a *lumped model*, which *contains lumped elements and parameters that describe the collective contraction dynamics of the sub-elements of the muscular tissue*.

According to Hill's approach, when the tendon stretches it affects the length and velocity of the muscle contraction and so the muscle is modeled in series to the tendons. The muscles and the tendon elements constitute a muscle-tendon unit (MTU) as shown in Figure 2.8-A. The classic Hill's type MTU of length l_{MTU} is composed of a muscle of length l_{ce} in series to a tendon of length l_{se} [24]. The muscle is made of a contractile element (CE) in parallel to an elastic element (PE) which models the connective tissue. As discussed in Section 2.4, the CE element is characterised by a force-length and a force-velocity relationship, and it is driven by an input activation a. When activated, the contractile element generates a force F^{ce} as a function of the current muscle length l_{ce}, contraction velocity $\dot{l}_{ce}$ and muscle activation input a. PE is a purely passive element, and it produces a resistive force F_{pe} when stretched beyond its slack length. The tendon is modeled as a non-linear spring (SE), and it is added in series to the muscle. The angle between the lines of action of the tendon and that of the muscle fibre is called pennation angle θ (Figure 2.8-A), and although for some muscles it is negligible, for others it is substantial [25]. The force generated by the CE and PE elements affects the force generated by SE, and vice versa. The system at equilibrium is described by

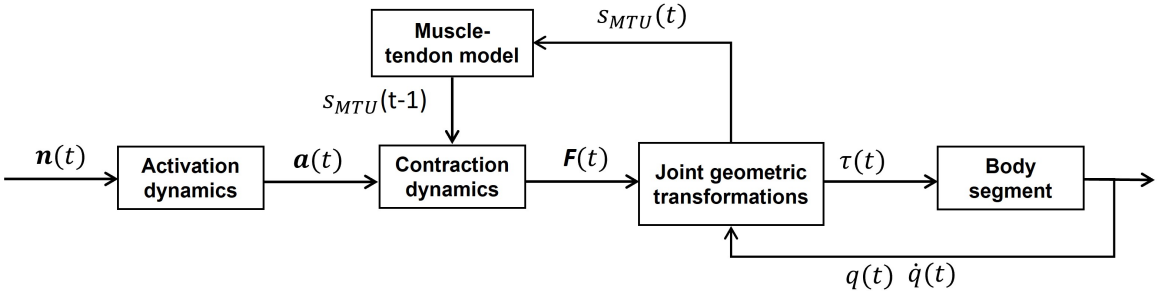

Figure 2.9: Scheme of the musculoskeletal system. The neural input $n(t)$ at time t is transformed into muscle activation $a(t)$ by the activation dynamics process. The muscle activation drives the contraction dynamics to generate the output force $F(t)$, given the current state of the muscle-tendon model. The muscle-tendon model state $s_{MTU} = \{l_{ce}, l_{MTU}, \dot{l}_{ce}, \dot{l}_{MTU}\}$ is constituted by the length of the CE component, the length of the MTU, and by the corresponding contraction velocities. The MTU force $F(t)$ is transformed from the MTU space to the joint space of the rigid body. Finally, the torque $\tau(t)$ is applied and the correspondent angular displacement is measured. The state of the muscle-tendon model is then updated.

the following non-linear dynamic equation:

$$F = \left[F_{ce}(l_{ce}, \dot{l}_{ce}, a) + F_{pe}(l_{ce})\right] cos\theta = F_{se}(l_{ce}, l_{MTC}) \tag{2.15}$$

Given the input activation a and the initial state of the muscle-tendon (l_{ce}, l_{mtu}, $\dot{l}_{ce}$, $\dot{l}_{mtu}$) the MTU generates as output the muscle-tendon force F.

The biomechanical properties of the muscle and tendon have been studied extensively during controlled in-vivo experiments. Based on the macroscopic properties described in Section 2.4, in this section, we provide insight into the fundamental mechanical properties of the skeletal muscle and tendon and derive the mathematical formulation of the active and passive elements of the MTU introduced in Figure 2.8-A. Researchers have explored different derivation of the MTU model, varying the arrangement of the elements composing its structure [214]. The muscle-tendon model used to derive the mathematical formulation of the contraction dynamics is the basis for the MTU structure used in the framework described in Chapter 4.

Below, we provide an overview of the steps to actuate a joint using an sEMG-driven musculoskeletal model. A scheme of the main components of the pipeline is provided in Figure 2.9. Firstly, the muscle-tendon dynamics is described by mathematically formulating the activation dynamic and contraction dynamic processes. As a result of the muscle-tendon dynamics the MTU force F is obtained based on the input activation and the previous state of the MTU. We then consider the geometrical aspects to define the transformation of variables

from the muscle-tendon space to the joint space, which will allow us to obtain the joint torque. Derivation of the forces generated as a result of the contraction dynamics is needed to then obtain the mathematical formulation of the muscle-tendon stiffness and damping, described in Section 2.4.4. The following sections focus on concepts that are fundamental for the understanding of the next chapters and it is by no means an extensive review of the work done in muscle-tendon modeling. The interested reader who wants to deepen their understanding is referred to additional material [25, 214].

Model of activation dynamics

The contraction dynamics of an MTU is driven by an input activation $a(t)$. This activation is the output of the activation dynamics process that transforms the neural excitation $n(t)$ into muscle activation $a(t)$. According to [223], the raw sEMG signals recorded from a target muscle represent the neural excitation $n(t)$, and it is suitable to drive a MTU. The activation dynamics process can be regarded as the rectification and filtering of the raw sEMG signal when the cut-off frequencies of the filters being used are those characterising the excitation (i.e., time for building up activation) and relaxation (i.e., deactivation time) process that drives the muscle activation. This excitation-relaxation process has been modeled using linear and non-linear first-order dynamic systems [223, 222, 216]. In the first case, the activation dynamics is characterised by a single time constant, whereas two time constants are used in the non-linear model, one associated with the excitation process and one associated with the deactivation time. The time constant of the excitation process is lower than the time constant during relaxation. This implies that the isometric force rises faster during excitation than relaxation, as it will be discussed in the next sections. In [87], a second-order model is used. The time constants are determined based on knowledge of the target muscles or estimated during a calibration procedure. The obtained activation signal is then normalised according to the maximum voluntary contraction, as required by the MTU design [24]. The normalised and processed sEMG signal is then transformed to keep into account the non-linear relationship between sEMG amplitude and force generation. In [173], it is shown that the isometric sEMG signal does not necessarily linearly relate to the muscle force. As the stimuli frequency increases, the MTU output force will increase up to a steady state value, where no further force can be produced by the muscles. To account for this non-linearity the normalised muscle activation is transformed using the following equation:

$$a(t) = \frac{e^{An(t)} - 1}{e^{A} - 1} \tag{2.16}$$

where A is a non-linearity factor varying in the range $[-3, 0]$. When $A = 0$ the relationship is linear, whereas the relationship is highly exponential when $A = -3$. the value of A is typically estimated during a calibration process.

Model of Contraction dynamics

The output of the activation dynamic process, described in the previous section, is the input to the contraction dynamics, described below. The contraction dynamics provides the force generated by the MTU given the MTU state s_{MTU} and an input activation a (Figure 2.9). The muscle force depends on the muscle state, and it is characterised by a force-length and force-velocity relationship discussed in Section 2.4. The force generated by the muscle is therefore represented by the following fundamental equation [90]:

$$F = F_{fl} F_{fv} F_{max} a \tag{2.17}$$

where F_{fl} is the normalised active force-length relation, F_{fv} is the normalised force-velocity relation, F_{max} is the maximum isometric force (i.e., force-length relationship), and a is the activation in the range [0, 1] which scales the maximum isometric force. Considering the Hill's type MTU introduced earlier (Figure 2.8-A), the force F in Equation 2.17 is given by the sum of the forces generated by CE and PE (Equation 2.15) which is equal to the force generated by the serial element. The forces generated by CE, PE and SE are derived below.

CE element The force generated by the CE element is based on the force-velocity relationship introduced by Hill to describe the heat associated with muscle contraction [90]. This formulation has then been rewritten to include the force-length relationship [24] as follows:

$$F_{ce} = F_{fl}(l_{ce}) \frac{F^{max} b_{hill} - a_{hill} \dot{l}_{ce}}{b_{hill} + \dot{l}_{ce}} \tag{2.18}$$

where F^{max} is the maximum isometric force, a_{hill} is a thermal constant related to the cross-section of the muscle, and b_{hill} defines the rate of energy dissipated. However, Equation 2.18 was derived only for shortening velocities, and it has been subsequently extended to account for eccentric forces [205].

PE element The passive tissue force-length relationship has been approximated by viscous-elastic models that may consist of a non-linear spring and a damper. However, the damper is usually neglected or assumed to be linear [214]. The passive force depends on the muscle fiber length. It is null for l_{ce} shorter than the optimal fiber length and increases exponentially

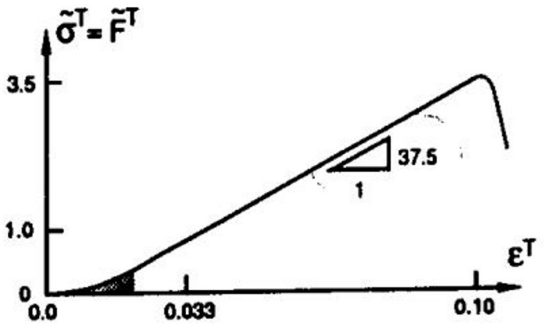

Figure 2.10: Figure from [223]. Normalised tendon force as a function of the normalised tendon strain.

thereafter according to the following equation:

$$F_{pe} = f_p(\bar{l^{ce}})F^{max} \tag{2.19}$$

where $\bar{l^{ce}}$ is the normalised CE length with respect to the optimal length and with $f_p(l)$ derived as follows [24]:

$$f_p(\bar{l^{ce}}) = \frac{e^{10(\bar{l^{ce}}-1)}}{e^5} \tag{2.20}$$

SE element Because the tendon is arranged in series to the muscle, the force generated by the muscles affects the tendon. The tendon is modeled as a non-linear spring that generates a force F_{se} only if extended over the slack length l_{se0}. Notice that F_{se} is not activation dependent as the tendon is a passive element. The force F_{se} is a function of the normalise strain $\varepsilon^T = \frac{l_{se}-l_{se0}}{l_{se0}}$. Given the strain, the normalised force generated by the tendon $\bar{F}^{se}$ is described by the following system of equations [24]:

$$\bar{F}_{se} = \begin{cases} 0 & , \varepsilon^T \leq 0 \\ 1480.3(\varepsilon^T)^2 & , 0 < \varepsilon^T < 0.0127 \\ 37.5\varepsilon^T - 0.2375 & , \varepsilon^T >= 0.0127 \end{cases} \tag{2.21}$$

The numerical values defining the toe region and the linear region are based on [223]. In the same study, based on the experimental observation that the tendon thickness is dependent on muscle strength the final tendon force is computed as follows:

$$F_{se} = \bar{F}^{se}F^{max} \tag{2.22}$$

In Figure 2.10, an example of force-length curve for the tendon is shown. In this plot, the force produced by the tendon decreases abruptly at $\varepsilon^T = 0.10$ before breaking.

Pennation angle: geometrical arrangement between muscle and tendon

The geometrical arrangement of the fibers and the connective tissue plays an important role in determining muscle force and the muscle-tendon biomechanical behaviour [75]. Generally, muscle fibers are arranged in parallel arrays, forming an angle (called pennation angle) between the line of pull of the muscle and the one of the tendon. The pennation increases as the length of the muscle fibers shorten. The greater the pennation angle the less force a muscle fiber contributes along the line of action [130]. Fibers can be arranged in a more complex geometrical configuration to create multipennate muscles with fibers orientated in different planes. In Figure 2.8-A the pennation angle θ is shown. Muscle-tendon length and the pennation are linked by an additional modeling constraint that determines the dimensionality of the muscle-tendon model [52]. Hill based models are typically one-dimensional models since the muscle thickness (i.e., the sine of the muscle-tendon length considering the pennation angle) is assumed constant [188]. Typically, the pennation angle with constant thickness is computed as follows:

$$\theta = sin^{-1}(\frac{l_{opt}\theta_o}{l_{ce}}) \tag{2.23}$$

where θ_o is the pennation angle at optimal length l_{opt}.

2.4.3 Geometric relation between muscle-tendon space and joint space

Biomechanically, the action of a muscle spanning a joint is defined as agonist if the joint acceleration is in the same direction as the acceleration imposed by the muscle [223]. A muscle is an antagonist if its action opposes the joint movement. Considering a single-joint motion such as flexion of the wrist, a wrist flexor muscle (e.g., Flexor Carpi Radialis) acts as an agonist, while a wrist extensor muscle (e.g., Extensor Carpi Radialis) acts as an antagonist, thus defining an agonist-antagonist pair. In the simple case of single joint motion, where the elbow is assumed to not move and to not affect the state of the wrist flexor and extensor muscles, the terms agonist and antagonist and flexor and extensor refer to the same muscle groups. In the rest of the thesis, we use the terms flexor and extensor to indicate these muscles or muscle-tendon units acting as flexor and extensor during isometric contractions or when no joint motion is specified. When a joint is spanned by multiple muscles (and correspondent tendons), these can be divided into groups of agonist and antagonist muscles

with respect to a joint motion. Muscles within the same group are synergistic since they produce torque that causes the same rotation about the joint. Consider m muscles-tendons acting on a single joint and generating m forces $(F^1...,F^i,...,F^m)$. The torque generated by muscle-tendon i is defined as the product between the F^i and the correspondent moment arm. By convention, agonist muscles have a positive moment arm for a given movement, while a negative moment arm indicates the function of an antagonist muscle [162]. For simplicity, consider the arrangement of the muscle-tendon unit on the links in a straight line connecting the origin and the insertion point of the muscular-tendinous system (Figure 2.8)-B. The length of the muscle-tendon unit may be determined as a function of the links' configuration, which depends on the joint position q. The moment arm r is the perpendicular distance from the line of action of the force F generated by the MTU to the centre of the joint rotation and it can be mathematically formalised given the muscle-tendon length l_{MTU} and q using the method proposed in [10]:

$$r(q) = -\frac{\partial l_{MTU}(q)}{\partial q} \tag{2.24}$$

Considering m muscles spanning n joints, the generic matrix of the moment arms $R \in \mathbb{R}^{m \times n}$, called muscle-space Jacobian, is defined as follows:

$$\mathbf{R} = \begin{bmatrix} \frac{\partial l^1_{MTU}(q1)}{\partial q1} & \cdots & \frac{\partial l^1_{MTU}(qn)}{\partial qn} \\ \frac{\partial l^2_{MTU}(q1)}{\partial q1} & \cdots & \frac{\partial l^2_{MTU}(qn}{\partial qn} \\ \cdots & \cdots & \cdots \\ \frac{\partial l^m_{MTU}(q1)}{\partial q1} & \cdots & \frac{\partial l^m_{MTU}(qn)}{\partial qn} \end{bmatrix} \tag{2.25}$$

These equations can be used to transform variables of the muscle-tendon space into corresponding variables in the joint space. The torque generated by applying the m forces is computed as follows:

$$\tau = FR \tag{2.26}$$

As stated above, the negative sign introduced in the moment arm definition, implies that a muscle induces positive work during shortening. In this thesis, we consider the case of a single-DoF actuation, modelled by the action of two MTU, with muscle elements acting as a flexor and extensor muscles. These muscle models receive as input the electromyographic activity of the Flexor Carpi Radialis and Extensor Carpi Ulnaris as detailed in Chapter 4, which triggers the contraction dynamics.

2.4.4 Muscle-tendon impedance

In Section 2.1.4 we have defined impedance as a dynamic operator that describes the forces generated by a rigid body under imposed motion. Adaptation of limb impedance is introduced in Section 2.2 as a crucial human motor control strategy to modulate the physical interaction between the human limb and the environment. We first clarify the following terminology which defines the impedance in three different spaces, the muscle-tendon space, the joint space and the Cartesian space (i.e., end-effector or limb end-point space):

- *Muscle-tendon impedance* is the resistance opposed by the active and passive components of the MTU to shortening or elongation.
- *Joint impedance* of a revolute joint quantifies the amount of torque needed to displace the joint. Given the muscle-tendon impedance, the Jacobian matrix of the moment arms R (Equation 2.25) can be used to transform the impedance from the muscle-tendon space to the joint space.
- *End-point limb impedance* is the impedance in the Cartesian space of the robot. The upper-limb can be considered a kinematic structure constituted of the shoulder, elbow and wrist joint, and the upper-arm, forearm and hand links. If we compare this kinematic structure to the generic one introduced in Section 2.1.2 the human hand corresponds to the robot end-effector.

In each of the cases listed above, impedance quantifies the resistance to imposed motion, and it can be summarised by the following dynamic properties: stiffness, damping, and inertia. These properties depend on intrinsic and extrinsic properties of the musculoskeletal system (Section 2.4). In this work, we assume that the muscle-tendon mass is lumped to that of the robot's link, and we focus on the stiffness and damping properties. Moreover, based on the distinction between active and passive force, introduced in the previous section, we distinguish between active and passive impedance if it characterises the contractile element (CE) or the passive ones (PE, SE).

Below we will define the stiffness and damping of the muscle and of the tendon. We then compute the overall impedance of the muscle-tendon unit and derive the equations to transform these quantities from the muscle space to the joint space. Impedance properties of the muscular-tendinous tissue are due to the co-contraction of agonist and antagonist muscles, but also to reflex feedback. In Section 2.2 we explained that the coactivation of agonist and antagonist muscles is the main strategy used by the CNS to modulate the impedance since neural feedback is affected by transmission latency. For this reason, the latter is considered beyond the scope of this thesis and not described in detail.

Muscle stiffness and damping

The dependence of the muscle force on the muscle length is referred to as spring-like behaviour. A distinction must be made between passive and active spring behaviour. The spring-like behaviour of muscles is often confused with the classic definition of passive stiffness (the ratio of the change in force to the change in length). However, the force-length relationship typical of muscles is also dependent on the neural input. Moreover, impedance is a nonlinear effect, and can not be described by a linear model, such as the one of a classic passive spring. Considering the fundamental force-length relationship introduced in Section 2.4, when the muscle fibers are stretched within 3% of their length, the force initially increases, but the stiffness remains relatively constant [209]. This stiffness is called *short range stiffness* and was found to approximate well the stiffness during isometric conditions [172]. However, when a muscle fiber is stretched at low velocities beyond the short-range stiffness, the stiffness is found to be higher than the stiffness in the isometric state. As shortening velocity increases, muscle stiffness decreases. When shortening stops, the stiffness is found to increase again. The short-range stiffness estimator is found to not be appropriate for estimating the muscle stiffness during dynamic movements [182].

Both muscular and tendinous tissues are characterised by viscous properties associated with energy dissipation. Viscosity is an active property as it depends on the neural input. A system that possesses this property is "damped", and the damping depends on the velocity. In general, damping is defined as a change in force to resist a change in velocity. An increase in lengthening velocity near zero produces a positive change in velocity and force resulting in a positive damping. When the muscle shortens, the change in velocity is negative, and the force decreases, leading again to a positive damping value. Muscle damping is characterised by high values near zero velocity, and lowest values at high shortening or lengthening velocities [114]. Since muscle force is dependent on the input activation, the impedance of a muscle increases with the activation level. Therefore, synergistic activating agonist and antagonist muscles allows modulation of the stiffness and damping of the muscle and joints.

Tendon stiffness and damping

In Section 2.4 we have described the stiffness of the tendon based on its force-length curve. The stiffness of the tendon increases with thickness, while longer tendons are more compliant [138]. When the tendon is stretched and then returns to its rest length, there is energy loss due to hysteresis. However, the elastic properties dominate over the dissipative ones. Compared to tendons, muscles have a much greater hysteresis due to the high dependence of force on velocity [214].

Total muscle-tendon stiffness and damping

Given two springs in series and two springs in parallel, their equivalent total stiffness is known to be equal to the sum of their inverse, and to the sum of the stiffnesses, respectively. Consider the muscle-tendon unit introduced in Figure 2.8 and assume for simplicity that the pennation angle is null. Because the muscle and the tendon are arranged in series, the overall stiffness of the muscle-tendon unit can be computed as follows given the muscle stiffness K_m and the tendon stiffness K_t:

$$K_{MTU} = \frac{K_m K_t}{K_m + K_t} \tag{2.27}$$

From this equation, it follows that the total stiffness is lower than the muscle or tendon stiffness alone. Similarly, the damping of the muscle-tendon unit is defined as follows:

$$D_{MTU} = \frac{D_m D_t}{D_m + D_t} \tag{2.28}$$

where D_m and D_t are the muscle and tendon damping, respectively.

Joint impedance

Joint stiffness and damping are related to the corresponding muscle quantities by the moment arm. While torque is proportional to the moment arm, stiffness and viscosity are proportional to the square of the moment arm. Consider a muscle-tendon unit generating a torque τ that causes the displacement of the joint q. The joint stiffness is derived as follows [94]:

$$K_J = \frac{d\tau}{dq} = \frac{d(r(q)F)}{d\left(\frac{l_{MTU}}{r(q)}\right)} = r(q)^2 \frac{dF}{dl_{MTU}} = r(q)^2 K_{MTU} \tag{2.29}$$

Where τ and $r(q)$ are the torque and moment arm, which in turn depend on the joint position q. F is the force generated by the MTU of length l_{MTU}. The same derivation can be written to obtain the joint damping definition:

$$D_J = \frac{d\tau}{d\dot{q}} = \frac{d(r(q)F)}{d\left(\frac{\dot{l}_{MTU}}{r(q)}\right)} = r(q)^2 \frac{dF}{d\dot{l}_{MTU}} = r(q)^2 D_{MTU} \tag{2.30}$$

Consider now two muscle-tendon units spanning the joint q acting as flexor and extensor muscles. The action of the two muscles opposes one another at the joint level, generating torques in opposite directions, while the stiffness and damping contribution is summed at the joint level. As a result, there are different combinations of torques that can generate the same net torque but different joint impedance. This is a crucial aspect of the neural musculoskeletal

system, that due to its high redundancy allows humans to independently control the joint kinematics and the impedance. Consider now m muscle-tendon units acting on n joints. The Jacobian of the moment arms (Equation 2.25) can be used to define the mapping of stiffness and damping from muscle-tendon space to the joint space as follows [214]:

$$\mathbf{K}_J = \mathbf{R}^T \mathbf{K}_{MTU} \mathbf{R} + \frac{\partial \mathbf{R}^T}{\partial \mathbf{q}} \mathbf{F}_{MTU}^T \tag{2.31}$$

where $\mathbf{F}$ and $\mathbf{q}$ are vectors of dimensions m and n. The second term of the joint stiffness considers the dependency of $\mathbf{R}$ on $\mathbf{q}$, and describes the contribution to joint stiffness given by the change in moment arms. The joint damping is described as follows:

$$D_J = \mathbf{R}^T \mathbf{D}_{MTU} \mathbf{R} \tag{2.32}$$

Both joint stiffness and damping matrices may include direct terms and cross-coupling terms (i.e., off-diagonal terms) depending on $\mathbf{R}$. While direct terms relate changes in the stiffness and damping at a given joint to the angular deflection at specific joint, cross-coupling terms relate changes in stiffness and damping of a joint to angular displacements of another joint.

2.5 The human wrist

In this thesis, we describe a surface EMG-driven framework that allows a human subject to control the kinematics and the impedance of a DoF of a robotic system, through contraction of muscles involved in wrist flexion-extension. The sEMG signals of relevant muscles are the input to the framework and drive muscle-tendon models used to actuate the DoF. For this reason, the kinematic and dynamic properties of the human wrist joint are reviewed.

The human wrist joint plays a crucial role in successful grasping and manipulation of objects since it allows suitable orientation of the hand to execute the grasp and maintains the interaction with the object stable. In this section, we describe the kinematic properties of the wrist joint and define a model of its kinematics (Section 2.5.1). The dynamic properties of the wrist are then reviewed. This includes a summary of the main muscles involved in wrist motion (Section 2.5.2) and a description of the impedance properties of the wrist joint (Section 2.5.3).

2.5.1 Wrist kinematics

The wrist joint allows the hand to assume any orientation, in the joint limits, with respect to the forearm. More specifically, the human wrist kinematics involves a complex in-plane and

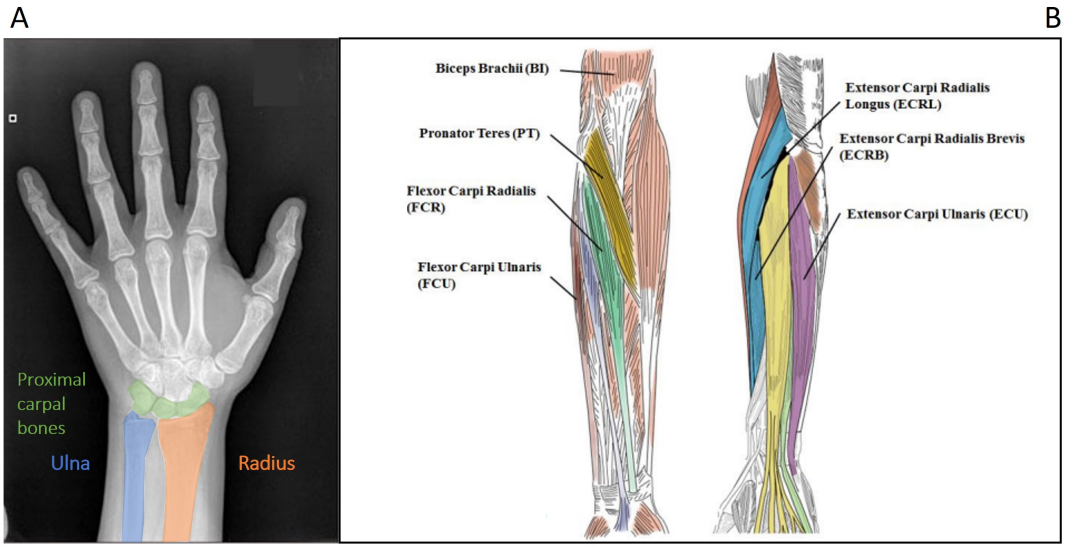

Figure 2.11: A) X-ray scan of a human hand plus wrist, showing the bones proximal to the wrist joint. The image is based on [122]. B) Scheme of the location of the main muscles of the forearm. Image taken from [141].

out-of-plane motion of the carpal bones (Figure 2.11-A) relative to the bones proximal to the wrist (forearm) [217]. Moreover, the carpal bones rotate and translate with respect to each other. This complex motion can be approximated and simplified as the combination of three motions of the hand with respect to the forearm: wrist flexion-extension, wrist ulnar-radial deviation and wrist pronation supination. In Section 2.1.2 we have introduced the concepts of rigid bodies, joints and kinematic chains. Let us define the wrist as a kinematic chain of two rigid links (i.e., the hand and the forearm) and three joints (i.e., flexion-extension, ulnar-radio deviation, pronation-supination). We assume that the amount of translation occurring at the wrist can be neglected without loss of global wrist functionality [112]. Now that we have identified the components of the kinematic chain, how are these articulated? Studies on the combined motion of the wrist biomechanics [155] show that the wrist possesses a kinematic hierarchy, meaning that the flexion-extension rotation carries the ulnar-radial deviation motion; and both motions are carried by the wrist pronation-supination. These kinematic constraints are well represented by the universal joint, obtained as a combination of revolute joints with non-intersecting axes. The wrist orientation can be represented as the angular displacements around the rotation axes fixed at the wrist, which rotates with the hand. This definition is in accordance with that of the Euler angles [53].

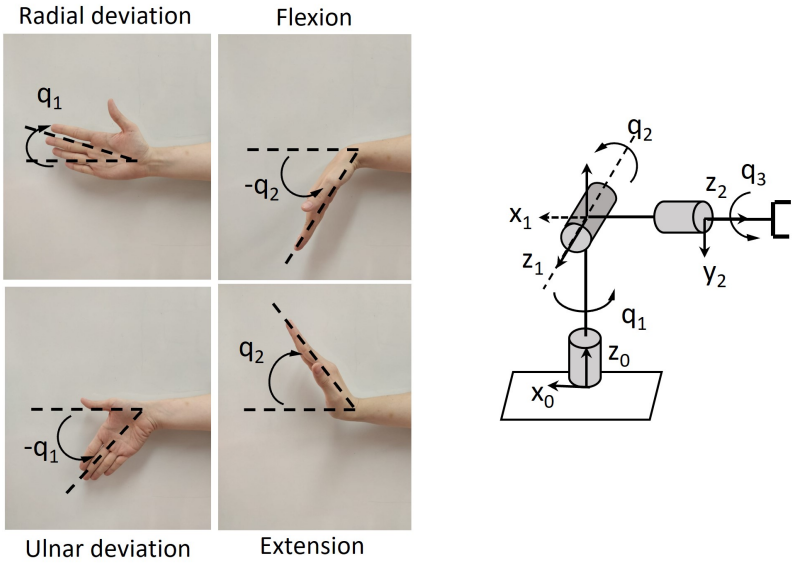

Figure 2.12: A) Scheme of the flexion-extension and ulnar-radial deviation DoFs. B) The wrist kinematics is represented as a combination of revolute joints with axes perpendicular to each other (i.e., universal joint).

Wrist motion coupling

Studies show that wrist flexion-extension and ulnar-radial deviation exhibit a coupling [128]. To understand this statement, consider the trajectory of wrist flexion-extension on a Cartesian space with axes corresponding to the joint positions of flexion-extension and ulnar-radial deviation, as shown in Figure 2.13. The path has a non-zero curvature, showing that the wrist deviates while doing flexion-extension on the side of the ulnar or radial deviation. The deviation depends on the direction and velocity of motion and researchers [35] have hypothesised it is due to the impedance properties of the wrist, which we will examine next.

2.5.2 Muscles spanning the wrist

The wrist joint is crossed by 24 muscles. For each degree of freedom of the wrist, we can group the muscles into agonists and antagonists with respect to wrist flexion and extension. The main muscles involved in *wrist flexion* are the *flexor carpi radialis* (FCR) and *ulnaris* (FCU), assisted by the flexors of the fingers and thumb and *palmaris longus*, and a*bductor pollicis longus* [149]. The extension motion of the wrist is given by the *extensor carpi radialis longus* and *brevis* (ECR), and the *extensor carpi ulnaris* (ECU) with assistance from the extensors of the fingers and thumb. The radial deviation is produced by the *pollicis longus*, FCR, ECR *longus* and *brevis*. The ulnar deviation is produced by the simultaneous

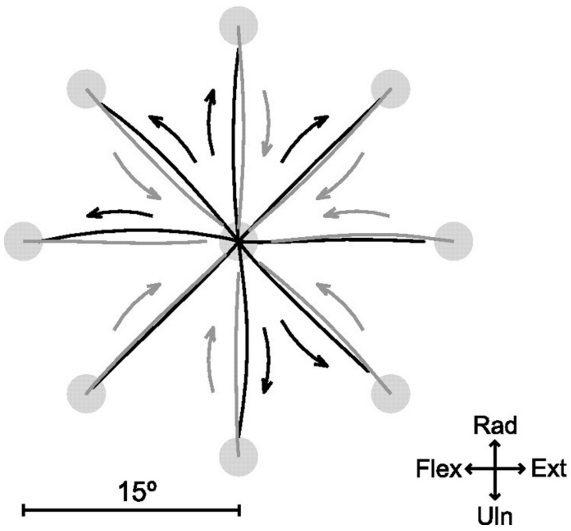

Figure 2.13: Image adapted from [35], showing the paths obtained while a human subject performs fast wrist rotations. The joint paths are represented on a Cartesian plane with axes corresponding to the joint position of the flexion-extension and ulnar-radial deviation DoFs.

contraction of the ECU and FCU. The main muscles involved in the wrist motion are represented in Figure 2.11-B. The neuromuscular system determines the impedance of the wrist (Section 2.2), which is constrained and affected by wrist kinematics. While reaching movements are mainly dominated by inertial effects, wrist rotation is mainly dominated by stiffness [35].

2.5.3 Wrist impedance

Impedance modulation is due to various factors, including intrinsic muscle mechanisms and spinal reflex pathways (Section 2.2), and it is constrained by the kinematics of the joint, and by coupling effects. This means that the impedance of flexion-extension, for instance, is coupled to the impedance of ulnar radial deviation. The passive wrist stiffness has been measured in [70]. This study showed that stiffness in ulnar-radial deviation is larger than the stiffness in flexion-extension. Gielen et al. [76] measured the 1-DoF wrist damping. It is suggested that as muscle contraction increases to achieve faster rotations, the damping increases. However, no conclusive results are drawn regarding the relationship between the damping of the two DoFs, as pointed out in [35]. The difference in muscle activity and timing might contribute to the different stiffness and damping of the two DoFs. In [33] it is shown that wrist rotations (flexion-extension and ulnar-radial deviation) exhibit a pattern of curvature which cannot be only attributed to neuromuscular noise. In [34] a linear model of wrist rotation dynamics for flexion-extension and ulnar-radial deviation is

formulated. Passive stiffness is found to mainly contribute to passive impedance, whereas passive damping and inertia are relevant only for fast movements. Moreover, inertia and passive damping coupling torques between the two DoFs are found to be negligible with respect to coupling stiffness effects. In [35], Charles and Hogan investigated the causes of this behaviour attributing the path curvature to the stiffness properties of the wrist. In the same study, Charles et al., show that the interaction torques between the DoFs are significantly smaller than the torques of each DoF, and the impedance couplings are negligible. Especially wrist inertia is reported to not contribute substantially to the overall impedance for moderate wrist rotation velocities. In [146], Milner and Cloutier investigate the ability of subjects to maintain the mechanical stability of the wrist during rapid flexion movements in the presence of instabilities introduced by a negative damping. Muscles co-contraction, wrist stiffness and damping are analysed for increasing values of negative damping. It is shown that subjects increased the co-contraction of flexor and extensor muscles in proportion to the amount of negative damping (i.e., load instability). An increase in muscle contraction was reflected in an increase in wrist stiffness and damping. However, damping changes in relation to coactivation were less consistent. The reflex contribution to wrist damping is also discussed in relation to the observation that stiffness and damping did not decrease as the subjects lowered muscles' co-contraction when the position oscillations were smoothed out.

Chapter 3

Related Work

Both industry and academic research put significant effort into advancing the state of the art in motor prostheses and providing amputees with natural, simultaneous control of multiple Degrees of Freedom (DoFs) of the artificial limbs. Progress in *upper-limb prostheses control* is the result of significant advancement in different research areas tackling aspects of the same problem. Progress in ergonomics and mechanical design of prostheses has resulted in multi-DoF robotic limbs that offer a dexterity comparable to that of humans. Surface electromyography has been a breakthrough in technology for designing non-invasive human-machine interfaces (HMIs) to record biological signals containing information about the human motor intent; advancement in surgery and medicine has allowed clinical translation of HMIs for prostheses control [1].

This chapter reviews the state-of-the-art control methods implemented on commercially available prostheses (Section 3.1) and those developed in academic research (Section 3.2). Control methods developed in robot manipulation do not necessarily translate into state-of-the-art controllers for prostheses. The design of methods for prostheses control has to be guided by a human-centred approach and it is constrained by inherent difficulties posed by the HMI as well as the information that can be extracted about the human motor intent. *The control methods described below are sEMG-driven and assume the possibility of recording the activity of at least a pair of agonist-antagonist muscles to directionally drive a DoF.* As described in the previous chapter, considering single DoF motions, a muscle (or a muscle-tendon model) is defined as agonist if the DoF acceleration is in the same direction as the acceleration imposed by the muscle. Given an agonist muscle, the action of a muscle opposing the joint motion is defined as antagonist. Three main categories of approaches can be identified: *conventional methods* used on commercially available devices that use the amplitude of sEMG signals directly as control command (Section 3.1); purely *data-driven methods* that learn a direct mapping from input sEMG signals to desired motor

functions (Section 3.2.1); *process-informed data-driven methods* that make use of sEMG-driven muscle-tendon models (Section 3.2.2). Finally, we review the state-of-the-art methods developed in academic research that aim to enable the user to voluntarily adapt the impedance properties of a robotic system (Section 3.2.3). For some methods, the distinction into the aforementioned categories is blurred and these approaches may be considered hybrid models.

In the domain of prostheses control, the difference between Degree of Freedom (DoF) and Degree of Control (DoC) should be clarified. The number of DoC is the number of independent control signals that can be provided by the user and these may not coincide with the number of DoFs of the prosthesis. Consider the task of closing the fingers of a prosthetic hand. This involves the control of multiple DoFs as each finger has at least 2 DoFs. However, the user may control the high-level motor control function by providing a single control signal (i.e., 1 DoC) and the control of the individual DoFs may be done automatically. To independently drive the DoFs a number of DoC equal to the number of DoFs is required, meaning that the activity of $2 \times DoFs$ muscles has to be recorded. In fact, the sEMG signals from a flexor and an extensor muscle need to be recorded to directionally control a DoF. The reader can understand the difficulties associated with the scaling of the sEMG measurement sites in relation to multi-DoFs control, and the reason why the motor function of opening and closing the hand is often done through a single DoC.

3.1 Commercially available devices

Conventional myoelectric control used in clinical settings is also known as “proportional” or “direct” control. According to this approach, the magnitude of sEMG signals of a pair of flexor-extensor muscles is used to proportionally drive a DoF of the prosthesis in position, velocity or torque [207]. Typically, in position-based proportional control, the motor voltage is controlled proportionally to the difference between the magnitude of the sEMG signal of the flexor and extensor muscles. This means that to maintain the same DoF position the level of muscles’ activation must be kept constant, which can lead to muscle fatigue and tiredness. Velocity-based proportional control overcomes this limitation since changes in activation are used as velocity commands and as a consequence null activation implies no motion. However, this approach may lead to unwanted motion since the method can not distinguish between changes in activation associated with changes in motion and those associated with changes in impedance [190]. This problem is more pronounced during fast motions when higher activation is usually required. Moreover, conventional approaches are typically limited to the control of a single DOF at a time. This is due to challenges imposed by the HMI itself. Residual muscles of the limb may be used to interface an amputee to

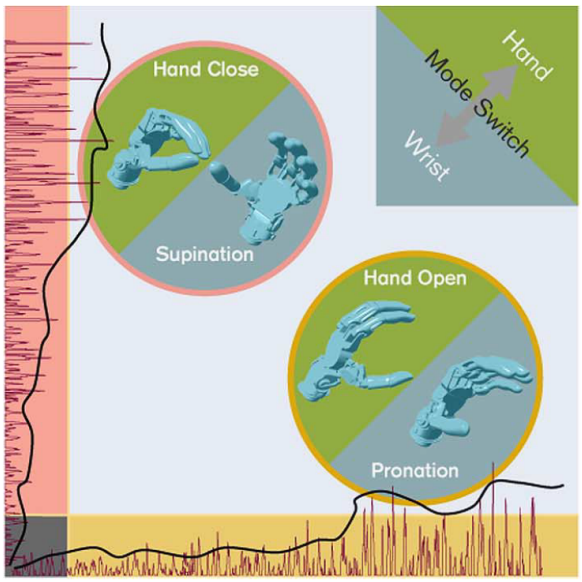

Figure 3.1: Illustration taken from [59] showing the working principle of a conventional control scheme implemented on commercially available prostheses. Two sEMG signals are used to control a single DoF at a time. Muscle co-contraction is used to toggle between control of different DoFs (e.g., hand opening-closing, hand pronation-supination).

the prosthesis, depending on the level of the amputation. Considering that a pair of sEMG signals is needed to control a single DoF, for multi-DoF control one would need a pair of sEMG signals for each DoF. However, this is often unfeasible due to the limited number of available myocontrol sites depending on the level of amputation and due to technical issues such as crosstalk (Section 2.3.2). As a result, only one DOF can be controlled at a time and the patient has to perform a specific muscle co-contraction or press a physical switch to toggle between DoFs [187], as illustrated in Figure 3.1. This control approach is sequential and switching between DoFs occurs in a fixed order. In summary, conventional control is difficult to deploy for multi-DoF control [59, 105]: the control is slow, unnatural and it requires considerable training and cognitive effort [17].

Pattern-recognition-based myoelectric control, initially explored in research, constituted a significant improvement over the conventional control discussed above since it allowed for indirect control of multiple DoFs at a time. Supervised learning methods, e.g., linear discriminant analysis (LDA), multi-layer neural networks, fuzzy techniques, wavelets, support vector machine (SVM), are trained offline to learn an association between patterns in sEMG features and predefined classes of motion [106, 5, 210]. The learned mapping is then used to classify incoming sEMG features in real-time. During the training phase, the amputee performs a series of predefined muscle contractions that are associated with specific classes of movement. These motor functions may include opening-closing of the

fingers or different types of grasps. In these cases, multiple DoFs constitute a single DoC, as the sEMG signals from only a pair of muscles are used to determine the motor commands. Typical sEMG features used by these methods might be the mean absolute value (MAV), the root mean square (RMS), the zero crossing, or frequency domain features [201]. A pattern-recognition-based approach was implemented on a prosthetic limb by Coapt (LLC) for the first time in 2017 [131]. In 2018, Ottobock used pattern recognition for allowing different types of grasps [163]. The low take-up of such techniques on commercially available devices might be due to different factors such as the sequential nature of the provided control and to challenges associated with the HMI. In fact, features extracted from the sEMG signals suffer from high variability and are strongly dependent on the selected time window [105] which can deteriorate the performance of these methods during daily control. Moreover, muscle fatigue, socket displacement, prosthesis use in conditions unseen during the training (e.g., arm posture, loaded/unload hand, external perturbations) and other factors of variability not included in the training samples can significantly affect the feature stability and lead to misclassification and execution of unwanted motions [191, 135, 201, 186]. One additional drawback of pattern-recognition approaches is the lack of proportional control for a specific motor function.

Regression-based algorithms have been explored in research for simultaneous and proportional control over multiple DOFs [206]. However, robust regression of more than 2 DoFs has proven challenging due to the training and to the difficulties associated with the HMI interface. It is in fact difficult for most of the amputees to generate more than two independent control signals [158]. *Multimodal approaches* have provided the prosthesis with some autonomy and assistance to the user. For instance, Ottobock has used tactile information to automatically adjust the grasping force of the robotic hand and prevent objects from slipping during manipulation. However, since some functions are fully controlled automatically this might lead to the execution of unwanted action that undermines the user acceptance [59].

Pattern recognition methods and regression approaches developed in academic research are discussed in the next section.

3.2 Academic research

Academic research has proposed different methods for decoding the human motor intent from sEMG signals. The majority of the proposed methods focus on decoding the human intent in terms of kinematics by using *purely data-driven methods* (Section 3.2.1) and *process-driven approaches* (Section 3.2.2) that include some domain knowledge about the muscle

contraction dynamics. These methods aim to increase the number of DoFs that can be controlled at a time. Fewer studies instead attempt to provide the user with simultaneous control of motion and impedance (Section 3.2.3) of the DoFs.

3.2.1 Data-driven methods

Simultaneous motion control over multiple DoFs is an open problem in motor prosthesis control, especially when *conventional methods* are used to implement the user's motor intent. Several pattern-recognition-based approaches have been investigated in literature to provide multi-class prediction [221, 86, 185, 30]. However, these approaches are limited by the need for extensive training which is time-consuming and frustrating for the patient. A common drawback, which affects pattern recognition-based algorithms, is the lack of proportional activation of the motion classes [71]. To address this issue and benefit from the advantages of proportional control, different methods have been proposed to enable proportional control in pattern recognition approaches [40, 43, 107, 31].

Besides pattern-based recognition methods, various linear and non-linear regression-based algorithms have been explored in literature for providing simultaneous and proportional control over multiple DOFs [156, 152, 108, 83, 197]. Unsupervised methods, such as those relying on Non-Negative Matrix Factorization (NNMF) allow to blindly extract activation signals without the need for a reference training trajectory or class labels. NNMF has been used to provide simultaneous and proportional control and has proved to be robust to technical issues such as electrode shifting [59]. Krasoulis et al. [115] demonstrate that non-linear regression methods outperform linear ones during the training phase, however, during testing on unseen data the performances were comparable. In recent years, deep learning methods are increasingly being explored to improve feature extraction and learn complex non-linear mapping between sEMG signals and target motion trajectories or motion classes [23, 218, 36, 9]. Although powerful, deep learning methods require large training data sets, which implies long training sessions. Moreover, because of the black-box nature of the algorithm, it is difficult to understand the internal representation of the model and correlate factors of variability in the training data to changes in the model representation. Moreover, these methods reported a performance that is comparable to that of less recent and simpler methods based on linear regression, Non-Negative Matrix Factorization (e.g., [109]). As a result, the higher complexity of the methods, the need for longer training sessions and the need for examples of DoFs' coactivation in the training set to train the methods for simultaneous control of DoFs (e.g., [218], [208]) are not necessarily justified.

Despite the advantages provided by some of the proposed methods, most of the approaches fail to provide robust control for more than 2 DoFs [177]. A few works in literature

attempt to provide simultaneous control of 3 DoFs using pattern recognition [159, 151]. Nonetheless, a clinical solution is not possible yet. Some of these rely on different types of HMI such as intramuscular sensors [198] or high-density sensors [199], proving that classic surface sEMG is the main bottleneck to allow robust estimation of the human motor intent. Augmenting the sEMG with other multisensory data (e.g., vision, tactile sensing, inertial sensors) is a promising approach explored to enrich the input information to the controllers and provide some level of autonomy to the prosthesis [54, 194, 150, 200]. For example, in [54] multisensory data are used to detect object slippage and provide an automatic reaction. This proved to improve the performance in routine grasping and force tracking tasks.

3.2.2 Process-driven methods

One of the main challenges when implementing purely data-driven methods to decode the human motor intent from sEMG signals is accounting for the non-linear and non-stationary characteristics of these signals [64] and model their complex non-linear relation to force generation. Progress in understanding and modeling the human musculoskeletal system has allowed to obtain biomechanical models capable of predicting physiologically accurate dynamics and kinematics of the muscular-tendinous and skeletal systems, respectively. Researchers have used this domain knowledge to develop sEMG-driven simulations of the musculoskeletal system that allow to decode the human motor intent in terms of kinematics and dynamics. Specifically, the simulation of *the forward dynamics of sEMG-driven musculoskeletal models can predict the forces and torques generated on the skeletal system by muscle-tendon models.* These simulations have mainly been used offline and have found applicability in different fields concerned with investigating the musculoskeletal dynamics of healthy able-bodied subjects and of subjects with neuromotor disorders, and for studying the biomechanical contribution of muscles to specific motions [195, 89, 183, 154]. The complexity of such simulations, and in particular of the muscle-tendon models, is a compromise between high prediction accuracy and retention of key model features that do not deteriorate significantly the prediction performance but require lower computational costs. This trade-off is crucial in applications that have real-time constraints, such as in prosthesis control.

One approach to muscle-skeletal modeling is to include multiple muscle-tendon units in order to closely mimic the human musculoskeletal system and obtain physiologically accurate predictions (e.g., [32, 134, 139]). This approach requires a high number of muscle-tendon units, anatomical knowledge of the arrangement of muscle-tendon models on the skeletal system and of their contraction dynamics. Each muscle-tendon unit is driven by an sEMG signal. The need for as many input sEMG signals as the number of muscle-tendon units is the main limitation, since the activity of some muscles might not be easily measured

by sEMG due to technical difficulties (e.g., crosstalk, deep muscles) and depending on the subject-specific anatomy. Finding an accurate placement of sEMG sensors to capture the activity of specific muscles while minimising the crosstalk is a non-trivial task that requires specific knowledge and training. Moreover, the parameters' values of each muscle-tendon unit are usually scaled or optimized using kinematic data recorded using motion capture systems. This technology might not be always available. These difficulties might be enhanced when the simulations are used for motor prostheses applications, as for amputees, depending on the level of amputation, functional muscles are likely to be (partially) missing [100], and some physiological parameters used in the muscle-tendon units can not be measured directly (e.g., moment arms of the remaining muscles) [176]. As a result, the complexity of the models and the computational cost makes this simulation approach impractical for real-time prosthesis control applications.

Considerable effort was put to simplify musculoskeletal simulations for their use in frameworks for real-time control of prostheses and other rehabilitation devices. Initial promising results on a single able-bodied subject [41] showed the possibility of reducing the model complexity and avoiding the need for an external motion capture system by relying on sensors embedded in the prosthesis. Other studies [181, 180] proposed a musculoskeletal model consisting of simplified muscle-tendon units to provide real-time ($<$ 10 ms per cycle) simulation of forces and torques generated at the knee joint with accuracy comparable to that provided by more complex models [181, 132, 26]. A more niche approach to address the limitations of complex simulations uses the so-called *lumped models* [123, 51, 57, 134]. According to this method, muscle-tendon units that contribute to the same motor function are grouped into a single muscle-tendon unit. For example, wrist flexors and extensors are grouped into two muscle-tendon units, one acting as flexor and the other as extensor which represent the overall functional behaviour of the two muscle groups.

Lumped models were used to predict 1-DoF ankle position from sEMG signals; the biomimetic model, tested by an amputee, is compared to a multi-layer neural network and it is reported to provide a smoother position trajectory suggesting that model-based approaches may offer advantages for prosthesis control [12]. A lumped muscle tendon modeling approach allows to drastically reduce the model complexity and computational burden by reducing the number of muscle-tendon units and sEMG channels. Usually, these models are subject-specific and the parameters' values of the muscle-tendon units are optimised using the joint torque measured during a training phase. In 2015, a preliminary study [44] proposed a simplified lumped model (based on [184]) consisting of four Hill's type muscle units (the tendon was not included) showing promising results in predicting individual and simultaneous activation of two DoFs (i.e., flexion-extension of the wrist and MCP joint). Each muscle

model required the optimization of five parameters and moment arms (considered constant for simplicity) using the measured joint torque. While the described approach is promising, the results are shown offline and for a single able-bodied subject. The same research group proposed in 2016 a further simplification of the previously proposed muscle-skeletal model [45], where the two joints skeletal model is modeled as a simple two-joint robot. The model is evaluated offline with five able-bodied subjects and a transradial amputee using the Pearson correlation coefficient as measure of prediction accuracy. A high average correlation was reported during single-joint motions for the first DoF (able-bodied 0.94%, amputee 0.92%) and the second DoF (able-bodied 0.88%, amputee 0.93%), respectively. The performance decreases during simultaneous activation of the joints (the joint-specific correlations drop to 0.75% and 0.56%, respectively). While these studies involved simple motions in the free space, other works investigated the robustness of their methods to different loading [166] and arm postures [165] during posture-reaching tasks in the free space with able-bodied subjects. The model used in [166, 165] is further extended to three DoFs, but tested only offline with a single able-bodied subject [164]. In [165] interesting initial results on the possibilities of using lumped models to obtain non-subject-specific muscle-tendon models is investigated.

Table 3.1: Summary of key aspects of sEMG-based methods that decode the human motor intent as joint motion and joint impedance.

	Participants		# sEMG	# DoF	Control approach	# DoC			Testing on Robot
	# Able-bodied	# Amputee				Motion	Stiffness	Damping	
[92]	8,5,6	-	4	1	Teleimpedance controller. The intended position and stiffness are decoded from sEMG signals, and are transferred to the prosthesis.	Position is proportional to estimated joint torque (linear model function of sEMG signals)	Linear function of sEMG signals	-	VSA-driven transradial prosthesis
[74]	6	1	5	1	Recurrent log-linearised Gaussian mixture used as pattern recognition method based on muscle synergies concept.	Motion is obtained by applying estimated joint torque (proportional to the normalised sum of sEMG signals' amplitude).	As in [202].	As in [202].	3D-printed prosthetic hand
[202]	1	1	8	3	Log-linearised Gaussian Mixture Network used to recognise patterns of motion and activate desired joint. Cooperation ratios between groups of flexors and extensor muscles are estimated and co-contraction level is computed.	Torque computed as proportional to the difference between activation levels. Motion is obtained using admittance filter with stiffness and damping estimated from sEMG signals.	Computed as polynomial function of muscle' activation. This stiffness is not used in the PID controller implemented on the robotic system.	Computed as polynomial function of muscles' activations. This damping is not used to implement PID controller on robotic system.	Prosthetic wrist plus hand
[29]	-	1	2	1	Conventional velocity controller with stiffness modulation and threshold-based method for avoiding unwanted motion due to muscles' coactivation.	velocity, proportional to sEMG signals' amplitude	Weighted average of sEMG signals amplitude	-	softHand Pro
[110]	1	-	6	1	MTUs for estimation of human intended joint torque.	Obtained by applied torque and estimated stiffness	A stiffness index is computed as the sum of torques from agonist and antagonist MTUs. This stiffness index is linearly remapped to a feasible range dependent on the task, subject and robot. Stiffness used in the controller.	set as function of stiffness	Lower limb Exoskeleton
[6]	2	-	2	1	Sinergy-based model for extraction of position and stiffness. Hand disturbance model to estimate disturbance torque. Disturbance torque added in PI controller. Compensation of Coulomb friction.	Estimated using hyperbolic tangent function model, driven by input variable defined as difference between sEMG signals' amplitude.	Estimated using hyperbolic tangent function model, driven by input variable defined as sum between s sEMG signals' amplitude.	-	softHand Pro
[45]	5	1	4	2	4 lumped muscle-tendon models	yes	-	-	-

	Participants		# sEMG	# DoF	Offline Testing		Online Testing	
	# Able-bodied	# Amputee			Experimental protocol	Evaluation	Experimental protocol	Evaluation
[92]	8,5,6 for the three exp	-	4	1	EMG signals and joint torque recorded to estimate parameters of torque and stiffness models	unclear differentiation between training and offline testing	Position modulation at constant stiffness; stiffness modulation at constant position; grasping of different objects (only one is fragile);	Completion time
[74]	6	1	5	1	5 single motions, 5 combined motions, each repeated for 2 secs. 20 random samples of motions used in training	-	10 motion patterns, including unseen combinations. External torque in the impedance controller set to zero. For amputee only: 4 single and a combined motion.	Classification accuracy is defined as completion time. No actual evaluation of impedance modulation. For the amputee, testing was done on motion used for training plus grasping of 3 objects (blocks, plastic bottle, notebook).
[202]	1	1	8	3	Estimation of parameter of stiffness and damping model (able bodied)	Exemplary results, no results across multiple reps	Unclear, shows just 1 rep for ccontrol of 3 joints. No combined DoFs control.	Exemplary results. No average results across repetitions, no external perturbations.
[29]	-	1	2	1	Tuning of gains and mapping of stiffness to feasible rage depending on hardware and experimental task. The subject performs muscle contractions at different levels of activation. Visual feedback about coactivation level is provided.	-	User familiarises with coactivating muscles for 5 min. User grasps and holds a plastic bar. An examiner pulls the bar away. Experiment 1: the subject does not oppose resistance. Experiment 2 (1 rep per method): the subject opposes resistance to maintain grasp. Proposed method compared to 3 other conventional control modalities (Fixed high stiffness and proportional position control, Fixed high stiffness and proportional velocity control, FIxed low stiffness, proportional velocity).	Maximum torque, mean torque, grasping time, amplitude of sEMG signals is reported for each control method. Survey on subject's feedback about the following tasks: lifting a heavy object, self-interaction, handshaking, walking while holding other subjects' hands, bimanual manipulation. Feedback from able-bodied subjects is also reported.
[110]	1	-	6	1	The subject wears the exoskeleton and performs quasistatic tasks. The sEMG signals and joint torque are recorded and used to train muscle model and to set other constants.	NRMSE between joint torque predicted by MTUs, and the reference torque.	sit-to-stand movements. 5 trials, with exoskeleton in zero torque mode (no assistance) 10 trials, with exoskeleton operated with the proposed scheme (some additional parameters for implementation of exoskeleton are calibrated)	No average results, exemplary results from some reps are reported to show assisting functionalities (human torque and stiffness reduction)
[6]	2	-	2	1	Hand opening, closing motions plus reps at 5 different levels of coactivations.	RMSE between predicted and reference position	Grasping of objects. The proposed method is compared to three control modalities are compared. (fixed high stiffness, fixed low stiffness)	Only qualitative discussion of results
[45]	5	1	4	2	Single Joint motion performed at constant and random speed. Combination of motions performed at speed decided by subject. Each movement repeated for 30 secs.	Person correlation coefficient to compare predicted motion and reference motion	-	-

3.2.3 Adaptive impedance control of upper-limb prostheses

Researchers have investigated different methods (Section 3.2.1, Section 3.2.2) to implement sEMG-driven controllers that allow human subjects to voluntarily control the kinematics of the (simulated) prostheses. However, *these approaches consider the prosthesis as a system isolated from the external environment* and *do not allow the user to regulate the impedance properties of the robot*. In Section 2.2 we discussed impedance adaptation of the limb as a key motor control strategy for humans interacting with unpredictable environments. Moreover, research in robotics showed that motion control is unsuitable for tasks where different sources of uncertainty lead to unexpected mechanical instabilities (Section 2.1.3). These observations led to the introduction of the impedance control paradigm by Neville Hogan [96] in 1985 to allow motion control and indirect control of the interaction dynamics between the robot end-effector and the environment (Section 2.1.4). The same Hogan postulated the importance of enabling such impedance behaviour on prosthetic limbs given that a human subject wearing an upper-limb prosthesis performs tasks that involve kinematically constrained motions or mechanical interaction with the environment [93]. As proof of concept, a biomimetic impedance control method was implemented on an sEMG-controlled prosthetic elbow and tested with an amputee [2, 3]. One important question posed in this study – and still valid today – is whether the poor acceptance rate of myoelectric prostheses, with the main reason related to lack of sensory feedback, could be improved by correctly interpreting the sEMG signals and decoding the motor intent in terms of kinematics as well as dynamics. *The driving research question underlying the works reviewed below and this thesis, is whether allowing impedance adaptation would improve the control of prosthetic limbs.* Humans adapt the limb impedance during movement by modulating the impedance at the level of the joint by co-activation of agonist and antagonist muscles. Given the association between muscle co-contraction and joint impedance, an additional signal defining the level of co-activation of groups of agonist and antagonist muscles is introduced in control schemes that attempt to enable the user to adapt the stiffness of the prosthesis.

In [92] the authors proposed an sEMG-based method for simultaneous control of the position and stiffness (i.e., two DoCs) of the fingers of a VSA-driven prosthesis (i.e., one DoF, hand opening-closing). However, the two DoCs are extracted from sEMG signals of different groups of flexor and extensor muscles: the joint stiffness is decoded from the activity of the muscles of the chest, while the joint position is obtained from the upper-arm muscles. This choice maximises the independence between sEMG signals to avoid the problem of decoding kinematics and dynamics from the same sEMG signals. This assumption eliminates the ambiguity in associating changes in sEMG with changes in the joint position or joint impedance, substantially avoiding the key challenge in the detection of motor intent. In the

study, the choice of using different muscle groups is based on the assumption that these provide similar stiffness. However, the validity of this assumption is unclear: the authors provide experimental results showing a correlation between the stiffness computed muscles of the forearm and the upper-arm, while it is unclear why the stiffness of the chest's muscles, used for the prosthesis control, is not tested for correlation. Moreover, as described in Section 2.4, the impedance properties of a muscle are strictly related to the muscle's state. As a result, this approach does not attempt to mimic the human-like stiffness but provides an engineered stiffness signal that can be used to control the robot's joint stiffness independently from its position. The feasibility of this approach and its intuitiveness were tested with five able-bodied subjects during grasping tasks (16 objects, among which only one is fragile), where the grasp accuracy is computed as the time required to complete the grasp. This evaluation provides limited insight into the control performance and the object-dependent adaptation of stiffness during the grasping tasks. The approach used to estimate stiffness is based on the index of muscle co-contraction proposed by Osu et al., [161]. This stiffness index was designed on the basis of two fundamental assumptions: (i) rectified sEMG signals are linearly proportional to the corresponding muscle's isometric tension and (ii) the stiffness of the muscle is linearly proportional to muscle tension. This implied that the rectified sEMG signals were linearly proportional to the stiffness. However, it was shown how this assumption is not valid for dynamic motions. Therefore, the following simplifications were made: linear tension-length and velocity-tension curves, and constant moment arms. While these assumptions are not physically plausible and can cause misleading estimations of joint stiffness and torque, the stiffness index provided a useful tool in comparative studies, where the change in stiffness is of interest.

In [29], the authors provide a solution to enable the simultaneous detection and control of joint stiffness and position from the same pair of sEMG signals. A simple index was defined to quantify the co-contraction of flexor and extensor muscles and a task-specific threshold to detect when the co-activation (i.e., stiffness modulation) occurred. The co-contraction index is used to overcome the difficulties associated with the conventional velocity-based proportional scheme (Section 3.1), which is highly sensitive to changes in muscles' coactivation since the magnitude of sEMG signals is directly used to proportionally drive the DoF. Based on the co-activation index and the magnitude of individual sEMG signals, a state machine is used to transition between three states ("stay", "open", and "close") and aid the velocity-based controller to open and close the fingers of a soft prosthetic hand. A stiffness index, estimated as a linear function of the sEMG signals magnitude, is used to adapt the proportional gain of the controller allowing simultaneous stiffness and motion modulation. This control method is tested against conventional methods (proportional and velocity control) with fixed high

and low gains by an amputee wearing a soft prosthetic hand [77]. The amputee performed tasks involving the manipulation of objects and the interaction with other human subjects (e.g., handshaking). We argue that this approach, and those methods computing stiffness and torque directly from the sEMG signals using linear models, are highly sensitive to the amplitude and shape of the sEMG signals. However, this study provides valuable insight into the user's personal feedback on the control methods being tested: results show that the amputee preferred the variable stiffness method; able-bodied subjects interacting with the amputee stated the interaction felt more human-like when the variable stiffness method was used. Similar conclusions were also provided by previous studies with able-bodied subjects [192, 19].

Other methods first estimate a reference stiffness and damping from the measured torque and then learn a model (e.g., a polynomial function) of the stiffness and damping [74, 202]. In [202] the joint stiffness damping estimated from the sEMG signs are used to decode the human intended motion (i.e., admittance filter), but these are not employed to implement a variable impedance controller on the robot, instead a fixed gains motion control is used. In [110], while Hill-based muscle-tendon models are used to estimate the joint torque, the joint stiffness is assumed to be proportional to the joint torque and it is computed as the sum of the absolute torque provided by the flexor and extensor muscles. The obtained stiffness is not used directly in the controller but is linearly mapped to the desired stiffness range according to the subject requirements, the type of task, and the robotic system. The mapping is learned during a calibration phase separate from the training process required for other components of the framework. In contrast to previously discussed works, muscle-tendon units are used to estimate the torque, avoiding simplifying assumptions on linear proportionality between sEMG signals and muscle forces. Moreover, while the studies discussed above did not consider the joint damping, in [110] it is set to vary proportionally to the joint stiffness, requiring calibration of a proportional constant. This estimation and use of joint damping aim to fulfil control stability requirements instead of decoding the human intended joint damping. The control performance provided by the framework was evaluated with an able-bodied subject on a knee exoskeleton with the aim of enabling the user to modulate the stiffness of the exoskeleton to vary the level of assistance provided by the device. In the context of upper-limb exoskeletons, a similar approach to stiffness estimation and use in the controller is adopted by [127], but a linear relationship between the square-root joint stiffness and the joint viscosity is assumed in order to obtain the join damping. Existing methods that attempt to enable simultaneous control of joint position and impedance of a single DoF and include muscle-tendon models (e.g., in [110, 202, 127]), estimate the joint stiffness directly from the magnitude of the sEMG signals, even when muscle-tendon models are used within

the pipeline and the impedance parameters could be retrieved from the muscle-tendon state. Moreover, the joint impedance is remapped to suitable ranges in a separate calibration phase. *This means that the dynamics of the muscle-tendon model does not match that of the robot, possibly leading to unwanted behaviour and instability. The work of this thesis provides a solution to this drawback.*

In [6] the authors propose a synergy-driven framework for controlling a single DoF of the SoftPro hand (i.e., opening-closing of fingers). The framework is based on the concept of teleimpedance, as in [110], and aims to transfer the stiffness and reference position estimated from sEMG signals to implement a position-based impedance controller on the robot. The joint stiffness and position are estimated from a pair of sEMG signals using a hyperbolic tangent activation function, typically used in neural network architectures. The models for stiffness and damping are a function of the sum and the difference of the sEMG signals' magnitude. The framework was tested with two able-bodied subjects. During the data acquisition phase, each subject is requested to perform hand opening-closing motions while the sEMG and reference joint position were recorded to train hyperbolic function for stiffness and position estimation, and for setting the upper-lower bounds for transferring stiffness. In the training, repetitions of motions at different levels of co-contraction are included. The online control performance provided by the teleimpedance framework was compared to that of a fixed-gain compliant and stiff controllers during grasping of objects characterised by different friction and elastic properties. No quantitative results are provided regarding the grasping performance across the subjects for the different controllers and objects. A qualitative analysis explains that the stiff controller caused deformation to some objects and abrupt changes in contact forces. This effect was not observed for the other controllers. The compliant controller did not always allow successful grasping depending on the object's weight and friction properties (detailed information about the characteristics of such objects is not provided). The teleimpedance controller instead allowed user-based modulation of stiffness. It should be noticed this framework included an additional component to estimate the grasping contact forces and to provide it as vibrotactile feedback to the user. Interestingly, this functionality enabled a reduction in muscle co-activations.

A detailed summary of key properties of related works is provided in Table3.1.

3.3 Conclusions on related work

In this chapter, we have provided a critical overview of relevant sEMG-driven control methods that have been developed in literature to extract information about the human motor intent and may be used to control upper-limb prostheses. Myoelectric prostheses control has been

dominated by motion-based control methods. Despite the technological breakthrough in designing sophisticated anthropomorphic prostheses, currently available HMIs and detection-of-human-intent algorithms allow a low-dimensional control, still limited to up to 2 DoFs, while the high-dimensional control over the multiple DoFs of the device is still an open problem. As a result, currently available multi-DoF devices can not be fully exploited to their potential, and the limitations often result in dissatisfaction and rejection of the prosthesis [17]. Different are the directions of possible improvement and future research in motor prosthesis control. On one hand, it is clear that the bottleneck is constituted by the noisy and low-bandwidth information provided by non-invasive HMI. On the other hand, we have to question whether the current algorithms to extract and implement the human motor intent are providing a correct use and interpretation of these sEMG signals. More sophisticated control methods that maximise the understanding of human intention have to be developed to compensate for the limitations of the sEMG-based HMI. Preliminary studies have shown that providing the prosthesis with semi-autonomous control can significantly improve the performance when attempting to control multiple DoFs and it lowers the cognitive burden on the human user [150]. The long-standing goal is to move away from prostheses that only passively react to the user's commands and allow the prosthesis to react proactively to the user's command in a collaborative human-robot physical interaction scheme. In this regard, adaptive controllers have been developed to enable robots to autonomously adapt their feedforward force, impedance [219], and reference trajectory [126] when interacting with an unknown environment. In [126] the adaptive behaviour has been analysed during tasks such as haptic identification or drilling, demonstrating a human-like adaptation to instabilities. Such approaches could be implemented on a prosthesis enriched with perception and learning abilities, to assist the user-based control. However, the actions of the robot have to comply with the human's intent or the user would not be willing to use a prosthetic device. To achieve this goal and progress in this research field it is still - in my opinion - necessary to first maximize the understanding of the human intention from sEMG signals and improve the state-of-the-art of methods that aim to implement the human motor intent in terms of desired motion, and desired impedance.

Studies on human motor control (Section 2.2), and robot control research (Section 2.1.4) has shown the importance of moving away from stiff prostheses and allow the user to voluntarily modulate the impedance behaviour of the artificial limbs, to be more compliant or stiffer depending on the task and the interaction with the environment. The neural impedance control typical of humans has inspired researchers to design bio-mimetic controllers that implement some macroscopic properties of the neural musculoskeletal system (Section 3.2.3). The reviewed related works are summarised in Table3.1. However, no commercial upper-limb

prosthesis used for daily living tasks allows adaptation of the impedance properties. Moreover, to the best of the authors' knowledge, no control method developed in research allows robust, intuitive, and simultaneous adaptation of the joint motion, stiffness, and damping of a single DoF. This is due to the challenges in decoding the human motor intent from low bandwidth surface electromyographic signals [84], and it is due to the high redundancy of human motor control. In fact, there is a non-unique mapping from sEMG signals to target joint kinematics since the same action can be performed at different levels of muscles contraction (i.e., impedance). This is also one of the main causes of performance deterioration of conventional and data-driven methods that do not take into account muscles' co-activation. Approaches implemented to simultaneously decode from the same sEMG signals the intended joint position and stiffness do not directly use the estimated joint impedance in the controllers. The stiffness extracted from the trained muscle-tendon models is typically tuned during a second calibration stage to satisfy the controller's stability constraints. *This approach creates a mismatch between the dynamics of the muscle-tendon model, which represents the user's motor intent, and the dynamics of the robot*. As a result, the user's controllability and the transparency of the control method are limited.

This thesis investigates this issue and introduces a framework that allows a human user to simultaneously control the motion, stiffness and damping of a DoF and implements this behaviour on a simulated prosthesis. This framework may be applied to other technologies that require to detect the human intent as kinematics and dynamics.

Chapter 4

Adaptive impedance control for upper-limb prostheses

In this chapter, we present a novel sEMG-driven framework that makes the two key contributions of this thesis, as outlined in Section 1.2. In contrast to previous work (Section 3.3), the proposed framework extracts three Degrees of Control (DoC) from only two sEMG signals allowing the user to simultaneously control the kinematics as well the dynamics of a DoF of a (simulated) robot through wrist flexion-extension. In the first contribution, we describe the design of the framework that includes a pair of sEMG-driven muscle-tendon models to decode the human motor intent about the kinematics, stiffness and damping of a joint and uses the estimated motor intent for implementing a joint space variable impedance controller on a simulated robot. In the second contribution, we tackle the problem of estimating muscle-tendon parameters' values that enable the user to use impedance modulation as an effective strategy to counter unexpected perturbations during online control tasks.

This chapter begins with a brief introduction (Section 4.1) that reminds the reader of the motivation of this thesis and summarises the conclusions drawn from the review of relevant related work, presented in the previous chapter. We then provide a high-level description of the framework (Section 4.2), we discuss the sEMG-base HMI used in this work and we provide an insight into the characteristics of the sEMG signals during dynamics wrist flexion-extension movements, performed at different levels of muscle impedance. We thus aim to provide a rationale, supported by experimental results, to the design approach of the framework. We justify the choice of using two sEMG signals recording the activity of the Flexor Carpi Radialis and the Extensor Carpi Ulnaris as representative of the flexor and extensor muscle groups for wrist flexion-extension. The framework requirements and assumptions are discussed. In Section 4.3 and Section 4.4 we proceed with the mathematical formulation of the two constituent blocks of the framework. The first is concerned with

decoding the human motor intent from a pair of sEMG signals, the second block implements the motor intent onto a simulated robot. Finally, Section 4.5 provides a solution to the ill-posed problem of estimating the parameters' values of the muscle-tendon units.

4.1 Introduction

The domain of application chosen in this work is upper-limb prosthesis, given that the human subject wearing the prosthesis physically interacts with the environment around, making impedance adaptation a critical property to ensure stable and safe interaction and enhance a more natural way of controlling the prosthesis.

Physical interaction with the external environment is a fundamental characteristic of grasping and manipulation tasks (Section 2.1.3). Successful execution of these tasks requires motion coordination and the adaptation of motor control strategies to account for instabilities arising from the mechanical interactions between our limb and the external environment. In fact, some tasks might be intrinsically unstable and unpredictable perturbations might cause our upper-limb to deviate from the desired position, or motion (Section 2.1.3). This case scenario was depicted at the beginning of Chapter 1, when we explained how the simple task of holding an umbrella can become unstable as soon as the wind blows unexpectedly. It has been shown in literature that the Central Nervous System (CNS) is capable of optimally adapting the mechanical properties of the limb to modulate the dynamics of the physical interaction with the environment and account for instability margins (Section 2.2).

These mechanical properties, known as *impedance*, comprise three parameters, namely stiffness, damping, and inertia, which explain the relationship between the forces generated by the neuro-musculoskeletal system and muscle-skeletal motion. Neuro-muscular impedance is associated with the notion of mechanical impedance, a dynamic operator that maps applied forces to displacements (Section 2.1.4). Stiffness is therefore defined as the resistance opposed to a change in position, damping is the resistance opposed to a change in velocity and finally, inertia is the resistance opposed to a change in acceleration. However, summarising the problem discussed in Section 2.4, human-like impedance substantially differs from the purely mechanical counterpart because of its dependence on neural input activation. In fact, the CNS regulates the limb's impedance by modulation of joint impedance by variation in muscle co-contraction. Considering the agonist and antagonist muscles spanning a joint, by appropriate modulation of the muscles' co-contraction the impedance properties can be modulated independently of the net joint torque applied to the joint. This mechanism allows us to increase the rigidity of the limb while maintaining the same posture, or perform similar motions with substantially different levels of limb impedance (Section 2.4.4). Many

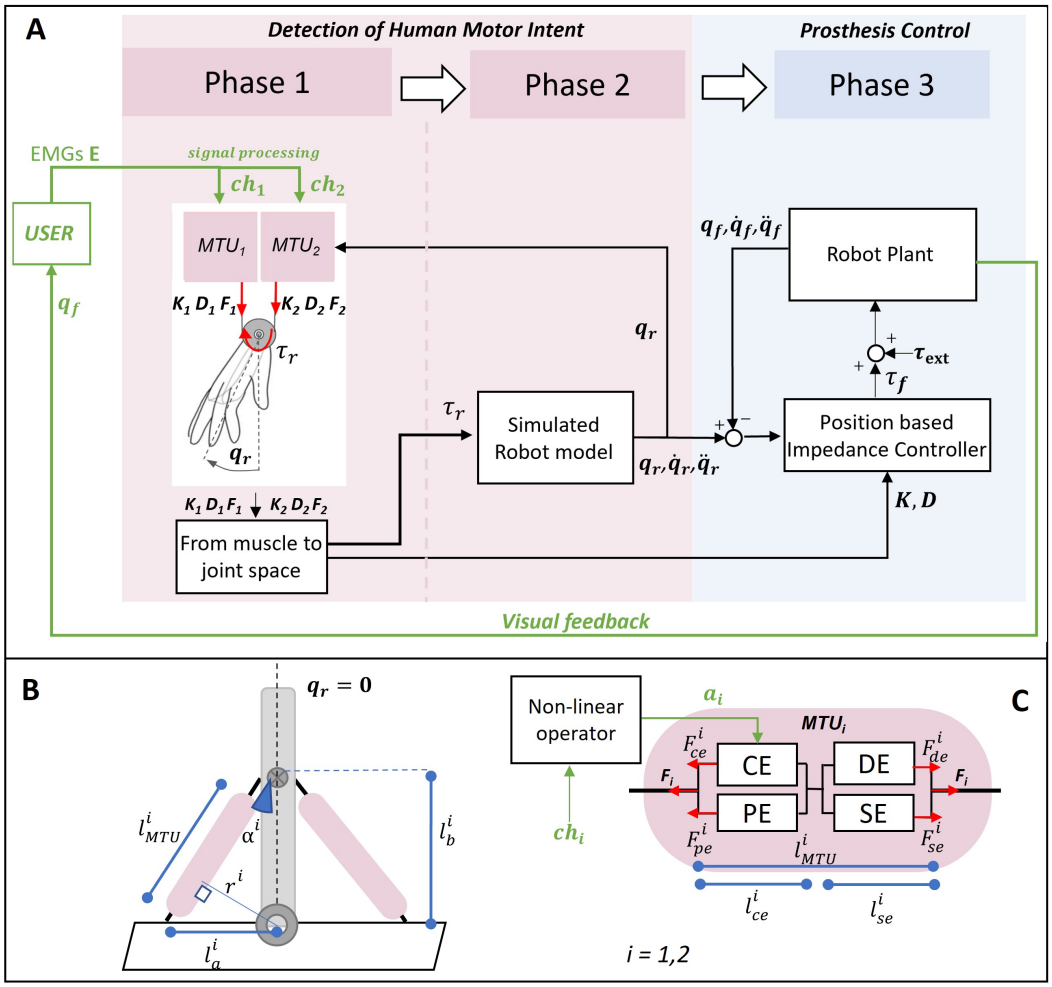

Figure 4.1: A) High-level block diagram of our framework to control a 1-DoF robot arm. The framework comprises a *Detection of Human Motor Intent* block and a *Prosthesis Control* block. The first block maps sEMG signals from the user's wrist muscles (ch_1, ch_2) to estimates of the user's motor intent in terms of kinematics, i.e., $s_r = (q_r, \dot{q}_r, \ddot{q}_r)$ and dynamics, i.e., joint stiffness and damping (K, D). The second block executes the motor intent on the robot plant, using a variable impedance controller to track s_r based on K and D. The framework's output q_f is also the visual feedback that can be used by the user to module impedance in response to external perturbation on the robot plant. B) Arrangement of muscle-tendon units on the link of the simulated robot model of the first block. C) Diagram of the forces generated by the elements within each muscle-tendon unit. MTU_i comprises muscle (CE, PE) and tendon components (DE, SEE) of length l^i_{ce} and l^i_{se} respectively.

studies have characterised the impedance properties of the human limbs, primarily focusing on the lower limb and on the shoulder-elbow, while fewer studies have investigated the impedance properties of the wrist. Advancement in muscle-skeletal modeling has allowed to better understand and model the dynamics of the muscle contraction and the actuation of the

musculoskeletal system and has inspired researchers to design control methods to implement the human-like impedance behaviour on robots [95].

Section 3.3 summarises the conclusions drawn from the review of the state-of-the-art control methods implemented on commercially available prostheses and those developed in research, highlighting the difficulties in translation of control methods for clinical application. The state-of-the-art control methods that attempt to detect the human-motor intent in terms of kinematics and dynamics are limited to a single DoF, and damping is often neglected or computed as a function of stiffness. Moreover, there is lack of consistency in approaches that make use of muscle-tendon models to estimate the joint torque. In fact, the stiffness and damping properties of the muscle-tendon models are often not used but these are estimated using other models. Moreover, either the estimated stiffness and damping are not directly employed to update the gains of the impedance controllers, or the stiffness and damping estimated from sEMG signals are remapped to ensure the control stability. This means that the dynamics of the muscle-tendon models, which drives the joint motion, does not match the dynamics implemented on the robotic system. In this work, we tackle this problem.

4.2 Framework overview

Figure 4.1-A provides an overview of our framework in the context of controlling a single DoF through wrist flexion and extension. The *Detection of Human Motor Intent* block takes as input the sEMG signals from the user's wrist flexor and extensor muscles (ch_1, ch_2) and estimates the user's motor intent in terms of reference kinematics $s_r = (q_r, \dot{q}_r, \ddot{q}_r)$, and joint stiffness K and damping D. This estimation is done in two phases. In *phase 1*, the sEMG signals drive the lumped muscle-tendon units (MTU_1, MTU_2) that generate the muscle-tendon forces (F_1, F_2) based on the muscle-tendon contraction dynamics and s_r. Note that the MTUs are virtually arranged on the link of the simulated robot model so that their action opposes one another as for agonist-antagonist muscles; MTUs' state and q_r are linked to each other (Figure 4.1-B). The muscle-tendon stiffness and damping are computed from the state of the MTUs. These muscle-tendon variables are then mapped to the joint space of the simulated robot model to obtain the joint torque τ_r, stiffness K, and damping D. In *phase 2*, τ_r is applied to the simulated robot model to actuate the robot's joint q_r and obtain the user-intended joint kinematics s_r.

The *Prosthesis control* block executes the motor intent obtained from the previous block on the (simulated) robot plant using a position-based variable impedance controller that tracks s_r based on K and D. The joint position q_f is the framework's output and visual feedback. If an external perturbation acts on the robot plant, the user can use this feedback to

modulate the plant's kinematics and impedance, reducing the error between s_r and the plant's state s_f.

The sEMG signals are processed using proprietary software. The framework is implemented using CoppeliaSim simulation environment [178] and MATLAB [140]. The software developed within this thesis is integrated within the framework for sEMG data acquisition and processing developed in the Bioengineering Laboratory of Imperial College London. We use the model of the *Puma 560* robot [11] as the simulated robot arm; we only consider the first two links of the robot model (Appendix D) and control joint 2 with our framework. In practice, this framework can be used to control a single DoF of any robot. In this work, we do not use a real prosthesis (unavailable to us), so the robot plant is simulated. If the framework was used with a real prosthesis, the *simulated robot model* in Figure 4.1-A would be a simulation of the prosthesis and the robot plant would be the real prosthesis. In the following sections, we refer to *simulated robot model* and *robot plant* despite the latter being simulated to indicate the two instances of the same robot model, used in the first and second blocks.

4.2.1 Input: analysis of sEMG signals during modulation of muscle impedance

In Section 2.3.2 we have introduced surface electromyography as a viable way for interfacing a human subject with a prosthesis due to its non-invasiveness and ease of use. Low-density electromyography is the HMI employed in this work, and specifically, the myoelectric armband (Myoband) by Thalmic Lab (see description in Section 2.3.2) is the device used. This choice is motivated by different characteristics of the device, ranging from its low cost to ease of use. In fact, the device streams data via Bluetooth and it is therefore portable and easy to set up in any experimental setting. The configuration of the 8 sEMG sensors in a bracelet allows to easily fit the device around the arm of able-bodied subjects, as well as amputees. Especially for amputees, the exact location of the sEMG sites might have to be determined by palpation and by visual inspection of the sEMG activity; having 8 sEMG sensors overlaying a section of the arm allows to simultaneously inspect 8 sEMG signals and can facilitate the process of localising the muscle activation sites. The non-invasiveness and ease of use come at the cost of dealing with noisy and low-bandwidth sEMG signals which provide limited temporal (200 Hz running frequency) and spatial resolution. In particular, the low spatial resolution due to the size and arrangement of the electrodes may amplify the instances of crosstalk (Section 2.3.2). In practice, this means that the sEMG signal recorded by a sensor might be a superimposition of the electrical activity of multiple muscles, making it difficult

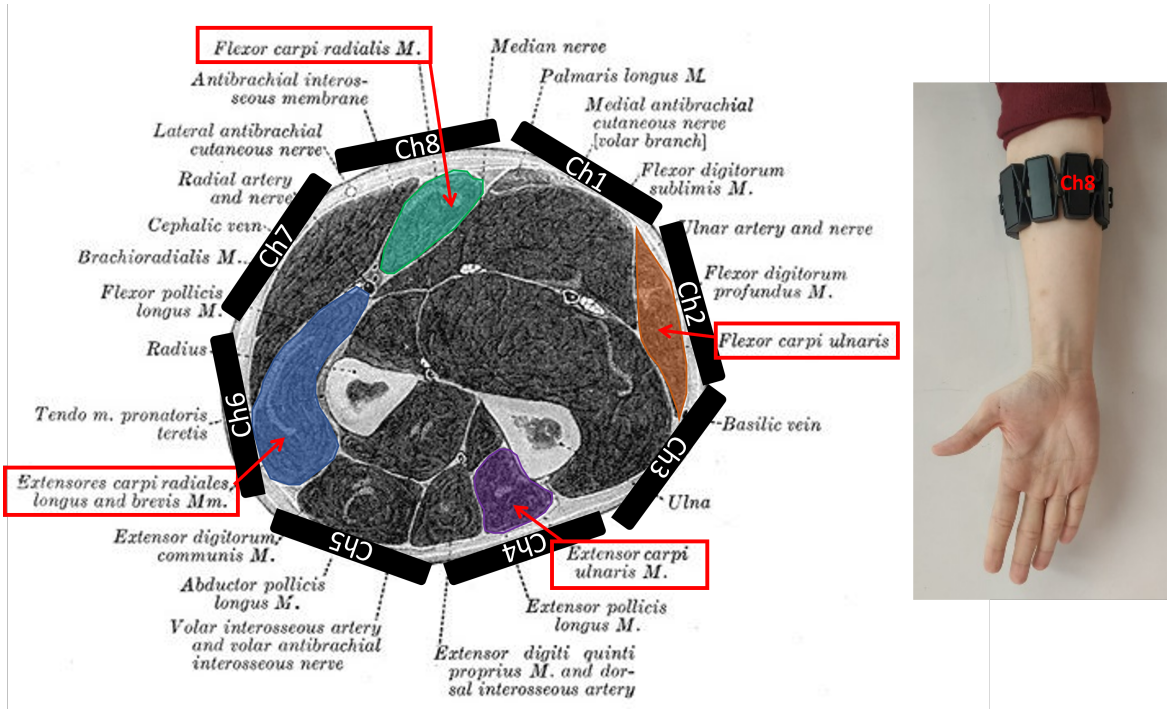

Figure 4.2: Cross section of the forearm to illustrate the muscles configuration with respect to the sEMG sensors of the Myoband (2.3.2). The main muscles involved in wrist flexion-extension are highlighted with colors. The Figure is modified from [37]

to isolate the activity of specific muscles of interest. As a result, the sEMG activity of a muscle might be recorded by multiple sensors. These technical issues are more pronounced when recording the sEMG signal of muscles involved in dynamic motions, where the sEMG features change rapidly due to the modulation of muscles' co-contractions. *In this work, we deal with sEMG signals that are contaminated by these sources of noise and variability, since we aim to enable a human subject to control the kinematics, stiffness and damping of a DoF through wrist flexion-extension by modulation of muscles co-contraction (i.e., modulation of impedance).* Moreover, given the high redundancy of the neuro-musculoskeletal system, we need to consider that muscles that do not contribute to the actuation of a specific joint might instead be functional to stabilize the joint and contribute to the overall level of joint impedance.

Here below we investigate the 8 sEMG signals recorded from the forearm's muscles of an exemplary able-bodied subject during dynamic and unconstrained wrist flexion-extension movements, performed at low and high muscle impedance. We are interested in (i) investigating the latent space of the sEMG features during flexion, and extension, performed at low

and high impedance; in (ii) identifying which channels (Ch) of the myoband are best suited to represent the global muscle activity of wrist's flexion-extension.

Myoband positioning

As explained above, we aim to capture the activity of the muscles involved in wrist flexion-extension. To do this the myoband is positioned approximately 5cm below the elbow so that the central sEMG sensor lies along the virtual medial line crossing the forearm and hand longitudinally and the sEMG sensors are placed on the most active areas of the main muscles spanning the wrist. In Section 2.5.2, the muscles involved in wrist motions are listed and illustrated in Figure 2.11. The following muscles are the most relevant for wrist flexion: the *Flexor Carpi Radialis* and *Ulnaris*; while the *Extensor Carpi Radialis Longus and Brevis*, and the *Extensor Carpi Ulnaris* are the main muscles involved in wrist extension [149]. In Figure 4.2 we show a cross-section of the forearm with the relevant muscles highlighted and a scheme of the myoband sensors placed around the forearm. This means that it is reasonable to assume that four muscles are mainly involved in wrist flexion-extension, and therefore the number of sEMG channels involved can be reduced from eight to four. In an ideal scenario where each sensor captures the activity of a single muscle, we would observe a significant change in magnitude of four out of eight sEMG signals, recorded during wrist flexion-extension. However, due to technical difficulties, and subject-specific anatomy, the problem of identifying the muscles activation for wrist flexion-extension is not trivial and specific assumptions have to be made. Before discussing methods to extract relevant muscles' activations for wrist flexion-extension, we provide experimental results to gain insight into the changes in the sEMG features during wrist impedance modulation.

In this preliminary experiment, the subject is requested to perform 10 repetitions of wrist extension-flexion, spanning the full range of mobility, while maintaining a low impedance in the first five repetitions and the highest possible impedance in the other repetitions. The kinematics of the wrist is also recorded using the Qualisys motion capture system [174]. The acquired myoelectric and kinematic data are shown in Figure 4.3. Repetition at low and high impedance are color-coded in blue and green, respectively. Let us consider the first repetition, executed in the time interval 0–10 sec, approximately. Observing the wrist flexion-extension position in the last plot, the DoF position initially increases as the subject performs extension, and then decreases when the subject returns to the rest position, and finally, it reaches negative values as the wrist is flexed. Generally, a repetition is characterised by a positive and negative peak, corresponding to extension and flexion. To identify which sEMG signals capture the activity of the muscles of interest one can visually inspect the signals and expect to observe a correspondence between peacks in the sEMG signals and

peaks in the kinematic data. Channel 3–6 show an increase in activation in correspondence with the positive peak observed in the position trajectory, and the activation peak recorded by channel 5 is the one with the highest magnitude across channels.

We conclude that channel 5 may capture the activity of the main extensor muscle. The same reasoning can be done to identify the channel for wrist flexion. In this case, both channels 7 and 8 have similar trends making this process difficult and visual inspection of other repetitions may be needed. While sEMG signals from repetitions at low impedance allow us to more easily observe an association between muscular activity and joint kinematics, it is in general more challenging to visually inspect and identify the relevant sEMG signal when flexion-extension is performed at different levels of muscles' co-activation. For instance, considering the sEMG signal of channel 8 during high impedance flexion-extension motions (last 5 repetitions) and contrasting it with the repetition at low impedance, it can be observed that there is substantial muscle activation during both flexion and extension (i.e., co-activation is observed). We can conclude that the sEMG features change substantially during modulation of muscle impedance due to modulation of muscles' co-activation, making the problem of decoding the human intent in terms of kinematics challenging if the coactivation is not taken into account. This is the cause of substantial performance deterioration for conventional and data-driven methods as explained in Section 3.1 and Section 3.2.1.

Identification of relevant sEMG channels for wrist flexion-extension

Considering the framework pipeline, a bottom-up approach is followed to define the number of channels needed. We aim to actuate a single DoF through flexion-extension movement using two lumped muscle-tendon models. These two models represent the activity of agonist and antagonist muscles. Given two muscle-tendon models, only two activations are needed, one to drive the contraction dynamics of each model. However, two agonists and two antagonists are mainly involved in flexion and extension (i.e., two sEMGs for flexion and two for extension). The problem of choosing input activation for the muscle-tendon models is that of extracting two activation signals from the eight provided by the Myoband, considering that four muscles are mainly involved in wrist flexion-extension. This means that at least four activation signals can potentially be extracted from the sEMG signals recorded by the Myoband. The following options have been investigated during the design of the proposed framework to choose the input sEMG signals:

- Instead of choosing specific sEMG channels, dimensionality reduction methods can be employed to blindly learn a latent two-dimensional space (the space of the activation signal given as input to the MTUs) embedded in the 8-dimensional space defined by the sEMG signals of the Myoband. This would avoid the need for subject-specific

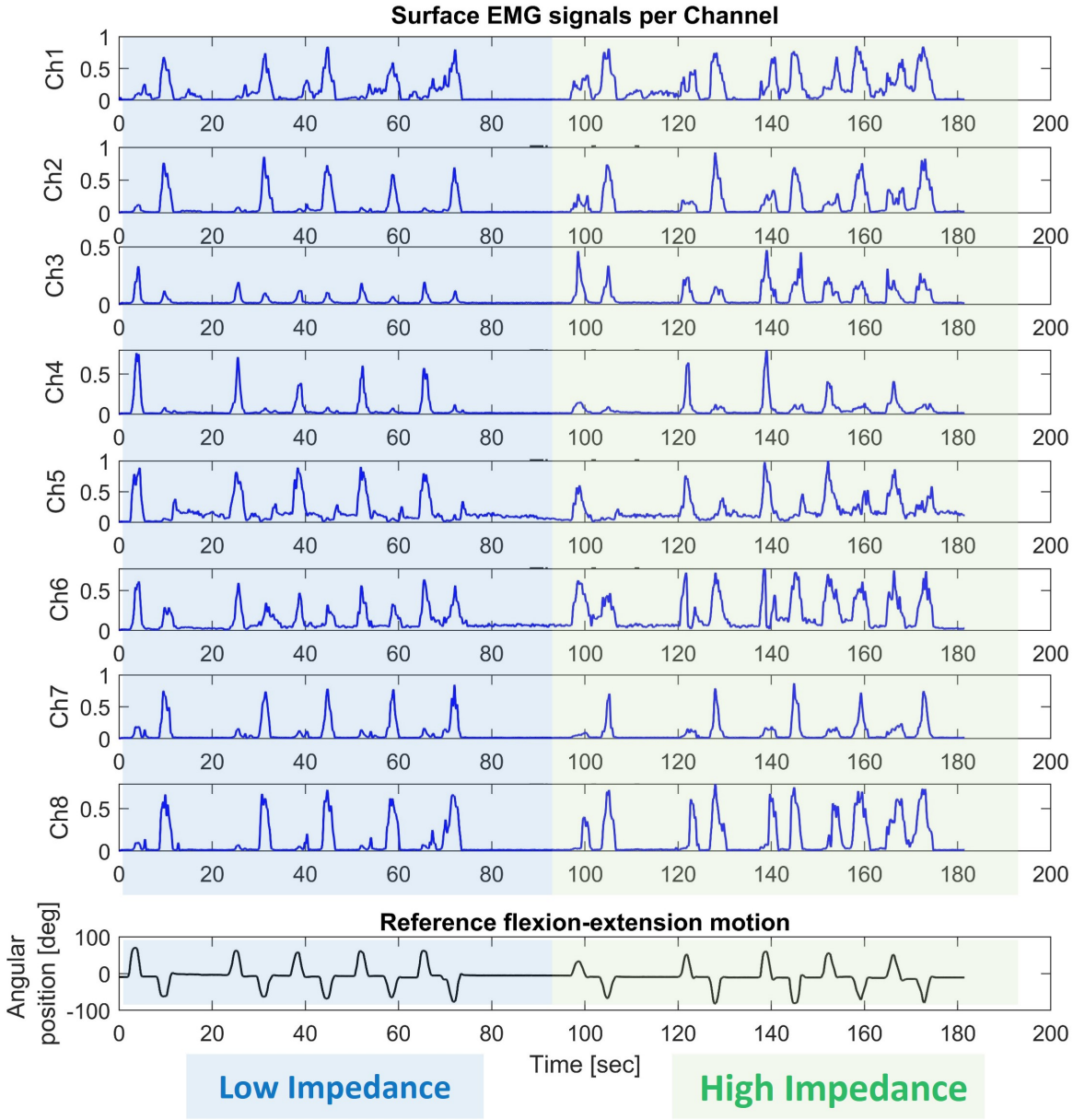

Figure 4.3: Processed surface sEMG signals recorded by the Myoband placed on the forearm of a volunteer as shown in Figure 4.2. The subject performs 5 repetitions of flexion-extension motion at low and high impedance. The corresponding wrist kinematics is shown in the last plot. These signals provide an insight into how the features of the sEMGs change due to modulation in muscles coactivation.

adjustment of the Myoband and manual selection of channels that capture the activity of muscles of interest. Given sEMG data recorded during the wrist flexion-extension only, the latent signals of the two-dimensional space would represent the overall activation related to flexion and extension and could be used as input to the muscle-tendon models. In practice, this means adding a block to the framework (Figure 4.1) that takes as input the processed matrix of sEMG signals E and outputs ch_1 and ch_2. Blind source separation methods such as Non-Negative-Matrix-Factorization (NNMF), Independent-Component-Analysis (ICA), and Autoencoders neural networks (AENN) have been previously used in data-driven frameworks [208] to automatically extract control commands from recorded sEMG signals. In particular, NNMF has been the mainstream method because of the inherent advantages it provides such as sparse coding, non-negative matrix decomposition (activation to muscle-tendon models must be non-negative) and ease of implementation. However, NNMF has different limitations [137] which are enhanced by the sudden changes in sEMG features due to modulation of muscles impedance. Different variations of offline and online NNMF with various constraints such as sparsity, orthogonality of the basis vectors, and regularization factors in the cost function have been implemented and investigated while developing the framework. However, none of these led to robust control performance as the signals estimated by the NNMF-based methods presented instances of missing or wrongly assigned activation peaks (i.e., peaks corresponding to flexion, were assigned to extension). Moreover, the lack of ground truth activation signals made it difficult to assess the NNMF performance in predicting activation signals and understand if the observed error in the predicted flexion-extension joint trajectory was due to issues in the NNMF or in other components of the pipeline, such as the muscle-tendon models. This ambiguity would have made the design and optimisation of the muscle-tendon models challenging and possibly based on wrong inputs. Therefore, we decided to extract the sEMG signals as explained in the next point.

- Given the unfeasibility of the first option, and the difficulties in identifying the sEMG signals corresponding to the 4 muscles (i.e., two flexors and two extensors) due to cross-talk and limitations imposed by the device itself (the sEMGs are arranged in a bracelet, meaning that the sensors can not be positioned at different distances from the elbow), it was decided to use two channels only, one for flexion and one for extension. The position of the myoband is adjusted according to the subject's anatomy in order to maximise the amplitude of the signal recorded by channel 4 and 8, for extension and flexion respectively. The Myoband positioning is guided by palpation and visual inspection of the sEMG signals to ensure that the selected channels overlay the most

active muscles during flexion-extention. In this process, we also optimise the Myoband position to avoid recording the activity of muscles involved in other motor functions. While channels 4 and 8, due to their position in the bracelet are the ones usually capturing the activity of the main extensor and flexor, depending on the subject's arm size, sensors adjacent to Ch_4 and C_8 may be selected.

In Figure 4.1 the matrix $E \in \mathbb{R}^{8\times T}$ contains the sEMG signal acquired in the time interval T by the sensors of the myoband. The variables ch_1 and ch_2 are the sEMG signals selected to drive the contraction dynamics of the two MTUs. The input activations may correspond to the signals recorded by channels 4 and 8 of the myoband, but as explained above the channel selection is subject-specific.

4.2.2 Output: impedance control and visual feedback

The output of the framework shown in Figure 4.1-A is q_f, the joint position of the (simulated) robot plant. During online testing, the subjects use q_f as visual feedback to adjust their muscles' contraction and make the robot plant move as desired. In the presence of external perturbations acting on the robot plant, q_f will start diverging from the user's desired position q_r depending on the joint stiffness K and damping D. This will trigger the subject's corrective action. Details on how the visual feedback is provided to the user are described in Section 5.3.2. In the later sections, we will explain how this behaviour is made possible by the design of the framework, where the MTUs state is only dependent on the state of the simulated robot model and it is therefore not directly affected by the perturbations.

4.2.3 Framework assumptions and requirements

The inputs to the framework are sEMG signals provided by *two channels* placed on the *Extensor Carpi Ulnaris* and on the *Flexor Carpi Radialis*, which drive two lumped muscle-tendon models. Based on the aforementioned assumption, the framework is designed to satisfy the following requirements:

1. The user's motor intent is decoded in terms of *wrist flexion-extension kinematics, joint stiffness and damping*.

2. The robot's impedance behaviour has to be updated based on the user's motor intent. This requires the implementation of a *variable impedance controller* on the robot's side.

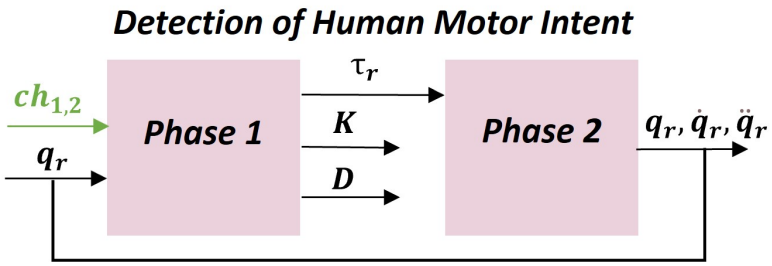

Figure 4.4: Scheme of inputs and outputs of the first block of the proposed framework. The *detection of human motor intent* block is split in two phases. *Phase 1* takes as input sEMG signals ch_1, ch_2 and the current joint position of the simulated robot q_r and outputs the human motor intent in terms of net torque at the joint τ_r, joint stiffness K and damping D. The torque τ_r is input to the *Phase 2* component which outputs the next state of the simulated robot $s_r = (q_r, \dot{q}_r, \ddot{q}_r)$. The stiffness K and D are not used in Phase 2, but input to the *Prosthesis control* block. More details are provided in Figure 4.1.

3. *The dynamics* (i.e., stiffness, damping) of the user's motor intent *has to match the one of the robot plant*.

4. A *corrective action* has to be implemented to ensure the subject can modify the muscles' activation to adjust the robot's kinematic and dynamic behaviour.

4.3 Detection of human motor intent

In the previous section (Section 4.2), technical details on sEMG placement and recording are provided. Specifically, we justify the choice of using two channels of the Myoband to record the sEMG of the *Flexor Carpi Radialis* and *Extensor Carpi Ulnaris* (ch_1, ch_2). These two sEMG signals are the input to the first of the two main blocks comprised in the framework, the *detection of human intent* component, discussed in this section.

The *detection of human intent* block maps the input sEMG signals $(ch_1(t), ch_2(t))$ to an estimate of the user's motor intent, namely the desired joint kinematics, joint stiffness and damping $(s_r(t), K(t), D(t))$. These are required to implement the human intended impedance behaviour on the (simulated) robot plant: $s_r(t)$ is the reference trajectory at time t for the impedance controller, $K(t)$ and $D(t)$ are the virtual stiffness and damping of the impedance model imposed in the adaptive control law.

The estimation of the human motor intent is done in two phases, described below in mathematical detail. A scheme of the input and output variables for these two phases of the first block is provided in Figure 4.4.

4.3.1 Phase 1: muscle-tendon dynamics

In *phase 1* a data-driven process-based approach which makes use of two lumped muscle-tendon units is used to model the macroscopic properties of flexor and extensor muscles involved in wrist flexion-extension. At each instant in time, given the current state of the MTUs, the input sEMG signals ($ch_1(t)$ and $ch_2(t)$) drive the forward dynamics of the lumped muscle-tendon models that for each MTU_i predicts the contraction force F_i and the state of the MTU at the next time step. In Figure 4.1-A, it can be observed that the MTUs receive as input the variable q_r. Since the MTUs are virtually arranged on the robot's link, as shown in Figure 4.1-B, the state of the MTUs depends on the joint position and q_r is used to update the muscle-tendon length l^i_{MTU} and the velocity $\dot{l}^{ii}_{MTU}$. Given the MTU_i state and the generated muscle force, the muscle-tendon stiffness K_1 and damping D_i are computed. The muscle force F_i, stiffness K_i and damping D_i are then mapped to the joint space of the simulated robot model using the Jacobian of the moment arms, as described in Section 2.4.3. The outputs of *Phase 1* are the net joint torque τ_r, the joint stiffness K and the joint damping D.

Firstly, we mathematically formulate the muscle-tendon model structure (Figure 4.1-C) and describe the muscle dynamics, which includes the *activation dynamics* and the *contraction dynamics*. The theoretical foundation of the activation and contraction dynamics was introduced in Section 2.4. We then derive the estimates of the muscle-tendon stiffness and damping. The geometrical arrangement of the MTUs on the simulated robot model, as illustrated in Figure 4.1-B, is discussed, and the Jacobian of the moment arms is computed. The latest is used to transform the output variables of the contraction dynamics and the muscle stiffness and damping from the muscle space to the joint space of the simulated robot moded.

From sEMG signals to input muscle activations

The classic procedure to filter raw sEMG signals E is described in Section 2.3.2 and it mainly involves signal rectification and filtering. According to the excitation-to-activation dynamics presented in [223], the rectified sEMG signal (i.e., before filtering) represents the net neural drive, while the rectified and filtered sEMG signal is associated with the net muscle activation and is suitable to drive the muscle-tendon contraction dynamics. Given the input neural drive, the *excitation dynamics* process provides the input activation. In this work, the excitation process is not relevant since the processed sEMG signals (i.e., sEMG envelopes) are used as muscle activations (Section 2.4). Differently from the reference model [81] each input activation ch_i is subsequently normalised $\bar{ch}_i$ in the range $[ch_i^{min} ch_i^{max}]$, where ch_i^{max} is the maximum value of ch_i recorded during the training session (Section 5.3.1) and ch_i^{min} is set

Table 4.1: List of independent and derived parameters of muscle-tendon dynamics.

	Independent parameters		Derived parameters	
	Parameter Name	**Parameter Description**	**Parameter Name**	**Parameter Description**
Non-lin Operator	A	Non-linear shape parameter in (-3,0)		
CE	F_{max}	Maximum isometric force	A_{rel}	Coordinate pole in $\dot{l}_{ce}(F_{ce})$ normalised to $aF_{max}F_{iso}(l_{ce})$
	l_{opt}	Optimal muscle length, i.e., length at which the maximum isometric force is reached	B_{rel}	Coordinate pole in $F_{ce}(\dot{l}_{ce})$ normalised to l_{opt}
	ΔW_{des}	Width of the descending branch of isometric curve	F_{iso}	Isometric force
	ΔW_{asc}	Width of ascending branch of isometric curve	$L_{A_{rel}}$	Length dependency of A_{rel}
	v_{des}	Exponent of descending branch of isometric curve	$L_{B_{rel}}$	Length dependency of B_{rel}
	v_{asc}	Exponent of ascending branch of isometric curve	$Q_{A_{rel}}$	Activation dependency of A_{rel}
	A_{rel0}	Maximum value of A_{rel}	$Q_{B_{rel}}$	Activation dependency of B_{rel}
	B_{rel0}	Maximum value of B_{rel}		
PE	L_{pe0}	Rest length l_{pe} normalised to optimal length l_{opt}	K_{pe}	factor of non-linearity in F_{pe}
	v_{pe}	Exponent of $F_{pe}(l_{ce})$ curve	l_{pe}	length of PE element, equal to l_{ce}
	$\hat{F}_{pe0}$	F_{pe} when $l_{ce} = \Delta W_{des}$		
DE	R_{de}	Minimum value of damping normalised to $d_{se,max}$	$d_{de,max}$	maximum value of damping coefficient
	D_{de}	Scaling factor for $d_{se,max}$		
SE	l_{se0}	Tendon slack length	K_{senl}	Stiffness of linear part of F_{se}
	ΔU_{nl}	Relative tendon stretch at non-linear transition	K_{sel}	Stiffness of non-linear part of F_{se}
	ΔU_l	Relative stretch in linear area for an increase in F_{se} of ΔF_{se0}		
	ΔF_{se0}	Force at non-linear transition		
	S_{ecc}	Increase in inclination of F_{ce} at transition between concentric and eccentric area		
	F_{ecc}	Normalised coordinate pole of $\dot{l}_{ce}(F_{ce})$ for eccentric contractions		

to the value of 0.0001, a minimum activation required to ensure numerical stability of the muscle-tendon model and based on the assumption of a constant minimal activation even in the absence of neural excitation [82]. Each signal is further processed using a non-linear operator accounting for the non-linearity in the activation-to-force relationship [132]:

$$a_i(t) = \frac{e^{A\bar{ch}_i(t)} - 1}{e^A - 1} \tag{4.1}$$

where the constant $A \in (-3, 0)$ determines the degree of non-linearity between $\bar{ch}_i$ and the activation signal a_i.

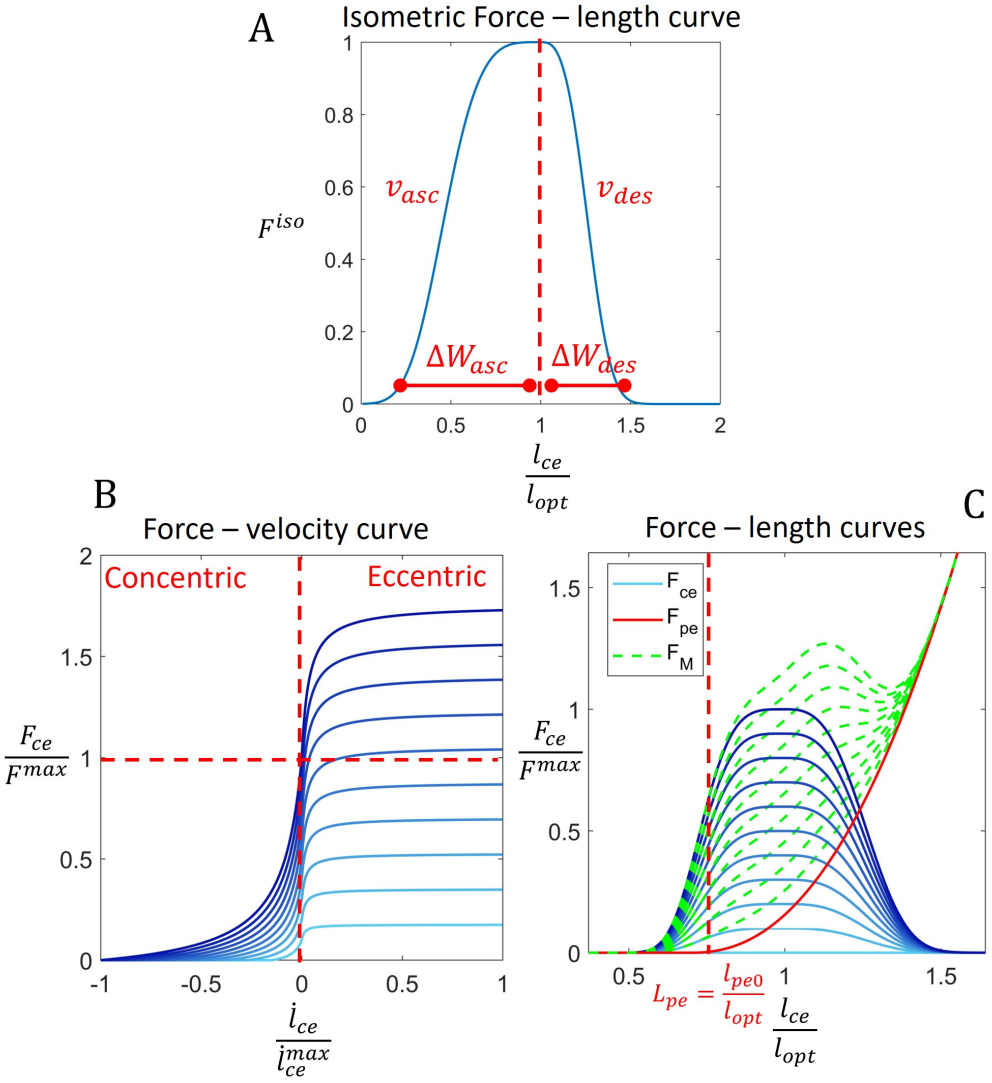

[ht]

Figure 4.5: A) Isometric force F_{iso} as a function of the normalised muscle length $\frac{l_{ce}}{l_{opt}}$; parameters characterising the shape of the curve are indicated in red and described in Table 4.1; B) Force-velocity relation between the normalised contractile force $\frac{F_{ce}}{F_{opt}}$ and the normalised muscle contraction velocity $\frac{\dot{l}_{ce}}{\dot{l}_{ce}^{max}}$. The force-velocity curves are plotted from light to dark blue as the input activation increases in magnitude. C) Normalised force-length relationship for the muscle component. The normalised contractile force $\frac{F_{ce}}{F_{opt}}$ dependence on muscle length is shown in blue (the dark blue curve corresponds to the maximum activation, while the lighter blue curve corresponds to lower input activation magnitude) for a given muscle contraction velocity, the force of the parallel element F_{pe} is shown in red. The muscle force is given by the sum of the passive and active forces (i.e., $F_{CE} + F_{PE}$), shown in green. The parallel element generates force above the normalised slack length $L_{pe0} = \frac{l_{pe0}}{l_{opt}}$. See Table 4.1 for a description of parameters.

Contraction dynamics

The biomechanical model of each MTU_i is based on the well-established Hill's phenomenological muscle-tendon model [90] introduced in Section 2.4. Specifically, we employ the model presented in [81] which demonstrated how including a damping element in parallel to the serial element enabled the suppression of high-frequency oscillations within the model. The MTU model's structure and mathematical formulation are outlined below, highlighting the differences with respect to the implementation used in the current work. Let us consider the muscle-tendon unit shown in Figure 4.1. Each MTU_i of length l^i_{MTU} is composed of a muscle of length l^i_{ce} in series to a tendon of length l^i_{se}, similarly to classic models discussed in Section 2.4. The muscle is modeled by a contractile element (CE) and a parallel elastic element (PE). The tendon is made up of a serial elastic element (SE) in parallel to a damper element (DE). The system at equilibrium is described by:

$$F^i_{ce}(l^i_{ce}, \dot{l}^i_{ce}, a_i) + F_{pe}(l^i_{ce}) = F^i_{se}(l^i_{ce}, l^i_{MTC}) + F^i_{de}(l^i_{ce}, \dot{l}^i_{ce}, \dot{l}^i_{MTC}, a_i) \tag{4.2}$$

where the input activation a_i is the input activation, $\dot{l}^i_{ce}$ is the muscle contraction velocity, $\dot{l}^i_{MTC}$ is the muscle-tendon contraction velocities and $F^i_{ce}, F_{pe}, F_{se}, F_{de}$ are the forces generated by the elements CE, PE, SE and DE, respectively. When CE is activated by a_i, CE and PE generate the forces F^i_{ce} and F^i_{pe}, which affect the equilibrium between the elements of the muscle and those of the tendon, starting the contraction dynamics. As a result l_{ce} starts contracting from its initial state $l^{init}_{ce} > l_{opt}$. The parameter l_{opt}, introduced later in the mathematical formulation of CE is the shortest length of CE at which the maximum F_{ce} is generated. The characteristics of each element composing the muscle-tendon model and determining the contraction dynamics are detailed below. The subscript i and the time dependency of each variable are dropped for clarity when describing a single MTU.

Contractile element CE In Section 2.4, we presented the theoretical foundations of the force-length and force-velocity relationship for a contractile, which characterise the mathematical description of the CE element. The force F_{ce} produced by CE depends on the current fibre length l_{CE}, contraction velocity $\dot{l}_{CE}$ and input activation a_i. In Figure 4.5-C, the normalised contractile force is plotted in blue and its dependence on the input activation is shown by the gradient of curves. When the contraction velocity is negative ($\dot{l}_{CE} \leq 0$) the muscle shortens (i.e., concentric contraction), otherwise for positive contraction velocities the muscle lengthens (i.e., eccentric contraction). The force-velocity is shown in Figure 4.5-B. In this work, the force generated by the contractile element differs from the formulation in

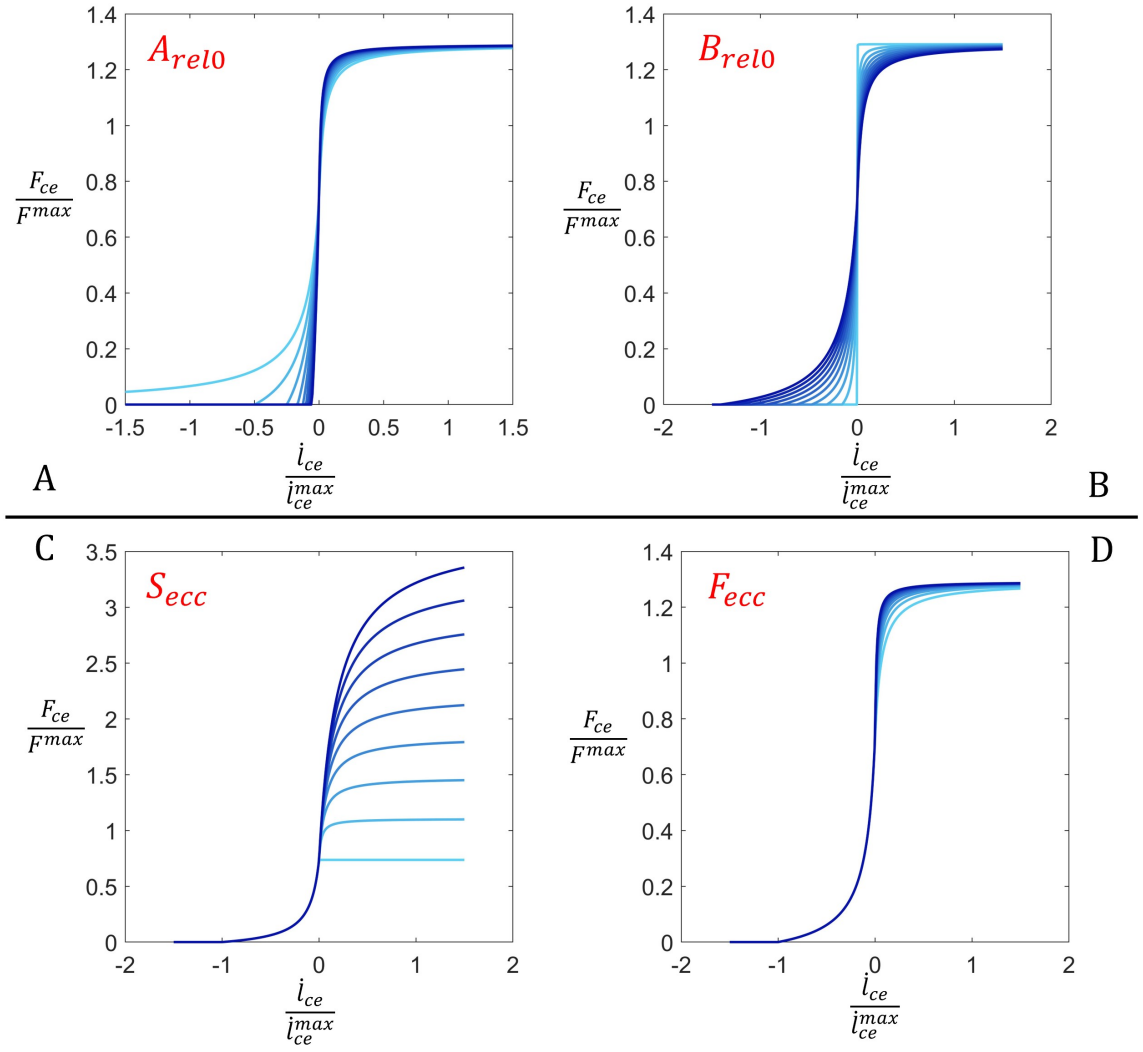

Figure 4.6: Normalise force-velocity curve for the contractile element showing how the relation scales with changes in the parameters $A_{rel0}, B_{rel0}, S_{ecc}, and F_{rel0}$. The parameters S_{ecc} and F_{ecc} affect only the eccentric contractions.

[81] in order to account for eccentric contractions as formulated in [82]:

$$F_{ce}(l_{ce},\dot{l}_{ce},a) = \begin{cases} F_{max}\left(\frac{aF_{iso}+A_{rel}}{1-\frac{\dot{l}_{ce}}{B_{rel}l_{opt}}} - A_{rel}\right) & , \dot{l}_{ce} \leq 0 \\ F_{max}\left(\frac{aF_{iso}+A_{rel,e}}{1-\frac{\dot{l}_{ce}}{B_{rel,e}l_{opt}}} - A_{rel,e}\right) & , \dot{l}_{ce} > 0 \end{cases} \tag{4.3}$$

where F_{isom} is the normalised isometric force generated by the contractile component shown in Figure 4.5-A and described in the following equation (the minus sign was incorrectly missing in [81]):

$$F_{iso}(l_{ce}) = \exp\left\{ -\left| \frac{\frac{l_{ce}}{l_{opt}} - 1}{\Delta W_{limb}} \right|^{\nu_{ce,limb}} \right\} \tag{4.4}$$

where l_{opt} is the optimal muscle length; ΔW_{limb} corresponds to ΔW_{asc} for $l_{ce} \leq l_{opt}$ and to ΔW_{des} for $l_{ce} > l_{opt}$. The parameters ΔW_{des} and ΔW_{asc} are the width of the normalized isometric curve in the descending or ascending branch of the curve, respectively. Similarly, $\nu_{ce,limb}$ corresponds to the parameters ν_{asc} and ν_{des} if it characterises the ascending or descending branch of the isometric force. The reader is reminded of the excitation and relaxation dynamics, characterised by different time constants. Excitation rises faster with respect to relaxation. This is reflected in the curve of the isometric force by suitably optimizing the parameters indicated in Figure 4.5-A. In equation 4.3, F_{max} is the isometric force at optimal length (i.e., $F_{isom}(l_{ce} = l_{opt})$); A_{rel} and B_{rel} are defined as follows:

$$A_{rel}(l_{ce}, a) = A_{rel0} L_{A_{rel}} Q_{A_{rel}} \tag{4.5}$$

$$L_{A_{rel}} = \begin{cases} 1 & , l_{ce} < l_{opt} \\ F_{iso}(l_{ce}) & , l_{ce} \geq l_{opt} \end{cases} \tag{4.6}$$

$$Q_{A_{rel}} = \frac{1}{4}(1 + 3a) \tag{4.7}$$

$$B_{rel}(l_{ce}, a) = B_{rel0} L_{B_{rel}} Q_{B_{rel}} \tag{4.8}$$

$$L_{B_{rel}} = 1 \tag{4.9}$$

$$Q_{B_{rel}} = \frac{1}{7}(3 + 4a) \tag{4.10}$$

where A_{rel} is the coordinate pole in the velocity-force curve normalised to $aF_{max}F_{isom}$; A_{rel0} is the maximum value of A_{rel}; B_{rel} is the coordinate pole in $F_{ce}(\dot{l}_{ce})$ normalised to l_{opt}; B_{rel0} is the maximum value of B_{rel}; $L_{A_{rel}}$ and $L_{B_{rel}}$ are the length dependency of A_{rel} and B_{rel}; $Q_{A_{rel}}$ and $Q_{B_{rel}}$ are the activation dependency of A_{rel} and B_{rel}. In Figure 4.6-A,B it can be observed how the force-velocity curve is affected by varying the parameters A_{rel0} and B_{rel0}. Equation 4.3 is obtained by reformulating the equation of the force-velocity relationship introduced by Hill and explained in Section 2.4.2, modified by adding the dependency on the activation. The eccentric parameters $A_{rel,e}$ and $B_{rel,e}$ are formulated as follows:

$$A_{rel,e} = -aF_{ecc}F_{iso} \tag{4.11}$$

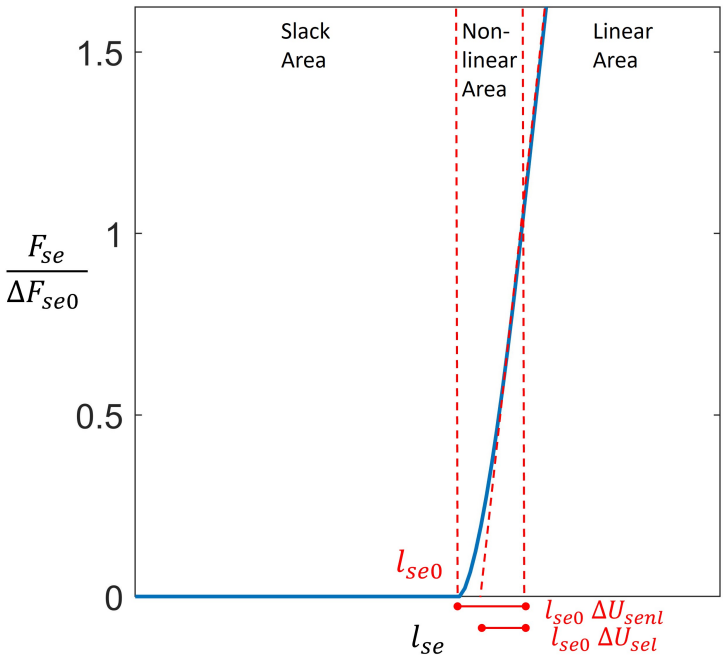

[ht!]

Figure 4.7: The tendon force is shown as a function of $l_{se} = l_{MTU} - l_{ce}$. The tendon force is normalised by the force ΔF_{se0} at the transition between the non-linear and linear area. The tendon starts producing force when extended above the slack length l_{se0}. The transition between the non-linear and linear area is for stretches above $l_{se0}\Delta U_{senl}$. When the tendon undergoes a further stretch of $l_{se0}\Delta U_{sel}$ the normalised force is equal to $\frac{2\Delta F_{se0}}{\Delta F_{se0}}$. The exponent characterising the non-linear curve is given by the ratio between ΔU_{senl} and ΔU_{sel}.

$$B_{rel,e} = \frac{B_{rel}(1 - F_{ecc})}{S_{ecc}(1 + \frac{A_{rel}}{aF_{iso}})} \tag{4.12}$$

Where F_{ecc} represents the coordinate pole in the velocity-force relation for eccentric contractions and S_{ecc} scales the intercept at $\dot{l}_{ce} = 0$ and the inclination of the curve force-velocity curve for eccentric contractions. In Figure 4.6-C,D, it can be observed how the force-velocity curve is affected by varying the parameters S_{ecc} and F_{ecc} considering a fixed input activation and l_{ce}.

Parallel Elastic Element PE The force generated by the PE element is shown in red in Figure 4.5-C. The force F_{pe} is characterized by a passive force-length relationship with respect to the muscle length l_ce. The *PE* element generates force only when stretched above the slack length l_{pe0}. The slack length is experimentally found to be a percentance of the

optimal length (Section 2.4). The force F_{pe} for $l_{ce} \geq l_{pe0}$ is modeled as an exponential curve:

$$F_{pe}(l_{ce}) = \begin{cases} 0 & , l_{ce} < l_{pe0} \\ K_{pe}(l_{ce} - l_{pe0})^{\nu_{pe}} & , l_{ce} \geq l_{pe0} \end{cases} \tag{4.13}$$

with stiffness K_{pe} obtained as follows:

$$K_{pe} = \hat{F}_{pe} \frac{F_{max}}{(l_{opt}(\Delta W_{des} + 1 - L_{pe0})^{\nu_{pe}}} \tag{4.14}$$

where $l_{pe0} = L_{pe0} l_{opt}$ is the rest length; L_{pe0} is rest length normalised with respect to the optimal length l_{opt}; $\hat{F}_{pe}$ is the force for $l_{ce} = \Delta W_{des}$; ν_{pe} is the exponent of the curve.

Serial Elastic Element SE The SE element is mathematically formulated as a continuous piece-wise non-linear relationship between force F_{se} and length $l_{se} = l_{MTU} - l_{ce}$ (Figure 4.7):

$$F_{se}(l_{se}) = \begin{cases} 0 & , l_{se} < l_{se0} \\ K_{senl}(l_{se} - l_{se0})^{\nu_{se}} & , l_{se} < l_{senl} \\ \Delta F_{se0} + K_{sel}(l_{se} - l_{senl}) & , l_{se} \geq l_{senl} \end{cases} \tag{4.15}$$

where l_{se0} is the tendon slack length below which no force is generated; l_{senl} is the length defining the transition from the non-linear relationship characterising the so-called toe region and beginning of the linear region; K_{senl} is the stiffness of the non-linear region; $\nu_{se} = \frac{\Delta U_{senl}}{\Delta U_{sel}}$ is the exponent of the curve in the toe region; K_{sel} is the stiffness of the linear region; ΔF_{se0} is the force at $l_{se} = l_{senl}$; these are defined as follows:

$$K_{senl} = \frac{\Delta F_{se0}}{(\Delta U_{senl} l_{se0})^{\nu_{se}}} \tag{4.16}$$

$$K_{sel} = \frac{\Delta F_{se0}}{(\Delta U_{sel} l_{se0})} \tag{4.17}$$

Serial Damping element SD In [81] a solution is proposed for high-frequency oscillations observed in Hill-type models consisting of only a CE, PE and SE element by adding a damping element in parallel to SE. The authors tested different MTU structures, adding a linear damping element in series or in parallel to CE, demonstrating that the serial damping, delocalised from the muscle component and added in parallel to the serial element suffices to damp the oscillations. Therefore, it is assumed that the damping coefficient of the DE element should be a function of the tendon extension velocity and the contractile force. The

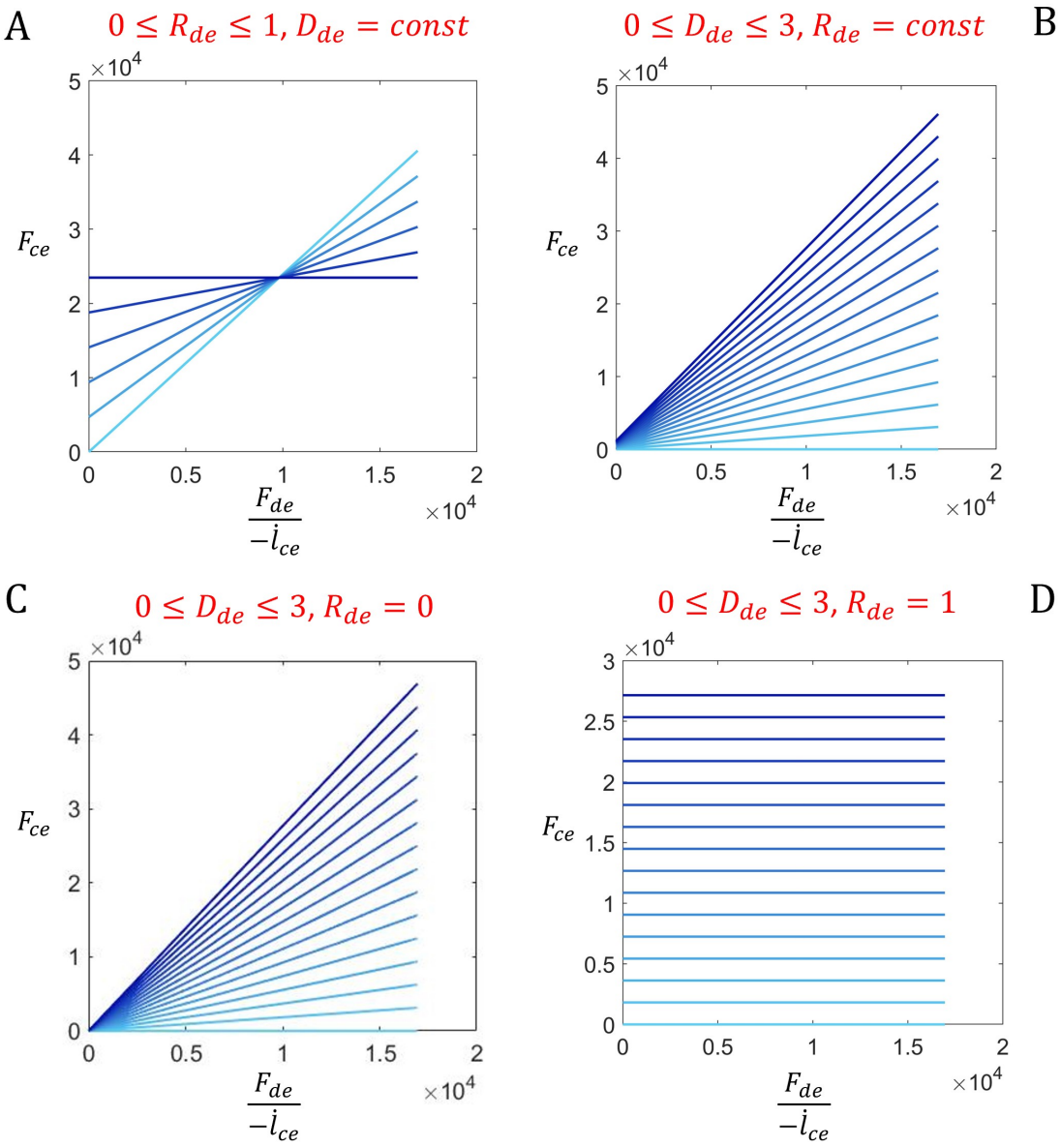

Figure 4.8: The relation between the contractile force F_{ce} and the damping coefficient $\frac{F_{ce}}{\dot{l}_{MTU}-\dot{l}_{ce}}$ is shown for changes in the parameters R_{de} and D_{de}. To visualise the effect of the varying parameters the curves are obtained considering the muscle-tendon velocity equal to zero for simplicity, and for a given activation and muscle-tendon length. The parameters are described in Table 4.1.

serial damping force is given by the following equation, where $\dot{l}_{MTC}$ is the MTU velocity and $\dot{l}_{CE}$ is the CE component velocity:

$$F_{de}(l_{ce},\dot{l}_{ce},\dot{l}_{MTC},a) = d_{de,max}\left((1-R_{de})\frac{F_{ce}(l_{ce},\dot{l}_{ce},a)+F_{pe}(l_{ce})}{F_{max}}+R_{de}\right)(\dot{l}_{MTC}-\dot{l}_{ce}) \tag{4.18}$$

where $d_{de,max}(l_{ce},a) = D_{de,max}\frac{F_{max}A_{rel0}}{l_{opt}B_{rel0}}$ and $D_{de,max}$ is a dimensionless constant representing the maximum damping coefficient at $F_{ce} = F_{max}$; R_{de} is the minimum value of damping at $F_{ce} = 0$. In Figure 4.8 we show how the relation between F_{ce} and the damping coefficient $\frac{F_{ce}}{\dot{l}_{MTU}-\dot{l}_{ce}}$ is affected by varying the parameters R_{de} and S_{de}.

Simulation of contraction dynamics The main steps to simulate the MTU dynamics are the following:

1. Given the initial muscle-tendon length l_{MTU}, and assuming $\dot{l}_{ce} = 0$ and $\dot{l}_{MTU} = 0$ Equantion 4.3 is solved for l_{ce} assuming the minimum activation u = 0.001.

2. Given the current state of the muscle-tendon unit (l_{ce}, $\dot{l}_{ce}$, l_{MTU}, $\dot{l}_{MTU}$) and the input activation u, we first calculate the forces generated by each element within the model. The next state of the muscle-tendon unit is obtained by substituting Equation 4.3 in the forces equilibrium Equation 4.2 which results in a quadratic equation when solved as a function of the contraction velocity $\dot{l}_{ce}$:

$$\dot{l}_{ce} = \frac{-C_1-\sqrt{C_1^2-4C_2C_0}}{2C_2} \tag{4.19}$$

   with coefficients formulated as in [81]:

$$C_2 = d_{de,max}(R_{de}-A_{rel}(1-R_{de})) \tag{4.20}$$

$$C_1 = -(C_2\dot{l}_{MTU}+D_0+F_{se}-F_{pe}+F_{max}A_{rel}) \tag{4.21}$$

$$C_0 = (l_{opt}B_{rel}d_{de,max}(R_{de}+(1-R_{de})uF_{iso})\dot{l}_{MTU}+l_{opt}B_{rel}(F_{se}-F_{pe}-F_{max}uF_{iso}) \tag{4.22}$$

   For eccentric contractions, the A_{rel} and B_{rel} have to be replaced by the corresponding eccentric parameters $A_{rel,e}$ and $B_{rel,e}$.

3. The new muscle length l_{ce} is obtained by numerically integrating $\dot{l}_{ce}$. In this work, the muscle-tendon length and velocity are determined by the configuration of the robot based on the assumption that the muscle-tendon units are virtually constrained on the

robot's link. In fact, it can be observed in Figure 4.1-A that the state of the simulated robot q_r is fed back to the muscle-tendon units. To formalise the muscle-tendon velocity and length equation it is first necessary to introduce the robot model and the arrangement of the MTUs on the link, which is discussed below in Section 4.3.3.

4.3.2 Phase 1: muscle stiffness and damping estimation

In this section, the stiffness and damping of the muscle and tendon are computed. These are then transformed from them muscle-tendon space to the joint space and used to implement an adaptive impedance controller on the simulated prosthesis.

Researchers have used different approaches to compute muscle-tendon stiffness (Section 3). Methods which incorporate muscle-tendon model commonly estimate the stiffness can be grouped in the following categories of approaches.

- Short range stiffness [220, 46].
  Given a Hill-based muscle-tendon model the muscle stiffness is defined as (i.e., short-range stiffness):
  $$K_m(t) = \frac{\gamma F_m(t)}{l_{opt}} \tag{4.23}$$
  where F_m is the force generated by the muscle component, l_{opt} is the muscle length at which the maxim force is generated, γ scaling constant. The tendon stiffness is computed as the slope of the dimensionless force-strain curve:
  $$K_t(t) = \frac{dF_t(t)}{dl_t(t)} \tag{4.24}$$
  Then, given the lever arm R, the joint stiffness is computed as follows, using the Jacobian of the moment arms R to map the muscle-tendon stiffness to the joint space:
  $$K(t) = \frac{K_m(t)K_t(t)}{K_m(t)+K_t(t)}R^2 \tag{4.25}$$
  The joint damping, if used in the controller is computed as function of the stiffness as follows:
  $$D(t) = 0.2\sqrt{K(t)} \tag{4.26}$$
  In this case D does not represent the human intended joint damping, but it the derivative gain, set to satisfy controller stability requirements. This approach to obtain a variable damping is also used in other studies (e.g., [110, 127]). Modeling the joint stiffness as short range stiffness disregards the dependencies of stiffness on muscle length and

velocity, substantially simplifying the estimates K_m. However, during dynamic motion, the stiffness is largely affected by changes in muscle length and velocity. Short range stiffness is shown to not be appropriate for modeling muscle stiffness during dynamic movements and it is shown to overestimate its value [172]. In fact, short range stiffness characterises the intrinsic stiffness of the muscles, when the fibers are stretched within 3% of the length [209], as discussed in Section 2.4.4.

- Stiffness as linear function of the magnitude of sEMG signals [110, 127].
  The computation of joint stiffness is based on the stiffness index proposed in [161], discussed in Section 3.2.3 Based on the assumption that simultaneous increase in flexor and extensor muscle forces acting on the joint does not change the net torque the stiffness is defined as follows:

$$K(t) = \alpha K_{index}(t) + \beta \tag{4.27}$$

  where α and β are constants to be identified experimentally, STI is the stiffness trend index and is defined below:

$$K_{index}(t) = |\sum_{flexor-i} \tau_i(t)| + |\sum_{extensor-j} \tau_j(t)| \tag{4.28}$$

  where the torque is estimated using muscle-tendon models.

In this work, the stiffness and damping of each MTU are first estimated from the muscle-tendon state and then mapped to the joint space. K_i is modeled as the muscle fiber stiffness K_m^i in series with the tendon's stiffness K_t^i, i.e., $K_i = K_m^i K_t^i/(K_m^i + K_t^i)$. In this work we choose to compute K_m^i as the directional derivative of $F_{ce}(l_{ce}^i, \dot{l}_{ce}^i, ch_i)$ with respect to unit vector of l_{ce}^i [179]:

$$K_m^i = \frac{\partial F_m^i(l_{ce}^i, \dot{l}_{CE}^i, ch_i)}{\partial l_{ce}^i} \tag{4.29}$$

This formulation takes into account the state of the muscle $(l_{ce}^i, \dot{l}_{ce}^i, ch_i)$ and eliminates in the stiffness computation the force component due to contraction velocity and change in activation. Similarly, K_t^i is computed as the directional derivative of $F_t^i = F_{se}^i + F_{de}^i$ with respect to unit vector of $l_{se}^i = l_{MTC}^i - l_{ce}^i$.

$$K_t^i = \frac{\partial F_t(l_{se}^i, \dot{l}_{SEE}^i)}{\partial l_{se}^i} \tag{4.30}$$

where $l^i_{se} = l^i_{MTC} - l^i_{ce}$ Muscle and tendon damping (D^i_m, D^i_t) are computed as directional derivatives with respect to muscle contraction velocity $\dot{l}^i_{ce}$ and tendon extension velocity $\dot{l}^i_{se} = \dot{l}^i_{MTU} - \dot{l}^i_{ce}$.

4.3.3 Phase 1: geometric arrangement of MTUs on robot's link

Figure 4.1-B provides an overview of the arrangement of the MTUs on the simulated robot model. Each MTU_i is virtually attached to the link from the Center of Mass (CoM) of the link (l^i_a) to a fixed base (l^i_b), i.e., the length of l^i_{MTU} varies as a function of q_r. Given α_i and the initial joint position $q_r = 0$, we can compute l^i_a as $l^i_{MTU} \sin\alpha_i$. l^i_a and l^i_b are kept constant during the simulation and control, while $l^i_{MTU}(q_r)$ and the moment arm $r^i(q_r)$ vary as a function of q_r. The length of the muscle-tendon unit i is computed as follows:

$$l^i_{MTU} = \sqrt{(l^i_a)^2 + (l^i_b)^2 - 2l^i_a l^i_b \cos(\pi/2 - q_r)} \tag{4.31}$$

where the muscle-tendon contraction velocity $\dot{l}^i_{MTU}$ is computed by numerical differentiation. To transform the muscle-tendon forces, stiffness, and damping to the joint space, we define the Jacobian matrix $\mathbf{R} = [r^1\ r^2] = [\frac{\partial l^1_{MTU}(q_r)}{\partial q_r}\ \frac{\partial l^2_{MTU}(q_r)}{\partial q_r}]^T$ containing the moment arms r^i of the two MTUs:

$$\begin{aligned} r^i(q_r) &= \frac{\partial l^i_{MTU}(q_r)}{\partial q_r} = l^i_b \sin\alpha^i(q_r) \\ \text{with} \quad \alpha^i(q_r) &= \text{acos}\left(\frac{-(l^i_a)^2 + (l^i_b)^2 + (l^i_{MTU})^2}{2l^i_{MTU} l^i_b}\right) \end{aligned} \tag{4.32}$$

The obtained Jacobian of moment arms R is used to transform τ_r, the muscle-tendon stiffnesses (K_1, K_2) and damping (D_1, D_2) from the muscle-tendon space to the joint space of the simulated robot model.

4.3.4 Phase 1: mapping from muscle space to joint space

Forces generated by MTU_i result in the net torque $\tau_r = [F_1, F_2]^T \mathbf{R}$. We compute the joint space stiffness considering also the contribution given by the varying moment arms as a function of q_r, according to the following definition of stiffness [98]:

$$K = \frac{\partial \tau_r}{\partial q_r} = \frac{\partial \mathbf{R}^T}{\partial q}[F_1, F_2]^T + \mathbf{R}^T diag([K_1, K_2])\mathbf{R} \tag{4.33}$$

The joint damping is computed as $D = \sum_{i=1}^{2}(D_i(r^i)^2)$.

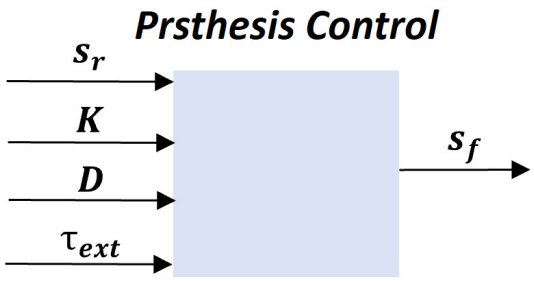

Figure 4.9: Scheme of input and outputs of the second block of the proposed framework. The *Prosthesis control* implements a variable impedance controller in the joint space of the robot plant. The inputs are the reference motion trajectory s_r, the joint stiffness K and damping D, provided by the *Detection of motor intent* block. External perturbations τ_{ext} may act on the robot. This block outputs the next state of the robot's plant s_f. More details are provided in Figure 4.1.

4.3.5 Phase 2: detect motor intent as kinematics

The net joint torque τ_r predicted by the two muscle-tendon units can not be used as input to implement a variable impedance controller, since this control scheme requires a motion trajectory and an impedance model as input 2.1.4. The impedance model is defined by the joint stiffness K and D, while the reference motion trajectory $s_r = (q_r(t), \dot{q}_r(t), \ddot{q}_r(t))$ is obtained by applying the $\tau_r(t)$ at the robot's joint using the forward dynamics model explained in Section 2.1.2.

4.4 Prosthesis control

The reader recalls that the proposed framework is constituted of two main blocks: the *detection of human intent* and the *prosthesis control*. In Section 4.3 we have mathematically formulated the first block of the framework, which decodes the motor intent from sEMG signals. This section describes how the motor intent is implemented on a simulated robotic system. The inputs and outputs of the two blocks are summarised in Figure 4.3 and Figure 4.4, respectively.

The human motor intent at time t is represented by the simulated robot state $s_r(t)$, stiffness $K(t)$, and damping $D(t)$. As stated earlier, our framework's second block executes this intent on the robot plant using a position-based variable impedance controller. The position-based variable impedance controller is used to track $s_r(t)$ by adapting $K(t)$ and $D(t)$. Consider the

generic dynamic model for a robot with a single rotational joint:

$$M\ddot{q}_r(t) + g(q_r(t)) = \tau_f(t) + \tau_{ext}(t) \tag{4.34}$$

where M is the link's joint space inertia, g is the gravity compensation torque, and $\tau_{ext}(t)$ is the external perturbation acting on the robot joint. Building on the impedance control paradigm without force-torque sensor readings [96], we define the control law as:

$$\tau_f = M\ddot{q}_r(t) + K(q_r(t) - q_f(t)) + D(\dot{q}_r(t) - \dot{q}_f(t)) + g(q_r(t)) \tag{4.35}$$

Note that we define an impedance behaviour that uses the natural robot's link inertia, due to the challenges in inertia shaping, and due to the low acceleration reached during control. We design the framework and define the muscle-tendon models' length and velocity as a function of s_r so that any external perturbation (τ_{ext}), e.g., a force field acting on the joint, affects s_f only, while the state of the simulated robot model s_r and the MTUs are unaffected and represent the user motor intent based on the input sEMG signal. This choice allows the implementation of the user's corrective action as the feedback loop of the impedance controller. In the absence of external perturbations ($\tau_{ext} = 0$), q_r matches q_f. If τ_{ext} is not zero, depending on K and D, q_f will start diverging from q_r. The joint position q_f serves as visual feedback for the user, who can adapt online the simulated robot's state and gains (K, D) by modulation of the muscles' coactivation.

4.5 Muscle-tendon models training

For the two blocks of the framework to work according to the requirements listed in Section 4.2.3, it is necessary to set suitable values for the parameters of the muscle-tendon units. This section is concerned with identifying and estimating the parameters of the muscle-tendon models and constitutes the second contribution of this thesis. As discussed in the previous section, the domain application imposes constraints on the framework design. In particular, the lack of experimental joint torque, joint stiffness and damping to use as ground truth, which would have allowed multi-output observations, makes the problem of identifying the model and estimating muscle-tendon parameters challenging. The muscle-tendon model structure used in the framework was described in the previous section and it is based [81]. This choice is the result of incremental work and testing of different muscle-tendon architectures in relation to the thesis's objective. Table 4.2 lists the variables of MTU_i that identify the muscle-tendon model structure and the vector of parameters $\bar{\mathbf{p}}$ to be optimised. Typically, the underlying optimization process minimizes the root mean square error (RMSE) between

	Parameter Name	Variable	Lower Bound	Upper Bound
CE	F_{max}	$\bar{p}_1$	1000	9000
	l_{opt}	$\bar{p}_2 l_{ce}^{init}$	$0.05 l_{ce}^{init}$	$0.085 l_{ce}^{init}$
	ΔW_{des}	$\bar{p}_3 \bar{p}_2$	$0.7\bar{p}_2$	$3.5\bar{p}_2$
	ΔW_{asc}	$\bar{p}_4 \bar{p}_2$	$0.7\bar{p}_2$	$3.5\bar{p}_2$
	v_{des}	$\bar{p}_5$	1.2	4
	v_{asc}	$\bar{p}_6$	1.2	4
	A_{rel0}	$\bar{p}_7$	0.1	0.4
	B_{rel0}	$\bar{p}_8$	1.1	5.1
PE	l_{pe0}	$\bar{p}_9 \bar{p}_2$	$0.7\bar{p}_2$	$0.95\bar{p}_2$
	v_{pe}	$\bar{p}_{10}$	1.1	3
	$\hat{F}_{pe0}$	$\bar{p}_{11} \bar{p}_1$	$0.5\bar{p}_1$	$1\bar{p}_1$
DE	D_{de}	$\bar{p}_{12}$	0.001	3
	R_{de}	$\bar{p}_{13}$	0	0.8
SE	l_{se0}	$\frac{2}{3} l_{MTU}$	$\frac{2}{3} l_{MTU}$	$\frac{2}{3} l_{MTU}$
	ΔU_{senl}	$\bar{p}_{14}$	0.02	0.07
	ΔU_{sel}	$\bar{p}_{14} \bar{p}_{15}$	$(1/3)\bar{p}_{15}$	$(2/3)\bar{p}_{15}$
	ΔF_{se0}	$\bar{p}_{16} \bar{p}_1$	$0.3\bar{p}_1$	$1\bar{p}_1$
	S_{ecc}	$\bar{p}_{17}$	1.2	2
	F_{ecc}	$\bar{p}_{18}$	0.5	2

Table 4.2: List of parameters defining each MTU structure. The parameters description can be found Table 4.1. In the column labelled "Variable", the parameters are written as a function of the variables $\bar{p}_i$ to be optimized. The lower and upper bound of each parameter is indicated in the last two columns and set experimentally and based on prior work [189].

a reference torque and the torque predicted by the MTUs τ_r without any prior knowledge of the interaction between elements within the MTU (e.g., [110]). This makes the MTUs parameters' optimization an ill-posed problem: multiple combinations of parameters can generate the same net joint torque (τ_{ref}) and thus the same reference joint position q_r, but most of these combinations may provide gains (K, D) that do not match the user-desired dynamic behaviour and can result in an unstable and ineffective impedance controller. This is a critical issue that undermines the model validity and transparency, making it difficult to fully understand the dynamics of the MTUs and to extract valid gain values.

We attempt to overcome the problem of a priori identifiability of the model and of estimating muscle-tendon parameters as follows:

1. enriching the training dataset;
2. making assumptions on the relative length between muscle and tendon elements;
3. reducing the number of parameters to estimate in order to maximize their inter-dependency by reparametrizing the model, and introducing domain knowledge on muscle-tendon contraction dynamics;
4. defining an optimization framework that includes the impedance controller and uses q_f as the optimization signal. In fact q_f is affected by the human inteded joint stiffness and damping.

(1) Enriching the training dataset As detailed in Chapter 4.2.1, the framework takes as input the EMG signals of the wrist flexor and extensor and predicts the joint position q_f. The latter is the only experimental observation output by the framework that can be used to optimize the muscle-tendon models. In Chapter Chapter 5.3 the experimental protocol to collect necessary data to train the model is discussed in detail, and an introductory summary is provided here. The training dataset consists of EMG data and the corresponding wrist flexion-extension joint position. The wrist kinematics is used as the ground truth signal to define an optimization problem and estimate muscle-tendon unit parameters. Since the same joint kinematics can underlie different joint impedance values (i.e., level of muscle co-contractions), EMG signals and corresponding kinematics data are collected for wrist flexion-extension movements performed at various levels of impedance.

(2) Relative length between muscle and tendon elements The choice of the MTUs parameters affects the interaction between the elements in the muscle and in the tendon, which (in turn) affects the muscle's and tendon's stiffness and damping. We found in initial sensitivity studies that the result of the optimization is highly sensitive to the relative lengths

of the muscle and the tendon since it affects the way each element of the muscle-tendon unit contributes to the overall force generated by the MTU. Existing literature investigating the relationship between architectural features of the MTUs and their contraction dynamics in relation to specific functionalities (energy storage, impedance modulation, etc) indicates that muscle-tendon systems characterised by a long tendon compared to the muscle enhance control and impedance modulation [215, 16]. This hypothesis on the functional properties enabled by such a MTU structure has been investigated by [175]. We rely on these studies and define the MTUs structure to have a long tendon compared to the muscle and set the tendon slack length to $\frac{2}{3}l^i_{MTU}$. The ratio between the muscle and tendon length is the same as the one of the muscle-tendon complex investigated in [175].

(3) MTU's parameters simplification Domain knowledge based on previous work discussed in Chapter 2 [223, 215, 81, 189] on muscle-tendon contraction is used to further constrain the muscle-tendon parameter space. We consider ranges of parameter values defined during identification studies in the literature and define lower- and upper-bound conditions for these parameters to constrain the optimization problem. Moreover, the model is reparametrized to maximize the interdependence between parameters (detailed in Table 4.2) (for example, the optimal muscle length is set as a function of the muscle length when the contraction velocity is zero). Preliminary sensitivity studies indicated that some parameters did not make any substantial contribution to the offline tracking performance. Based on this observation, the parameter space of the MTU is simplified as follows: (i) the pennation angle, i.e., the angle between the muscle and the tendon, is set to be constant at zero; and (ii) l^i_{opt} is learned directly from data and assumed to be constant instead of being a function of the input activation [132, 110]. Additional constraints to the optimization problem are detailed below.

(4) Optimization signal Typically, as discussed in Chapter 3.1 the torque τ_r is used as the optimisation signal in the problem of estimating muscle-tendon parameters. However, different combination of muscle-tendon parameters can provide the same net torque. Given the input data (EMG signals), the model structure and a set of parameters, the muscle-tendon model provides the joint torque, stiffness, and damping, as a result of the contraction dynamics and mapping of variables from the muscle-tendon parameter space to the joint space. While the joint stiffness and damping cannot be experimentally measured in the considered set-up, in the proposed framework these values are used as gains of a position-based variable impedance controller. This inherently limits the set of muscle-tendon parameter solutions to those that not only enable the desired kinematics but also provide stiffness and damping values that ensure the system's stability. The output of the position-based impedance controller

q_f, which depends on the interaction dynamics defined by the gains (K, D), was used as optimization signal and compared to the reference joint kinematics to define the cost function for estimating the muscle-tendon parameters.

We formally define the prediction function $f : \mathbb{R}^{m+2} \rightarrow \mathbb{R}$ that acts on the input defined by the sEMG signals $[ch_1(t), ch_2(t)] \in \mathbb{R}^2$ and the parameters of the MTUs $\overline{\mathbf{p}} \in \mathbb{R}^m$ to produce the final joint position $q_f(t) \in \mathbb{R}$:

$$q_f(t) = f([ch_1(t), ch_2(t)]; \overline{\mathbf{p}}) \tag{4.36}$$

The constrained optimization problem given training data (E, q_f^{tain}) collected in the time interval $[0, T]$ is defined as:

$$\begin{aligned} \min_{\overline{\mathbf{p}}} \quad & \sqrt{\frac{\sum_{t=1}^{T}(f([ch_1(t), ch_2(t)]; \overline{\mathbf{p}}) - q_f^{train}(t))^2}{T}} \\ \text{s.t.} \quad & lb \leq \overline{\mathbf{p}} \leq ub \end{aligned} \tag{4.37}$$

Here, $q_f^{train}(t) \in \mathbb{R}$ is the measured wrist flexion-extension angular position, $\mathbf{lb}$, $\mathbf{ub} \in \mathbb{R}^m$ are the lower and upper bound values of $\overline{\mathbf{p}}$ shown in Table 4.2 and T is the length of the trajectories. Additionally, the following constraints are added to the optimization problem to prevent numerical instability and aid the optimization convergence:

- $W_{des}^i + W_{asc}^i < l_{ceInit}^i$, where l_{ceInit}^i is the initial state of the muscle when $q_r = 0$. This ensures that the CE element operates in the muscle-length range.
- if $l_{ce}^i < 0.001 l_{opt}^i$ or $l_{ce}^i > 0.95(l_{MTU}^i - l_{see0}^i)$ set $\dot{l}_{ce}^i = 0$. This ensures that $l_{MTU}^i = l_{ce}^i + l_{see0}^i$ while considering that the tendon can not be compressed.
- constraints on joint stiffness and damping $K > 0, D >= 0$ to ensure the impedance controller stability.
- The constraint that limits the maximum extension of the tendon (l_{se}^i) is set to 10% of l_{se}^i [215] after which the tendon is assumed not to generate force.

Robot model for the *Simulated prosthesis* and the *Robot plant*

The *simulated robot model* and the *robot plant*, indicated in Figure 4.1, have different purposes in the framework: the first belongs to *the detection of human motor intent* block, the second one represents the prosthesis. One approach could have been to design the simulated robot model to match a model of the human wrist by defining a simple two-link robot

(forearm, hand) with a revolute joint (i.e., flexion-extension) and dynamic parameters (i.e., links mass, inertia, center of mass) set to average values of the human hand. However, the kinematics and dynamics of the two robots would not match. The joint stiffness and damping estimated from the muscle-tendon models would need to be tuned and remapped to a range of values that allows the robust control of the robot plant. We discussed how this approach creates a mismatch between the dynamics of the MTUs and that of the robot plant. This is further discussed in the next section. Another option would be to set the robot plant to have human-like parameters so that the two models match. This option was initially explored but then abandoned for two main reasons: 1) the final future goal is to deploy the framework on a real prosthesis or robotic arm which has kinematics and dynamics that differs from that of the humans' ; 2) due to the low values of the average inertia of the human hand the controller results insensitive to changes in τ_r since the magnitude of the net torque given by the hills model is significantly smaller than the compensation torques. This means that the controllers are insensitive to changes in the muscle-tendon model parameters, making the optimization problem challenging.

The aim of this work is not to closely imitate the wrist kinematics structure and the wrist's passive dynamics but to design a framework that retains key features that enhances the user's controllability of the (simulated) robotic system.

4.5.1 Importance of impedance controller in the optimization pipeline

As discussed in Section 4.5, our optimization method uses the joint position trajectory of the robot's plant q_f as an optimization signal, instead of q_r or a reference joint torque. This choice is motivated by the fact that q_f is affected by K and D since these are used as gains in the position-based impedance controller. This means that the muscle-tendon models' parameters have to be optimised to ensure that q_f matches q_f^{train}, while ensuring that the dynamics of the muscle-tendon units support the implementation of a stable impedance controller and enhances the control performance of the user. Existing methods discussed in Section 3.2.3 instead use the joint torque τ_r or q_r as optimization signal, and if the stiffness or damping are estimated from the MTUs, these have to be tuned in a separate phase to ensure the control stability. The importance of including the impedance controller in the optimization framework is explained below and shown in Figure 4.10. The figure shows the offline evaluation of the framework on the entire dataset. Training data were collected from 20 repetitions of flexion-extension motions. The first five repetitions are performed at low impedance, whereas repetitions 6–10 are done at high impedance. In repetitions 11 and 12 the subject performs isometric contractions, and the remaining repetitions the subject performs flexion-extention in a desired range and impedance level. We trained the

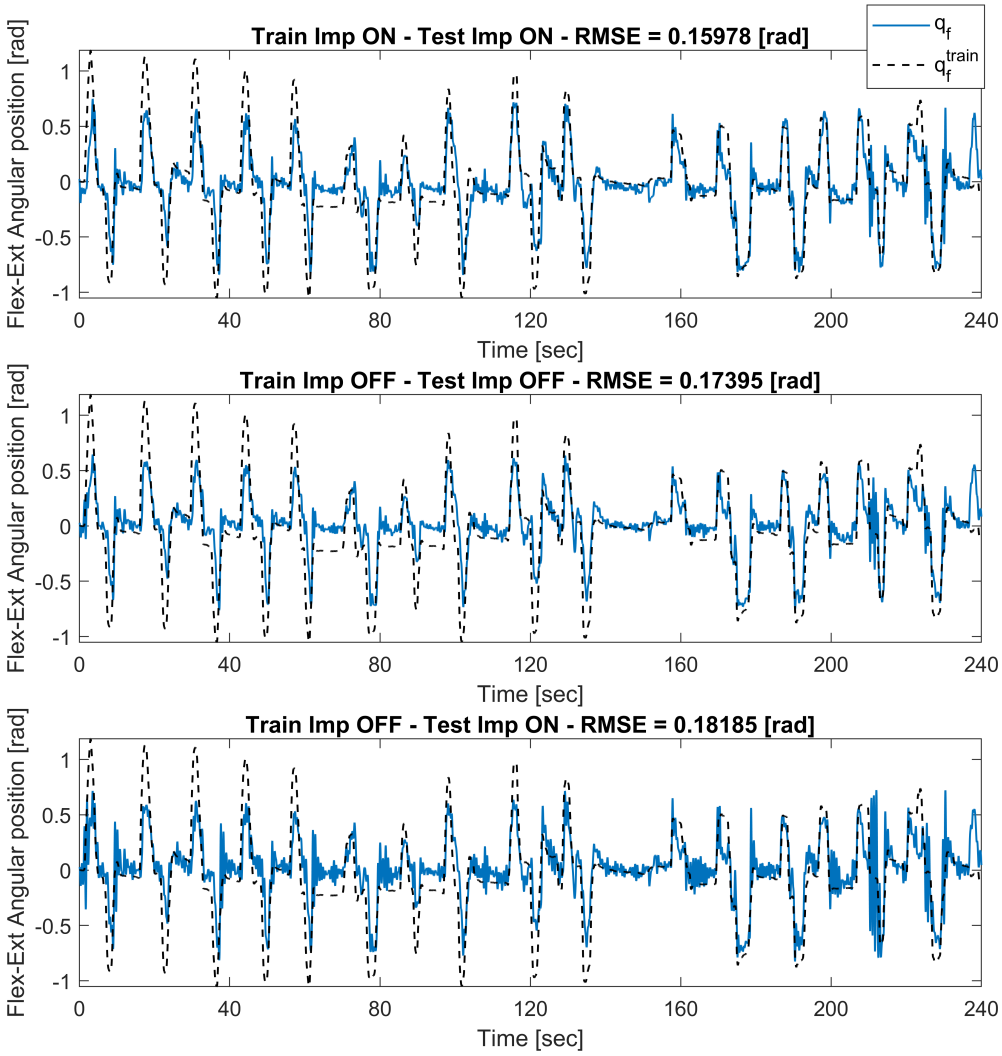

Figure 4.10: Preliminary results to discuss framework design choice. Trajectory tracking during offline evaluation of the framework. The black dotted line is the ground truth position of the wrist flexion-extension. The blue line is the predicted trajectory under the following conditions: (top) framework optimization and evaluation included the impedance controller: q_f; (center) framework training and testing did not include the impedance controller: q_r; and (bottom) the optimization framework did not include the impedance controller, but the evaluation framework included the impedance controller: q_f.

MTUs on the collected data using q_f or q_r. When q_r is used as optimization signal the impedance controller and the "robot plant" are not included in the optimization framework. The estimated MTUs parameters' values are used to then test the offline training error when

the framework included the impedance controller and the robot plant. In summary, three different cases are shown in the figure:

- the framework is the one presented in Figure 4.1, and it *included* the impedance controller and the robot plant. The framework architecture during training and evaluation of the trained framework on the training data is the same, therefore the RMSE values between q_f and q_f^{train} are the same during training and evaluation.
- the framework *did not include* the impedance controller and the robot plant in the training, as well as in the evaluation phase. In this case, the RMSE error is computed between q_r and q_f^{train}. The training and evaluation errors are the same.
- The framework *did not include* the impedance controller and the robot plant in the training phase. The RMSE in the training phase is computed between q_r and q_f^{train}. Then, the impedance controller and the "robot plant" are included in the framework used for the evaluation. The new RMSE is computed between q_f and q_f^{train}.

The offline flexion-extension prediction, reported in the third plot of Figure 4.10, shows that the stiffness K and damping D estimated from the MTUs cannot be used directly as gains in the impedance controller. In fact, this leads to oscillatory behaviour and instabilities of the robot's plant, as it can be observed by comparing the predicted joint trajectories in the three cases. This explains why in related works the stiffness estimated from the MTUs had to be tuned to be used in the control law of the impedance controller implemented on the robot. This solution allows stable control but does not support the key requirement of implementing the MTUs' dynamics on the robot.

Chapter 5

Experimental design

This chapter details the methodology needed to evaluate the proposed framework and compare its performance to a baseline method. We designed two experimental protocols. The first (Section 5.3.1) describes the protocol for the acquisition of myographic and kinematic data relevant to wrist flexion-extension. The collected data are neeed to train the proposed framework and the baseline. The second experimental protocol (Section 5.3.2) defines an online control experiment where the subject is given real-time control of the (simulated) robot plant and has to perform reaching tasks in the free space and in the presence of unexpected perturbations that require adaptation of impedance to stabilize the interaction with the environment and successfully complete the task. We investigate the controllability provided by the proposed framework and compare it to that of the baseline. We thus aim to answer the following research questions introduced in Chapter 1:

- *Does the proposed framework provide the subject with increased controllability due to the possibility to adapt the stiffness and the damping of the robotic system?*

In Chapter 3 we have discussed the related work in prosthesis control and summarised key characteristics of the most relevant related studies in Table3.1. There is however a lack of consistency in the experimental evaluation of methods during online control. Specifically, studies that perform an online evaluation, design highly controlled experiments that limit the modulation of muscle co-activation, which would be the primary cause of performance deterioration. Methods that enable simultaneous control of the position and stiffness of one or two DoFs, if evaluated online, often do not design experiments that require adaptation of impedance for the successful execution of the task [92, 202, 74]. Moreover, either the execution time and the success rate are often the only performance measures used to analyse the results [92, 74], or only qualitative results or exemplary results are provided ([202, 110, 6]). This limits the evaluation of the overall task performance and does not provide insight into

the influence of stiffness adaptation on the execution of the entire task.

In Section 5.1, we describe the composition of participants who took part in the experiments (Section 5.1.1), the experimental set-up (Section 5.1.2), and the baseline used to compare the performance of the proposed framework (Section 5.1.3). In Section 5.2, we list the hypotheses being evaluated regarding the online performance on the proposed framework and the baseline. The experimental design and protocols of the *offline tracking experiment* and the *online target reaching experiment* are detailed in Section 5.3. The optimization method used to train the muscle-tendon units of the proposed framework and the baseline is described in Section 5.4. Finally, the evaluation methods to assess the online control performance of the framework and the baseline are discussed in Section 5.5. This includes the description of performance measures for the evaluation of the task outcome (Section 5.5.1) and for the evaluation of the impact of stiffness and damping modulation on the entire task execution (Section 5.5.2); a survey to collect the user's personal feedback on the perceived controllability provided by the methods (Section 5.5.3); the term controllability and its use in this thesis is clarified. The experimental results of the offline and online experiments are discussed in the next chapter.

5.1 Participant selection and experimental setup

5.1.1 Human participants

Eight able-bodied, right-handed volunteers without neuromuscular disorders (five females, three males, age: 27.87 ± 3.64) and a transradial amputee (female, age: 65), took part in our study approved by the University of Birmingham and the Imperial College London Research Ethics Committees. All participants read and signed informed consent before participating in the experiments and did not have prior experience in myocontrol. The following information were collected about the amputee. Her condition (neurofibromatosis) led to the amputation below the elbow of the left, not dominant, arm in 2016. The participant stated that because of the amputation and disease she feels the remaining muscles of the forearm are constantly tight and tense. This might make it harder for her to perceive differences in muscles' co-activation.

The relatively small number of participants is due to the difficulty in finding participants willing to make the desired time commitment, and due to the recruiting challenges imposed by the COVID-19 pandemic. Moreover, we did not have the means to recruit amputee, since our laboratory (Computer Science, University of Birmingham) could not facilitate the correct conditions to recruit amputees and run experiments with this target population. The case

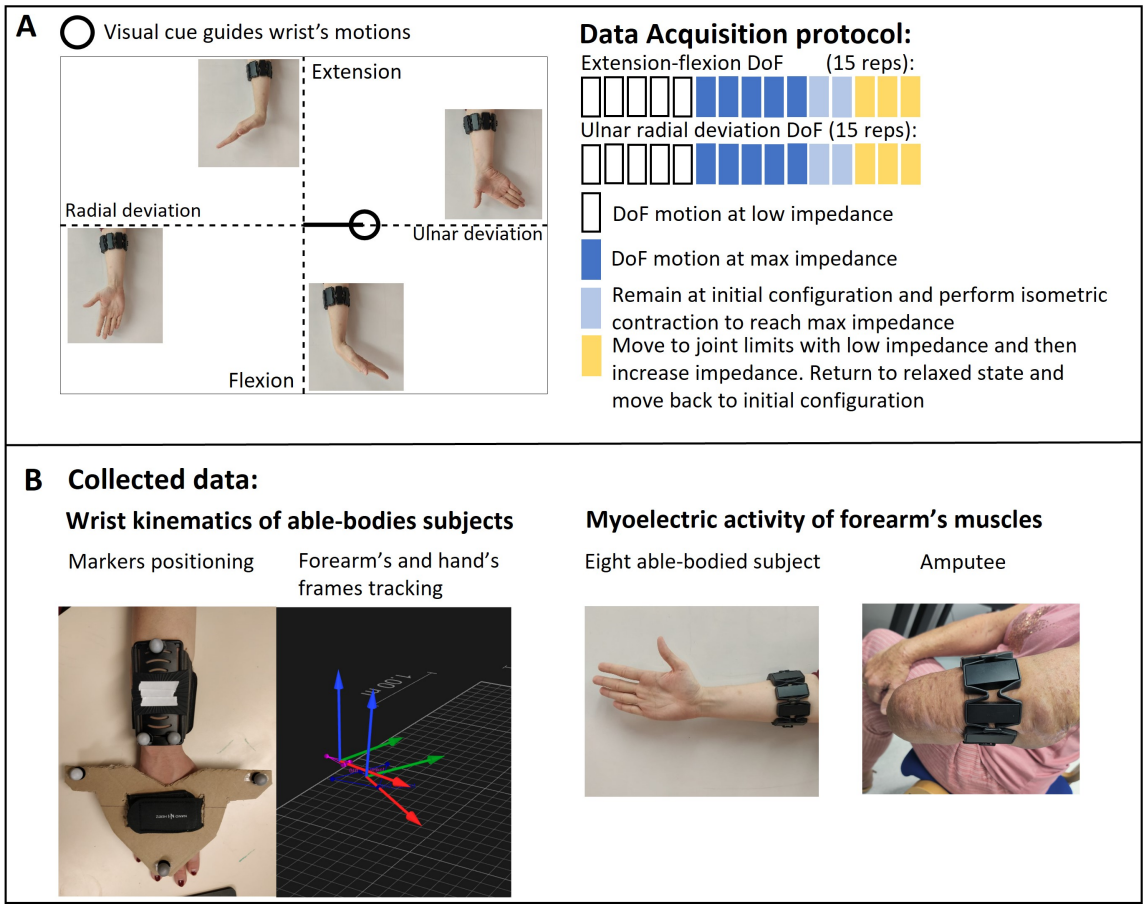

Figure 5.1: A) Data acquisition: subject's wrist motions are guided by a visual cue (black circle), and the data acquisition protocol. B) Experimental setup for data collection of myoelectric and kinematics data. The wrist position of able-bodied subjects is tracked using two reference frames, defined by three retroreflective markers on the forearm and on the hand, respectively. The wrist position is computed given the position of the hand frame with respect to the forearm one. The frames are firstly aligned, then the angle between the two red arrows defines the flexion-extension wrist angle. Positive angles imply that the subject is performing wrist extension.

study with an amputee included in this work was made possible thanks to the support of the Bioengineering Laboratory of Imperial College London. In addition to the time commitment for the experiments, travelling constraints did not allow us to run experiments with more amputees.

For these reasons, we conducted experiments mainly with able-bodied volunteers and a case study with a transradial amputee. While the results for a single amputee do not allow us to draw any conclusion on how the framework might perform for the transradial amputee target population, it provides initial promising results on the possibility of transferring the framework's methods and acquired knowledge from able-bodied subjects to amputees.

Overall, the composition of participants is in line with relevant work found in the literature (e.g., [74, 202]), discussed in Section 3.2.3. While [29] and [157] evaluated their framework with a single amputee and no able-bodied subjects, [92], [110], [157] did not test with any amputees.

5.1.2 Experimental setup

During the experiments, each participant sat in front of a screen, with their arm along the side of the body in a neutral resting position. The screen displays a Cartesian space with axes representing the angular position of two DoFs at the wrist, ulnar-radial deviation and flexion-extension, as shown in Figure 5.1-A. The participants wore a Myoband (eight sEMG sensors, working frequency of 200 Hz, details in Section 2.3.2) to record the forearm's muscle activations $\mathbf{E}(t)$ as they performed wrist motions guided by the visual cues moving along the axes of the Cartesian space. The myoband was positioned approximately 5 cm below the elbow joint, as shown in Figure 5.1-B) and as detailed in Section 4.2.1. The myoband positioning, guided by palpation and visual inspection the sEMG signals, aimed to maximise the activity recorded from the Flexor Carpi Radialis and the Extensor Carpi Ulnaris, and minimize the crosstalk from adjacent muscles. The same procedure was followed for able-bodied subjects and for the amputee. However, for the amputee, an anatomical correspondence of these muscles could not be expected due to the amputation. In this case, the Myoband was positioned to identify the two most active areas of the forearm's muscles when the subject contracted the muscles while thinking about performing wrist flexion-extension.

The wrist position of able-bodied subjects was tracked with a Qualisys motion capture system [174], as shown in Figure 5.1-B, using two sets of 3 retroreflective markers on the participants' forearm and hand. The Qualsys API was used to define 2 reference frames representing the forearm's and the hand's position in the space, respectively. The hand frame is translated so that its origin matches the forearm's frame origine. The rotation required

to align the axes of hand frame to those of the forearm frame allowed to compute the wrist flexion-extension $\mathbf{q}_f^{train}$. The raw sEMG signals are filtered as described in Section 2.3.2. All experiments were run on a computer with an Intel i7-8809G, 3.10GHz CPU and a Radeon RX Vega M GH graphic card.

5.1.3 Baseline

The baseline framework was built on a data-driven regression method developed in [109]. Specifically, in the study, an artificial neural network (NN) was used to learn a mapping from sEMG signals to the reference kinematics. The newtwork is a two-layer perceptron with 3 hidden neurons. The implementation of the method was available to us, avoiding bias from implementation. The same training data was used to train our framework and the baseline. The latter was trained to match the performance reported in the reference paper [109]. In order to ensure accurate motion tracking and robustness to perturbation occurring during online control, a high-stiffness PD controller was then used to track the joint position q_r predicted by the NN. This controller had constant high stiffness ($K_B = 100$ [N/rad]) and damping computed assuming a critically damped system ($D_B = \sqrt{K_B/4}$ [Ns/rad]) [116]. For the baseline, q_f was the output position when tracking q_r with K_B and D_B. The choice of a purely data-driven baseline was motivated by the fact that existing methods that include MTUs do not directly use the stiffness (or damping) predicted by the muscle-tendon models; the joint stiffness is instead tuned for stable position tracking during a separate calibration phase, which is, in principle, equivalent to the use of a high-stiffness position controller in cascade to the NN.

5.2 Hypotheses

We experimentally evaluated the following hypotheses regarding the *online control performance* of the proposed framework (M) which includes muscle-tendon models and the baseline (B):

(H1) M achieves comparable or higher performance than B in the absence of a perturbation field, and outperforms B when the user has to interact with perturbations.

(H2) Regulation of joint stiffness and damping is an effective strategy to adapt to perturbations.

(H3) The user's perceived controllability is higher with M than with B, especially when the user has to interact with external perturbations.

The first hypothesis H1 refers to the first contribution of this thesis (Section 1.2) and evaluates the overall performance provided by the control methods with respect to the task outcome. Hypotheses H2 concerns the analysis of modulation variable stiffness and damping during the task execution. Hypothesis H3 refers to both contributions. Note that the data acquisition experiment aims to collect data needed to train the methods being evaluated. The offline tracking performance is not evaluated as a hypothesis, but it is a requirement to then proceed with the online testing of the control methods and evaluation of the hypotheses. Our choice of focusing on the evaluation of the online control of the methods is motivated in Section 6.1.1.

5.3 Experimental protocol

For each participant, experiments were conducted in three sessions. In the first session, we collected sEMG signals and kinematic data relevant to wrist motion to train our framework M and the baseline B. The other two sessions involve the online testing of M and B on separate days to avoid muscle fatigue and involuntary bias due to the order in which frameworks were evaluated. In fact, suppose the user performs the tasks with M. At the end of the experiment the user might have learned how to better execute the task or might have muscle fatigue. If B is tested immediately after the results might be biased due to the aforementioned reasons.

5.3.1 Data collection

In this section, we detail the experimental protocol for acquisition of data to train the proposed framework and the baseline. The experimental setup is that described in Section 5.1.2. As shown in Figure 5.1-A, the subject viewed on the screen a Cartesian space with axes corresponding to wrist joint positions (in *Degrees*) of ulnar-radial deviation and flexion-extension. The upper and lower limits for flexion-extension and ulnar-radial deviation were set to anatomically feasible ranges, [-80,80] and [-40,40], respectively. For a single trial for each DoF, a visual cue (black circle) moved along the axis from the origin to the DoF's upper limit, and then to the lower limit, to finally return to the origin of the axes. The subject was instructed to move their wrist to proportionally match the cue's position (i.e., as the cue moves along the flexion axis the subject has to proportionally flex the wrist). A single trial was run for each DoF to ensure the subject moved the wrist correctly. The subject is requested to perform 15 repetitions of flexion-extension and 15 repetitions of ulnar-radial deviation while modulating the impedance properties of their wrists as illustrated in Figure 5.1-A. For each DoF, the first 5 repetitions are performed at low impedance (in Figure 5.1-A repetitions color coded in white), meaning that the subject keeps the muscles as relaxed as possible;

repetitions 5–10 are executed at maximum impedance (Figure 5.1-A, blue); repetitions 11 and 12 involve isometric contractions (Figure 5.1-A, pale blue), which means the subject started with the wrist in the rest position, gradually increased the muscle co-contraction as the visual cue moves from the origin, then released the co-contraction as the visual cue returned to the origin. Finally, in the last three repetitions, the subject moves the wrist in a chosen range, and increases and releases the impedance before changing the direction of motion (Figure 5.1-A, yellow).

Notice that even when we activate a single DoF (e.g., ulnar-radial deviation), there is some unintentional motion along the other DoF (i.e., flexion-extension). For this reason, although we focus on controlling a single DoF (flexion-extension), we asked the subject (during data collection) to perform repetitions of ulnar-radial deviation so that we could observe the indirect flexion-extension motion and use this small amplitude motion in the training and testing data.

During the experiment, data from 15 trials of each type of motion were collected (i.e., 30 trials total) for all the able-bodied subjects. The data gathered included sEMG signals and wrist kinematic data (i.e., flexion-extension $\mathbf{q}_f^{train}$). The experimental protocol was modified as follows for the amputee: firstly, the amputee was not asked to perform ulnar-radial deviations given how difficult it was for the participant to generate other two independent muscle activations that could be used as control signals; secondly, $\mathbf{q}_f^{train}$ was the trajectory of the visual cue the participant has to follow during the training experiment as done in previous studies [109]. The lack of data regarding ulnar-radial deviation, despite providing less information compared to the able-bodied subjects, did not substantially affect the training and subsequent online testing of the methods since the latter is focused on flexion-extension only. The experiment takes less than 15 minutes. While the number and type (i.e., level of impedance) of repetitions are defined to avoid muscle tiredness, and the subject was encouraged to take breaks as needed to avoid muscle fatigue. Details on the optimization method to train the proposed framework and the baseline are provided in Section 5.3.1.

5.3.2 Online reaching task experiment

This experiment had the two following objectives which guided the experimental design:

- Investigate the controllability provided by M and B when the subject performs a task that requires impedance modulation of the robot's joint;

- Investigate if the proposed framework provides higher controllability than the baseline, due to the possibility to adapt the robot's joint stiffness and damping.

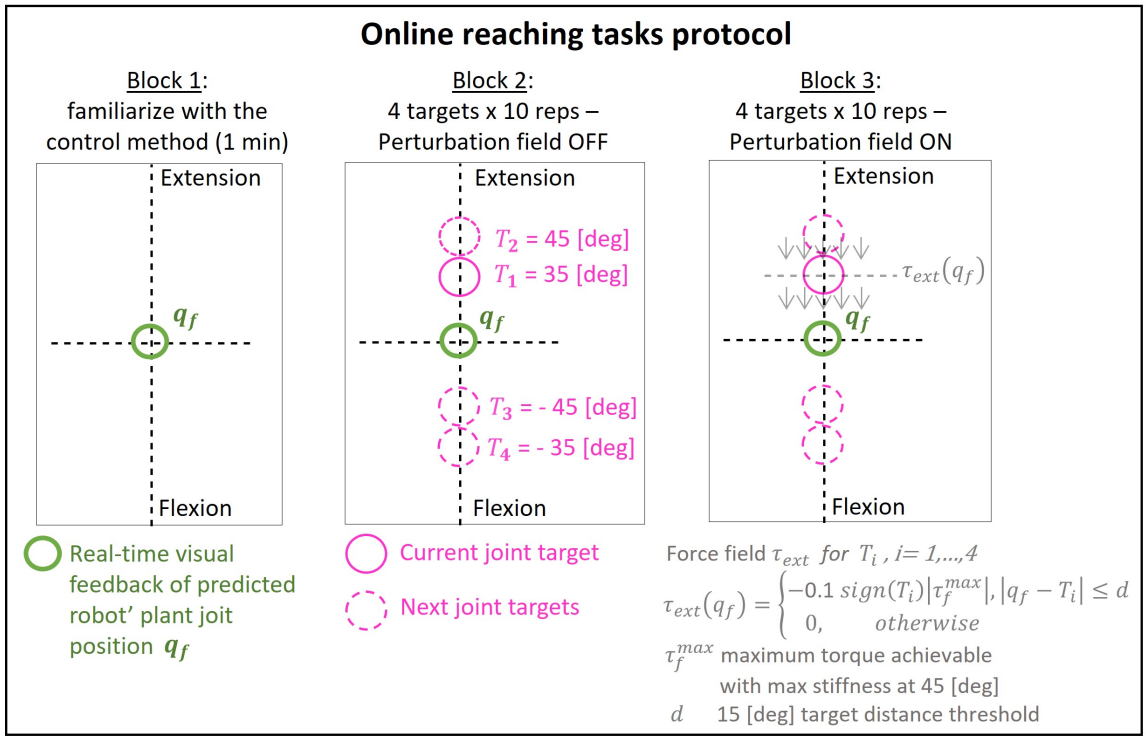

Figure 5.2: Reaching task experimental protocol. In block 1 the subject has visual feedback about the robot plant's joint position q_f (green circle); in block 2 the subject has to reach a target T_i (pink circle), hence move the green circle in the pink target and maintain the position for 3 seconds; in block 3 the reaching task is performed in the presence of a uniform repellent force field τ_{ext}.

The term *controllability* and its definition within this work is discussed in Section 5.5.3. In this work, controllability is quantified through the performance measures described in Section 5.5, which evaluate different aspects of the online control performance. In each trial of online testing, a participant had visual feedback of their predicted wrist position q_f represented on the Cartesian space as a green circle (Figure 5.2) and could voluntarily control the circle by performing wrist flexion-extension. The task required the subject to control the green circle to reach a target position T_i (purple circle) as accurately and quickly as possible. Once at the target, the subject had to maintain the position for three seconds. Every time the subject entered the target circle but could not maintain the position (i.e., the green circle intersected the target circle) the 3-second dwelling time is reset. The radius of the circle representing q_f and the target T_i were eight and six density-independent pixels respectively, requiring precise control. The experimental trials for each subject were divided into three blocks illustrated in Figure 5.2:

- *Block 1:* familiarisation with the control interface and mapping of muscles contraction to corresponding displacements of the cursor; notice that no targets and external perturbations are included in this phase.
- *Block 2:* reaching tasks in the free space (4 targets x 10 reps);
- *Block 3:* reaching tasks in the presence of a perturbation field τ_{ext} that pushed q_f away from the target (4 targets x 10 reps);

At the beginning of each session, the subject was told that different motor control strategies could be explored (e.g., relaxed movement or changing muscle co-activation), but the subject had no prior knowledge of the method (M or B) being tested. The subject was told that some force would perturb q_f, but no information about the force field such as the type, magnitude, and location, was provided. The force field was activated when the distance from the centres of the cursor q_f and the target T_i was within 15 [deg] (variable d in Figure 5.2). The magnitude of the force field was defined as a percentage of the maximum torque τ_f^{max} generated by the subject during training for M by considering the maximum stiffness generated at 45 [deg]; its average, across all participants, was $\approx 20Nm$. Below, we discuss specific aspects of the experimental design.

User interface for experiments

The implementation of the interface provided to the user builds on the software developed in the Bioengineering Laboratory of Imperial College London. The two-dimensional representation of the wrist position has been extensively tested by the group and extensively used

in literature (e.g., previously for the baseline in [109]), proving to provide intuitive visual feedback to the user. However, considering that the visual feedback about the predicted wrist position substantially differs from the three-dimensional control and visual feedback of the biological wrist, we gave the subjects time to familiarise themselves with the controller and with the mapping from the biological wrist action space to the two-dimensional space of the interface. In this way, we attempt to minimize factors that could affect the task execution in initial trials to allow a fair comparison of the controllers' performances. Notice block one takes approximately 1 minute and has the aim of letting the subject familiarise with the interface and controllers, not with the tasks of reaching the targets.

Visual feedback

While we provide visual feedback on the real-time position of the robot's joint, visual feedback on the stiffness was considered during the design of the experiment and of the interface presented to the user. This could have been done by designing the cursor as an ellipse with axis length along the flexion-extension direction function of the normalised user stiffness. However, the variable shape of the cursors would have interfered with the task requirements (i.e., match the target circle and maintain the position). We did not investigate another way of providing visual feedback on impedance, but we designed a task (i.e., reaching target positions in the presence of perturbations with constraints on posture maintenance and motion precision) where the subject could benefit from impedance adaptation to achieve better performance. Impedance adaptation is therefore task-driven, implicit in the user control strategy, and the practical effectiveness of modulating impedance depends on the control method being used. Moreover, joint stiffness and damping are interdependent and affected by the joint position, and history of muscles' activation. This makes the design of stiffness and damping targets difficult and possibly infeasible for the subject.

Magnitude of force field

The magnitude of the perturbation had to be high enough to perturb q_f so that the subject could visually perceive a mismatch between q_f and their motor intent. However, due to the number of repetitions, the magnitude of the perturbation was kept relatively low to avoid excessive muscle co-contraction and tiredness. While the baseline does not enable explicit modulation of stiffness and damping, specific consideration have to be made regarding the design of the force field magnitude in relation to the maximum torque, stiffness and damping enabled by the proposed framework. When controlling the robot with the proposed framework, the impact of an external perturbation on the robot's plant depends on the muscle-

tendon model (trained specifically for each subject) and on the subject's level of muscles' co-activation (i.e., the impedance of the robot's plant). To allow comparison of performance across subjects, the perturbation magnitude needs to be subject-specific and was determined as a percentage of the maximum torque τ_f^{max}, obtained considering the maximum stiffness (i.e., maximum co-contraction) that could be generated by the subject during the training phase at 45 [deg]. The contribution of damping was not considered because of its high dependence on joint velocity which could lead to an overestimation of τ_f^{max}. The impact of different force field magnitudes (i.e., percentages of τ_f^{max}) was investigated in preliminary experiments, concluding that 10% of the computed maximum torque (i) was adequate to provide visual feedback perceived by the subject as perturbation of q_f and to trigger the need of increasing the activation of muscles to counter the force field; (ii) did not generate excessive muscle tiredness; (iii) was suitable for the baseline, in relation to the proportional and derivative gains of the high-stiffness PD controller.

5.4 Offline training method

For each subject, we trained M and B using the data acquired in the training phase. For the amputee, the reference trajectory of the wrist flexion-extension q_f^{train} needed to train M and B was the trajectory of the visual cue in the training phase, that guided the participant's muscles contractions. Moreover, the data of each trial were visually inspected to make sure the sEMGs and the trajectory were coherent, and the subject did not execute unintentionally the wrong motion. The kinematic data were aligned to the sEMG data by to maximize the correlation between the normalised trajectory and the normalised difference between the sEMG signals corresponding to flexion-extension. This proved to be robust since the peaks in the joint kinematic trajectory matched the peaks in the sEMG signals. A 60-40 split of the collected data (EMG signals and corresponding wrist reference kinematics) was used for training and validating the muscle models, with optimization based on Simulated Annealing (500 iterations, 5000 function evaluations, initial value of temperature 300, annealing interval 50) [204] since the cost function has discontinuous derivatives. A summary of the working principle of Simulated annealing is provided in Appendix A. The baseline was trained using the same training and testing dataset.

Next, we describe the performance measures used to evaluate the results of the online experiment.

5.5 Online tasks evaluation method

The evaluation of the online testing experiment provided by M and B is analysed in three steps. First, we discuss the performance measures by which we evaluate the task outcome for M and B; we then analyse the task execution and the time evolution of the robot's state q_f for both M and B. Finally, we ask the participants to complete a survey on the perceived controllability provided by M and B, considering the performance of the methods in the absence and presence of external perturbations. The one-tailed Mann–Whitney U test [142] was used to measure the statistical significance (p-values < 0.05) of the difference in performance provided by M and B. The analysis is performed across able-bodied participants, and across the trials performed by the amputee. A comparative discussion between the amputee and able-bodied performance is provided in the next chapter.

5.5.1 Task outcome performance measures

The design of the reaching target tasks during online control is common in the literature and is based on Fitt's study [67] on human motor performance. Fitt's study, based on Shannon work's in Communication Theory [193], demonstrated that any motor task conveys a finite amount of information limited by the capacity of the system to perform the task rapidly and accurately. These measures have been extensively used to assess prostheses' control performance for purely data-driven methods [212]. In this thesis, we selected six performance measures to evaluate the performance of the reaching task for four targets $T_i = (T_{ix}, T_{iy})$ expressed in ulnar-radial and flexion-extension coordinate:

- *Success Rate* (SR) [%]: proportion of successful trials, with a trial considered successful if the subject reached the target within 30 seconds and held the position for three seconds;

- *Time to Reach* (TR) [sec]: time to complete the trial, with 30 seconds as the maximum allowed completion time;

- *Throughput* (TP) = $\frac{ID}{TR}$) [bit/sec]: TP measures the ability to deliver information during TR through the control method being evaluated, considering the task difficulty. It is computed based on Fitt's extension of Shannon's law, as the ratio between the index of difficulty (ID) and TR, where $ID = \log_2(\frac{A}{W} + 1)$ [bit] takes into account the difficulty associated with targets of specific radius and distance from the origin. To obtain the ID for each target, considering the matrix of the targets **Targets** = $[T_1, ..., T_4]^T$, **A** is a vector containing the sum of the absolute values of the normalised coordinate of the

targets, $\mathbf{A} = \left|\frac{\mathbf{Targets}_{:,1}}{\max(\mathbf{Targets}_{:,1})}\right| + \left|\frac{\mathbf{Targets}_{:,2}}{\max(\mathbf{Targets}_{:,2})}\right|$. W is the radius (8 density-independent pixels) normalised by the largest target angle found in **Targets**. The larger ID, the larger the difficulty associated with the task. The value of TP ranges from $-\infty$ (if CT is ∞) to $+\infty$ (if CT is zero). In this experiment, as shown in Figure 5.2 the targets are along the flexion-extension axis, and the targets closer to the origin have an equal index of difficulty, which is lower with respect to the ID of the two targets at 45 and -45 [deg], respectively.

- *Path Efficiency* (PE = $100 * \frac{optimal\,path}{actual\,path}$) [%]: the ratio between the length of the optimal path to the target (i.e., Euclidean distance) and the length of the trajectory executed by the subject in Cartesian coordinates. This measure does not depend on the path length.

- *Energy (E) [J]*: the power used by the system for rotational motion during the time interval $t_f - t_i$. It is defined as $E = \int_{t_i}^{t_f} \tau_f(t)\dot{q}_f \, \mathrm{d}t$, the time integral over the trial duration $(t_f - t_i)$; this measure is affected by the values of the controller gains. In particular, since B has high fixed gains it is expected to observe higher values of energy for B with respect to M.

- *Near Miss* (NM) [#]: number of times the subject entered the target circle but did not maintain the position for three seconds, intersecting the target circle with the green circle of q_f. The measure is indicative of the subject's ability to accurately control the cursor.

All these measures are affected by the distance to the target, which may impact the difficulty of the task. The performance measures are thus weighted by the index of difficulty (ID) to allow comparison across reaching tasks with different targets.

5.5.2 Task execution measures

The performance measures discussed above provide an indirect evaluation of the impact of joint stiffness and damping modulation. Especially during reaching tasks performed in the presence of the perturbations, the time taken to smooth out the oscillations imposed by the perturbation and reach the target affects the performance measures. Since stiffness and damping modulation can be used by the subject as an effective strategy to shorten this stabilization time, impedance modulation has an impact on the values of the performance measures. To provide insight into the impact of impedance modulation in relation to the execution of the entire task, we expand the performance evaluation by considering the other two following measures:

Movement smoothness

Impedance adaptation of the limb and incremental learning of the task allow humans to learn how to perform a task more smoothly [14]. The smoothness of a motion is defined by considering the presence of sudden acceleration and deceleration which intuitively affect the continuity of the movement. Smoothness can thus be used to analyse the subject learning when using a new controller. We computed the *smoothness* of q_f using the SPectral ARC length (SPARC) measure [14]. Among the measures of smoothness proposed in literature to evaluate smoothness SPARC is chosen since it is independent of the duration and amplitude of the movement. SPARC formulation is based on the concept that a smoother movement is composed of a lower amount of high-frequency components. Based on the assumption that the Fourier spectrum of a smooth time domain signal tends to be smooth, SPARC uses the Fourier magnitude spectrum of the speed profile to quantify the smoothness of a time domain trajectory. Further details on the SPARC measure are provided in Appendix B.2. The measure ranges from $-\infty$ to zero. The closer the value to zero the smoother the trajectory being evaluated. A higher value is obtained if the subject successfully counters the external perturbations.

Mutual information

Mutual information (MI) quantifies the amount of information that a random variable contains about another random variable (see Appendix B.1). This concept can also be interpreted as the reduction in the amount of uncertainty about a random variable, given by the information provided by another random variable. MI value varies from zero to infinity, and it is equal to zero if and only if the two variables are strictly independent. MI has been successfully applied to dynamic systems analysis to quantify the predictability (i.e., reduction in uncertainty) of an object's dynamics given its motion (e.g. [15]). In this thesis we consider the mutual information between τ_f and q_r to quantify the predictability of q_r given τ_f; Since q_r is the unperturbed reference trajectory and τ_f is the torque that results in q_f, we expect MI to increase when q_r matches q_f (i.e., when the subject quickly counters the perturbation). Additionally, we computed the conditional MI (See Appendix B.1) between q_r and q_f given K and D respectively, to provide insights into the contribution of stiffness and damping to the reduction in position error $q_r - q_f$ provided by the controller. In this thesis, the computation of the MI is based on the non-parametric method detailed in [225].

5.5.3 Definition of the term *controllability* within this work

In control system theory, the term controllability refers to the ability to move a system from any given state to any desired state. There are various definitions of conditions for controllability depending on the dynamic system being evaluated. Moreover, any proof of controllability is highly dependent on the hardware being used and assessment of controllability is particularly important when deploying a control method on the hardware. Therefore, in this thesis, the term controllability differs from the meaning seen in classical control theory. Rather, we define controllability as the overall online control performance, quantified using the performance measures defined in Section 5.5.1 and Section 5.5.2.

5.5.4 Survey of user's perception of controllability

The controllability provided by a control method determines the subject's perception of the effectiveness, intuitiveness and robustness of the method being evaluated. We, therefore, decided to explore the user's *perceived controllability* provided by M and B to determine if the proposed method allows the subject to counter perturbation in a more intuitive and natural way and if the subject considered modulation of impedance co-contraction as a strategy to accomplish the task. The participants were asked to answer the following six questions about M and B at the end of each experimental session:

1. *Q1)* How is the match between your motor intent and the cursor motion?
2. *Q2)* Did the system execute your motion command in a timely way?
3. *Q3)* Was the control precise? Did the cursor oscillate around the desired position?
4. *Q4)* Can you describe the force field?
5. *Q5)* What was your strategy to counter perturbations?
6. *Q6)* Did impedance modulation (muscle co-contraction) help to counter perturbations?

Users had to choose from one of three options (mostly good, good with some instances of low controllability, and poor) for the first three questions; the other questions allowed free-form answers.

Chapter 6

Experimental results

In this chapter, we discuss key results of the offline training and testing of the proposed method (M) and the baseline (B). We then discuss in detail the results of the online control experiments based on the experimental evaluation described in the previous chapter. All participants (eight able-bodied subjects and the transradial amputee, Section 5.1.1) completed the data acquisition experiment and subsequently took part in the online reaching task experiment. Finally, all subjects completed the survey investigating their feedback on the online control performance provided by M and B. The data acquisition and online testing of the methods took about two hours, spread over two days, for each able-bodied person; ≈ 30 minutes for initial preparation and data collection, and ≈ 90 minutes for online testing with our framework and the baseline. This process took ≈ 6 hours for the amputee because multiple mental and physical factors make it harder for them to learn to express intent. The time commitment requirement, the availability of amputees, and the COVID-19 pandemic strongly influenced the size and composition of the study group.

The offline tracking results are presented in Section 6.1. We discuss quantitative results of the offline evaluation of M and B across able-bodied subjects and for the amputee. Additionally, we present an example of offline evaluation of M and B, and we provide a comparative discussion on the tracking performance achieved by the two methods. Finally, we discuss studies in literature that reported discrepancies between the offline and online control performance of methods for prosthesis control. We thus justify our focus on the online evaluation of the methods. The online control results are described in Section 6.2. We present quantitative results in support of the hypotheses listed in Section 5.2 using the performance measures described in the previous chapter to evaluate the outcome of the reaching tasks as well as the entire task execution. We provide an in-depth discussion on the control strategies used by the subjects and investigated whether impedance adaptation contributed to the observed control performance. Finally, in Section 6.3, we describe exemplary data from

trials performed by an able-bodied participant and by the amputee, providing insight into the entire task execution.

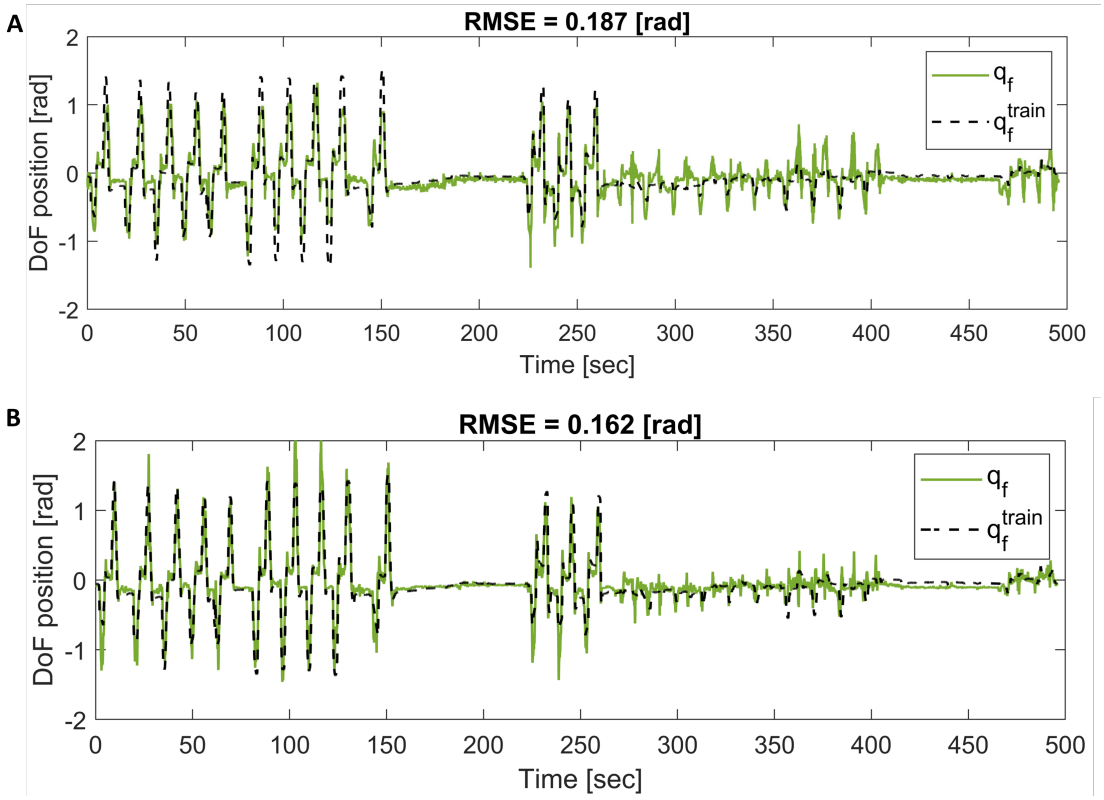

Figure 6.1: A) Trajectory tracking during offline evaluation of the proposed framework. B) Trajectory tracking during offline evaluation of the baseline. The black dotted line is the ground truth position (q_f^{train}) of the flexion-extension DoF. The joint position trajectory (q_f) is obtained in each plot by evaluating the corresponding framework on the entire dataset.

6.1 Offline tracking experimental results

The proposed framework and the baseline are trained as explained in Section 5.3.1. Recall that the proposed framework includes a pair of muscle-tendon models to actuate a single DoF. Only two sEMG signals are used and input to the framework. The baseline, on the other hand, uses a neural network to directly map the eight sEMG signals recorded by the Myoband to the desired joint trajectory. The estimated joint trajectory is then tracked by a fixed gains high-stiffness controller. For able-bodied subjects, the average values of the estimated muscle-tendon models' parameters are reported in Table C.1, and those for the amputee are reported in Table C.2 of Appendix C. Moreover, in the same appendix we provide an example

of the force-length-velocity relationship for the elements of a trained muscle-tendon model. Considering the able-bodied subjects' results, the average root mean square error (RMSE) between the predicted and reference joint position for M and B obtained during offline testing is $RMSE_M = 0.2291 \pm 0.0457$ and $RMSE_B = 0.1763 \pm 0.0435$, respectively. The baseline achieved higher prediction accuracy than the proposed framework. In Figure 6.1, we provide an example of trajectory tracking results for an able-bodied subject. For completeness, the trained framework and baseline are evaluated on the entire dataset, with the results shown in Figure 6.1-A and Figure 6.1-B, respectively. In these figures, the black dotted line represents the ground truth trajectory of flexion-extension DoF, while the green line is the flexion-extension trajectory predicted by the methods. We observe that the baseline achieves a lower tracking error (RMSE), but it overestimates the repetitions performed at high impedance, e.g., between 80-150 secs. This may due to the nature of the algorithm, which does not explicitly learn the joint impedance and may provide a less accurate prediction of kinematics in repetitions where the subject substantially modulate the muscle co-activation. The lower magnitude repetitions of joint flexion-extension predicted after the time instant t = 275 [ms], correspond to the indirect flexion-extension motions occurring when the participant performs ulnar and radial deviations. Due to the kinematic and dynamic coupling between the DoF of the wrist (Section 2.5.1), we observe some indirect activation of the flexion-extension DoF during this time interval because flexion-extension and ulnar-radial deviation cannot be completely decoupled. These indirect flexion-extension motions are overestimated by the proposed framework, potentially because M trains muscle models driven by specific sEMG activations, whereas B jointly considers all eight sEMG signals as inputs. In Section 4.2.1 we discussed the implication of choosing sEMG signals recorded by specific sEMG channels and justify our choice. We discuss in the next chapter possible limitations related to this choice. However, it can be observed that B provides a more noisy estimate than M; the baseline substantially overestimates the position trajectory in certain repetitions where the subject performs wrist motion at higher impedance (e.g., $t = [90 - 125]$).

For the amputee, the tracking errors are $RMSE_M = 0.4014$ and $RMSE_M = 0.5817$, respectively. The substantially higher RMSE values compared to the one obtained for the amputees is mainly due to the impossibility of recording the biological wrist traject and the use of an engineered trajectory. As discussed in the previous chapter, the reference flexion-extension position for the amputee is the trajectory of the visual cue displayed on the screen to guide the subject's muscles' contractions during the data acquisition section. As a result, the muscle activity of the subject is not always accurately synchronised to the reference trajectory, making the training of the models harder. To mitigate this problem the peaks of the reference trajectory were aligned at best to the signal obtained as the difference

between the sEMG signals of Ch_1 and Ch_2. More details on the offline evaluation for the amputee are reported in Appendix C for the interested reader. Below, we explain why this thesis focuses on the online control evaluation, and why the offline tracking results may not be good indicators of the online control performance of the evaluated methods.

6.1.1 Trade-off between offline tracking accuracy and online controllability

The online control task of reaching a target is goal-driven and belongs to the *activity domain* [91]. Therefore, the evaluation methods used to analyse the data collected during this experiment, discussed in detail in Section 5.5, include performance measures which evaluate the task's outcome and also the overall controllability provided to the subject. Controllability is prioritised over prediction accuracy (i.e., the total error between the predicted joint position q_f and human biological wrist flexion-extension). This is motivated by experimental results showing that high offline prediction accuracy does not necessarily imply high controllability during online control and execution of goal-oriented tasks [160, 109]. In [109], the online performance of three purely data-driven methods (i.e., linear regression, non-negative matrix factorization and neural network. The latter is the baseline considered in this work) with substantially different offline prediction accuracy proved to be similar during online testing. We think the discrepancy between offline and online performance might be due to the following reasons. Firstly, the sEMG data collected to train the models do not contain features typical of online control when the subjects continuously interact with the prosthesis and the environment and adapt their muscles' contraction based on visual feedback of the prosthesis' state. In fact, during data collection experiments the subject is asked to perform motions at a constant speed, while during online control the subject has visual feedback of the state of the prosthesis and continuously modifies the muscle contraction to achieve the task. As a result, the training data sets do not contain the fast-changing features of sEMG signals typical of online adaptation and thus lack of sufficient information to properly train the control methods. This problem affects all categories of methods, including process-driven ones. Secondly, purely data-driven methods learn a direct mapping from sEMG signals to kinematics and might therefore fail to distinguish between the changes in muscles' activation associated with the joint motion, and those contributing to joint impedance adaptation. This second reason is not considered in the referenced study, since the conducted experiments do not involve modulation of muscle contraction to regulate the limb impedance. From the result presented in [160, 109], it is therefore difficult to understand whether an experimental

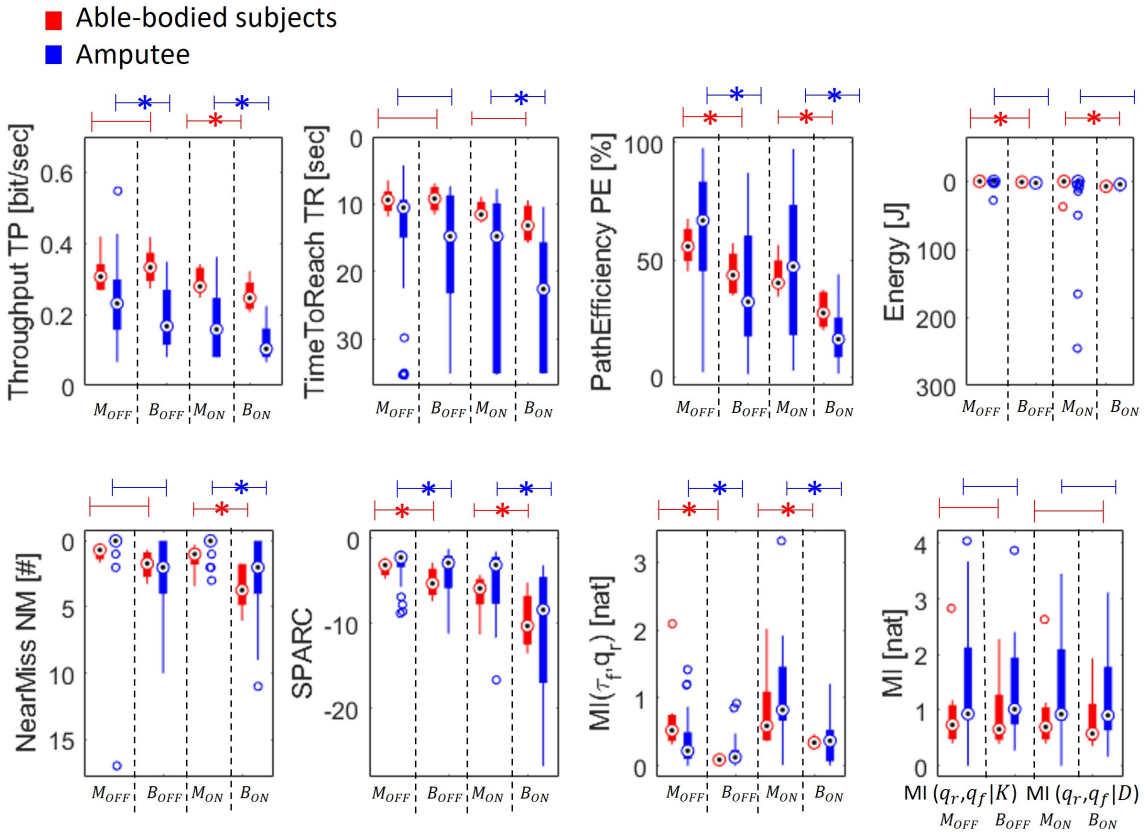

[h!]

Figure 6.2: Values of performance measures for the able-bodied subjects (red) and the amputee (blue) for the proposed framework (M) and the baseline (B) in the presence (M_{ON}, B_{ON}) and absence (M_{OFF}, B_{OFF}) of perturbations. Each red group contains the average performance of the eight subjects (averaged over 40 trials); each blue group contains the 40 trials for the amputee. A statistically significant improvement of the median, computed between M_{OFF}-B_{OFF} and M_{ON}-B_{ON}, is highlighted with an asterisk.

protocol that includes repetition of motions at different level of muscles' activation, would reduce the discrepancy between offline tracking accuracy and online control performance.

However, in this thesis, due to the aforementioned reasons, the online control performance is prioritised over the offline prediction accuracy. Moreover, our data acquisition protocol includes a variety of flexion-extension motions performed at different speeds, and at different levels of muscle co-activation to attempt to include fast-changing sEMG features typically observed during online control.

6.2 Online control experimental results

Below, we describe key results of the experimental evaluation of the online control experiments described in the previous chapter. We discuss the results of able-bodied participants and of the amputee separately, due to the difference in the number of participants from the two target populations. This section is concluded with a comparative analysis of the results obtained for the able-bodied participants and the amputee.

6.2.1 Able-bodied participants

Figure 6.2 includes the results in support of our hypotheses on the online control performance provided by M and B (Section 5.2). The average performance across the eight able-bodied participants is shown in red for the proposed framework (Figure 6.2, M_{OFF} M_{ON}) and for the baseline (Figure 6.2, B_{OFF} B_{ON}). For each performance measure, each box plot represents the distributions of the average across-trials values of the performance measure for the eight participants (i.e., distribution defined by eight points). The performance of each subject is therefore averaged over the 40 trials for that participant to avoid bias or dependence between individual trials of a participant. In Figure 6.2, instances of M providing a statistically significant improvement over B are shown with a red asterisk at the top of the plot for the corresponding measure.

Results in support of hypothesis H1

Firstly, we test if our findings support *H1*. Unlike B, M consistently enabled successful task completion with or without perturbation: the success rate SR was 95% and 82.19% for M and B (respectively) without perturbation, and 93.75% and 76.87% with perturbation. Considering the values of performance measures reported in Figure 6.2, while M and B provided comparable values for the time to reach the target TR and the throughput TP in the absence of perturbations, M provides a significant improvement in TP when reaching tasks are performed in the presence of perturbations. Additionally, M provides a significantly higher path efficiency (PE) than B with and without perturbations; these results are in accordance with the much lower number of near misses (NM) of M than B with or without perturbations. Even the energy (E) used by M is significantly lower than that used by B, with or without perturbations, as hypothesised. B was expected to provide higher values for E since the baseline uses a fix-gains high stiffness controller, while the proposed framework allows to modulated the controller gains according to the human intended joint stiffness and damping. However, it should be considered that the high stiffness controller should support a

more consistent rejection of the imposed perturbations, while the response of the proposed framework to perturbation depends on the estimates of the subject joint impedance, which may be low if the perturbation is not expected. Overall, *these results support H1 and show that M outperforms B in terms of task outcome when the subject performed reaching tasks in free space and in the presence of external perturbations*.

Results in support of hypothesis H2

Below, we test if our findings support *H2*. We evaluated whether online modulation of joint stiffness and damping, compared to the fixed gains of the baseline, could be used as a strategy to improve the task execution in terms of smoothness of the motion and to counter the perturbations imposed by the force field. The value of SPARC reported in Figure 6.2 was significantly better with M than with B, with or without perturbations. This implies that participants were better able to smooth out the oscillations imposed by perturbations when using M. Notice that the smoothness decreased (as expected) for both M and B when perturbations were included since the force field affects the robot's plant state used to compute the SPARC measure. One explanation for the variance in SPARC when using M (with perturbations) is that the perturbation initially had an impact if the subject was operating with low impedance, but the subject then appropriately adjusted the gains. When using B, on the other hand, gains remained at a fixed high value, which enabled the rejection of perturbations and accurate tracking. However, for the baseline, the high-stiffness PD controller also attempted to track inaccurate estimates of the intended joint position provided by the regression algorithm of the baseline (see Section6.3 for exemplary results of this issue).

We further investigate the contribution of the joint stiffness and damping to the torque τ_f and observed that M provided a significantly higher MI between τ_f and q_r compared with B, with or without perturbation. These results, especially those obtained in the presence of external perturbation, may imply that the subjects were able to use modulation of joint stiffness and damping to smooth the oscillations imposed by the force field and stabilise the system to achieve the task. There was no significant difference in MI(q_r, q_f,K) and MI(q_r, q_f,D) with or without perturbations. This result may be due to different factors affecting the validity of the measures. While we expected to observe a correlation between the reduction in the discrepancy between q_f and q_r, it may not be possible to correlate changes in trajectory discrepancy and individual changes in stiffness and damping, as the relative contribution of stiffness and damping may vary from trial to trial and according to the subject's strategy. As discussed later considering the results from the collection of the participant's feedback, different strategies were used by the subjects, including increasing

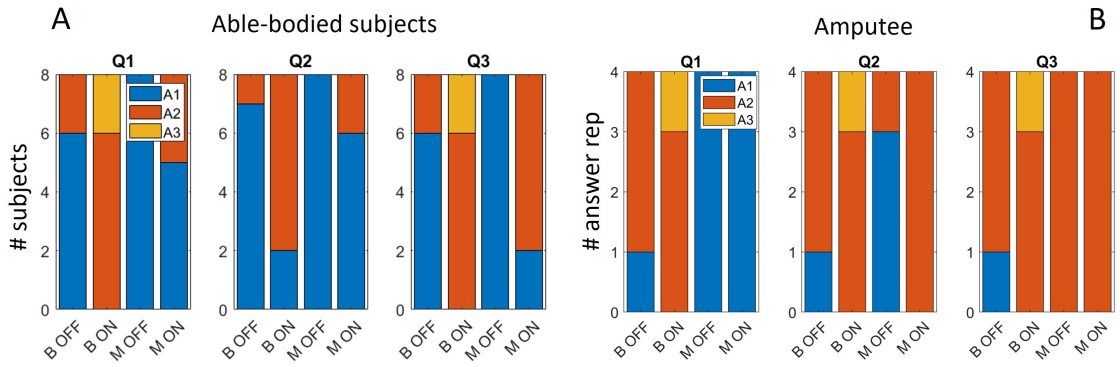

[ht]

Figure 6.3: A) Able-bodied volunteers' responses to Q1–3 of the questionnaire, completed at the end of the session with or without external perturbations. Possible answers were A1 (good), A2 (good, but some instances for lower performance), and A3 (poor, with many instances of poor performance). Each category shows the fraction of subjects who provided a certain answer. B) Amputee's responses to Q1-Q3; the participant was requested to answer questions after every 10 trials, i.e., four times per session.

the wrist impedance as the perturbation displaced the (simulated) robot plant or maintaining high impedance since the beginning of the trial to reduce the impact of the perturbations. Moreover, since participants did not have prior knowledge of M or B, some outliers could have been due to the subject taking some time to determine how to successfully reach the target. Overall, these results strongly support *H1* and *H2*.

Results in support of hypothesis H3

Finally, we investigated the perceived controllability of M and B (*H3*) among able-bodied subjects to determine if M is rated higher than B in terms of perceived controllability. Answers to questions Q1–3 of the survey, detailed in Section 5.5.4, are summarized in Figure 6.3-A. The subjects could provide three answers (A1–3) to indicate whether the methods completely satisfied some aspects of the control, or there were instances of low controllability or the methods provided low controllability. Subjects indicated that M provided a better match between motor intent and cursor motion (Q1), resulting in more timely execution (Q2) of motor commands, and more precise control (Q3) than B; results were more pronounced with perturbations, where two subjects reported that B provided low controllability.

To further investigate the subject's perception of controllability provided by the methods, we asked the participants to describe the characteristics of the perturbations based on the interactions observed during the experimental trials (Q4). Interestingly, the subjects had more correct and consistent perception and description of the force field when using M. Six out of eight subjects (proportion) gave a correct description of the perturbation field when

using M while two subjects were unsure and did not know how to describe the force field; with B, five out of eight subjects could not correctly describe the location of the force field and the others were unsure. More detailed answers are provided below. According to Subject 1, the perturbation field had a higher magnitude when using B, and it required more effort to complete the task. Subject 2 said the perturbation field was located on the positive axis (extension) when using B, while the subject stated that a repellent perturbation field was localised around the target when testing with M. Subject 3 is not sure how to describe the force field when using B, while when using M the subject states that there might be a force pulling towards the origin when approaching the target. Subject 5 felt the force field was stronger around the target, and in general weaker around the targets further away when using B. The magnitude and direction of motion felt randomised. When using M, the subject stated that the force field was localised around the target, it seemed almost uniform and pulling away from the target. Subjects 4–7 stated that there was a repellent force field in both cases. Subject 8 is not sure on how to describe the force field, in both cases, when using M and B the subject states it might be a parabolic force field around the target. From these answers, we conclude that M provides the user with a better way of discriminating the undesired effects related to the action of the perturbation and those due to inherent limitations of the methods.

For Q5, all the subjects had the same control strategy with B: maintain low muscle co-contraction and move the wrist until the joint limit is reached. Notice that this strategy avoids higher muscle co-activation. With M, two subjects did not significantly increase muscle co-contraction, but the other six adapted joint impedance to counter perturbations. Among the six subjects, 5 said they would reach the target and then increase the muscles' co-contraction to maintain the position, and one subject increased the co-contraction from the start of the trial to immediately reject perturbations. These different strategies are likely to affect the values of some of the performance measures.

For Q6, all subjects agreed impedance modulation did not improve performance with B; two subjects stated that it resulted in the worst perceived controllability and the cursor would suddenly jump to a different joint position. With M, on the other hand, six out of eight subjects indicated that impedance adaptation helped counter perturbations; two subjects were unsure. These results support *H3* and correspond to the quantitative results described above (for *H1* and *H2*).

6.2.2 Amputee participant

The distribution of the performance measures over the 40 trials per session, in the presence and absence of perurbations, is reported in Figure 6.2-A in blue, next to the distribution of performance across able-bodied subjects. While the two target populations are different

in size, we provide a comparative discussion considering the amputee's performance with respect to that of the able-bodied subjects. For the amputee, we observed that M provided a higher proportion of successful trials than B, with or without perturbation: 87.50% and 65% for M and B without perturbations, and 80% and 55% with perturbations. While there was an overall decrease in throughput (TP) for the amputee compared with the able-bodied subjects, M provided a significantly higher TP compared with B, with or without perturbations. Also, while there was no significant difference in the time to reach the target (TR) for the able-bodied participants, for the amputee M provided a significantly shorter TR than B with perturbations. M also provided a significantly higher path efficiency (PE) than B, with or without perturbations. Notably, PE was comparable to or higher than with able-bodied participants. We observed no significant difference in Energy between M and B, whereas NM was significantly higher with B than with M in the presence of perturbations. These observations support *H1*. In the context of *H2*, we observed that SPARC and MI between τ_f and q_r were significantly better with M than with B, with or without perturbation. There was no significant difference in MI(q_r, q_f,K) and MI(q_r, q_f,D) for M compared with B, with or without perturbations, as observed for the able-bodied participants. Overall, these results support *H1* and *H2*.

Finally, Figure 6.2-C summarizes the amputee's responses to questions Q1–3 of the survey (Section 5.5.4). We asked the subject to answer questions four times per session (i.e., after every 10 targets) in an attempt to obtain more reliable answers considering that the participant had to take longer breaks. Similar to the responses from able-bodied participants, the amputee indicated that M provided better controllability than B, and correctly described the force field (Q4) with M. The participant stated that the flexion motion felt more difficult than the extension motion, especially when reaching the targets further away. For Q5, the amputee's control strategy when using B changed from tensing up the muscles to trying to minimally co-activate the muscles "or the cursor would jump too far" (see next section and Figure 6.10); this was an example of the baseline incorrectly assigning an increase in activation to a change in position. When using M, the amputee focused on co-contracting the muscles of the forearm when needed. For Q6, the subject was unsure if impedance modulation by muscle co-activation improved the performance with B since the cursor would sometimes oscillate unexpectedly. However, when using M, the amputee indicated three times out of four that stiffening the muscles helped counter the perturbations, and mentioned that it only once led to some overshoot. Overall, these results support *H3* and match the results reported for *H1* and *H2*. This personal feedback is particularly interesting considering the subject's condition, and her statement regarding the difficulties in perceiving the level of contraction of her muscle.

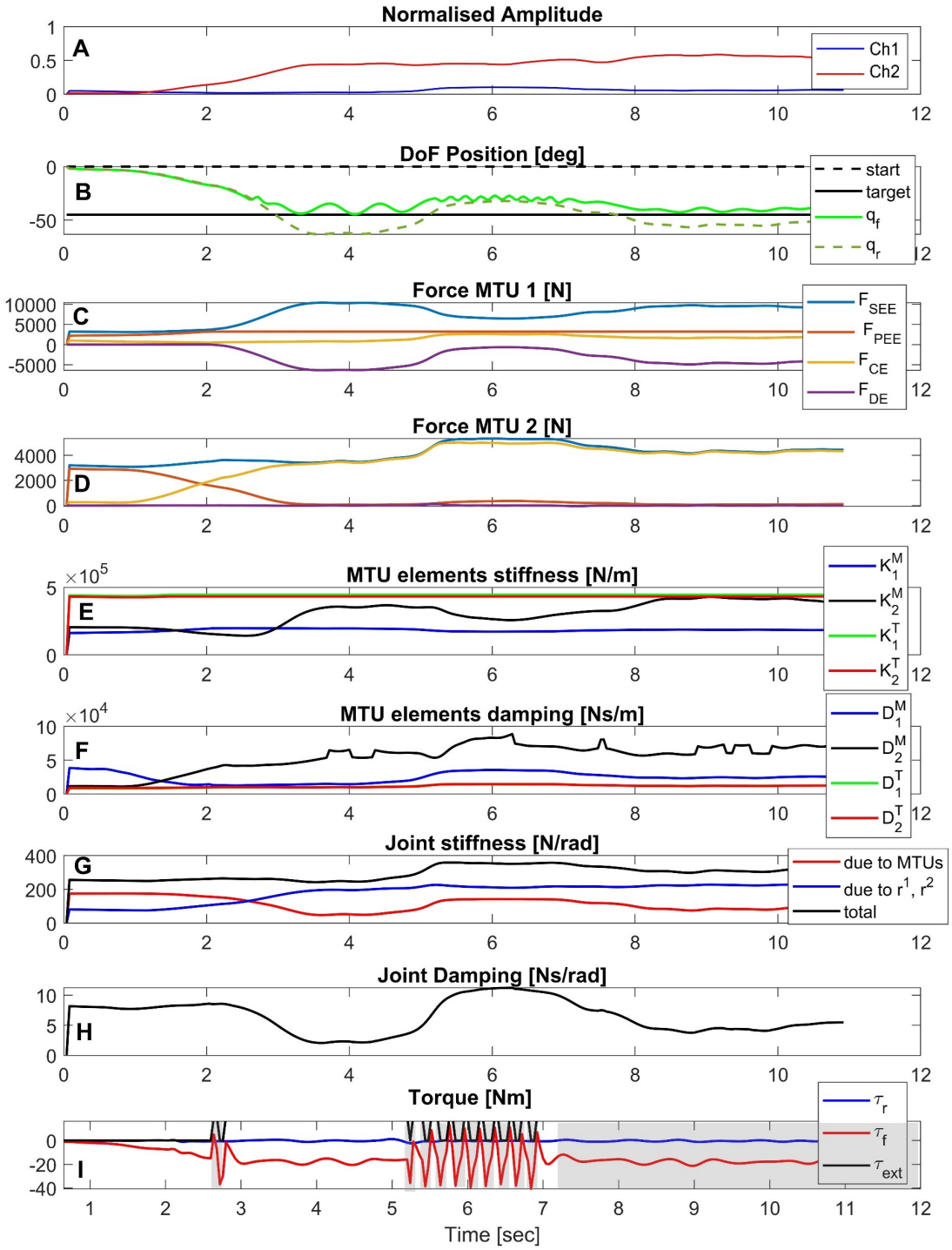

Figure 6.4: Proposed framework. Example of a successful trial. We plot the time evolution of the most relevant MTU variables and controller/robot variables while an able-bodied subject performs a reaching task in the presence of a perturbation field. The system stabilises in less than two seconds.

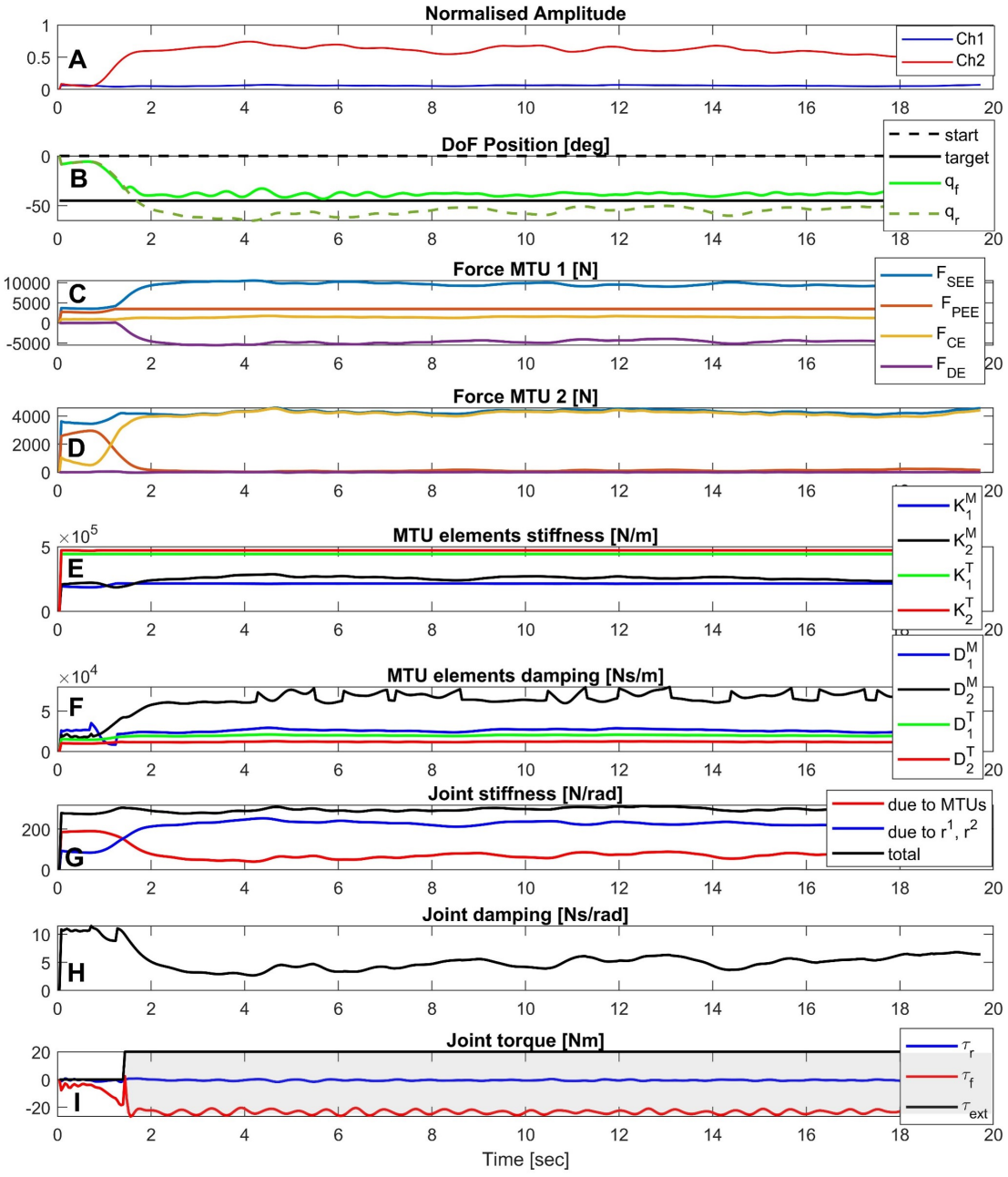

Figure 6.5: Proposed framework. Example of failed trial. We plot the time evolution of the most relevant MTU variables and controller/robot variables while an able-bodied subject performs a reaching task in the presence of a perturbation field.

6.3 Time evolution of controllers' state variables during online trials

In this section, we provide insight into the entire execution of the online reaching task. We consider exemplary trials from an able-bodied subject and the amputee, and we show the time evolution of key state variables of the evaluated methods. An example of successful (Figure 6.4) and failed (Figure 6.5) trial is reported for an able-bodied participant when using the proposed framework. Two examples of successful trials (Figure 6.7, Figure 6.8) and one of a filed trial (Figure 6.6) are reported for the same able-bodied subject using the baseline. We then show an example of successful trial for the amputee when using M (Figure 6.9) and when using B (Figure 6.10).

6.3.1 Able-bodied participant

Firstly, we describe trials performed with the proposed framework and then trials obtained with the baseline.

Proposed framework

We show two illustrative examples of reaching tasks executed by an able-bodied subject in the presence of a perturbation field. In the first example in Figure 6.4, the subject successfully reached the target, whereas in the second example in Figure 6.5 the subject failed to reach the target. In each of these two figures, we plot:

A normalised input to the MTUs (ch_1, ch_2) representative of the activity of the flexor and extensor muscles.

B joint position q_r (dotted green line) output by forward dynamics and q_f (continuous green line) output by the impedance controller, as the subject attempts to move q_f from the initial position (black dotted line) to the target position (continuous black line).

C forces generated by the elements of MTU_1.

D forces generated by the elements of MTU_2.

E stiffness of $muscle_1$ (K_1^M) and $muscle_2$ (K_2^M), and the stiffness of $tendon_1$ (K_1^T) and $tendon_2$ (K_2^T).

F damping of $muscle_1$ (K_1^M) and $muscle_2$ (K_2^M), and the damping of $tendon_1$ (K_1^T) and $tendon_2$ (K_2^T).

G stiffness of the MTUs in the joint space (black signal), where the red signal is the stiffness contribution of the contraction dynamics of MTUs, and the blue signal is the stiffness contribution of the moment arms as a function of $q_r(t)$.

H the damping of the MTUs in the joint space.

I the torque command provided by the impedance controller τ_f and the perturbation torque τ_{ext} due to the force field.

In the first example, the subject receives visual feedback on the effect of the perturbation and modifies their muscle activation in an attempt to negate the effect of the perturbation; the increase in co-activation in Figure 6.4-A between 5-8 seconds corresponds to an increase in joint stiffness K_2^M and damping D_2^M—see Figure 6.4-G, H. In Figure 6.4-B, we observe a discrepancy between q_r, unaffected by the perturbation field, and q_f, the output of the position-based impedance controller that "tracks" q_r using the joint stiffness and damping based on the estimates provided by the MTUs. The error between the two trajectories decreases when the subject modulates the wrist impedance.

The time intervals during which the subject experiences the perturbation field are shaded grey in Figure 6.4-I, i.e., τ_{ext} is not equal to zero. Figure 6.4-D shows the forces generated by the elements of MTU_2, the muscle-tendon unit corresponding to flexion, i.e., contracting the muscle. We observe that the force generated by the active element and by the elastic component of the tendon, F_{CE} and F_{SEE} respectively, are mainly active. In the second example, on the other hand, only muscle-tendon unit MTU_2 is activated. We thus hypothesise that the *low co-activation has an impact on task performance and the ability to counter the perturbation*, as the subject cannot generate the necessary torque to move through the perturbation field.

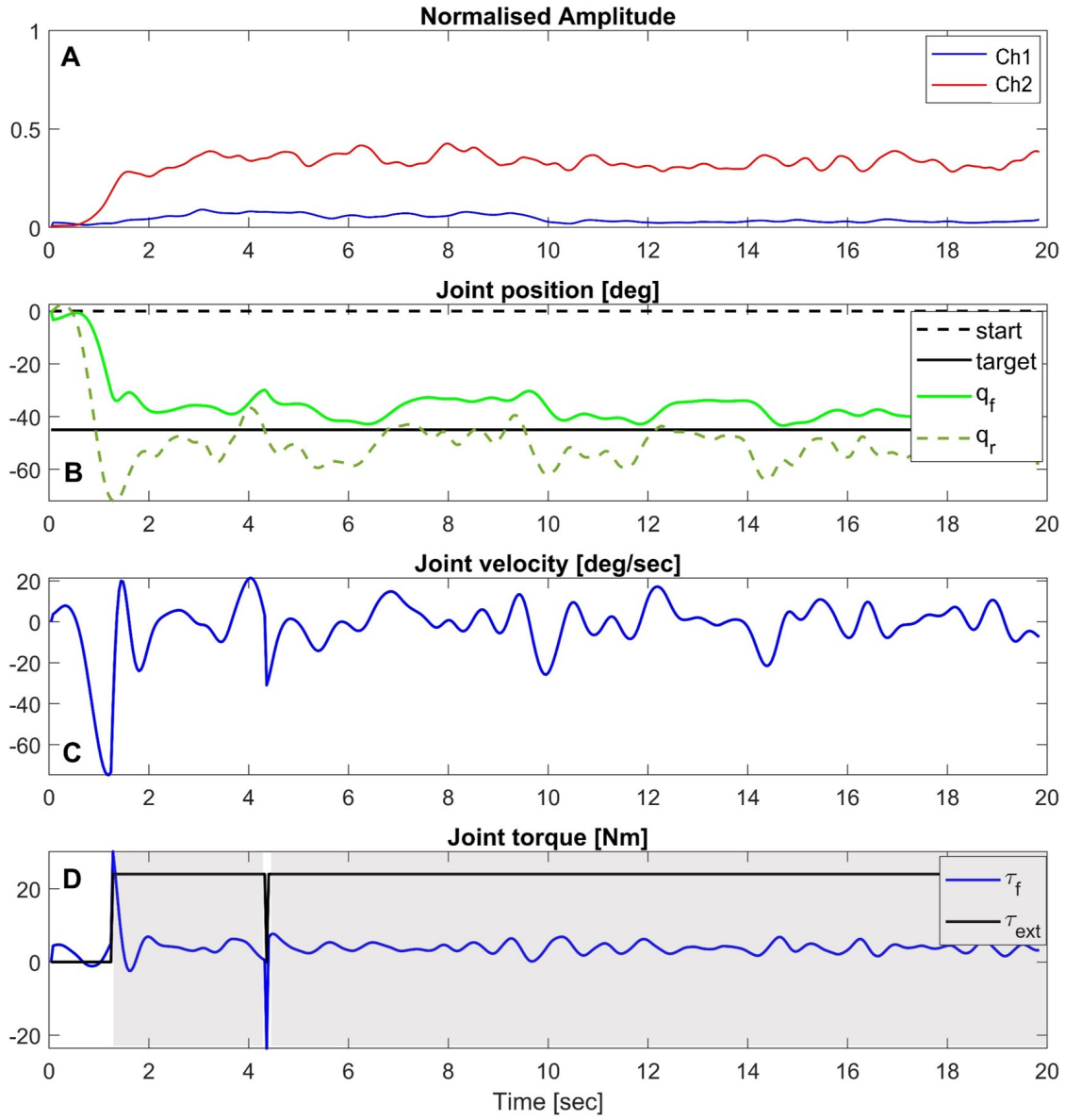

Figure 6.6: Baseline. Example of a failed trial. Here, we plot the time evolution of the controller/robot variables, while the subject performs a reaching task in the presence of a perturbation field. The subject fails to stabilize the system and go through the force field.

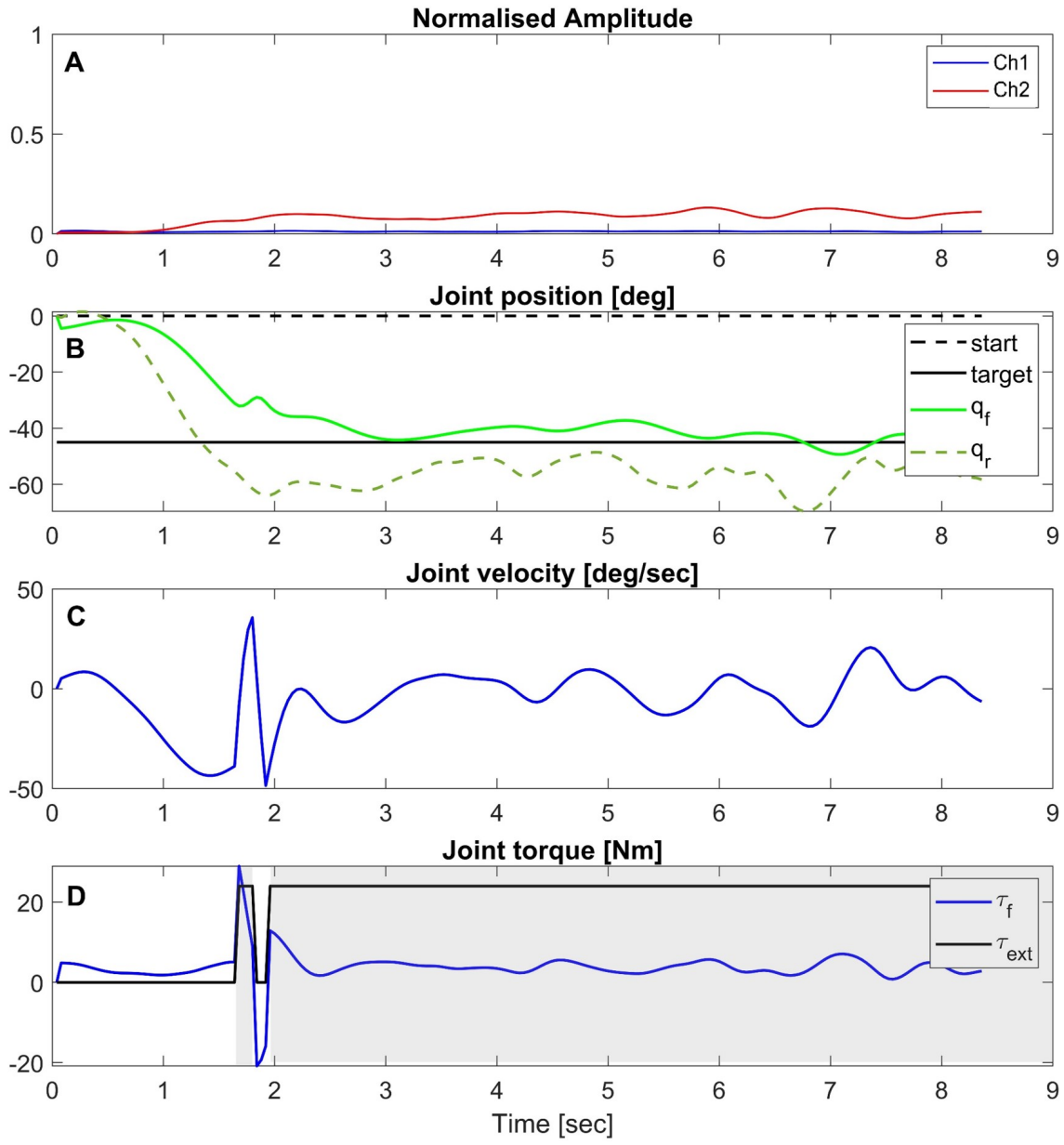

Figure 6.7: Baseline. Example of a successful trial. Time evolution of the controller/robot variables while the subject performs a reaching task in the presence of a perturbation field using baseline. Example of successful trial where the subject is able to counter the perturbation field.

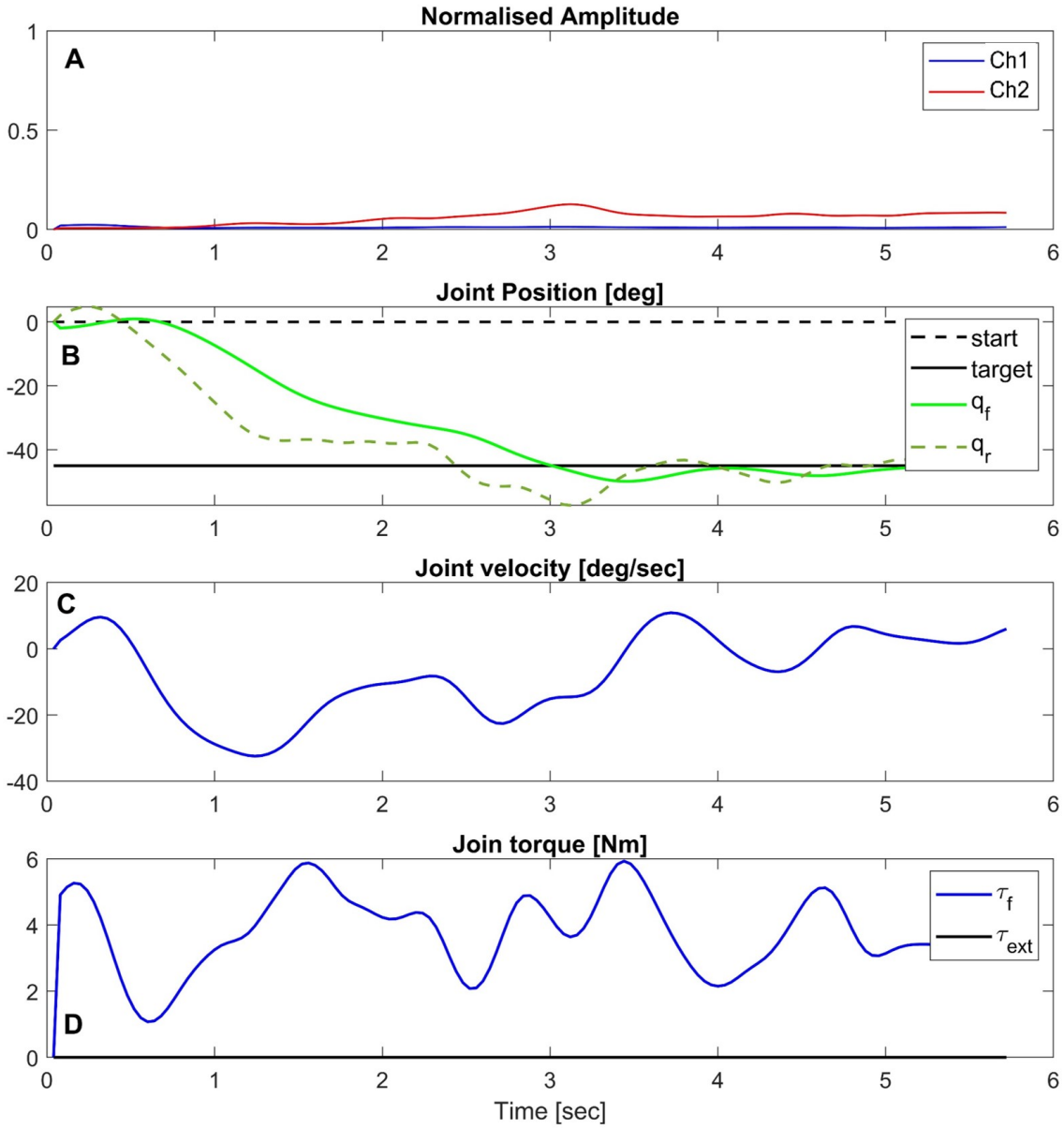

Figure 6.8: Baseline. Example of a successful trial. Time evolution of the controller/robot variables while the subject performs a reaching task in the absence of a perturbation field using baseline.

Baseline

We show plots corresponding to three illustrative examples of reaching tasks with the baseline framework: (i) Figure 6.6 shows a failed trial with perturbation; (ii) Figure 6.7 shows a successful trial in which the subject counters the effect of the perturbation field; and (iii) Figure 6.8 summarizes a successful trial in the absence of perturbations. In each figure, we plot the following signals:

A normalised sEMG channels (ch_1, ch_2) that represent the activity of the flexor and extensor muscles. Recall that the baseline considers all eight sEMG signals from the myoband as input.

B joint position q_r (dotted green line) output by the neural network, q_f; (continuous green line) output by the PD controller when tracking q_r, as the subject attempts to move q_f from the initial position (black dotted line) to the target position (continuous black line).

C joint velocity.

D torque output of PD controller (τ_f) and the perturbation torque due to the force field (τ_{ext}).

We observe that although the magnitude of ch_2 in Figure 6.6-A is approximately five times the magnitude of ch_2 in Figure 6.7-A, the reference joint position q_r output by the neural network estimator is (on average) very similar. The difference is in the smoothness of the estimated trajectory; it is less smooth in Figure 6.6-B, potentially due to the higher co-activation of the muscles. This may be the reason why the first trial resulted in a failure whereas the second one was successful. This experimental result, and our (potential) explanation of how co-contraction of muscles results in successful trials, reflect the feedback provided by the human subjects regarding their strategy to counter perturbations when using B.

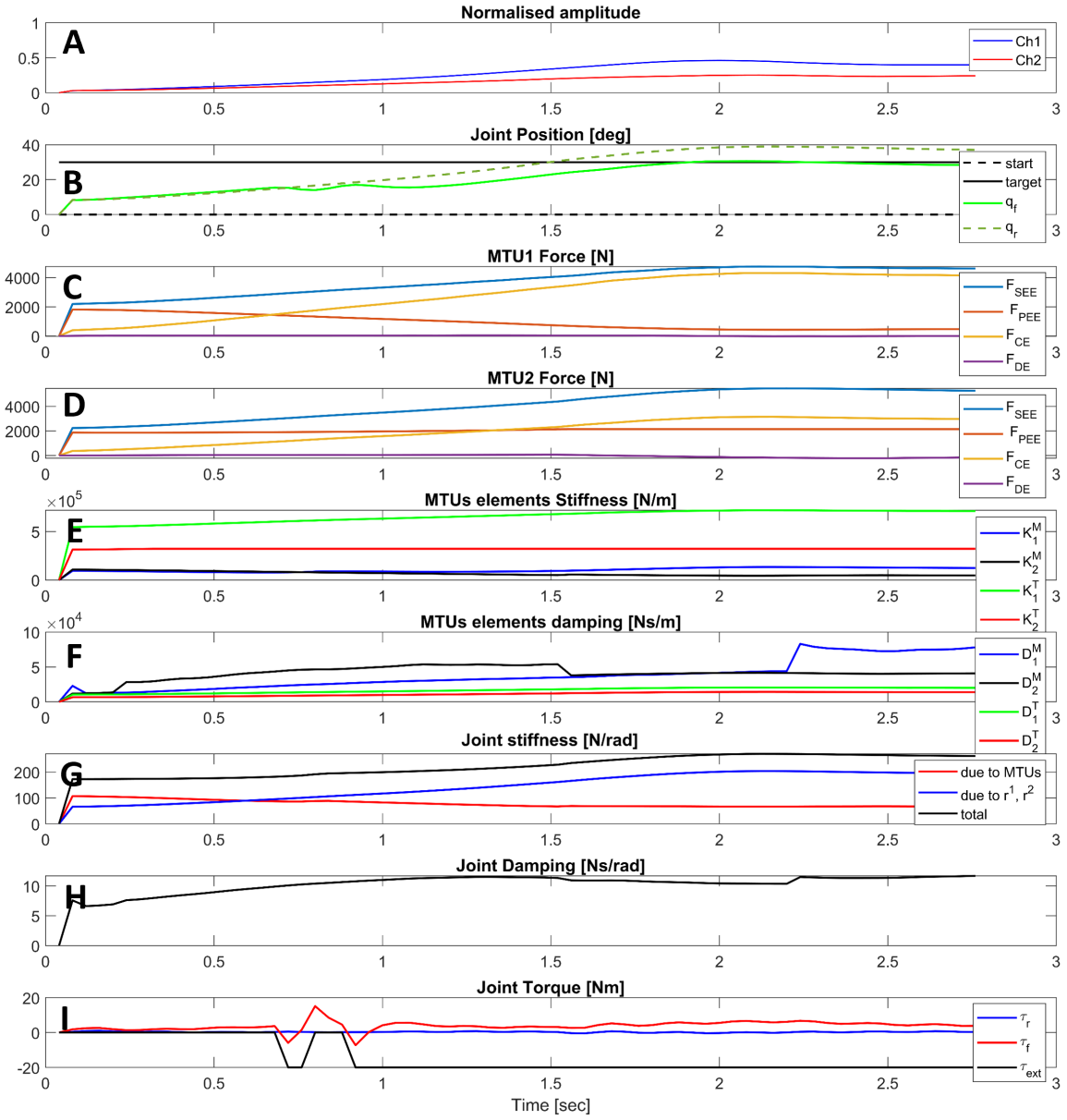

Figure 6.9: Proposed method. Example of successful trial for the amputee. We plot the time evolution of the most relevant MTU variables and controller/robot variables while the subject performs a reaching task in the presence of a perturbation field.

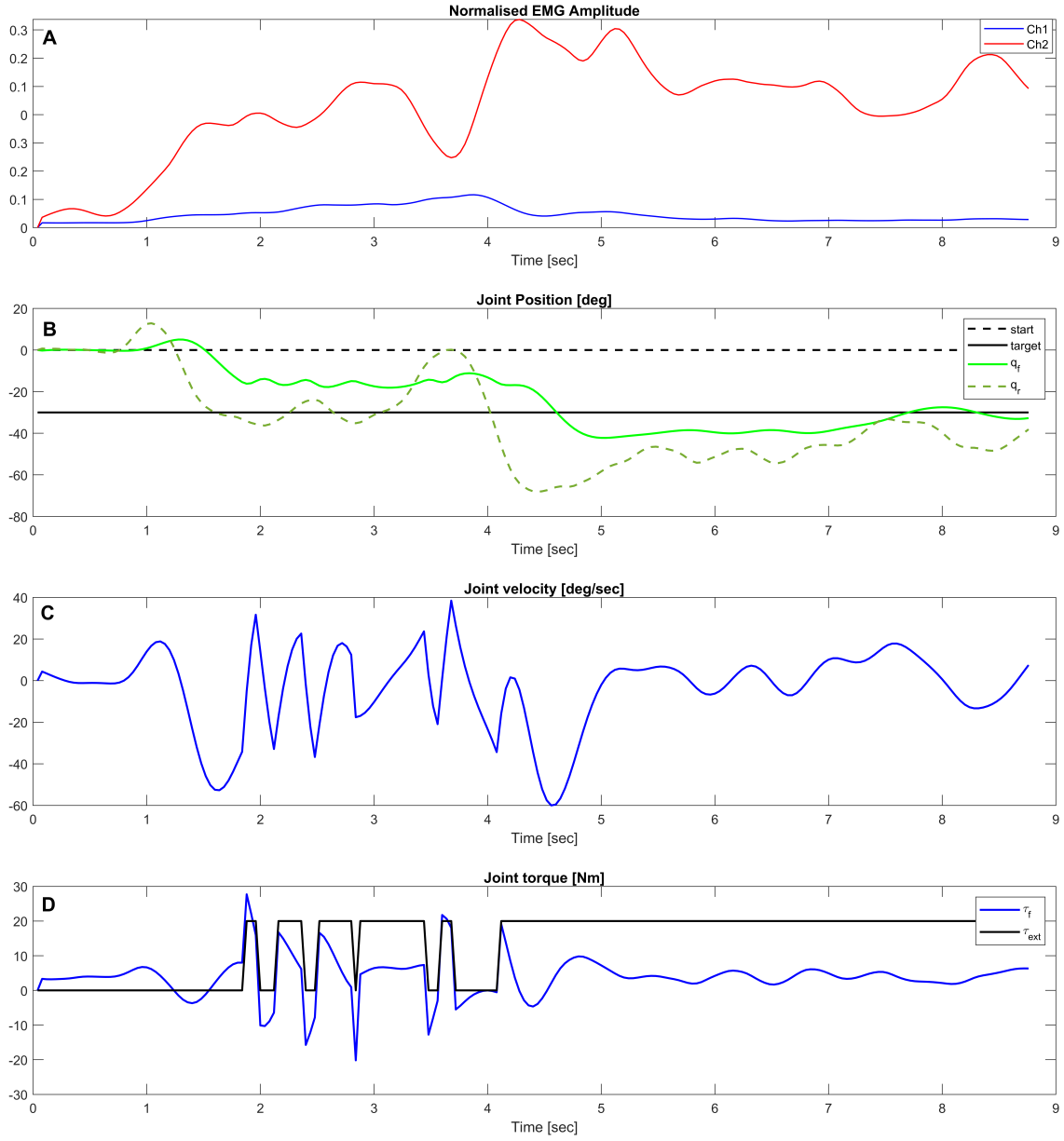

Figure 6.10: Baseline. Example of successful trial. Time evolution of the controller/robot variables while the amputee performs a reaching task in the presence of a perturbation field with the baseline.

6.3.2 Amputee

Two examples of successful trials are presented, one for the proposed framework (Figure 6.9) and one for the baseline (Figure 6.10). The description of the viable described in each figure is the same as that for the able-bodied subject, discussed in the previous section.

Proposed framework (M)

The evolution of the state variables is similar to that of the able-bodied participant in the results provided in the previous section. It can be observed in Figure 6.9 that the amputee starts increasing the activation of the single MTUs, resulting in a higher co-activation (Figure 6.9-A) from about 1.5 seconds into the trial. The increase in co-activation results in an increase in stiffness (Figure 6.9-G) and a change in damping (Figure 6.9-H) that allows the subject to maintain the target position. Notive that in this trial the subject is performing wrist extension, and therefore Ch_1 has higher activation than Ch_2 and this is reflected in the values of individual muscle stiffness and damping.

Baseline (B)

It can be observed in Figure 6.10 that the amputee attempts to increase the muscle activation between 1–3 seconds and after 4 seconds to counter the force field. However, this increment in activation is mapped to a sudden change in position at ≈ 4.5 seconds as it can be observed in the position and joint trajectories. The amputee then decreased the muscle coactivation and managed to maintain the target position. This is an example of experimental result is in agreement with the personal feedback provided by the subject and discussed in Section 6.2.2 reguirding the low robustness of the baseline to sudden changes in muscles' co-activation. The latter is mapped to a change in position.

6.4 Discussion

In this chapter, we provided experimental results in support of the hypotheses formulated in Section 5.2 regarding the online control performance provided by the proposed framework and the baseline (H1) and regarding the impact of enabling simultaneous control of the kinematics as well as the impedance of the simulated robot (H2). Moreover, we collected the feedback of the participants regarding the control performance provided by the proposed framework and the baseline, to investigate whether our framework provided an improved overall controllability with respect to the baseline and allowed the subjects to exploit modulation of muscles' co-contraction (i.e., impedance). We showed that the proposed framework

resulted in a significantly better performance compared to the baseline, and allowed the able-bodied participants to exploit joint stiffness and damping adaptation as a means to modulate the physical interaction between the robot's plant and the environment. While the methods were tested with a single amputee, the obtained results were coherent with those of the able-bodied participants. This is a promising result, especially considering the amputee performance and personal feedback in relation to the participant's difficulties in perceiving differences in muscle co-contraction, as explained in Section 5.1.1. This may indicate that our framework provides more intuitive control and higher controllability than the baseline, which is also what was reported by the able-bodied participants. Overall, the proposed method outperform the baseline. Because our framework estimates the human motor intent in terms of kinematics *and* dynamics (stiffness, and damping) and utilises this information to implement the feedback loop of the impedance controller, unlike prior work, it provides robust simultaneous control of joint kinematics, joint stiffness, and damping based on only two sEMG signals. The obtained results validate the contributions made in this thesis, which is the design and implementation of an sEMG-based framework that meets the requirements listed in Section 4.2.3.

Chapter 7

Conclusion and future work

Experimental studies on human motor control show that the central nervous system exploits intrinsic mechanical properties of the muscles to adapt the limb impedance with time and according to task requirements (Section 2.2). Regulation of limb impedance is a crucial motor control strategy because unaffected by the latency of neural pathways, it allows humans to promptly respond to external perturbations arising from the physical interaction between the upper-limb and the environment. Joint impedance modulation is achieved by coactivation of flexor and extensor muscles spanning the limb's joints which allows modifying the joint impedance independently of the joint torque. For this reason, the same joint kinematic may underlie infinite possible solutions of joint dynamics. Therefore, describing the motor intent only in terms of kinematics extremely limits its understanding.

The design of control schemes that mimics crucial characteristics of the human neuromuscular system, such as adaptation of the joints impedance, is today an open problem that concerns different research areas from robot manipulation to rehabilitation robotics. In the latter case, the detection of the motor intent is crucial to design shared control strategy to assist, augment and substitute motor functions. This requirement is crucial in motor prostheses since these rehabilitation devices aim to decode the user's motor intent and replicate it on a robotic device to substitute the motor function of the missing limb. However, today, none of the commercially available upper-limb prostheses detect the human motor intent in terms of kinematics and dynamics, and allows the user to adapt the impedance properties of the artificial limb.

Motivated by the observation that impedance control is a crucial motor control strategy in humans, and driven by the goal of maximising the understanding of the user motor intent, as explained in Chaper 1, we investigate the problem of decoding the human motor intent in terms of kinematics and dynamics and of implementing this intent in coherent manner on a (simulated) robotic system. Upper-limb prostheses control is the long term domain

of application chosen for this work and the motivation for specific design choices of the proposed framework (Section 4), such as the use of non-invasive surface EMG sensors to interface with the user's neuromuscular system and to decode the motor intent.

In Chapter 4, we describe the contributions of this thesis. *We presented a novel sEMG-based framework for enabling a human subject to simultaneously control the kinematics and the joint stiffness and damping of a DoF of a simulated robot while contracting the muscles involved in wrist flexion-extension*. To do this, we developed a hybrid framework which incorporated domain knowledge about macroscopic properties of the muscle contraction dynamics. Two Hill-type muscle-tendon units are used to decode the intended joint torque, stiffness, and damping (Section 4.3). The motor intent is used to define an adaptive impedance controller with input reference trajectory and impedance gains updated according to the estimated human motor intent. In contrast with previous work, in order to ensure that the intended dynamics (i.e., the one estimated from the muscle-tendon units) matched the dynamics of the robot plants, the impedance model is implemented using the gains directly estimated from the muscle-tendon units (Section 4.4). This required modifying the design of the muscle-tendon models and implementing an optimization method to train the models' parameter values (Section 4.5) to obtain at each point in time a reference trajectory, stiffness, and damping that suitably represented the motor intent and that ensured the control stability.

The proposed framework was evaluated during online control experiments, designed in simulation, where the subject had to perform reaching tasks in the presence of perturbations that required impedance modulation of the robot for successful task execution (Section 5.3.2). We contrasted our framework's performance to that of a baseline (Section 5.1.3) constituted by a data-driven method that learns and predicts the joint kinematics from sEMG signals and a high stiffness controller with fixed gains that tracks the estimated motor intent on the robot. We addressed the *research questions* discussed in Section 1.2: does the proposed framework provide improved functionalities with respect to the baseline? Does the user exploit adaptation of joint impedance to successfully complete the task and maintain the system stable? Moreover, we provide experimental results in support of our hypotheses (Section 5.2) on the methods' control performance. The proposed framework and baseline were tested with eight able-bodied participants and a transradial amputee. In Chapter 6, we demonstrated that the proposed framework provided a significant improvement in task performance for able-bodied participants, especially in the presence of external perturbations; the amputee's results were in accordance with those of the able-bodied participants. These results demonstrated, that our method, which enables the users to adapt the joint stiffness and damping of the robot's joint, contributed to improved online control performance. Notice that we neither measure the human joint impedance nor claim to learn stiffness and damping

values that match the biological ones. Instead, our computational framework provides a coherent representation of the dynamics of the muscle-tendon units and that of the robot, leading to improved controllability and transparency with respect to the baseline and the methods discussed in Section 3.2.3. While different studies on human motor control have characterised the human joint impedance and musculoskeletal properties in great detail (Section 2.4), today none of the commercially available upper-limb prostheses enables *impedance adaptation* of a *single robot's joint*, and t*here are no works proposed in the literature that enable simultaneous control of joint kinematics, stiffness, and damping for more than a single DoF*. Our framework is a step forward in addressing these challenges. While upper-limb prostheses control is the domain application considered in this thesis, the proposed work is on the detection of user motor intent from sEMG signals and on its implementation on a robot. The framework applicability is therefore not limited to motor prostheses, but it may be relevant to other rehabilitation and assistive devices, to other HRI scenarios (e.g., teleoperation), and to robot manipulation applications (e.g., aid the design of variable impedance controllers). Overall, this work opens up multiple directions for future research to expand the proposed framework, and to address some of its limitations. We discuss these below.

- **muscle-tendon model architecture**
  Further exploration of the online control performance provided by different muscle-tendon architectures will be investigated in future work. Identification of intrinsic parameters and structure simplification of muscle-tendon models will be carried out with the aim of limiting the parameter estimation uncertainty while retaining the control performance provided by the framework proposed in this thesis. In particular, guided by the experimental observation provided in [214], a first experiment may investigate the contribution of the tendon element to the overall control performance, including the ability to modulate joint stiffness and damping. Given the muscle-tendon model structure, the muscle-tendon unit geometrical arrangement on the robot link, and the number of units used for actuating a 1-DoF (kinematics and Impedance) may impact the control performance and has to be experimentally tested. As discussed in Chapter 6.1.1, the impact of such modelling modifications must be investigated during online control, when the subject has visual feedback of the state of the (simulated) prosthesis and adapts the muscle contractions to achieve the desired control performance. The experimental protocol to evaluate such muscle-tendon architecture may be designed to investigate how fast the user adapts to the interface (learning) and the retention of such learning over different days. These aspects may provide further insight into evaluating the performance benefit provided by different models.

- **Single DoF**

  Current sEMG-based control methods presented in literature enable only low-dimensional control of kinematics, and robust simultaneous control of 3-DoFs is still limited (Section 3.2.1). While the use of electromyography to detect the human motor intent constituted a revolutionary step in the field and allowed to move away from body-powered prostheses, it is also one of the main limiting factors to enable the control over multiple DoF of state-of-the-art prostheses. Simultaneous control of multi-DoFs is challenging because it is difficult to extract sEMG signals that can be used to independently control each DoF. This issue is more pronounced for amputees since the number of activation sites for myocontrol might be limited due to the amputation [100]. We decided to focus on the control of 1-DoF through wrist flexion-extension because the control of the wrist kinematics and dynamics is crucial in most activities of daily living that involve grasping and manipulation of objects. In fact, these tasks involve mechanical coupling between the robot and the environment. Therefore, interaction forces at the contact points should be considered in the control schemes. We are not aware of methods that allow robust adaptation of the kinematics, stiffness, and damping of multiple DoF. We validated the framework on a single DoF to isolate confounding factors that may contribute to error propagation and to thoroughly analyse the operation of the framework's components. The insights we obtained will enable us to expand the framework for multi-DoF control. However, the most challenging part of this extension will be to isolate suitable control inputs from sEMG signals. This is based on observations from initial experimental results on 2-DoF control obtained from two subjects. We expanded the framework presented in this thesis to enable a subject to simultaneously control two DoFs of a simulated robot through wrist flexion-extension and ulnar-radial deviation. Two pairs of muscle-tendon models had to be used to directionally activate the two joints. To drive the four muscle-tendon units, we used four sEMG signals to measure the activity of the *flexor carpi radialis* and *ulnaris*, and the *extensor carpi radialis* and *ulnaris* (Figure 2.11). The proposed framework was trained considering single-DoF motions as in the experimental protocol described in Section 5.3.1. Initial results indicated that the two subjects could robustly perform reaching tasks in the absence of perturbations, and thus perform single as well as combined DoF motions. However, in the presence of perturbations, when the subjects had to increase the muscle co-contraction to maintain the system stability and at the same time reach the target, the control performance deteriorated. For example, when the subject had to perform flexion with higher impedance, the change in muscle activation cause the ulnar-radial DoF to deviate. We believe this is due to the fact that the input

activations (i.e., the sEMG signals) are not independent, while we assume that control of the two DoF is decoupled (i.e., the action of the MTUs of flexion-extension do not affect ulnar-radial deviation). For the interested reader, some examples of our initial control results are included in the GitHub repository in [65].

- **Surface electromyography and detection of human motor intent**
  Modulation of joint impedance is the result of the synergistic activity of more than a pair of flexor-extensor muscles. Multiple muscles span the wrist joint, as explained in Section 2.5, and contribute to the joint motion and impedance modulation. This means that targeting a single flexor and a single extensor muscle per motor function, as it is done in this work, may reduce the information about human motor intent. We believe this is one of the causes of performance deterioration when simultaneously controlling two DoFs, as explained in the previous point. However, the low-density sEMG sensors used in this thesis did not allow us to explore whether the motor intent decoded from two sEMG channels targeting specific muscles limits the controllability provided to the user and the estimation of stiffness and damping. Sensors with a higher spatial and temporal resolution may be employed in future work to extract multiple input activations from sEMG data and investigate the framework's performance in relation to different designs of the inputs to the muscle-tendon units.

- **Lack of real-world experiments**
  The lack of evaluation on a real robotic system is a limitation of this work. The design of the framework and the choice of using a generic simulated robot is to allow future testing on a robotic system that is not necessarily tied to an upper-limb prosthesis. This is because, despite the effort in the research community to design prostheses that allow variable impedance control, none of the commercially available ones enable this functionality yet. Moreover, in order to perform real-world tasks it is desirable to at least provide the user with 2-DoF control. For these reasons, our current and future research are focused on expanding the framework to 2-DoFs before proceeding with testing on a real prosthesis or manipulator.

- **Joint stiffness and damping contributing to the observed controllability**
  The conditional mutual information between q_r and q_f given the stiffness or damping, discussed in Section 6.2, provides an initial indication of the contribution of joint stiffness and damping to system stability. However, we did not observe any statistically significant difference between the mutual information values during task execution in the presence and absence of perturbations. We plan to explore this more thoroughly by considering different tasks and force fields that require specific joint stiffness or

damping modulation (e.g., posture maintenance; reaching tasks in velocity-dependent force fields), with the aim of assessing the relative contribution of stiffness and damping to the overall impedance behaviour.

- **Subject specific and across-subjects models**
  An interesting future direction of research could involve the investigation of whether the proposed framework could provide high controllability without user-specific model training. This means investigating the generalisation properties of the proposed framework. One approach is to evaluate the controllability provided by the framework when the muscle-tendon parameters' values are set to the average values obtained from subject-specific models. This assumes that the across-subject model retains features that enable the user to learn a mapping from muscle contraction to the desired motor outcome on the (simulated) robotic device. This is especially interesting in the context of upper-limb prostheses, where long training sessions are a burden for the subject. The control performance provided by non-subject-specific control methods may be determined by the ability of the subject to adapt to the interface. In this regard, future work could investigate if the proposed framework, which includes process-driven models and is designed to enhance control transparency, would enable the user to adapt more quickly to the framework with respect to purely data-driven controllers and other methods implemented on commercially available prostheses.

Bibliography

[1] Todd A Kuiken, Laura Miller, Robert D Lipschutz, Blair Lock, Kathy Stubblefield, Paul D Marasco, Ping Zhou, and Gregory Dumanian. Targeted reinnervation for enhanced prosthetic arm function in a woman with a proximal amputation: A case study. 369:371–80, 03 2007.

[2] Cary Abul-Haj and Neville Hogan. An emulator system for developing improved elbow-prosthesis designs. IEEE transactions on biomedical engineering, (9):724–737, 1987.

[3] Cary J Abul-Haj and N Hogen. Functional assessment of control systems for cybernetic elbow prostheses. i. description of the technique. IEEE Transactions on Biomedical Engineering, 37(11):1025–1036, 1990.

[4] Soumyadipta Acharya, Matthew S Fifer, Heather L Benz, Nathan E Crone, and Nitish V Thakor. Electrocorticographic amplitude predicts finger positions during slow grasping motions of the hand. Journal of Neural Engineering, 7(4):046002, may 2010. doi: 10.1088/1741-2560/7/4/046002. URL https://doi.org/10.1088%2F1741-2560%2F7%2F4%2F046002.

[5] Abidemi Bolu Ajiboye and R Fff Weir. A heuristic fuzzy logic approach to emg pattern recognition for multifunctional prosthesis control. IEEE Transactions on Neural Systems and Rehabilitation Engineering, 13(3):280–291, 2005.

[6] Arash Ajoudani, Sasha B Godfrey, M Catalano, Giorgio Grioli, Nikos G Tsagarakis, and Antonio Bicchi. Teleimpedance control of a synergy-driven anthropomorphic hand. In 2013 IEEE/RSJ International Conference on Intelligent Robots and Systems, pages 1985–1991. IEEE, 2013.

[7] Hayder FN Al-Shuka and R Song. Adaptive hybrid regressor and approximation control of robotic manipulators in constrained space. International Journal of Mechanical & Mechatronics Engineering, IJMME-IJENS, 17(3):11–19, 2017.

[8] Julian Alcazar, Robert Csapo, Ignacio Ara, and Luis M Alegre. On the shape of the force-velocity relationship in skeletal muscles: The linear, the hyperbolic, and the double-hyperbolic. Frontiers in physiology, 10:769, 2019.

[9] Ali Ameri, Mohammad Ali Akhaee, Erik Scheme, and Kevin Englehart. Regression convolutional neural network for improved simultaneous emg control. Journal of neural engineering, 16(3):036015, 2019.

[10] KN An, K Takahashi, TP Harrigan, and EY Chao. Determination of muscle orientations and moment arms. Journal of biomechanical engineering, 106(3):280–282, 1984.

[11] Brian Armstrong, Oussama Khatib, and Joel Burdick. The explicit dynamic model and inertial parameters of the puma 560 arm. In Proceedings. 1986 IEEE international conference on robotics and automation, volume 3, pages 510–518. IEEE, 1986.

[12] Samuel K Au, Paolo Bonato, and Hugh Herr. An emg-position controlled system for an active ankle-foot prosthesis: an initial experimental study. In 9th International Conference on Rehabilitation Robotics, 2005. ICORR 2005., pages 375–379. IEEE, 2005.

[13] Sivakumar Balasubramanian, Alejandro Melendez-Calderon, and Etienne Burdet. A robust and sensitive metric for quantifying movement smoothness. IEEE transactions on biomedical engineering, 59(8):2126–2136, 2011.

[14] Sivakumar Balasubramanian, Alejandro Melendez-Calderon, Agnes Roby-Brami, and Etienne Burdet. On the analysis of movement smoothness. Journal of neuroengineering and rehabilitation, 12(1):1–11, 2015.

[15] Salah Bazzi and Dagmar Sternad. Human control of complex objects: towards more dexterous robots. Advanced Robotics, 34(17):1137–1155, 2020.

[16] MB Bennett1, RF Ker1, Nicola J Imery, and R McN Alexander1. Mechanical properties of various mammalian tendons. Journal of Zoology, 209(4):537–548, 1986.

[17] Elaine Biddiss and Tom Chau. Upper-limb prosthetics: critical factors in device abandonment. American journal of physical medicine & rehabilitation, 86(12):977–987, 2007.

[18] E. Bizzi, F.A. Mussa-Ivaldi, and N. Hogan. Regulation of multi-joint arm posture and movement. Progress in Brain Research, 64:345 – 351, 1986. ISSN 0079-6123. doi: http://dx.doi.org/10.1016/S0079-6123(08)63428-7. URL http://www.sciencedirect.com/science/article/pii/S0079612308634287. The Oculomotor and Skeletalmotor Systems: Differences and Similarities.

[19] Amy A Blank, Allison M Okamura, and Louis L Whitcomb. Task-dependent impedance and implications for upper-limb prosthesis control. The International Journal of Robotics Research, 33(6):827–846, 2014.

[20] Andrea Bonetto and Lynda F. Bonewald. Chapter 16 - bone and muscle. In David B. Burr and Matthew R. Allen, editors, Basic and Applied Bone Biology (Second Edition), pages 317–332. Academic Press, second edition edition, 2019. ISBN 978-0-12-813259-3. doi: https://doi.org/10.1016/B978-0-12-813259-3.00016-6. URL https://www.sciencedirect.com/science/article/pii/B9780128132593000166.

[21] William E Boyce, Richard C DiPrima, and Douglas B Meade. Elementary differential equations and boundary value problems. John Wiley & Sons, 2021.

[22] David J Braun, Florian Petit, Felix Huber, Sami Haddadin, Patrick Van Der Smagt, Alin Albu-Schäffer, and Sethu Vijayakumar. Robots driven by compliant actuators: Optimal control under actuation constraints. IEEE Transactions on Robotics, 29(5): 1085–1101, 2013.

[23] Nan Bu, Osamu Fukuda, and Toshio Tsuji. Emg-based motion discrimination using a novel recurrent neural network. Journal of Intelligent Information Systems, 21 (2):113–126, Sep 2003. ISSN 1573-7675. doi: 10.1023/A:1024706431807. URL https://doi.org/10.1023/A:1024706431807.

[24] Thomas S Buchanan, David G Lloyd, Kurt Manal, and Thor F Besier. Neuromusculoskeletal modeling: estimation of muscle forces and joint moments and movements from measurements of neural command. Journal of applied biomechanics, 20(4):367, 2004.

[25] Thomas S Buchanan, David G Lloyd, Kurt Manal, and Thor F Besier. Neuromusculoskeletal modeling: estimation of muscle forces and joint moments and movements from measurements of neural command. Journal of applied biomechanics, 20(4): 367–395, 2004.

[26] Thomas S Buchanan, David G Lloyd, Kurt Manal, Thor F Besier, et al. Estimation of muscle forces and joint moments using a forward-inverse dynamics model. Medicine and Science in Sports and exercise, 37(11):1911, 2005.

[27] Jonas Buchli, Freek Stulp, Evangelos Theodorou, and Stefan Schaal. Learning variable impedance control. The International Journal of Robotics Research, 30(7):820–833, 2011.

[28] Etienne Burdet, Rieko Osu, David W Franklin, Theodore E Milner, and Mitsuo Kawato. The central nervous system stabilizes unstable dynamics by learning optimal impedance. Nature, 414(6862):446–449, 2001.

[29] Patricia Capsi-Morales, Cristina Piazza, Manuel G Catalano, Antonio Bicchi, and Giorgio Grioli. Exploring stiffness modulation in prosthetic hands and its perceived function in manipulation and social interaction. Frontiers in Neurorobotics, 14:33, 2020.

[30] Claudio Castellini and Markus Nowak. Emg-based prediction of multi-dof activations using single-dof training: a preliminary result. In Proceedings of MEC—Myoelectric Control Symposium, pages 45–49, 2014.

[31] Nicolò Celadon, Strahinja Došen, Iris Binder, Paolo Ariano, and Dario Farina. Proportional estimation of finger movements from high-density surface electromyography. Journal of neuroengineering and rehabilitation, 13(1):73, 2016.

[32] E. K. Chadwick *, D. Blana, A. J. van den Bogert, and R. F. Kirsch. A real-time, 3-d musculoskeletal model for dynamic simulation of arm movements. IEEE Transactions on Biomedical Engineering, 56(4):941–948, April 2009. ISSN 0018-9294. doi: 10.1109/TBME.2008.2005946.

[33] Steven K Charles and Neville Hogan. The curvature and variability of wrist and arm movements. Experimental brain research, 203:63–73, 2010.

[34] Steven K Charles and Neville Hogan. Dynamics of wrist rotations. Journal of biomechanics, 44(4):614–621, 2011.

[35] Steven K Charles and Neville Hogan. Stiffness, not inertial coupling, determines path curvature of wrist motions. Journal of neurophysiology, 107(4):1230–1240, 2012.

[36] Tom Chau. A review of analytical techniques for gait data. part 2: neural network and wavelet methods. Gait & posture, 13(2):102–120, 2001.

[37] Mohammad Chaudhry, Humna Aminullah, Margaret A Sinkler, and Abdul Arain. Anatomy, shoulder and upper limb, forearm compartments. 2019.

[38] Chuanzhi Chen, Hong Nie, Jinbao Chen, and Xiaotao Wang. A velocity-based impedance control system for a low impact docking mechanism (lidm). Sensors, 14 (12):22998–23016, 2014.

[39] Cynthia A Chestek, Vikash Gilja, Christine H Blabe, Brett L Foster, Krishna V Shenoy, Josef Parvizi, and Jaimie M Henderson. Hand posture classification using electrocorticography signals in the gamma band over human sensorimotor brain areas. Journal of neural engineering, 10(2):026002, 2013.

[40] Erina Cho, Richard Chen, Lukas-Karim Merhi, Zhen Xiao, Brittany Pousett, and Carlo Menon. Force myography to control robotic upper extremity prostheses: a feasibility study. Frontiers in bioengineering and biotechnology, 4:18, 2016.

[41] Andrea Cimolato, Giovanni Milandri, Leonardo S Mattos, Elena De Momi, Matteo Laffranchi, and Lorenzo De Michieli. Hybrid machine learning-neuromusculoskeletal modeling for control of lower limb prosthetics. In 2020 8th IEEE RAS/EMBS International Conference for Biomedical Robotics and Biomechatronics (BioRob), pages 557–563. IEEE, 2020.

[42] SIDNEY Cohen and F Green. Force-velocity characteristics of esophageal muscle: effect of acetylcholine and norepinephrine. American Journal of Physiology-Legacy Content, 226(5):1250–1256, 1974.

[43] Mathilde Connan, Eduardo Ruiz Ramírez, Bernhard Vodermayer, and Claudio Castellini. Assessment of a wearable force-and electromyography device and comparison of the related signals for myocontrol. Frontiers in neurorobotics, 10:17, 2016.

[44] Dustin L Crouch and He Huang. Musculoskeletal model predicts multi-joint wrist and hand movement from limited emg control signals. In 2015 37th Annual International Conference of the IEEE Engineering in Medicine and Biology Society (EMBC), pages 1132–1135. IEEE, 2015.

[45] Dustin L Crouch and He Huang. Lumped-parameter electromyogram-driven musculoskeletal hand model: A potential platform for real-time prosthesis control. Journal of biomechanics, 49(16):3901–3907, 2016.

[46] Lei Cui, Eric J Perreault, Huub Maas, and Thomas G Sandercock. Modeling short-range stiffness of feline lower hindlimb muscles. Journal of biomechanics, 41(9): 1945–1952, 2008.

[47] Paul R Davidson and Daniel M Wolpert. Motor learning and prediction in a variable environment. Current Opinion in Neurobiology, 13(2):232 – 237, 2003. ISSN 0959-4388. doi: https://doi.org/10.1016/S0959-4388(03)00038-2.

[48] Carlo J De Luca. The use of surface electromyography in biomechanics. Journal of applied biomechanics, 13(2):135–163, 1997.

[49] Carlo J De Luca, Alexander Adam, Robert Wotiz, L Donald Gilmore, and S Hamid Nawab. Decomposition of surface emg signals. Journal of neurophysiology, 96(3): 1646–1657, 2006.

[50] Carlo J De Luca, L Donald Gilmore, Mikhail Kuznetsov, and Serge H Roy. Filtering the surface emg signal: Movement artifact and baseline noise contamination. Journal of biomechanics, 43(8):1573–1579, 2010.

[51] Paul DeVita and Tibor Hortobagyi. Functional knee brace alters predicted knee muscle and joint forces in people with acl reconstruction during walking. Journal of applied biomechanics, 17(4):297–311, 2001.

[52] Taylor JM Dick and James M Wakeling. Geometric models to explore mechanisms of dynamic shape change in skeletal muscle. Royal Society open science, 5(5):172371, 2018.

[53] James Diebel. Representing attitude: Euler angles, unit quaternions, and rotation vectors. Matrix, 58(15-16):1–35, 2006.

[54] Strahinja Dosen, Marko Markovic, Kelef Somer, Bernhard Graimann, and Dario Farina. Emg biofeedback for online predictive control of grasping force in a myoelectric prosthesis. Journal of NeuroEngineering and Rehabilitation, 2015. doi: 10.1186/s12984-015-0047-z.

[55] KA Edman. Double-hyperbolic force-velocity relation in frog muscle fibres. The Journal of physiology, 404(1):301–321, 1988.

[56] KAP Edman. Contractile performance of striated muscle. Muscle Biophysics, pages 7–40, 2010.

[57] Michael F Eilenberg, Hartmut Geyer, and Hugh Herr. Control of a powered ankle–foot prosthesis based on a neuromuscular model. IEEE transactions on neural systems and rehabilitation engineering, 18(2):164–173, 2010.

[58] M. S. Erden and A. Billard. End-point impedance measurements across dominant and nondominant hands and robotic assistance with directional damping. IEEE Transactions on Cybernetics, 45(6):1146–1157, June 2015. ISSN 2168-2267. doi: 10.1109/TCYB.2014.2346021.

[59] D. Farina, N. Jiang, H. Rehbaum, A. Holobar, B. Graimann, H. Dietl, and O. C. Aszmann. The extraction of neural information from the surface emg for the control of upper-limb prostheses: Emerging avenues and challenges. IEEE Transactions on Neural Systems and Rehabilitation Engineering, 22(4):797–809, 2014. doi: https://doi.org/10.1109/TNSRE.2014.2305111.

[60] D. Farina, N. Jiang, H. Rehbaum, A. Holobar, B. Graimann, H. Dietl, and O. C. Aszmann. The extraction of neural information from the surface emg for the control of upper-limb prostheses: Emerging avenues and challenges. IEEE Transactions on Neural Systems and Rehabilitation Engineering, 22(2):797–809, 2014. doi: 10.1109/TNSRE.2014.2305111.

[61] Dario Farina, Corrado Cescon, and Roberto Merletti. Influence of anatomical, physical, and detection-system parameters on surface emg. Biological Cybernetics, 86(6):445–456, Jun 2002. ISSN 1432-0770. doi: 10.1007/s00422-002-0309-2. URL https://doi.org/10.1007/s00422-002-0309-2.

[62] Dario Farina, Corrado Cescon, and Roberto Merletti. Influence of anatomical, physical, and detection-system parameters on surface emg. Biological cybernetics, 86(6):445–456, 2002.

[63] Dario Farina, Roberto Merletti, and Roger M. Enoka. The extraction of neural strategies from the surface emg. Journal of Applied Physiology, 96(4):1486–1495, 2004. doi: 10.1152/japplphysiol.01070.2003. URL https://doi.org/10.1152/japplphysiol.01070.2003. PMID: 15016793.

[64] Kristin A Farry, Ian D Walker, and Richard G Baraniuk. Myoelectric teleoperation of a complex robotic hand. IEEE Transactions on Robotics and Automation, 12(5):775–788, 1996.

[65] Laura Ferrante. URL https://github.com/LauFe/Supporting-Material-PhD-thesis.git.

[66] Laura Ferrante, Mohan Sridharan, Claudio Zito, and Dario Farina. Toward a framework for adaptive impedance control of an upper-limb prosthesis. arXiv preprint arXiv:2209.04937, 2022.

[67] Paul M Fitts. The information capacity of the human motor system in controlling the amplitude of movement. Journal of experimental psychology, 47(6):381, 1954.

[68] T. Flash and F. Mussa-Ivaldi. Human arm stiffness characteristics during the maintenance of posture. Experimental Brain Research, 82(2):315–326, Oct 1990. ISSN 1432-1106. doi: 10.1007/BF00231251. URL https://doi.org/10.1007/BF00231251.

[69] Tamar Flash and F Mussa-Ivaldi. Human arm stiffness characteristics during the maintenance of posture. Experimental brain research, 82(2):315–326, 1990.

[70] Domenico Formica, Steven K Charles, Loredana Zollo, Eugenio Guglielmelli, Neville Hogan, and Hermano I Krebs. The passive stiffness of the wrist and forearm. Journal of neurophysiology, 108(4):1158–1166, 2012.

[71] Anders Fougner, Øyvind Stavdahl, Peter J Kyberd, Yves G Losier, and Philip A Parker. Control of upper limb prostheses: Terminology and proportional myoelectric control—a review. IEEE Transactions on neural systems and rehabilitation engineering, 20(5):663–677, 2012.

[72] D. W. Franklin. Impedance control: Learning stability in human sensorimotor control. In 2015 37th Annual International Conference of the IEEE Engineering in Medicine and Biology Society (EMBC), pages 1421–1424, Aug 2015. doi: 10.1109/EMBC.2015.7318636.

[73] D. W. Franklin, R. Osu, E. Burdet, M. Kawato, and T. E. Milner. Adaptation to stable and unstable dynamics achieved by combining impedance control and inverse dynamics model. Journal of Neurophysiology, 90(5):3270–3282, 2003. doi: 10.1152/jn.01112.2002.

[74] Akira Furui, Shintaro Eto, Kosuke Nakagaki, Kyohei Shimada, Go Nakamura, Akito Masuda, Takaaki Chin, and Toshio Tsuji. A myoelectric prosthetic hand with muscle synergy–based motion determination and impedance model–based biomimetic control. Science Robotics, 4(31):eaaw6339, 2019.

[75] Carl Gans and Abbot S Gaunt. Muscle architecture in relation to function. Journal of Biomechanics, 24:53–65, 1991.

[76] CC Gielen and James Charles Houk. Nonlinear viscosity of human wrist. Journal of Neurophysiology, 52(3):553–569, 1984.

[77] Sasha Blue Godfrey, Kristin D Zhao, Amanda Theuer, Manuel G Catalano, Matteo Bianchi, Ryan Breighner, Divya Bhaskaran, Ryan Lennon, Giorgio Grioli, Marco Santello, et al. The softhand pro: Functional evaluation of a novel, flexible, and robust myoelectric prosthesis. PloS one, 13(10):e0205653, 2018.

[78] Hiroaki Gomi and Mitsuo Kawato. Human arm stiffness and equilibrium-point trajectory during multi-joint movement. Biological Cybernetics, 76(3):163–171, Apr 1997. ISSN 1432-0770. doi: 10.1007/s004220050329. URL https://doi.org/10.1007/s004220050329.

[79] A. M. Gordon, A. F. Huxley, and F. J. Julian. The variation in isometric tension with sarcomere length in vertebrate muscle fibres. The Journal of Physiology, 184 (1):170–192, 1966. doi: https://doi.org/10.1113/jphysiol.1966.sp007909. URL https://physoc.onlinelibrary.wiley.com/doi/abs/10.1113/jphysiol.1966.sp007909.

[80] Sten Grillner. Muscle Stiffness and Motor Control - Forces in the Ankle During Locomotion and Standing, pages 195–215. Springer US, Boston, MA, 1974. ISBN 978-1-4613-4502-2. doi: 10.1007/978-1-4613-4502-2_13. URL https://doi.org/10.1007/978-1-4613-4502-2_13.

[81] Michael Günther, Syn Schmitt, and Veit Wank. High-frequency oscillations as a consequence of neglected serial damping in hill-type muscle models. Biological Cybernetics, 97(1):63–79, 2007.

[82] D.F.B. Haeufle, M. Günther, A. Bayer, and S. Schmitt. Hill-type muscle model with serial damping and eccentric force–velocity relation. Journal of Biomechanics, 47(6): 1531 – 1536, 2014. ISSN 0021-9290. doi: https://doi.org/10.1016/j.jbiomech.2014.02.009. URL http://www.sciencedirect.com/science/article/pii/S0021929014001018.

[83] Janne M Hahne, F Biessmann, Ning Jiang, H Rehbaum, Dario Farina, FC Meinecke, K-R Müller, and LC Parra. Linear and nonlinear regression techniques for simultaneous and proportional myoelectric control. IEEE Transactions on Neural Systems and Rehabilitation Engineering, 22(2):269–279, 2014.

[84] Janne M Hahne, Marko Markovic, and Dario Farina. User adaptation in myoelectric man-machine interfaces. Scientific reports, 7(1):1–10, 2017.

[85] Levi J Hargrove, Kevin Englehart, and Bernard Hudgins. A comparison of surface and intramuscular myoelectric signal classification. IEEE transactions on biomedical engineering, 54(5):847–853, 2007.

[86] Levi J Hargrove, Erik J Scheme, Kevin B Englehart, and Bernard S Hudgins. Multiple binary classifications via linear discriminant analysis for improved controllability of a powered prosthesis. IEEE Transactions on Neural Systems and Rehabilitation Engineering, 18(1):49–57, 2010.

[87] Herbert Hatze. A comprehensive model for human motion simulation and its application to the take-off phase of the long jump. Journal of biomechanics, 14(3):135–142, 1981.

[88] CJ Heckman and Roger M Enoka. Motor unit. Comprehensive physiology, 2(4): 2629–2682, 2012.

[89] JS Higginson, FE Zajac, RR Neptune, SA Kautz, and SL Delp. Muscle contributions to support during gait in an individual with post-stroke hemiparesis. Journal of biomechanics, 39(10):1769–1777, 2006.

[90] Archibald Vivian Hill. The heat of shortening and the dynamic constants of muscle. Proceedings of the Royal Society of London. Series B-Biological Sciences, 126(843): 136–195, 1938.

[91] Wendy Hill, Øyvind Stavdahl, Liselotte Norling Hermansson, Peter Kyberd, Shawn Swanson, and Sheila Hubbard. Functional outcomes in the who-icf model: establishment of the upper limb prosthetic outcome measures group. JPO: Journal of Prosthetics and Orthotics, 21(2):115–119, 2009.

[92] Elif Hocaoglu and Volkan Patoglu. semg-based natural control interface for a variable stiffness transradial hand prosthesis. Frontiers in Neurorobotics, 16, 2022.

[93] N Hogan. Prostheses should have adaptively controllable impedance. In Control Aspects of Prosthetics and Orthotics, pages 155–162. Elsevier, 1983.

[94] Neville Hogan. Adaptive control of mechanical impedance by coactivation of antagonist muscles. IEEE Transactions on automatic control, 29(8):681–690, 1984.

[95] Neville Hogan. Impedance control: An approach to manipulation. In 1984 American control conference, pages 304–313. IEEE, 1984.

[96] Neville Hogan. Impedance control: An approach to manipulation: Part ii—implementation. 1985.

[97] Neville Hogan. The mechanics of multi-joint posture and movement control. Biological cybernetics, 52(5):315–331, 1985.

[98] Neville Hogan. Mechanical impedance of single-and multi-articular systems. In Multiple muscle systems, pages 149–164. Springer, 1990.

[99] Matthew Howard, David J Braun, and Sethu Vijayakumar. Transferring human impedance behavior to heterogeneous variable impedance actuators. IEEE Transactions on Robotics, 29(4):847–862, 2013.

[100] Stephanie Huang and Daniel P Ferris. Muscle activation patterns during walking from transtibial amputees recorded within the residual limb-prosthetic interface. Journal of neuroengineering and rehabilitation, 9(1):1–16, 2012.

[101] AF Huxley. Muscular contraction. The Journal of physiology, 243(1):1–43, 1974.

[102] Andrew F Huxley. Muscle structure and theories of contraction. Prog. Biophys. Biophys. Chem, 7:255–318, 1957.

[103] Hugh Huxley and Jean Hanson. Changes in the cross-striations of muscle during contraction and stretch and their structural interpretation. Nature, 173(4412):973–976, 1954.

[104] Han-Jeong Hwang, Soyoun Kim, Soobeom Choi, and Chang-Hwan Im. Eeg-based brain-computer interfaces: a thorough literature survey. International Journal of Human-Computer Interaction, 29(12):814–826, 2013.

[105] Mark Ison and Panagiotis Artemiadis. The role of muscle synergies in myoelectric control: trends and challenges for simultaneous multifunction control. Journal of neural engineering, 11(5):051001, 2014.

[106] Ning Jiang, Deborah Falla, Andrea d'Avella, Bernhard Graimann, and Dario Farina. Myoelectric control in neurorehabilitation. Critical Reviews™ in Biomedical Engineering, 38(4), 2010.

[107] Ning Jiang, Johnny LG Vest-Nielsen, Silvia Muceli, and Dario Farina. Emg-based simultaneous and proportional estimation of wrist/hand kinematics in uni-lateral trans-radial amputees. Journal of neuroengineering and rehabilitation, 9(1):42, 2012.

[108] Ning Jiang, Hubertus Rehbaum, Ivan Vujaklija, Bernhard Graimann, and Dario Farina. Intuitive, online, simultaneous, and proportional myoelectric control over two degrees-of-freedom in upper limb amputees. IEEE transactions on neural systems and rehabilitation engineering, 22(3):501–510, 2013.

[109] Ning Jiang, Ivan Vujaklija, Hubertus Rehbaum, Bernhard Graimann, and Dario Farina. Is accurate mapping of emg signals on kinematics needed for precise online myoelectric control? IEEE Transactions on Neural Systems and Rehabilitation Engineering, 22(3):549–558, 2013.

[110] Nikos Karavas, Arash Ajoudani, Nikos Tsagarakis, Jody Saglia, Antonio Bicchi, and Darwin Caldwell. Tele-impedance based assistive control for a compliant knee exoskeleton. Robotics and Autonomous Systems, 73:78–90, 2015.

[111] Bernhard Katz. The relation between force and speed in muscular contraction. The Journal of physiology, 96(1):45, 1939.

[112] Robert A Kaufmann, H James Pfaeffle, Brad D Blankenhorn, Kathryne Stabile, Doug Robertson, and Robert Goitz. Kinematics of the midcarpal and radiocarpal joint in flexion and extension: an in vitro study. The Journal of hand surgery, 31(7): 1142–1148, 2006.

[113] Scott Kirkpatrick, C Daniel Gelatt Jr, and Mario P Vecchi. Optimization by simulated annealing. science, 220(4598):671–680, 1983.

[114] Robert F Kirsch, Djordje Boskov, and William Z Rymer. Muscle stiffness during transient and continuous movements of cat muscle: perturbation characteristics and physiological relevance. IEEE Transactions on Biomedical Engineering, 41(8):758–770, 1994.

[115] Agamemnon Krasoulis, Sethu Vijayakumar, and Kianoush Nazarpour. Evaluation of regression methods for the continuous decoding of finger movement from surface emg and accelerometry. In 2015 7th International IEEE/EMBS Conference on Neural Engineering (NER), pages 631–634. IEEE, 2015.

[116] Klas Kronander and Aude Billard. Learning compliant manipulation through kinesthetic and tactile human-robot interaction. IEEE transactions on haptics, 7(3):367–380, 2013.

[117] Klas Kronander and Aude Billard. Stability considerations for variable impedance control. IEEE Transactions on Robotics, 32(5):1298–1305, 2016.

[118] JOJWGSJ Kubanek, KJ Miller, JG Ojemann, JR Wolpaw, and G Schalk. Decoding flexion of individual fingers using electrocorticographic signals in humans. Journal of neural engineering, 6(6):066001, 2009.

[119] Andras Kupcsik, Marc Peter Deisenroth, Jan Peters, Ai Poh Loh, Prahlad Vadakkepat, and Gerhard Neumann. Model-based contextual policy search for data-efficient generalization of robot skills. Artificial Intelligence, 247:415–439, 2017.

[120] F Lacquaniti, M Carrozzo, and N A Borghese. Time-varying mechanical behavior of multijointed arm in man. Journal of neurophysiology, 69 5:1443–64, 1993.

[121] Dale A Lawrence. Impedance control stability properties in common implementations. In Proceedings. 1988 IEEE International Conference on Robotics and Automation, pages 1185–1190. IEEE, 1988.

[122] Jang Hyung Lee and Kwang Gi Kim. Applying deep learning in medical images: the case of bone age estimation. Healthcare informatics research, 24(1):86–92, 2018.

[123] SL Lehman and BM Calhoun. An identified model for human wrist movements. Experimental Brain Research, 81(1):199–208, 1990.

[124] Eric C Leuthardt, Gerwin Schalk, Jonathan R Wolpaw, Jeffrey G Ojemann, and Daniel W Moran. A brain–computer interface using electrocorticographic signals in humans. Journal of neural engineering, 1(2):63, 2004.

[125] Gwyn N Lewis, Colum D MacKinnon, Randy Trumbower, and Eric J Perreault. Co-contraction modifies the stretch reflex elicited in muscles shortened by a joint perturbation. Experimental brain research, 207(1):39–48, 2010.

[126] Yanan Li, Gowrishankar Ganesh, Nathanaël Jarrassé, Sami Haddadin, Alin Albu-Schaeffer, and Etienne Burdet. Force, impedance, and trajectory learning for contact tooling and haptic identification. IEEE Transactions on Robotics, 34(5):1170–1182, 2018.

[127] Zhijun Li, Zhicong Huang, Wei He, and Chun-Yi Su. Adaptive impedance control for an upper limb robotic exoskeleton using biological signals. IEEE Transactions on Industrial Electronics, 64(2):1664–1674, 2016.

[128] Zong-Ming Li, Laurel Kuxhaus, Jesse A Fisk, and Thomas H Christophel. Coupling between wrist flexion–extension and radial–ulnar deviation. Clinical biomechanics, 20(2):177–183, 2005.

[129] Ke Liao, Ran Xiao, Jania Gonzalez, and Lei Ding. Decoding individual finger movements from one hand using human eeg signals. PloS one, 9(1):e85192, 2014.

[130] Richard L Lieber and Samuel R Ward. Skeletal muscle design to meet functional demands. Philosophical Transactions of the Royal Society B: Biological Sciences, 366(1570):1466–1476, 2011.

[131] Coapt LLC. URL https://www.coaptengineering.com/resources.html.

[132] David G Lloyd and Thor F Besier. An emg-driven musculoskeletal model to estimate muscle forces and knee joint moments in vivo. Journal of biomechanics, 36(6): 765–776, 2003.

[133] David G Lloyd and Thor F Besier. An emg-driven musculoskeletal model to estimate muscle forces and knee joint moments in vivo. Journal of biomechanics, 36(6): 765–776, 2003.

[134] DG Lloyd and TS Buchanan. A model of load sharing between muscles and soft tissues at the human knee during static tasks. Journal of biomechanical engineering, 118(3):367–376, 1996.

[135] Thomas Lorrain, Ning Jiang, and Dario Farina. Influence of the training set on the accuracy of surface emg classification in dynamic contractions for the control of multifunction prostheses. Journal of NeuroEngineering and Rehabilitation, 8(1):25, May 2011. ISSN 1743-0003. doi: 10.1186/1743-0003-8-25. URL https://doi.org/10.1186/1743-0003-8-25.

[136] Madeleine M Lowery, Nikolay S Stoykov, Julius PA Dewald, and Todd A Kuiken. Volume conduction in an anatomically based surface emg model. IEEE Transactions on Biomedical Engineering, 51(12):2138–2147, 2004.

[137] Emily L Mackevicius, Andrew H Bahle, Alex H Williams, Shijie Gu, Natalia I Denisenko, Mark S Goldman, and Michale S Fee. Unsupervised discovery of temporal sequences in high-dimensional datasets, with applications to neuroscience. Elife, 8: e38471, 2019.

[138] Constantinos N Maganaris and John P Paul. In vivo human tendon mechanical properties, 1999.

[139] Kurt Manal, Roger V Gonzalez, David G Lloyd, and Thomas S Buchanan. A real-time emg-driven virtual arm. Computers in biology and medicine, 32(1):25–36, 2002.

[140] MATLAB version 9.5.0.1586782 (R2018b) Update 8. The Mathworks, Inc., Natick, Massachusetts, 2018.

[141] Martine McGregor. A Biomechanical Investigation of Load Sharing at the Distal Forearm. PhD thesis, 09 2017.

[142] Patrick E McKnight and Julius Najab. Mann-whitney u test. The Corsini encyclopedia of psychology, pages 1–1, 2010.

[143] Nicholas Metropolis, Arianna W Rosenbluth, Marshall N Rosenbluth, Augusta H Teller, and Edward Teller. Equation of state calculations by fast computing machines. The journal of chemical physics, 21(6):1087–1092, 1953.

[144] Theodore E Milner. Adaptation to destabilizing dynamics by means of muscle cocontraction. Experimental brain research, 143:406–416, 2002.

[145] Theodore E Milner and Caroline Cloutier. Compensation for mechanically unstable loading in voluntary wrist movement. Experimental Brain Research, 94:522–532, 1993.

[146] Theodore E Milner and Caroline Cloutier. Damping of the wrist joint during voluntary movement. Experimental brain research, 122:309–317, 1998.

[147] Djordje Mitrovic, Stefan Klanke, and Sethu Vijayakumar. Learning impedance control of antagonistic systems based on stochastic optimization principles. The International Journal of Robotics Research, 30(5):556–573, 2010. doi: 10.1177/0278364910387653.

[148] Federico Montagnani, Marco Controzzi, and Christian Cipriani. Is it finger or wrist dexterity that is missing in current hand prostheses? IEEE Transactions on Neural Systems and Rehabilitation Engineering, 23(4):600–609, 2015.

[149] Keith L Moore, Arthur F Dalley, and Anne MR Agur. Clinically oriented anatomy. Lippincott Williams & Wilkins, 2013.

[150] Jeremy Mouchoux, Stefano Carisi, Strahinja Dosen, Dario Farina, Arndt F Schilling, and Marko Markovic. Artificial perception and semiautonomous control in myoelectric hand prostheses increases performance and decreases effort. IEEE Transactions on Robotics, 37(4):1298–1312, 2021.

[151] Silvia Muceli and Dario Farina. Simultaneous and proportional estimation of hand kinematics from emg during mirrored movements at multiple degrees-of-freedom. IEEE transactions on neural systems and rehabilitation engineering, 20(3):371–378, 2011.

[152] Silvia Muceli and Dario Farina. Simultaneous and proportional estimation of hand kinematics from EMG during mirrored movements at multiple degrees-of-freedom. IEEE Transactions on Neural Systems and Rehabilitation Engineering, 20(3):371–378, 2012.

[153] Ferdinando A Mussa-Ivaldi, Neville Hogan, and Emilio Bizzi. Neural, mechanical, and geometric factors subserving arm posture in humans. Journal of neuroscience, 5 (10):2732–2743, 1985.

[154] Richard R Neptune, Steven A Kautz, and Felix E Zajac. Contributions of the individual ankle plantar flexors to support, forward progression and swing initiation during walking. Journal of biomechanics, 34(11):1387–1398, 2001.

[155] CP Neu, 3rd Crisco, JJ, and SW Wolfe. In vivo kinematic behavior of the radio-capitate joint during wrist flexion–extension and radio-ulnar deviation. Journal of biomechanics, 34(11):1429–1438, 2001.

[156] Johnny LG Nielsen, Steffen Holmgaard, Ning Jiang, Kevin B Englehart, Dario Farina, and Phil A Parker. Simultaneous and proportional force estimation for multifunction myoelectric prostheses using mirrored bilateral training. IEEE Transactions on Biomedical Engineering, 58(3):681–688, 2010.

[157] Chuanxin M Niu, Qi Luo, Chih-hong Chou, Jiayue Liu, Manzhao Hao, and Ning Lan. Neuromorphic model of reflex for realtime human-like compliant control of prosthetic hand. Annals of Biomedical Engineering, 49(2):673–688, 2021.

[158] Markus Nowak, Ivan Vujaklija, Agnes Sturma, Claudio Castellini, and Dario Farina. Simultaneous and proportional real-time myocontrol of up to three degrees of freedom of the wrist and hand. IEEE Transactions on Biomedical Engineering, 2022.

[159] Max Ortiz-Catalan, Bo Håkansson, and Rickard Brånemark. Real-time and simultaneous control of artificial limbs based on pattern recognition algorithms. IEEE Transactions on Neural Systems and Rehabilitation Engineering, 22(4):756–764, 2014.

[160] Max Ortiz-Catalan, Faezeh Rouhani, Rickard Brånemark, and Bo Håkansson. Offline accuracy: a potentially misleading metric in myoelectric pattern recognition for prosthetic control. In 2015 37th Annual International Conference of the IEEE Engineering in Medicine and Biology Society (EMBC), pages 1140–1143. IEEE, 2015.

[161] Rieko Osu, David W Franklin, Hiroko Kato, Hiroaki Gomi, Kazuhisa Domen, Toshinori Yoshioka, and Mitsuo Kawato. Short-and long-term changes in joint co-contraction associated with motor learning as revealed from surface emg. Journal of neurophysiology, 88(2):991–1004, 2002.

[162] James C Otis, Ching-Chuan Jiang, Thomas L Wickiewicz, MG Peterson, Russell F Warren, and Thomas J Santner. Changes in the moment arms of the rotator cuff and deltoid muscles with abduction and rotation. JBJS, 76(5):667–676, 1994.

[163] ottobock. URL https://www.presseportal.de/pm/32079/3938363.

[164] Lizhi Pan, Dustin Crouch, and He Huang. Musculoskeletal model for simultaneous and proportional control of 3-dof hand and wrist movements from emg signals. In 2017 8th International IEEE/EMBS Conference on Neural Engineering (NER), pages 325–328. IEEE, 2017.

[165] Lizhi Pan, Dustin L Crouch, and He Huang. Myoelectric control based on a generic musculoskeletal model: Toward a multi-user neural-machine interface. IEEE Transactions on Neural Systems and Rehabilitation Engineering, 26(7):1435–1442, 2018.

[166] Lizhi Pan, Andrew Harmody, and He Huang. A reliable multi-user emg interface based on a generic-musculoskeletal model against loading weight changes. In 2018 40th Annual International Conference of the IEEE Engineering in Medicine and Biology Society (EMBC), pages 2104–2107. IEEE, 2018.

[167] Liam Paninski. Estimation of entropy and mutual information. Neural computation, 15(6):1191–1253, 2003.

[168] Paul F. Pasquina, Melissa Evangelista, A.J. Carvalho, Joseph Lockhart, Sarah Griffin, George Nanos, Patricia McKay, Morten Hansen, Derek Ipsen, James Vandersea, Josef Butkus, Matthew Miller, Ian Murphy, and David Hankin. First-in-man demonstration of a fully implanted myoelectric sensors system to control an advanced electromechanical prosthetic hand. Journal of Neuroscience Methods, 244:85 – 93, 2015. ISSN 0165-0270. doi: https://doi.org/10.1016/j.jneumeth.2014.07.016. URL http://www.sciencedirect.com/science/article/pii/S0165027014002672. Brain Computer Interfaces; Tribute to Greg A. Gerhardt.

[169] Eric J. Perreault, Robert F. Kirsch, and Patrick E. Crago. Effects of voluntary force generation on the elastic components of endpoint stiffness. Experimental Brain Research, 141(3):312–323, Dec 2001. ISSN 1432-1106. doi: 10.1007/s002210100880. URL https://doi.org/10.1007/s002210100880.

[170] Eric J Perreault, Robert F Kirsch, and Patrick E Crago. Effects of voluntary force generation on the elastic components of endpoint stiffness. Experimental brain research, 141(3):312–323, 2001.

[171] Eric J. Perreault, Robert F. Kirsch, and Patrick E. Crago. Voluntary control of static endpoint stiffness during force regulation tasks. Journal of Neurophysiology, 87(6): 2808–2816, 2002. ISSN 0022-3077. URL http://jn.physiology.org/content/87/6/2808.

[172] Serge Pfeifer, Heike Vallery, Michael Hardegger, Robert Riener, and Eric J Perreault. Model-based estimation of knee stiffness. IEEE transactions on biomedical engineering, 59(9):2604–2612, 2012.

[173] JR Potvin, RW Norman, and SM McGill. Mechanically corrected emg for the continuous estimation of erector spinae muscle loading during repetitive lifting. European journal of applied physiology and occupational physiology, 74(1):119–132, 1996.

[174] Qualisys. URL https://www.qualisys.com/.

[175] PM Rack and HF Ross. The tendon of flexor pollicis longus: its effects on the muscular control of force and position at the human thumb. The Journal of physiology, 351(1): 99–110, 1984.

[176] V S Ramachandran and W Hirstein. The perception of phantom limbs. The D. O. Hebb lecture. Brain, 121(9):1603–1630, 09 1998. ISSN 0006-8950. doi: 10.1093/brain/121.9.1603. URL https://doi.org/10.1093/brain/121.9.1603.

[177] Aidan D Roche, Ben Lakey, Irene Mendez, Ivan Vujaklija, Dario Farina, and Oskar C Aszmann. Clinical perspectives in upper limb prostheses: An update. Current Surgery Reports, 7(3):1–10, 2019.

[178] E. Rohmer, S. P. N. Singh, and M. Freese. V-rep: A versatile and scalable robot simulation framework. In 2013 IEEE/RSJ International Conference on Intelligent Robots and Systems, pages 1321–1326, 2013. doi: 10.1109/IROS.2013.6696520.

[179] Massimo Sartori, Monica Reggiani, Dario Farina, and David G Lloyd. Emg-driven forward-dynamic estimation of muscle force and joint moment about multiple degrees of freedom in the human lower extremity. PloS one, 7(12):e52618, 2012.

[180] Massimo Sartori, Monica Reggiani, Enrico Pagello, and David G Lloyd. Modeling the human knee for assistive technologies. IEEE Transactions on Biomedical Engineering, 59(9):2642–2649, 2012.

[181] Massimo Sartori, Monica Reggiani, Antonie J van den Bogert, and David G Lloyd. Estimation of musculotendon kinematics in large musculoskeletal models using multi-dimensional b-splines. Journal of biomechanics, 45(3):595–601, 2012.

[182] Massimo Sartori, Marco Maculan, Claudio Pizzolato, Monica Reggiani, and Dario Farina. Modeling and simulating the neuromuscular mechanisms regulating ankle and knee joint stiffness during human locomotion. Journal of neurophysiology, 114(4): 2509–2527, 2015.

[183] Katherine R Saul, Wendy M Murray, VR Hentz, and Scott L Delp. Biomechanics of the steindler flexorplasty surgery: a computer simulation study. The Journal of hand surgery, 28(6):979–986, 2003.

[184] Katherine R Saul, Xiao Hu, Craig M Goehler, Meghan E Vidt, Melissa Daly, Anca Velisar, and Wendy M Murray. Benchmarking of dynamic simulation predictions in two software platforms using an upper limb musculoskeletal model. Computer methods in biomechanics and biomedical engineering, 18(13):1445–1458, 2015.

[185] Erik Scheme and Kevin Englehart. Electromyogram pattern recognition for control of powered upper-limb prostheses: state of the art and challenges for clinical use. Journal of Rehabilitation Research & Development, 48(6), 2011.

[186] Erik J Scheme, Kevin B Englehart, and Bernard S Hudgins. Selective classification for improved robustness of myoelectric control under nonideal conditions. IEEE Transactions on Biomedical Engineering, 58(6):1698–1705, 2011.

[187] RN Scott and PA Parker. Myoelectric prostheses: state of the art. Journal of medical engineering & technology, 12(4):143–151, 1988.

[188] Stephen H Scott and David A Winter. A comparison of three muscle pennation assumptions and their effect on isometric and isotonic force. Journal of biomechanics, 24(2):163–167, 1991.

[189] Carol Y Scovil and Janet L Ronsky. Sensitivity of a hill-based muscle model to perturbations in model parameters. Journal of biomechanics, 39(11):2055–2063, 2006.

[190] Harold H Sears and Julie Shaperman. Proportional myoelectric hand control: an evaluation. American journal of physical medicine & rehabilitation, 70(1):20–28, 1991.

[191] Jonathon W Sensinger, Blair A Lock, and Todd A Kuiken. Adaptive pattern recognition of myoelectric signals: exploration of conceptual framework and practical algorithms. IEEE Transactions on Neural Systems and Rehabilitation Engineering, 17(3):270–278, 2009.

[192] Jonathon W Sensinger et al. User-modulated impedance control of a prosthetic elbow in unconstrained, perturbed motion. IEEE Transactions on biomedical engineering, 55(3):1043–1055, 2008.

[193] Claude Elwood Shannon. A mathematical theory of communication. The Bell system technical journal, 27(3):379–423, 1948.

[194] Ahmed W Shehata, Leonard F Engels, Marco Controzzi, Christian Cipriani, Erik J Scheme, and Jonathon W Sensinger. Improving internal model strength and performance of prosthetic hands using augmented feedback. Journal of neuroengineering and rehabilitation, 15(1):1–12, 2018.

[195] KB Shelburne and MG Pandy. Determinants of cruciate-ligament loading during rehabilitation exercise. Clinical biomechanics, 13(6):403–413, 1998.

[196] Bruno Siciliano, Oussama Khatib, and Torsten Kröger. Springer handbook of robotics, volume 200. Springer, 2008.

[197] Lauren H Smith, Todd A Kuiken, and Levi J Hargrove. Evaluation of linear regression simultaneous myoelectric control using intramuscular emg. IEEE Transactions on Biomedical Engineering, 63(4):737–746, 2015.

[198] Lauren H Smith, Todd A Kuiken, and Levi J Hargrove. Evaluation of linear regression simultaneous myoelectric control using intramuscular emg. IEEE Transactions on Biomedical Engineering, 63(4):737–746, 2015.

[199] Martyna Stachaczyk, Seyed Farokh Atashzar, Sigrid Dupan, Ivan Vujaklija, and Dario Farina. Multiclass detection and tracking of transient motor activation based on decomposed myoelectric signals. In 2019 9th International IEEE/EMBS Conference on Neural Engineering (NER), pages 1080–1083. IEEE, 2019.

[200] Julia Starke, Pascal Weiner, Markus Crell, and Tamim Asfour. Semi-autonomous control of prosthetic hands based on multimodal sensing, human grasp demonstration and user intention. Robotics and Autonomous Systems, 154:104123, 2022.

[201] Dennis Tkach, He Huang, and Todd A Kuiken. Study of stability of time-domain features for electromyographic pattern recognition. Journal of neuroengineering and rehabilitation, 7(1):21, 2010.

[202] T. Tsuj, O. Fukuda, H. Shigeyoshi, and M. Kaneko. Bio-mimetic impedance control of an emg-controlled prosthetic hand. In Proceedings. 2000 IEEE/RSJ International Conference on Intelligent Robots and Systems (IROS 2000) (Cat. No.00CH37113), volume 1, pages 377–382 vol.1, 2000. doi: 10.1109/IROS.2000.894634.

[203] Toshio Tsuji, Yusaku Takeda, and Yoshiyuki Tanaka. Analysis of mechanical impedance in human arm movements using a virtual tennis system. Biological Cybernetics, 91(5):295–305, Nov 2004. ISSN 1432-0770. doi: 10.1007/s00422-004-0515-1. URL https://doi.org/10.1007/s00422-004-0515-1.

[204] Peter JM Van Laarhoven and Emile HL Aarts. Simulated annealing. In Simulated annealing: Theory and applications, pages 7–15. Springer, 1987.

[205] Arthur J van Soest and Maarten F Bobbert. The contribution of muscle properties in the control of explosive movements. Biological cybernetics, 69(3):195–204, 1993.

[206] Ivan Vujaklija. Novel control strategies for upper limb prosthetics. In International Conference on NeuroRehabilitation, pages 171–174. Springer, 2018.

[207] Ivan Vujaklija, Dario Farina, and Oskar C Aszmann. New developments in prosthetic arm systems. Orthopedic research and reviews, 8:31, 2016.

[208] Ivan Vujaklija, Vahid Shalchyan, Ernest N. Kamavuako, Ning Jiang, Hamid R. Marateb, and Dario Farina. Online mapping of emg signals into kinematics by autoencoding. Journal of NeuroEngineering and Rehabilitation, 15(1):21, Mar 2018. ISSN 1743-0003. doi: 10.1186/s12984-018-0363-1. URL https://doi.org/10.1186/s12984-018-0363-1.

[209] B Walmsley and U Proske. Comparison of stiffness of soleus and medial gastrocnemius muscles in cats. Journal of Neurophysiology, 46(2):250–259, 1981.

[210] Gang Wang, Zhiguo Yan, Xiao Hu, Hongbo Xie, and Zhizhong Wang. Classification of surface emg signals using harmonic wavelet packet transform. Physiological measurement, 27(12):1255, 2006.

[211] DR Wilkie. The mechanical properties of muscle. British medical bulletin, 12(3):177–182, 1956.

[212] Matthew R Williams and Robert F Kirsch. Evaluation of head orientation and neck muscle emg signals as command inputs to a human–computer interface for individuals with high tetraplegia. IEEE Transactions on Neural Systems and Rehabilitation Engineering, 16(5):485–496, 2008.

[213] David A Winter. Biomechanics and motor control of human movement. John Wiley & Sons, 2009.

[214] Jack M. Winters. Hill-Based Muscle Models: A Systems Engineering Perspective, pages 69–93. Springer New York, New York, NY, 1990. ISBN 978-1-4613-9030-5. doi: 10.1007/978-1-4613-9030-5_5. URL https://doi.org/10.1007/978-1-4613-9030-5_5.

[215] Jack M Winters. Hill-based muscle models: a systems engineering perspective. In Multiple muscle systems, pages 69–93. Springer, 1990.

[216] Jack M Winters and Lawrence Stark. Analysis of fundamental human movement patterns through the use of in-depth antagonistic muscle models. IEEE transactions on biomedical engineering, (10):826–839, 1985.

[217] Ge Wu, Frans CT Van der Helm, HEJ DirkJan Veeger, Mohsen Makhsous, Peter Van Roy, Carolyn Anglin, Jochem Nagels, Andrew R Karduna, Kevin McQuade, Xuguang Wang, et al. Isb recommendation on definitions of joint coordinate systems of various joints for the reporting of human joint motion—part ii: shoulder, elbow, wrist and hand. Journal of biomechanics, 38(5):981–992, 2005.

[218] Peng Xia, Jie Hu, and Yinghong Peng. Emg-based estimation of limb movement using deep learning with recurrent convolutional neural networks. Artificial organs, 42(5): E67–E77, 2018.

[219] Chenguang Yang, Gowrishankar Ganesh, Sami Haddadin, Sven Parusel, Alin Albu-Schaeffer, and Etienne Burdet. Human-like adaptation of force and impedance in stable and unstable interactions. IEEE transactions on robotics, 27(5):918–930, 2011.

[220] Shaowei Yao, Yu Zhuang, Zhijun Li, and Rong Song. Adaptive admittance control for an ankle exoskeleton using an emg-driven musculoskeletal model. Frontiers in Neurorobotics, 12:16, 2018. ISSN 1662-5218. doi: 10.3389/fnbot.2018.00016. URL https://www.frontiersin.org/article/10.3389/fnbot.2018.00016.

[221] Aaron J Young, Lauren H Smith, Elliott J Rouse, and Levi J Hargrove. Classification of simultaneous movements using surface emg pattern recognition. IEEE Transactions on Biomedical Engineering, 60(5):1250–1258, 2012.

[222] George I Zahalak. Modeling muscle mechanics (and energetics). Multiple muscle systems, pages 1–23, 1990.

[223] Felix E Zajac and Michael E Gordon. Determining muscle's force and action in multi-articular movement. Exercise and sport sciences reviews, 17(1):187–230, 1989.

[224] Felix E. Zajac, Richard R. Neptune, and Steven A. Kautz. Biomechanics and muscle coordination of human walking: Part i: Introduction to concepts, power transfer, dynamics and simulations. Gait & Posture, 16(3):215 – 232, 2002. ISSN 0966-6362. doi: https://doi.org/10.1016/S0966-6362(02)00068-1. URL http://www.sciencedirect.com/science/article/pii/S0966636202000681.

[225] Zhengmin Zhang. Estimating mutual information via kolmogorov distance. IEEE Transactions on Information Theory, 53(9):3280–3282, 2007.

Appendix A

Simulated annealing

Simulated annealing (SA) [113] is a stochastic global search optimization method, suitable for non-linear or discontinuous objective functions. The algorithm is based on the Metropolis Monte Carlo integration algorithm [143], extended to include a temperature-based schedule to improve the efficiency of the algorithm's searching. The term "annealing" refers to the process of heating a material and then slowly cooling it, to change its physical and chemical properties. The temperature t is a key parameter used for regulating the probability of accepting a new point and it is obtained according to an annealing schedule Temperature. The main steps of SA are briefly explained below and outlined in Algorithm 1. Given an

Algorithm 1 Pseudocode of simulated annealing

$x \leftarrow x_0$
$e \leftarrow E(x_0)$
$t \leftarrow t_0 > 0$
$i \leftarrow 0$
while stop criteria not met **do**
    Randomly select x_{test} in the neighborhood of x
    $e_{test} = E(x_{test})$
    if $e_{test} - e < 0$ **then**
        $x \leftarrow x_{test}$
        $e \leftarrow e_{test}$
    else if $P(e, e_{test}, t) > x_{rand} = Random(0,1)$ **then**
        $x \leftarrow x_{test}$
        $e \leftarrow e_{test}$
    end if
    $k \leftarrow k+1$
    $t \leftarrow Temperature(k)$
end while

initial point x_0, the initial value of the cost function $E(x_0)$, and an initial temperature t_0, at each iteration k, the algorithm makes the following steps:

- A new solution is randomly generated in a neighbourhood of the current solution and the objective function value $E(x_{test})$ for x_{test} is computed.
- The distance of the new point from the current point is based on a probability distribution with a scale proportional to the temperature. The probability of making the transition from the current state x to the candidate state x_{test} depends on the acceptance probability $P(e, e_{test}, t)$. The algorithm accepts the new point if it lowers the cost. If the solution x_{test} raises the objective function value (i.e., $e_{test} > e$), a random number x_{rand} is generated between 0 and 1. The probability of transitioning to the new solution depends on the acceptance probability P, and it may be proportional to the temperature and inverse proportional to $e_{test} - e$ (e.g., the Boltzman distribution [204]). if $x_{test} < P(e, e_{test}, t)$ the solution is accepted. This allows the optimization process to avoid getting trapped in local minima and increases the chances of global exploration of the solutions.
- The temperature is reduced from the initial value to zero according to an annealing schedule defined by the function Temperature(). A linear, slow decrease rule may be used, which reduces the temperature at a different rate.

This process of searching is repeated until a stopping criterion is met (e.g., the maximum number of iterations is reached, or objective function value reduction is below tolerance). The temperature plays a key role in the algorithm as it affects the probability of accepting a new point that raises the objective function values. Reducing the temperature is equivalent to decreasing the chance of accepting solutions that raise the objective function values (i.e., the extent of the search is decreased). Increasing the temperature increases the chance of accepting a worse solution together with the chance of escaping a local minimum. A reannealing step may be used to increase the temperature after a number of points have been accepted, by modifying the iteration number according to the current and initial temperature, and the objective function values.

Appendix B

Concepts underlying used performance measures

Below, we summarise fundamental concepts underlying the performance measures used for the evaluation of the online task experimental results described in Section 5.3.2.

B.1 Mutual Information

Mutual information [167] is a concept from information theory that quantifies the information that can be obtained about a random variable X, given another random variable Y. To mathematically define MI, the concept of entropy is first introduced. In the following derivations, we consider discrete random variables X and Y acting over the sets X and X.

The entropy H(X) quantifies the expected uncertainty about X and it is mathematically formulated as follows:

$$H(X) = -\sum_{x \in X} P(x) \log P(x) \tag{B.1}$$

Given the joint probability P(X,Y), the conditional entropy H(X|Y) is defined as follows:

$$H(X|Y) = -\sum_{x \in X} \sum_{y \in Y} P(x,y) \log P(x|y) \tag{B.2}$$

The conditional entropy quantifies the remaining uncertainty about X given the value of Y.

Based on the definition of entropy and conditional entropy, the mutual information MI(X,Y) is defined as follows:

$$MI(X,Y) = H(X) - H(X|Y) = \sum_{x \in X} \sum_{y \in Y} P(x,y) \log \frac{P(x,y)}{P(x)P(y)} \tag{B.3}$$

Where P(x) and P(y) are the marginal distribution, and P(x,y) is the joint distribution of X and Y. The logarithm may be the natural logarithm or the base 2 logarithm, and the MI is then expressed in [nats] or [bits] respectively. The mutual information between two variables is zero if and only if these are statistically independent. Considering the concept of entropy, MI is interpreted as the reduction in the uncertainty of a random variable due to the knowledge of the other random variable. The relation between MI(X,Y), H(X), H(Y) and H(X|Y) is

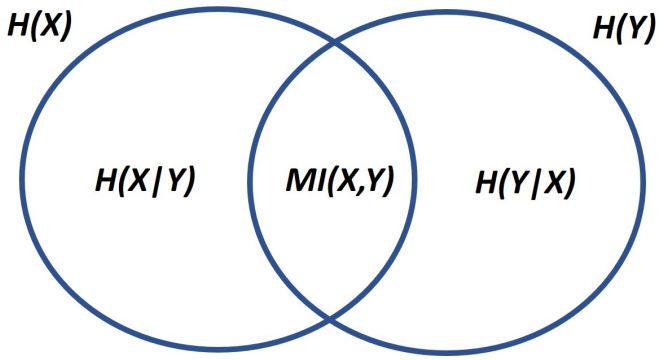

Figure B.1: Venn diagram showing the relation between mutual information and entropy of two random variables X and Y.

illustrated in Figure B.1 using the Venn diagram. The MI of X and Y, given another discrete random variable Z, is given by the following equation:

$$MI(X,Y|Z) = H(X|Z) - MI(X|Y,Z) \tag{B.4}$$

B.2 Measure of motion smoothness

The SPectral ARC length (SPARC) measure [14] is based on the Spectral Arc Length measure (SAL) [13], used in motor control and rehabilitation research to estimate the smoothness of a discrete motion trajectory. Both measures are based on the concept that a smoother movement is composed of a lower amount of high-frequency components. Moreover, it is assumed that the Fourier spectrum of a smooth time domain signal tends to be smooth. The Fourier magnitude spectrum can therefore be used to quantify the smoothness of a time domain trajectory. Given the velocity trajectory $v(t)$ and its Fourier magnitude spectrum $V(\omega)$, The SAL measure in frequency range $0-\omega_c$ is defined as follows:

$$SAL \triangleq -\int_0^{\omega_c} \left[\left(\frac{1}{\omega_c}\right) + \left(\frac{d\hat{V}(\omega)}{d\omega}\right)\right]^{\frac{1}{2}} d\omega \tag{B.5}$$

where $\hat{V}(\omega)$ is the Fourier magnitude spectrum normalised with respect to $V(0)$. In SPARC, ω_c is defined in an adaptive manner, depending on a threshold on V and an upper bound limit on ω_c, indicated as ω_c^{max} and defined as follows:

$$\omega_c \triangleq min\Big\{\omega_c^{max}, min\Big\{\omega, \hat{V}(r) < \frac{V(r)}{V(0)} \; \forall \; r > \omega\Big\}\Big\} \tag{B.6}$$

Both SAL and SPARC share properties that are key for a measure to appropriately quantify the degree of smoothness. However, differently from SAL, SPARC is not dependent on the movement amplitude and duration. This improvement allows to the definition of a standard measure that can be used across different types of movements. The code provided in [14] is used to implement the SPARC measure within this thesis.

Appendix C

Offline experiments: additional results

In this appendix, we include additional information on the optimization of the proposed framework and the baseline. We report the average muscle-tendon parameters' values across the able-bodied subjects in Table C.1 and for the amputee in Table C.2, respectively. An example of a trained model is considered and the force-length-velocity (Figure C.1) and impedance-force-velocity (Figure C.2) three-dimensional curves are shown. In Figure C.3 and Figure C.4, we show the offline evaluation of the methods for the amputee. The trials for the evaluation are chosen after visually inspecting the sEMG data, to make sure the amputee is performing the correct motion. In fact, there were instances where the subject performed flexion instead of extension, for example. As described in Section 5.3.1 the reference joint trajectory q_f^{train} for the amputee corresponds to the trajectory of the visual cue shown on the screen to guide the muscle contraction during the data acquisition experiment. The positive and negative peaks of q_f^{train} have been automatically aligned to match, where possible, the peaks found in the signal obtained as the difference between the two sEMG signals.

Table C.1: Average values of the muscle-tendon models' parameters for the able-bodied subjects.

	Parameter name	Variable	Lower Bound	Upper Bound	$MTU_1(mean)$	$MTU_1(std)$	$MTU_1(mean)$	$MTU_2(std)$
CE	F_{max}	$\bar{p}_1$	1000	9000	8.0832e+03	1.8728e+03	8.1738e+03	1.7937e+03
	l_{opt}	$\bar{p}_2 l_{ce}^{init}$	$0.05 l_{ce}^{init}$	$0.085 l_{ce}^{init}$	0.0850	1.4836e-17	0.0849	1.7263e-04
	ΔW_{des}	$\bar{p}_3 \bar{p}_2$	$0.7\bar{p}_2$	$3.5\bar{p}_2$	0.2975	0.0116	0.2548	0.0422
	ΔW_{asc}	$\bar{p}_4 \bar{p}_2$	$0.7\bar{p}_2$	$3.5\bar{p}_2$	0.3026	0.0151	0.2999	0.0178
	v_{des}	$\bar{p}_5$	1.2	4	1.9498	1.1521	1.5665	0.5501
	v_{asc}	$\bar{p}_6$	1.2	4	3.6641	0.9039	3.6421	0.5726
	A_{rel0}	$\bar{p}_7$	0.1	0.4	0.1234	0.0465	0.1161	0.0456
	B_{rel0}	$\bar{p}_8$	1.1	5.1	1.3863	0.4383	1.0051	0.1284
PE	l_{pe0}	$\bar{p}_9 \bar{p}_2$	$0.7\bar{p}_2$	$0.95\bar{p}_2$	0.7000	1.1869e-16	0.7000	1.1869e-16
	v_{pe}	$\bar{p}_{10}$	1.1	3	2.1689	0.1581	1.9219	0.0975
	$\hat{F}_{pe0}$	$\bar{p}_{11} \bar{p}_1$	$0.5\bar{p}_1$	$1\bar{p}_1$	0.7473	0.0216	0.7314	0.0175
DE	D_{de}	$\bar{p}_{12}$	0.001	3	2.6328	0.2848	2.3750	0.2799
	R_{de}	$\bar{p}_{13}$	0	0.8	0.0378	0.0117	0.0417	0.0010
SE	l_{se0}	$\frac{2}{3} l_{MTU}$	$\frac{2}{3} l_{MTU}$	$\frac{2}{3} l_{MTU}$	0.2000	2.9672e-17	0.2000	2.9672e-17
	ΔU_{senl}	$\bar{p}_{14}$	0.02	0.07	0.0557	0.0035	0.0513	0.0077
	ΔU_{sel}	$\bar{p}_{14} \bar{p}_{15}$	$(1/3)\bar{p}_{15}$	$(2/3)\bar{p}_{15}$	0.0327	0.0071	0.0317	0.0053
	ΔF_{se0}	$\bar{p}_{16} \bar{p}_1$	$0.3\bar{p}_1$	$1\bar{p}_1$	2.5409e+03	748.2483	2.8338e+03	707.7229
	S_{ecc}	$\bar{p}_{17}$	1.2	2	1.5533	0.3405	1.2944	0.1325
	F_{ecc}	$\bar{p}_{18}$	0.5	2	1.6572	0.1281	1.7487	0.0071

Table C.2: Values of muscle-tendon models' parameters for the amputee.

	Prameter Name	Variable	Lower Bound	Upper Bound	MTU_1	MTU_2
CE	F_{max}	$\bar{p}_1$	1000	9000	6.7945e+03	7.1809e+03
	l_{opt}	$\bar{p}_2 l_{ce}^{init}$	$0.05 l_{ce}^{init}$	$0.085 l_{ce}^{init}$	0.0850	0.0850
	ΔW_{des}	$\bar{p}_3 \bar{p}_2$	$0.7\bar{p}_2$	$3.5\bar{p}_2$	0.3400	0.3387
	ΔW_{asc}	$\bar{p}_4 \bar{p}_2$	$0.7\bar{p}_2$	$3.5\bar{p}_2$	0.3400	0.3400
	v_{des}	$\bar{p}_5$	1.2	4	1.4807	1.2112
	v_{asc}	$\bar{p}_6$	1.2	4	3	3
	A_{rel0}	$\bar{p}_7$	0.1	0.4	0.2250	0.1000
	B_{rel0}	$\bar{p}_8$	1.1	5.1	1.7750	1.1500
PE	l_{pe0}	$\bar{p}_9 \bar{p}_2$	$0.7\bar{p}_2$	$0.95\bar{p}_2$	0.7000	0.7000
	v_{pe}	$\bar{p}_{10}$	1.1	3	1.7500	2.1250
	$\hat{F}_{pe0}$	$\bar{p}_{11} \bar{p}_1$	$0.5\bar{p}_1$	$1\bar{p}_1$	0.7359	0.7359
DE	D_{de}	$\bar{p}_{12}$	0.001	3	2.8438	2.5938
	R_{de}	$\bar{p}_{13}$	0	0.8	0.0500	0.0422
SE	l_{se0}	$\frac{2}{3} l_{MTU}$	$\frac{2}{3} l_{MTU}$	$\frac{2}{3} l_{MTU}$	0.2000	0.2000
	ΔU_{senl}	$\bar{p}_{14}$	0.02	0.07	0.0576	0.0576
	ΔU_{sel}	$\bar{p}_{14} \bar{p}_{15}$	$(1/3)\bar{p}_{15}$	$(2/3)\bar{p}_{15}$	0.0372	0.0376
	ΔF_{se0}	$\bar{p}_{16} \bar{p}_1$	$0.3\bar{p}_1$	$1\bar{p}_1$	5.6904e+03	2.4236e+03
	S_{ecc}	$\bar{p}_{17}$	1.2	2	1.9734	1.9813
	F_{ecc}	$\bar{p}_{18}$	0.5	2	1.5038	1.7557

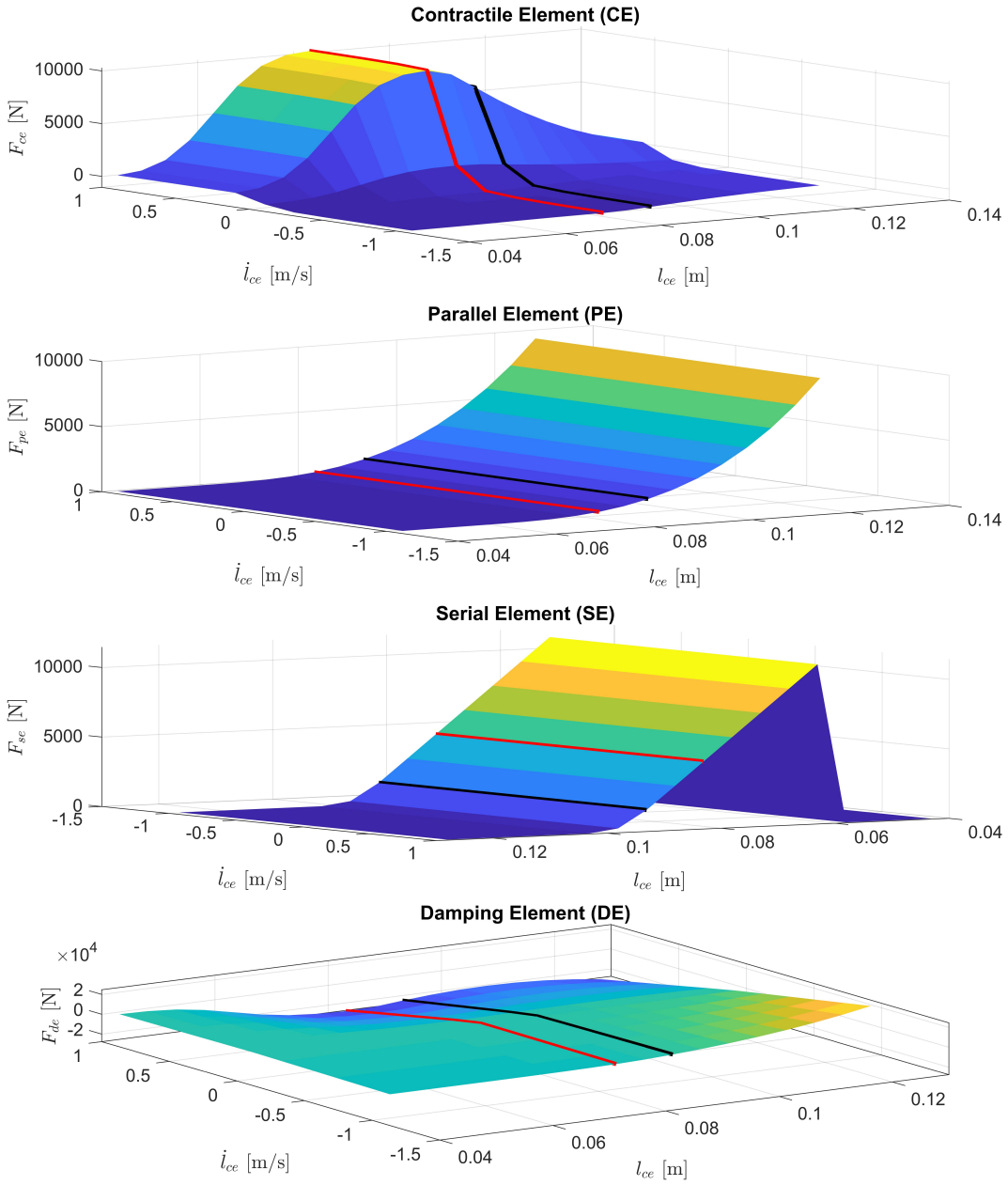

Figure C.1: Three-dimensional plot of the force-length-velocity surfaces for the elements of an MTU. The black line indicates the initial muscle length, while the red line is the optimal muscle length.

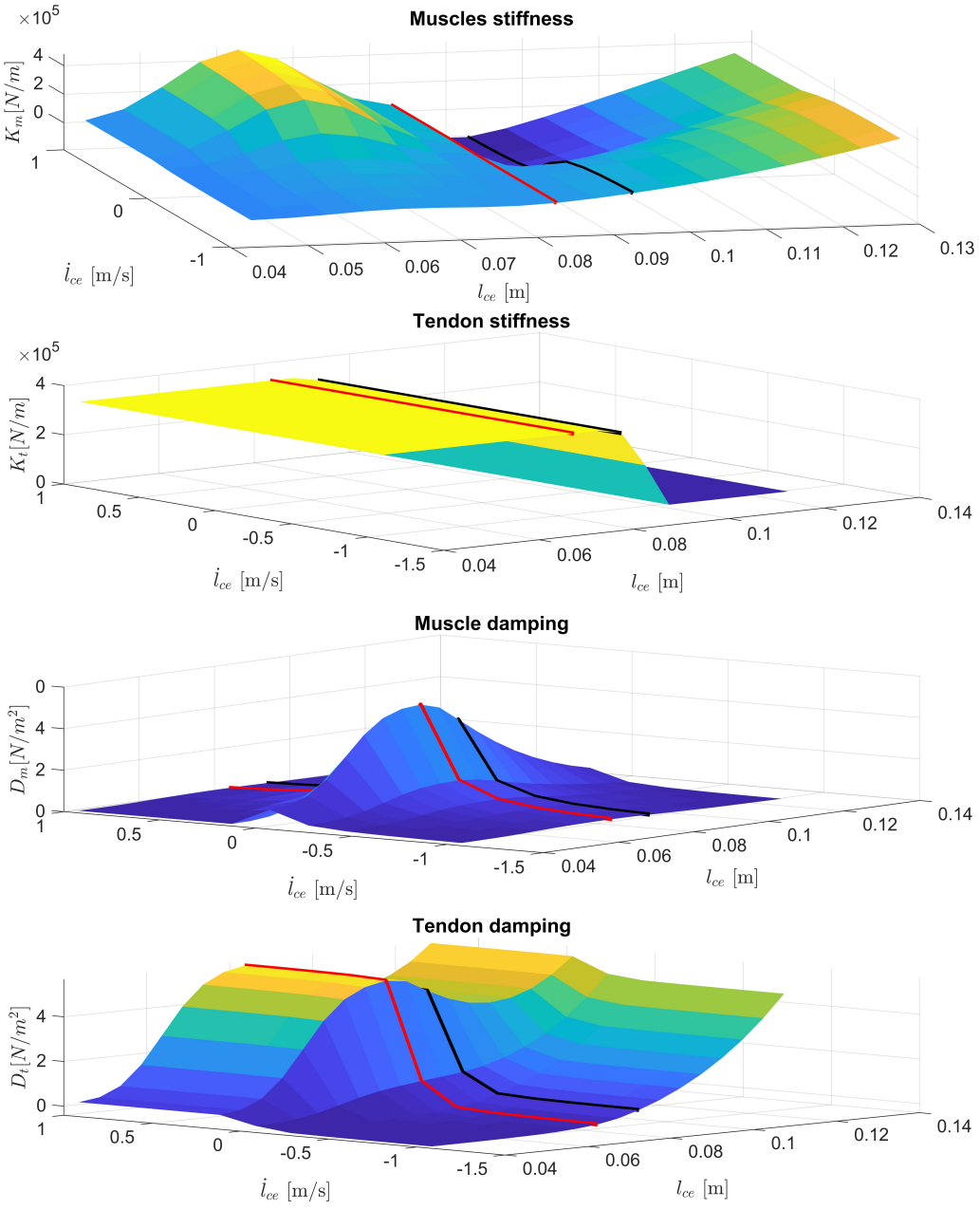

Figure C.2: Three-dimensional plot of the impedance-length-velocity surfaces for the elements of an MTU. Stiffness and damping are considered. The black line indicates the initial muscle length, while the red line is the optimal muscle length.

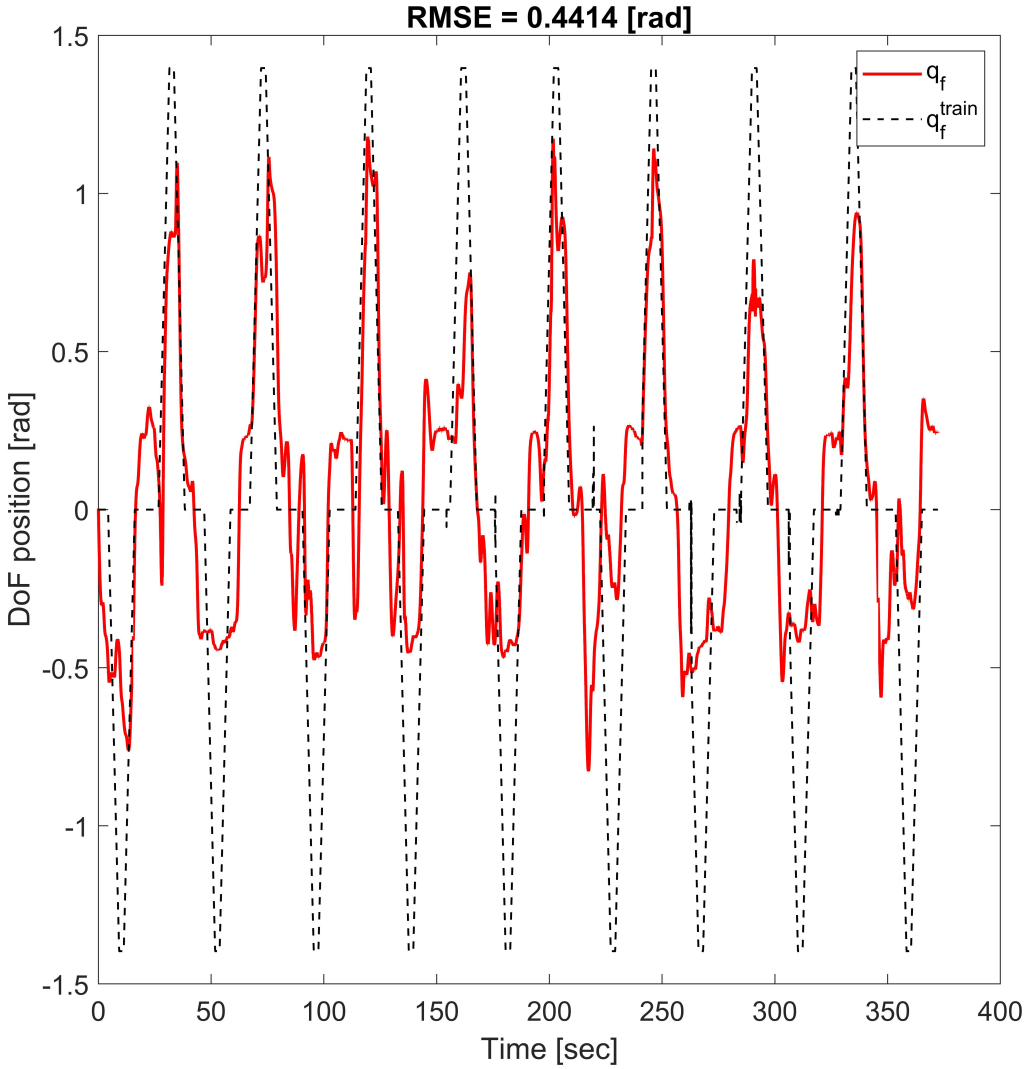

Figure C.3: Trajectory tracking during offline evaluation of the proposed framework. The black dotted line is the ground truth position (q_f^{train}) of the flexion-extension DoF. For the amputee, q_f^{train} corresponds to the visual cue used during data collection to guide the subject's muscle contraction or wrist motion.

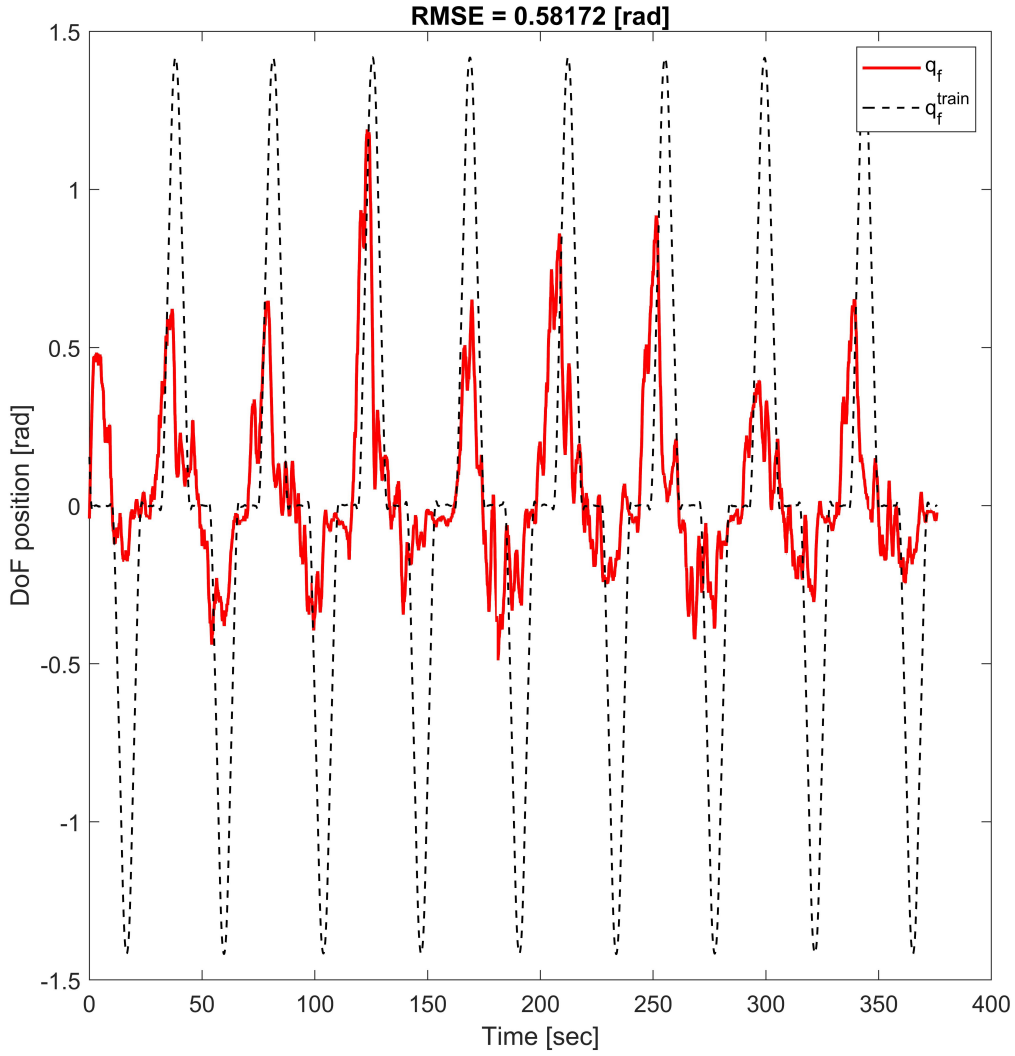

Figure C.4: Trajectory tracking during offline evaluation of the baseline. The black dotted line is the ground truth position (q_f^{train}) of the flexion-extension DoF. For the amputee, q_f^{train} corresponds to the visual cue used during data collection to guide the subject's muscle contraction or wrist motion.

Appendix D

Model of Puma 560 robot

Table D.1: Description of the dynamic parameters of the two first links of the Puma 560 robot. For each $link_i$ (i = 1,2) we report the mass, the center of mass (CoM), and the diagonal terms of the link's inertia. According to the DH convention [196] d_i, a_i and α_i are the link length, offset and twist, respectively.

Dynamics parameters			
Link i	Mass [Kg]	CoM [m]	Inertia [Kgm^2]
1	0	[0 0 0]	[0 0.35 0]
2	17.40	[0.068 0.006 -0.016]	[0.130 0.524 0.539]

DH parameters				
Joint i	α_{i-1} [deg]	θ_i [deg]	a_{i-1} [m]	d_i [m]
1	90	q_{1}	0	0
2	0	q_{2}	0.4318	0

In Table D.1, we report the dynamic parameters and the Denavit-Hartenberg (DH) parameters defining the structure of the robot model used in this work. We consider only the first two joints of the original model of the Puma robot [11]. The second DoF is actively controlled with the methods discussed in the thesis.